Structural and Spectroscopic Studies of Molecular Semiconductor Donor:Acceptor Systems for Organic Optoelectronics

Dissertation

der Mathematisch-Naturwissenschaftlichen Fakultät

der Eberhard Karls Universität Tübingen

zur Erlangung des Grades eines

Doktors der Naturwissenschaften

(Dr. rer. nat.)

vorgelegt von
Giuliano Duva
aus
Rom, Italien

Tübingen

2019

Gedruckt mit Genehmigung der Mathematisch-Naturwissenschaftlichen Fakultät der Eberhard Karls Universität Tübingen

Tag der mündlichen Prüfung:	24.05.2019
Dekan:	Prof. Dr. Wolfgang Rosenstiel
1. Berichterstatter:	Prof. Dr. Frank Schreiber
2. Berichterstatter:	JProf. Kaharina Broch

to Antonella

CONTENTS

DEUTSCHE ZUSAMMENFASSUNG

Organische Halbleiter sind faszinierende Systeme. Sie sind in den letzten Jahrzehnten von immer größer werdendem Interesse für optoelektronische Anwendungen und haben für sich ein wichtiges Stück Markt gewonnen. Ein Beispiel ist die Herstellung von OLED-Bildschirmen. Auf der anderen Seite bieten sie weiterhin spannende Herausforderungen in der Festkörper Physik. Die Möglichkeiten der chemischen Synthese, immer neue Materialien durch passende Funktionalisierungen zu erzeugen, bietet fruchtbaren Boden zur Untersuchung der strukturellen und optischen Eigenschaften und ihren Zusammenhang in dünnen organischen Schichten. Die in dieser Dissertation hauptsächlich untersuchten Halbleitersysteme gehören, im Gegensatz zu den Polymeren, zu der Kategorie der kleinen Moleküle. Solche Molekularen Halbleiter können durch Vakuumdeposition auf Substrate aufgedampft werden. Diese Methode ermöglicht einen hohen Kontrollgrad mit Blick auf die Wachstumsmechanismen auf einem Substrat.

Diese Arbeit fokussiert sich auf Donor:Akzeptor Systeme (D:A Systeme) hergestellt mittels *Organic Molecular Beam Deposition* (OMBD). Solche Mischsysteme sind interessant, denn sie betreffen das viel diskutierte Thema der Moleküldotierung zur Steigerung der Leitfähigkeit funktioneller organischer Schichten in optoelektronischen Bauelementen. Der Begriff der Moleküldorierung ist an den klassischen Begriff der Dotierung in anorganischen Halbleitern wie Silizium angelehnt und bezeichnet den Zusatz kleiner molekularer Halbleiter zu bestehenden organischen Schichten zwecks der Erzeugung von freien Ladungsträgern. Es existieren verschiedene Modelle, die versuchen, die mikroskopischen Mechanismen der Moleküldorierung in D:A Systemen in Bezug auf Wechselwirkungen durch Ladungstransfer nachzuvollziehen. Bei Polymersystemen können solche Wechselwirkungen einem Ionisationsprozess zugeordnet werden. In D:A Systemen bestehend aus kleinen Molekülen geschieht der Prozess des Ladungstransfers oft schon im Grundzustand innerhalb eines supramolekularen Komplexes, häufig D:A Komplex genannt.

In dieser Arbeit wurden organische Dünnschichtsystemen, genauer D:A Mischungen, mit OMBD nach der sogenannten *Bulk Heterojunction* Architektur hergestellt, d.h. die Donor- und Akzeptor-Moleküle wurden gleichzeitig auf das Substrat aufgedampft. Mithilfe einer solchen Architektur kann man die Anzahl an D:A Komplexen maximieren und dadurch den Aufbau von D:A Co-kristallen beobachten. Die optischen und strukturellen Eigenschaften von D:A Co-kristallen und deren Zusammenhang lassen sich am besten untersuchen, indem man das D:A Mischungsverhältnis in den Filmen systematisch variiert. Dies stellt gleichzeitig eine Annährung zur Untersuchung der Einzelsysteme dar. Die Untersuchung der strukturellen Eigenschaften schließt den Effekt der Molekülorientierung mit ein, was für anisotropische molekulare Halbleiter einen grundlegenden Aspekt darstellt, der in der Literatur häufig nicht erwähnt wird. Diese Arbeit leistet daher einen wichtigen Beitrag: es wird ein breiteres Verständnis bezüglich der strukturellen und optischen Eigenschaften und deren Zusammenhangs in organischen Dünnschichten gewonnen. Dies bezieht sich im Besonderen auf die Erweiterung der untersuchten D:A Materialkombinationen und auf die Berücksichtigung des Effekts der Orientierung in anisotropischen molekularen Halbleitern. Die in dieser Arbeit enthaltenen Ergebnisse bieten daher eine erweiterte Perspektive für die Entwicklung optoelektronischer Bauelemente aus organischen Halbleitermaterialien.

Im folgenden wird ein kurzer Überblick über die Inhalte der Dissertation gegeben. In Kapitel eins wird eine Einführung der für diese Arbeit relevanten Themen gegeben. Im zweiten Kapitel werden die wichtigsten Aspekte der Theorie zu molekularen Halbleitern und deren Wechselwirkung mit Strahlung vorgestellt. Kapitel drei beinhaltet eine umfassende Beschreibung der verwendeten experimentellen Methoden, insbesondere die zur Röntgenstreuung an Oberflächen und zur Infrarot-Spektroskopie. In Kapitel vier sind die Ergebnisse nach Absätzen wie folgt organisiert.

- *Kapitel 4.1. Vergleichsstudie zu den strukturellen und optischen Eigenschaften der zwei D:A Paare DIP:F6TCNNQ und 6T:F6TCNNQ.* Für beide Systeme wird der Aufbau eines Co-kristalls beobachtet. Allerdings findet man für DIP:F6TCNNQ eine ausgeprägtere anisotropische 2D-Filmstruktur als für 6T:F6TCNNQ, was sich in der Anisotropie der optischen Absorption im sichtbaren und nahen Infrarot-Bereich widerspiegelt.

- *Kapitel 4.2. Echtzeit-Messungen für DIP:F6TCNNQ Mischungen mit DIP-Überschuss mittels Röntgenreflektivität.* Die Modellierung von Echtzeit-Daten ermöglicht es, wertvolle Informationen zur Entwicklung der Rauigkeit an der Oberfläche in Abhängigkeit der Filmdicke und des D:A Mischungsverhältnisses zu erhalten. Dies erlaubt es, Wachstumsprozesse in gemischten aber phasen-getrennten Systemen zu beschreiben.

- *Kapitel 4.3. Orientierungskontrolle bei stäbchenförmigen (*rod-like*) organischen Halbleitermolekülen.* Es wurde ein Herstellungsverfahren auf Basis von OMBD entwickelt, mit dessen Hilfe es möglich ist, die Molekülorientierung so zu beeinflussen, dass die lange Achse der Moleküle parallel zum Substrat liegt und die organischen Schichten einen kristallinen Aufbau haben. Der Effekt der Umorientierung der Moleküle auf ihre optischen Eigenschaften wird gezeigt und unterscheidet sich je nach System. Die Orientierungskontrolle war auch für die DIP:F6TCNNQ Co-kristalle möglich.

- *Kapitel 4.4. Quantifizierung von Ladungstransfer im Grundzustand.* Mittels polarisationsmodulierter Infrarot-Reflexions-Absorptions-Spektroskoopie (PM-IRRAS) unterstützt von komplementärer Charakterisierung durch Röntgenstreuung wird der Grad an Ladungstransfer im Grundzustand bei DIP:F6TCNNQ-Filmen quantifiziert. Der Vergleich mit den Ergebnissen des Polymersystems P3HT:F6TCNNQ liefert neue Erkenntnisse zur genauen Charakterisierung des Ladungstransfers.

- *Kapitel 4.5. Charakterisierung zusätzlicher D:A Systeme* Im ersten Teil dieses Kapitels wird eine Vergleichsstudie zwischen den D:A Systemen DIP:TCNNQ und DIP:F6TCNNQ vorgestellt, in der die elektrische Leitfähigkeit dem jeweiligen Mischungsverhältnis zugeordnet wird. Im zweiten Teil werden Röntgenstreuungsdaten zur Bestimmung der Einheitszellen des Donors DBTTF und seiner Co-Kristalle mit den jeweiligen Akzeptoren TCNNQ und F6TCNNQ verwendet. Die Parameter der Einheitszelle von DBTTF und vom DBTTF:TCNNQ Co-Kristall konnten dank der guten 2D Textur gefittet werden. Für DBTTF:F6TCNNQ konnte keine Einheitszelle angepasst werden. Für das DBTTF:TCNNQ Co-Kristall wurden zwei Polymorphe gefunden.

Kapitel fünf fasst die Ergebnisse dieser Arbeit zusammen und fasst sie in einem Kontext. Zudem werden zukünftige Möglichkeiten für Anwendungen in optoelektronischen Bauelementen vorgestellt. Im sechsten Kapitel Daten angehängt, die die in Kapitel vier gezeigten Ergebnisse und geführten Diskussionen weiter unterstützen und vervollständigen.

CHAPTER 1

INTRODUCTION

This chapter contains the motivation for the work behind this thesis. Several applications of organic semiconductors are shown, with focus on the functional properties of thin films. Such functional properties are discussed in relationship to the concepts of heterostructure and molecular doping of organic materials via *donor:acceptor charge-transfer interactions. In this context, a quick overview of the literature concerning molecular doping is given and some models proposed to describe the generation of free charge carriers are briefly discussed. The convergence of heterostructure and donor:accaptor charge-transfer interactions to the study of donor:acceptor co-crystals is delineated. Finally an overview of the contents of this thesis is given.*

The discovery of conductive properties in iodine-doped polymer polyacetylene in the late '70s by the group of Heeger [1] represented a technological paradigm shift of organic materials with semiconducting properties. The possibility of achieving high conductivities and/or mobilities in conjugated organic materials has paved the way to their use in a number of applications. In particular, since the beginning of the XXI century there has been a tremendous flourishing of devices at least partially employing organic molecular semiconductors (OSCs). This phenomenon goes so far, that many companies producing electronic appliances reserve a slice of their production for including OSC-based technology (mostly displays) in their products.

1.1 State of the art, motivation and aims of the thesis

It will be useful, now, to broadly classify organic semiconducting materials into two groups: oligomers and polymers. In order to undock the definition of oligomeric semiconducting materials from just being building blocks of polymers, in the course of this thesis the use of the word "oligomer" will be mostly dropped in favor of the common wording "small molecules" or "small-molecular OSCs", as opposed to semiconducting polymers. Due to their tunable electronic properties and wide range of structural properties, OSCs are perfectly suitable for being used in different (opto-)electronic devices, examples of which are shown in Fig. 1.1. Here, for the sake of brevity, only a summary illustration of the several applications is given. For an exhaustive discussion of the several device applications of OSCs and the physical mechanisms underlying them, the reader is addressed to specialized literature.

For instance, organic field-effect transistors (OFETs, Fig. 1.1a) with very high ON/OFF ratios have been demonstrated employing a huge variety of OSCs in several device architectures [2]. Polymeric [3, 4] as well as small-molecular materials [5, 6] and mixtures of them [7] have been employed in thin films and molecular single crystals [8, 9] in a number of works, of which the collection we [1] present here constitutes only a very small portion. For such devices p-, n- and

[1] The personal pronoun "we" indicates, as it is common in the scientific literature, me and the group of people I have been working with during my doctoral studies. Without this teamwork, none of the contents of this thesis could have been produced, therefore this pronoun assumes the meaning "we as a group".

ambipolar transport has been demonstrated [10–14].

The application of OSCs in sensors (Fig. 1.1b) is closely related to their use in OFETs. Indeed, embedding the functional organic film in an OFET architecture represents the simplest way to transpose the "sensing" signal to an external circuit. The electric signal carried by such sensors can originate by several sources [15, 16]: interactions with analytes, pressure or acoustic waves, temperature, light or magnetic fields. Interestingly, the OSC active layer(s) can be functionalized with suitable chemical groups in order to increase the sensitivity to a given analyte [17]. In general, many efforts are being devoted to the optimization of the selectivity and sensitivity in such devices [18, 19].

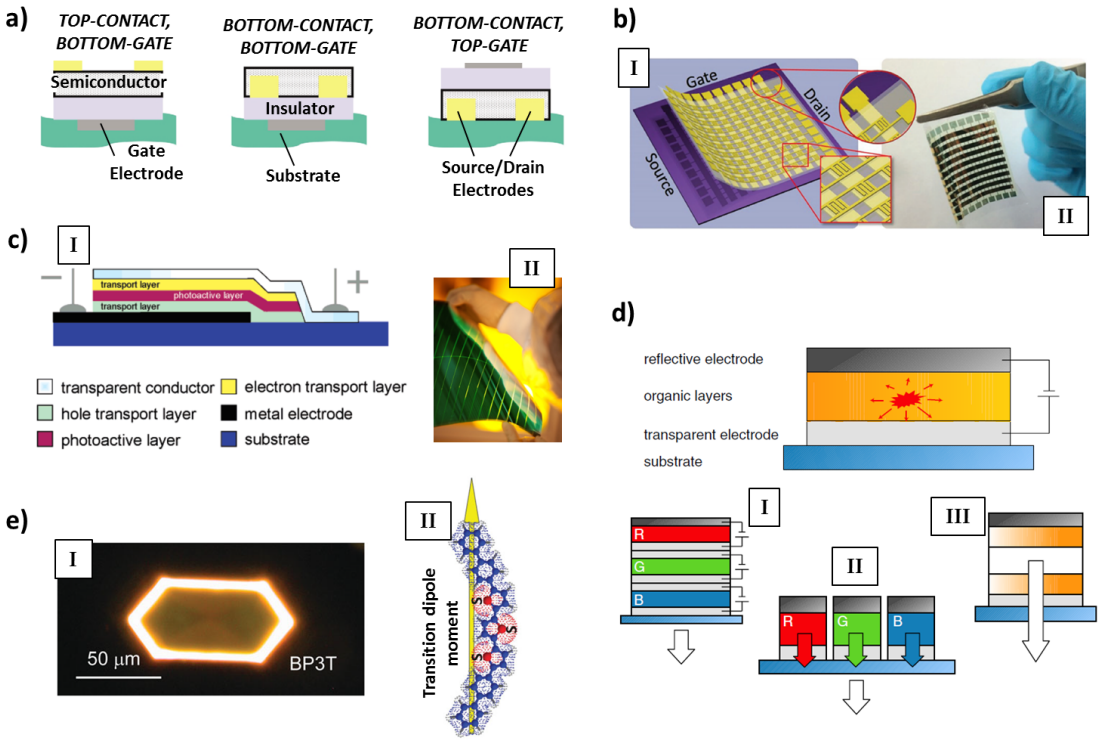

Figure 1.1: Schematics and examples of architectures for the application of OSCs in optoelectronic components. **a)** Organic Field-Effect Transistor (OFET) with different geometries for source, drain and gate contacts. Adapted from Ref. [2]. **b)** Use of an OFET device embedded in a sensor array. **[I]** Schematic of the sensor matrix where each single "pixel" is constituted by the "top-contact, bottom-gate" OFET structure shown in **a)**. **[II]** Actual size of the sensor array. Adapted from Ref. [19]. **c)** Schematics and real example of an organic solar cell. **[I]** Basic layered structure showing the photoactive layer for exciton generation sandwiched between electron- and hole-transport layers, respectively. Adapted from [20]. **[II]** Example of commercially available solar cell on a flexible substrate. Adapted from Heliatek®. **d)** (TOP) Basic structure of an organic light-emitting diode (OLED), where the organic layers shown in the center have, among others, the function of producing light *via* radiative recombination of electrons with holes. (BOTTOM) Some OLED architectures for production of white light, where the letters "R", "G" and "B" indicate organic layers with red, green and blue emission, respectively: **[I]** vertical stack; **[II]** pixels; **[III]** single emitter, where the orange-shaded boxes represent optional functional layers to improve carrier transport from the contacts. Adapted from Ref. [21]. **e) [I]** Microscope image showing the characteristic edge-emission of a molecular biphenyl-terthienyl (BP3T) single crystal, which is responsible for its lasing properties. **[II]** Molecular structure and transition dipole moment of BP3T molecule. Adapted from Ref. [22].

Other kinds of applications for OSCs in which enormous progress has been demonstrated are organic light-emitting diodes (OLEDs, Fig. 1.1d) and organic solar cells (or organic photovoltaics, OPV, Fig. 1.1c). In the simplest approximation, these applications can be seen as one being the

"opposite" of the other [23, 24]. In OLEDs, an external voltage is applied in order to inject an electron and a hole, respectively, from the contacts into some transport layers towards a central recombination layer, where radiative charge recombination takes place. In OPV, the generation of an exciton (coulombically bound electron-hole pair) takes place under illumination. The hole and the electron need to be separated and afterward each charge carrier migrates to the contacts, thereby generating a current. Huge efforts have been devoted to understanding the interrelationships between device parameters and efficiency through the manipulation of the constituting organic materials, substrates, device architecture and fabrication processes. Several insights and examples can be found in Refs. [20, 21, 25–27], which however represent only a minor part of the vast literature on this topic. Remarkably, for non-transparent organic solar cells based entirely on small-molecular semiconductors, a world-record efficiency of 13.2% has been recently achieved by Heliatek®, which serves as an example taken from industry of the huge potential of this class of materials for applications in OPV.

The use of molecular single crystals as materials capable of lasing (Fig. 1.1e) dates back to the late '60s/early '70s [28, 29]. Later, polymers embedded in microcavities have also been shown to exhibit lasing capabilities [30]. Up to now, a large number of materials and device architectures have been introduced as promising systems for laser applications, for which the reader is addressed to Refs. [22, 31–33].

One of the key factors pushing the transfer of fundamental research on OSCs onto an industrial level is the perspective of low-cost fabrication processes that are scalable on large areas for optoelectronic devices as well as the possibility to employ flexible substrates [34]. These two aspects rely on the relatively low energy input into the manufacturing processes compared to inorganic materials, which allows the use of printing techniques on plastic substrates.

The possibility to chemically design OSCs on the molecular scale represents another factor that largely determines the success of this material class. However, it is important to remiind that the extremely high degree of flexibility concerning the chemical design of the monomeric unit comes together with a dramatic entanglement of molecular structure and functional properties in the solid state [35, 36].

Besides the virtually unlimited possibilities of chemical design, the possibility to realize different architectures for the functional organic layers in optoelectronic devices represents another key aspect. Often, several compounds are mixed in order to affect the functional properties of organic thin films in a desired way. The combination of different materials and thin film architectures is called "heterostructure" [37]. In a planar heterostructure, the interface between two materials, A and B, viewed from the side is constituted by an uninterrupted line (see e.g. Fig. 5.2). Vacuum deposition techniques are particularly suited for the realization of such heterostructures, with a material B deposited on top of a material A [38]. Conversely, in a bulk heterostructure the two materials A and B are mixed on a molecular level. The number of interfaces is generally much larger than in the case of planar heterostructures. Importantly, the interplay between the thermodynamics of binary mixtures and the kinetic factors pertaining diffusion processes may give rise to a variety of mixing behaviors.

As mentioned above, achieving high conductivity in films of OSCs is a key point that allows their use in devices. Both polymers [39, 40] and small-molecular OSCs [41, 42] have been successfully doped by small inorganic molecules. However, due to their small size compared to the constituents of the surrounding organic matrix, inorganic dopants might show high tendency to diffuse through the matrix itself. In order to circumvent the problem of dopant diffusion while still obtaining the benefit of a higher conductivity, molecular doping has been realized[43–46], namely, a matrix of an organic semiconducting material is doped with a small-molecular OSC. Hence, molecular doping can be regarded as a particular declination of the heterostructure concept for OSCs. Notice that, in the context of doping of organic semiconductors to increase the conductivity, heterostructures are also called "heterojunctions".

Different models have been proposed to define the mechanisms of molecular doping for different material combinations [47–50]. In general, doping occurs as charge-transfer (CT) already in the ground-state of the system. For the prototypical donor polymer poly(3-hexylthiophene) (P3HT, Fig. 3.5) p-doped with the acceptor 2,3,5,6-tetrafluoro-7,7,8,8-tetracyanoquinodimethane (F4TCNQ), the widely accepted doping mechanism involves the transfer of one electron from P3HT to one F4TCNQ molecule, which generates a mobile hole on the polymer chain and a negative polaron on F4TCNQ [51]. This ionization process of the donor (D) and acceptor (A) species

is denominated integer CT.

Integer CT has also been suggested for the small molecules N,N,N',N'-tetrakis(4-methoxyphenyl)benzidine (MeO-TPD) mixed with F4TCNQ [52] and for 2,2′,7,7′-tetrakis(N,N-diphenylamino)-9,9-spirobifluorene (Spiro-TAD) mixed with the strong acceptor 1,3,4,5,7,8-hexafluorotetracyanonaphtoquinodimethane (F6TCNNQ, Fig. 3.6) [53]. However, in general the nature of the D:A interactions mechanisms leading to CT in the ground-state and subsequently to the generation of mobile carriers in small-molecular OSCs are not yet fully understood. In particular, the simplistic model of an integer electron(hole) being transferred from the material's HOMO(LUMO) to the dopant's LUMO(HOMO) in case of p-(n-)doping has been recently questioned, and a CT model based on the formation of a supramolecular D:A complex *via* frontier orbital hybridization has been proposed [54, 55]. This is illustrated in Fig. 1.2a for the prototypical small-molecular OSC pentacene (PEN) as donor and F4TCNQ as acceptor.

The transition from Fig. 1.2a to Fig. 1.2b depicts how a D:A supramolecular complex can be embedded in a unit cell and thereby form a D:A co-crystal (or "co-crystallite" as a synonym). Such structures can form during the co-deposition in vacuum of a donor and an acceptor materials following the heterostructure concept. In this thesis we often observe the formation of co-crystals. Importantly, while the pristine compounds generally show absorption of light in the visible range, due to the newly formed supramolecular complex the energy gap of a co-crystal is generally smaller, which might explain the lowest-energy absorption bands located typically in the near-IR range observed for several D:A material combinations [48, 55, 57].

Several scenarios have been proposed to elucidate doping mechanisms starting from the formation of a supramolecular complex [47–49]. One of them suggests that the D:A co-crystals, formed as a consequence of D:A interactions in the supramolecular complexes itself, act as dopants for the surrounding matrix of the semiconductor material. Fermi-Dirac statistics imply that at room T only a very small fraction of the D:A complexes are ionized. This could rationalize the high doping concentrations (some %) required to achieve acceptable conductivities for device applications, several orders of magnitudes higher than those required for p- and n-doping of Si, the latter lying typically between 10^{-4} and 10^{-6} [58].

The question of the formation of mobile charge carriers from strongly bound electron-hole pairs is therefore closely related to the microscopic mechanisms leading to CT in molecular doping. This topic has been recently discussed in Ref. [50] for the case of integer-CT molecular complexes, and the authors argued that local disorder has a major contribution in lowering the Coulomb barrier for exciton dissociation. Overall, the interplay between generation of free carriers *via* doping and charge mobility related to structural order [59, 60] determines the film conductivity, which is a key parameter for optoelectronic devices. From these considerations follows the importance of studying the structural properties of thin films of OSCs and of identifying those systems that tend to form D:A co-crystals. Co-crystal formation has been already observed for several OSCs in mixed D:A thin films, where here we recall PEN:perfluoropentacene(PFP) [61, 62], diindenoperylene(DIP):PFP [63], picene(PIC):PFP [64] and quaterthiophene(4T):[F$_x$]TCNQ (x = 1,2,4) [48].

Assuming that the formation of a D:A co-crystal is energetically favored, it should be always kept in mind that kinetic factors involved in thin film growth might occasionally prevail over simple equilibrium arguments derived from thermodynamics. This might translate in the situation illustrated in Fig. 1.2c. The bulk heterojunction is realized by co-evaporation of donor and acceptor in vacuum. The blue-colored regions indicate domains in which D:A co-crystallites have formed. However, some green and red-colored areas can be observed where the pristine compounds have phase-separated. These are regions where donor and acceptor did not mix efficiently to form the thermodynamically favored co-crystal. In general, the microstructure or morphology of a bulk heterojunction can vary a lot and affect the performance of optoelectronic devices like in solar cells [27, 65] (Fig. 1.2d).

One aim of this thesis is to broaden the spectrum of D:A combinations of molecular materials studied. In particular, we identify the formation of D:A co-crystals in binary mixtures of OSCs for several material combinations and we systematically study how the choice of the materials affects the structural and optical properties of thin films. In order to be able to carry out his investigation we adopted the bulk heterojunction approach, which potentially maximizes the number of D:A complexes formed in the film. The systematic variation of the D:A mixing ratio from an excess of the donor to an excess of the acceptor allows to precisely track the changes of film optical properties back to the development of specific crystalline structures and their orientation with

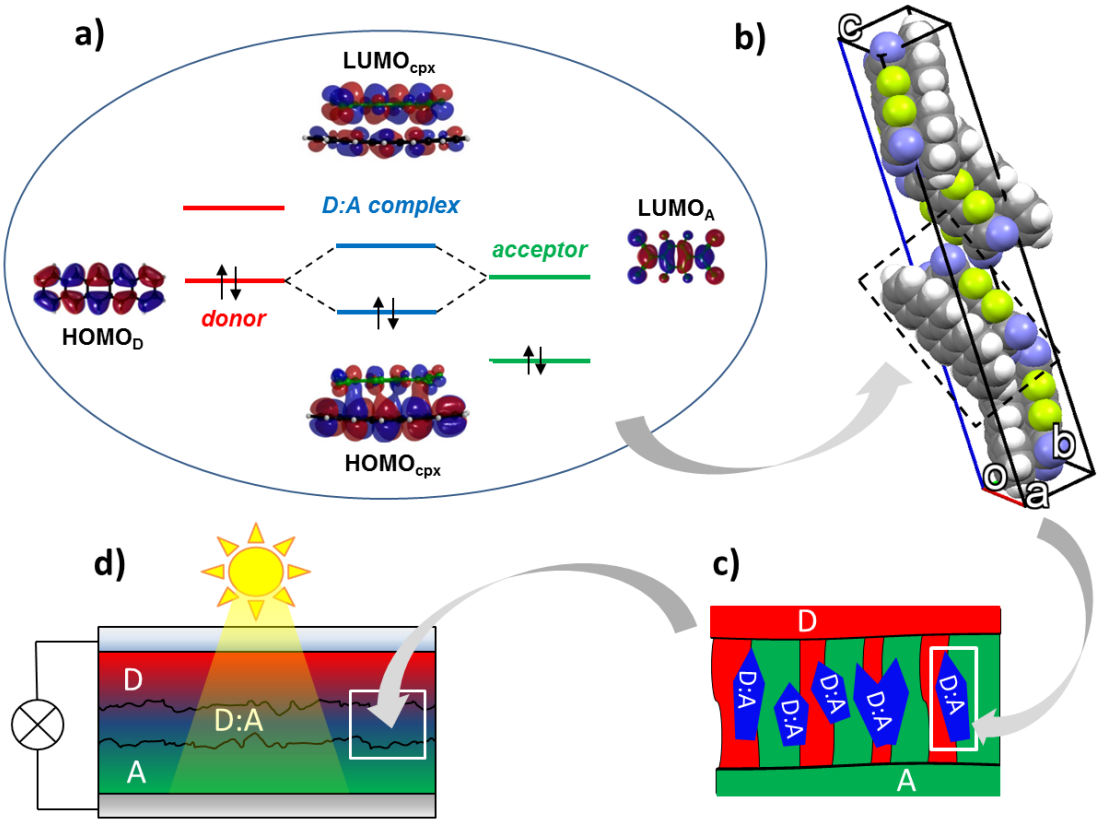

Figure 1.2: Illustration of the components on the molecular scale of the functional layers of an optoelectronic device. **a)** D:A CT interactions in the ground-state within a supramolecular complex lead to the formation of new hybrid levels, where the hybrid HOMO gets doubly occupied. Density-functional theory calculations of the indicated frontier orbitals for pentacene (D), F4TCNQ (A) and their supramolecular complex are adapted from Ref. [54]. **b)** Unit cell of a D:A co-crystal embedding a D:A supramolecular complex. Represented here is the unit cell of a picene:F4TCNQ co-crystal adapted from Ref. [56]. **c)** The unit cell belongs to one of the many co-crystallites (blue areas) forming in a co-evaporated D:A film according to the bulk heterojunction architecture. Due to the non-equilibrium processes involved in thin film growth, some amount of the pristine donor (red) and acceptor (green) might not mix and therefore form phase-separated domains. **d)** Schematic representation of an organic solar cell. The organic layers in contact with the electrodes are composed by the pristine donor and acceptor materials, respectively, whereas the central D:A layer is realized as bulk heterojunction by co-deposition of donor and acceptor materials. Such an architecture can be realized, for instance, by depositing the D:A layer on top of the D layer in a planar heterojunction fashion, and analogously for the A layer on top of the D:A layer. Notice that the interface roughness between the layers is represented. The top contact consists in a transparent conductive oxide which allows light to penetrate into the photoactive D:A layer.

respect to the substrate surface. The comparison of several D:A systems allows us to gain a more complete picture of the interplay between molecular structure, energy level alignment and mixing behavior, which remains so far one of the most elusive aspects in the realization of optoelectronic components.

Another aim of this thesis is to illustrate the use of highly sensitive experimental techniques to study relatively complicated systems like D:A mixtures. Also in this case, systematic variation of the D:A mixing ratio proves highly beneficial for a solid interpretation of the data. We therefore recommend further application of these combined approaches.

We also aim at demonstrating an OMBD-based film growth method which can be exploited to select the film structural and optical properties *via* control of the molecular orientation. This

method can be applied in principle to all D:A combinations studied in this work and thus expands the possibilities of a given molecular material to achieve a required set of functional properties.

1.2 Summary of the thesis

Below, the results of this thesis are summarized. For a quick overview, in Fig. 1.3 a chart is shown with a map of the main results and the complementary experimental techniques used.

The material combination exhibiting DIP as donor and F6TCNNQ as acceptor is the most thoroughly investigated in this work. We start by introducing the structural and optical properties of DIP:F6TCNNQ thin films in different mixing ratios in comparison with α-sexithiophene (6T):F6TCNNQ thin films (box Ia in Fig. 1.3). For both kinds of mixtures we show the formation of D:A co-crystals and the presence of strong optical transitions located in the near-infrared (NIR) portion of the spectrum, below the gap of the pristine compounds. For the lowest-energy transition we suggest their attribution to the fundamental HOMO-LUMO transition in the supramolecular complexes. For DIP:F6TCNNQ, we show a more pronounced uniaxial anisotropy of film texture and optical properties than for 6T:F6TCNNQ, as well as tendency to thin film smoothing in mixtures with excess DIP.

The latter finding pushes us to carry out real-time and *in situ* X-ray reflectivity investigations on DIP:F6TCNNQ blends (box II in Fig. 1.3) with varying F6TCNNQ content but keeping an excess of DIP. By applying the kinematical approximation and several growth models, on one side, and the Parratt formalism on the other side, we suggest a general mechanism to explain roughness evolution in binary mixtures as a function of mixing ratio. This mechanism concerns the different vertical growth rate of D:A co-crystallites and pristine crystallites of the excess donor, respectively, which has opposite effects on film roughness depending on the thickness regime.

Since a functional interface between two materials is defined by surface roughness and relative orientation of the small molecules, a special effort is dedicated to understanding how to control molecular orientation (box III in Fig. 1.3) and, at the same time, obtain crystalline films. We establish a procedure involving film deposition *via* OMBD at very low substrate temperature followed by a gentle annealing up to nearly film desorption. This procedure allows to orient DIP molecules on silicon oxide exclusively adopting an edge-on orientation with the long molecular axis parallel to the substrate surface (lying-down orientation), whereas DIP grows at room temperature in an upright-standing orientation. The mechanism suggested for the achieved orientation selection appears to be a general mechanism for rod-like OSCs and in principle it can be extended to other molecule/substrate combinations. As an example of this we additionally show how the orientation of the DIP:F6TCNNQ co-crystal can also be selected.

The last series of investigations on DIP:F6TCNNQ mixtures features a comparative study with P3HT:F6TCNNQ mixed films by means of infrared spectroscopy (box Ib in Fig. 1.3). For these investigations we use a particular setup which allows to investigate a broader spectral range with much better signal-to-noise compared to standard transmission measurements. In this study we compare the shifts of vibrational modes that are sensitive to the degree of ground-state CT (GS-CT) in OSCs, in particular of the C$\equiv$N stretching of F6TCNNQ, and we calculate the GS-CT degree in DIP:F6TCNNQ. We compare these data with the data for P3HT:F6TCNNQ, where for the latter system an integer GS-CT is expected. We conclude that solely analyzing the C$\equiv$N stretching mode shift is not enough to establish a correct picture of the CT strength in P3HT:F6TCNNQ, and that a conclusive analysis has to include the C$=$C stretching modes of F6TCNNQ and their relative intensity compared to the C$\equiv$N stretching.

In the last section we present the results on other D:A systems (Ic in Fig. 1.3). First we use DIP as donor but we change the acceptor from F6TCNNQ to the weaker TCNNQ (lower electron affinity than F6TCNNQ) and we investigate the relationship between electrical conductivity behavior as a function of D:A mixing ratio *vs.* nature of the acceptor used. We find an interesting difference in the behavior of the conductivity for the two D:A systems, respectively, and we suggest an explanation relying on the dependence of carrier mobility on mixing behavior. Additionally we use the same two acceptors TCNNQ and F6TCNNQ but we investigate their mixtures with the donor dibenzotetrathiafulvalene (DBTTF). For this donor, the unit cell parameters of the thin-film polymorph are fitted. For both D:A combinations we observe the formation of a D:A co-crystal. However, DBTTF:TCNNQ films exhibit a higher degree of uniaxial anisotropy and it is therefore possible

to fit the unit-cell parameters of the co-crystal from the X-ray diffraction pattern of the equimolar mixture. For this D:A combination we also discuss the presence of different polymorphs.

The subsequent chapter contains a critical discussion of all the obtained results. Some perspectives for future application-oriented research based on the results of this thesis are also presented. Finally, the thesis concludes with several Appendixes containing additional data and discussions that complement the Results chapter.

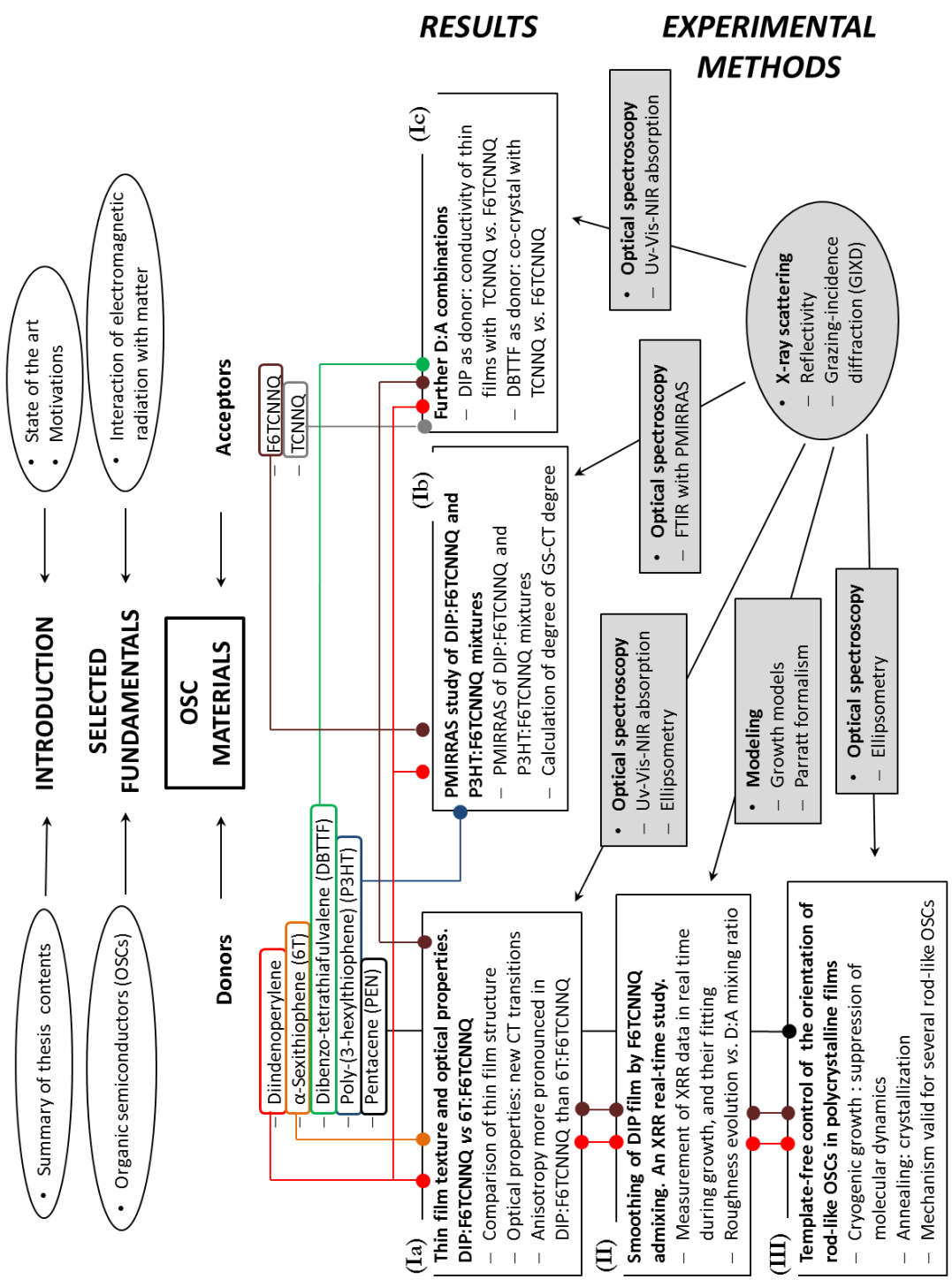

Figure 1.3: Conceptual map of this thesis. Many of the results focus on DIP:F6TCNNQ as a D:A combination, which was the system most thoroughly investigated. The experimental methods are reported in gray boxes.

CHAPTER 2

SELECTED FUNDAMENTALS

This chapter illustrates some fundamental concepts of solid state physics. The choice of the topics and the detail of each is preparatory to the discussion of the results contained in this thesis and is not intended to be exhaustive [1]*. The first part provides an overview of the nature of solid state interactions in "soft" materials and illustrates some thermodynamical arguments pertaining binary mixtures. The coupling between vibrations and charge-transport in molecular materials is then presented, followed by some key aspects of growth processes of molecular thin films. The second part deals with the fundamental optical functions describing the interaction of electromagnetic radiation with matter. Some basic definitions of the dielectric response in solids and the formalism of refraction at interfaces are introduced. The formation of excitons in molecular solids and the possible scenarios for charge-transfer are considered next. The closure of the chapter illustrates general aspects of the interaction of matter with X-rays, especially elastic scattering at crystals. Throughout the chapter, connections between the fundamental concepts illustrated and their application to the study of molecular materials are highlighted.*

2.1 Organic semiconductors

The ability to control of the functional properties of thin films of OSCs requires knowledge of the nature of the "weak" intermolecular interactions and the resulting "soft" solid state cohesion forces, as opposed the strong covalent or ionic bonds of an atomic solid like a metal, a salt, a semiconductor like Si or an insulator like diamond. Additionally, the dynamic processes involved in thin film growth must be taken into account since they determine the rate or probability at which solid state intermolecular interactions occur and govern to a large extent film morphology. An essential element in thin film growth is then the presence of a substrate, i.e. a supporting surface with a given energetic landscape which, at least at the beginning of film growth, can interact with the molecular components and may therefore affect self-assembly processes. For film deposition from solution, the presence of a solvent further complicates the description of growth processes, but this case is not treated in this thesis.

It should be emphasized that predicting growth scenarios of thin films based on equilibrium or near-equilibrium arguments might occasionally fail. This is due to the non-equilibrium character of thin film growth [66]. However, by invoking energetic arguments one can predict some basic features of the solid state packing of molecular solids and their mixing behavior. It will be useful within this thesis to recall some considerations for perfect crystals at equilibrium as a starting point to describe complicated growth scenarios.

[1] For this and for the subsequent sections of the theoretical background as well as for the subsequent ones, the choice of textbooks as main references is partly based on personal knowledge, partly on factors related to "tradition" and relevance of a given book within the single research group. Such works contain many references to early works, which here for the sake of a simpler source referencing we omit to specify. The interested reader is invited to consult the books cited in this thesis as well as the references therein.

2.1.1 Electron conjugation in organic materials [2]

The formation of a chemical bond between two atoms (homo- or heteroatomic) consists in a binding force provided by the charge distribution of the valence electrons. Solutions of the Schrödinger equation with the system Hamiltonian H:

$$H = T_N + T_e + V. \tag{2.1}$$

provide the eigenstates and eigenvalues of the chemically bound state. In Eq. 2.1 we separate contributions of the kinetic energies of the atomic nuclei and of the electrons, respectively T_N and T_e, and the total potential energy of the system, V.

A useful approximation to solve this problem consists in using a linear combination of *valence* atomic orbitals (LCAO) with different values of the total orbital momentum (MO) as test functions within the Rayleigh-Ritz variational principle. This is called the LCAO-MO or Hund-Mulliken method. A result of the LCAO-MO method is that a state of lower energy than the isolated atomic orbitals can be found, which allows a higher electron density to be found between the atomic nuclei, thereby producing a bonding effect Such an approach allows to rationalize the more covalent or ionic bond character of simple molecules like HCl or NaCl in terms of the magnitude of the coefficients entering the LCAO-MO.

2.1.1.1 Types of hybrid bonds involving s and p orbitals

The LCAO-MO treatment allows to rationalize the different strength observed for C-C bonds in organic molecules in terms of different modalities of hybridization. Let us consider the ground state of the isolated C atom with its electronic configuration $1s^2 2s^2 2p^2$. Another state, very close in energy to this one, has configuration $1s^2 2s^1 2p^3$, which therefore exhibits now three electrons in $2p$ states, respectively $2p_x$, $2p_y$ and $2p_z$ orbital. From this easily accessible configuration, the C valence orbitals can hybridize in several ways (Fig. 2.1a-c).

In the methane molecule, CH_4, the singly occupied C $2s$ orbital forms four independent linear combinations with the three singly occupied $2p$ orbitals. Four hybrid sp^3 orbitals result, oriented towards the vertices of a tetrahedron. Each of these four hybrid orbitals on the C atom forms a bond with the singly occupied, sphero-symmetric $1s$ H atomic orbital, resulting in four bonds oriented in a tetrahedron fashion with equal angles of 109.6° between them (Fig. 2.1a). For these bonds, the component of the orbital angular momentum along the bond direction is zero, from which this kind of orbital is called σ.

The ethylene molecule, C_2H_4, exhibits a commonly denominated "double bond" between the two carbon atoms, C = C. Here the C valence orbitals form sp^2 hybrids, namely, three independent linear combinations of the $2s$ with only two of the $2p$ orbitals. The two sp^2 hybrids of each C atom form then σ bonds with H atoms. The third $2p$ orbital, which we will indicate as $2p_z$ for convention, hosts one electron and remains non-hybridized and therefore a second C — C bond is formed. The latter originates from purely p orbitals and therefore the component of the angular momentum along the bond direction is $\pm\hbar$: this is called a π orbital, or π bond (Fig. 2.1b).

In the acetylene (or ethyne) molecule, C_2H_2, only one $2p$ orbital and the $2s$ orbital of C hybridize, giving a total of two possible linear combinations called sp orbitals The remaining two $2p$ orbitals remain unhybridized. This originates a C ≡ C triple bond constituted by one σ bond formed between the hybrid sp states and two π bonds formed between the unhybridized $2p$ orbitals (Fig. 2.1c). The remaining sp orbitals form σ bonds with H. For instance, a triple bond between C and N is of importance for the study of CT interactions in D:A systems, as we will see in the Results section 4.4.

The sp^2 type of orbital hybridization and the consequent formation of double bonds is of special importance in organic materials. In linear as well as poly-cyclic unsaturated hydrocarbons the alternation of single and double bonds leads to peculiar physico-chemical properties compared to unsaturated hydrocarbons where this bond alternation is absent, for example higher reactivity and lower energetic optical absorption bands compared to saturated hydrocarbons. These properties derive from the fact that the electrons participating to the π bonds are *delocalized* along these

[2] The treatment of chemical bonds in molecules contained in this paragraph is mostly taken from the book of Bransden [67]. For the treatment of conjugation, the first chapter of the book of Salem [68] has also been consulted. All other sources are explicitly indicated.

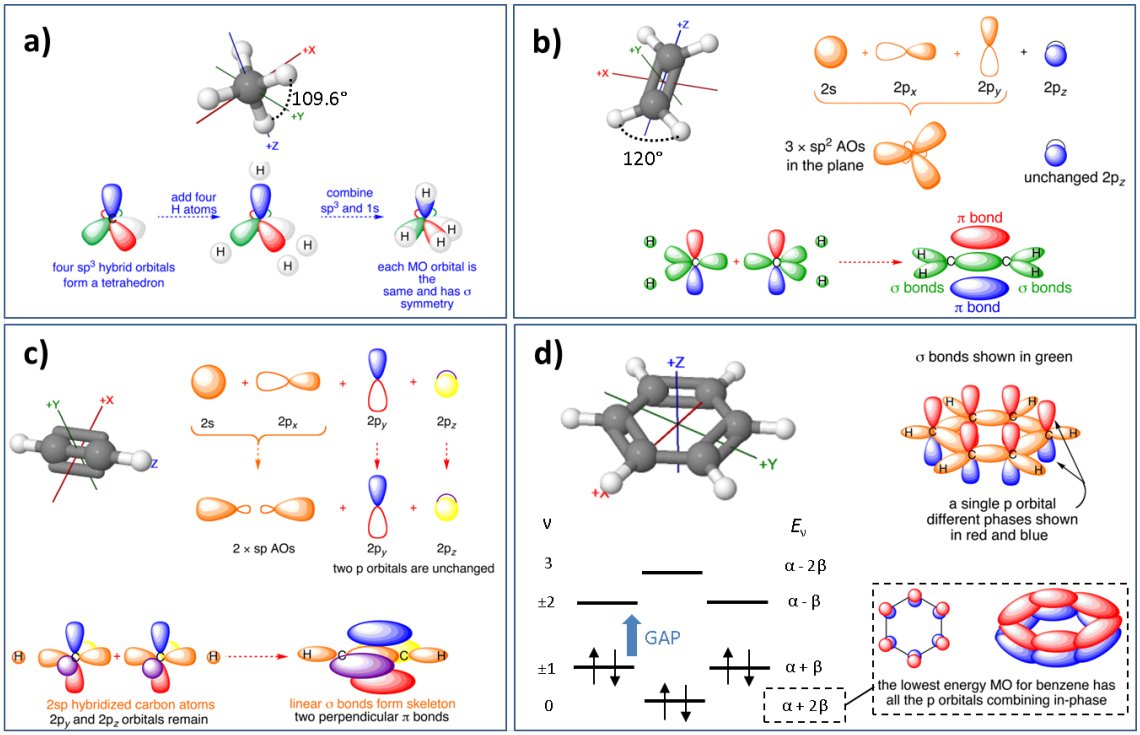

Figure 2.1: Molecular structure and schemes of bond formation in the smallest organic molecules: **a)** methane (CH_4), **b)** ethylene (C_2H_4), **c)** acetylene or ethyne (C_2H_2), **d)** benzene (C_6H_6). For benzene, the Hückel method leads to the definition of six eigenstate ν and eigenvalues E_ν as a function of two parameters, α and β, with $\beta < 0$. Of the six eigenstates, three are bonding and occupied, whereas three are anti-bonding and occupied in the ground-state. Adapted from [69].

molecules. Such delocalization is termed *conjugation* of the π electrons (or π-conjugation) and is a common feature of all OSCs, being the reason for their bandgap lying often in the visible range of the spectrum, as we shall illustrate briefly.

The benzene molecule, C_6H_6 (Fig. 2.1d), represents a classical example of how the LCAO-MO can be used to predict the π conjugation. The example of benzene is useful since this the hexacyclic molecule can be considered "the building block" of many, more complex OSCs. To calculate eigenvalues and eigenstates, an approach called Hückel method is adopted which greatly simplifies the problem. The ordering of the benzene energy levels according to the Hückel method is shown in Fig. 2.1d, where also the level occupation from the six π electrons and the resulting electronic gap are shown, the latter defined as the distance between the top occupied and the bottom unoccupied level.

The Hückel method can be applied to more complex conjugated molecules and is able to provide insights into several physico-chemical properties. Notice that a simplified Hückel-like approach has been recently used to describe the formation of a supramolecular CT complex with hybridized HOMO and LUMO levels in the ground state (see Selected Fundamentals section 2.2).

2.1.1.2 Free electron in a box

The complexity of the Hückel method increases rapidly with the size of the molecule under study. In order to obviate to this, it has been shown that conjugated systems can also be described by the model of a free electron in a box [70, 71], showing qualitative agreement with the experiments. For instance, a "classical" result of the particle in a state with quantum number n in a box of length L is that the total energy depends on n^2/L^2, and this dependence is actually observed for the HOMO-LUMO transition of several systems like cyanine dyes and polyenes [72], as shown in Fig. 2.2a, where L represents in this case the number of units forming a molecule. As shown by the Stanford group of John R. Platt in a series of papers [73], the model can be extended to other

types of π-conjugated systems by adjusting the shape of the box. The results of the particle-in-a-box model (Fig. 2.2a) are in qualitative agreement with more advanced calculations (Fig. 2.2b) in predicting the red-shift of the lowest absorption as the size of the conjugated system increases, analogous to the case of a 2D box.

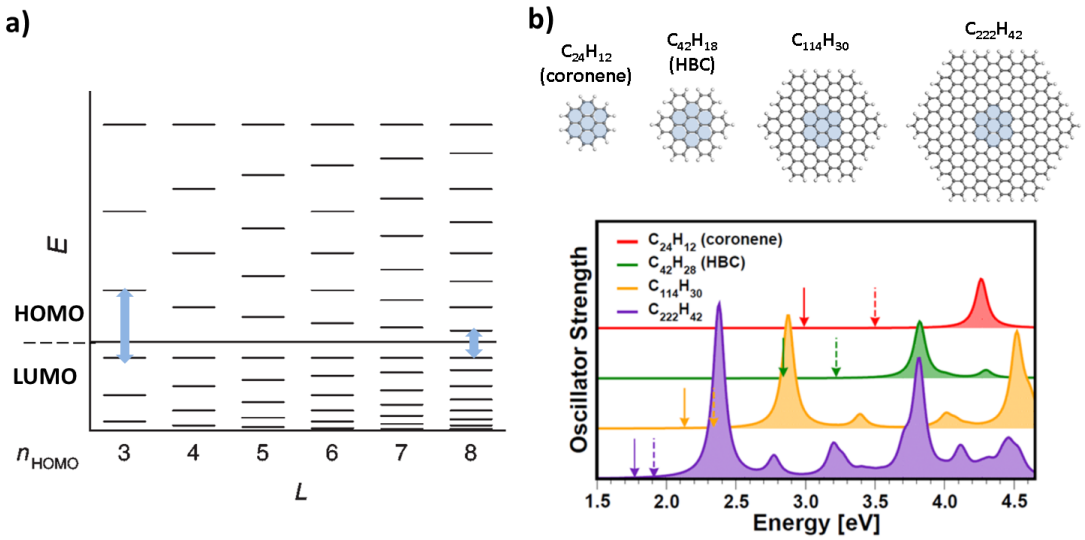

Figure 2.2: **a)** Energy levels of a free electron in a one-dimensional box in which a small periodic potential, representing the bond order alternation in linear polyenes, is present. In ordinate, the chain length L scales with the number of electrons in the HOMO state, n_{HOMO}. The HOMO-LUMO difference, indicated by the blue double arrow, decreases as L increases. Adapted from Ref. [72]. **b)** [TOP] Series of coronene derivatives of increasing molecular weight, which represent a 2D-box of increasing size; [BOTTOM] corresponding absorption spectra simulated using advanced computational methods. The forbidden transitions (indicated by the arrows) as well as the lowest-energy absorptions shift to lower energies with increasing molecule/box size. Adapted from Ref. [74].

In summary, both the Hückel and the particle-in-a-box models are able to qualitatively describe the electron delocalization occurring along the skeleton of molecular OSCs and to empirically predict band edges falling in the visible range, which accounts for the typically colored aspect of these materials in solution. The concept of π-conjugation is fundamental for understanding the "soft" cohesion forces acting in the solid state of molecular materials, which is the topic of the next paragraph.

2.1.2 Solid state interactions in molecular materials [3]

In the previous paragraph we examined the nature of conjugated bonds in organic molecules. Here we consider inter-molecular interactions that determine cohesion and molecular packing in molecular solids. Such interactions are determined by forces that can have different strength and direction.

2.1.2.1 Permanent dipoles and van der Waals interactions

We first consider the case of the interaction of two fixed dipoles, $\mathbf{p}_1$ and $\mathbf{p}_2$, at a distance r. This represents the case of a molecule that exhibits one or more polar bonds or side-groups. In this case the interaction potential V is proportional to r^{-3} and the corresponding force can be attractive or repulsive depending on the relative orientation of the dipoles.

[3] The concepts of this paragraph are mostly taken from the book of Schwörer and Wolf on molecular solids, Ref. [75]. Different references cited are indicated.

A polar side group of a molecule can interact with a portion of a neighboring molecule that does not exhibit any net dipole. In this case, the net dipole on the polar bond generates an electric field $\mathbf{E}$ at the non-polar region, which thus becomes polarized. The induced dipole $\mathbf{p}_{ind}$ is related to the polarizability α by:

$$\mathbf{p}_{ind} = \alpha \mathbf{E} \tag{2.2}$$

In this case, an attractive force, also called *inductive* force, between the permanent dipole and the polarized region is generated, with a potential energy proportional to αr^{-6}.

Cohesion forces in crystals of OSCs are often originated by fluctuations in charge distribution in a given volume portion of a molecule, which correspondingly induce fluctuating dipoles on a neighboring molecule. These attractive forces caused by charge fluctuations are termed *dispersive* or van der Waals forces, in order to distinguish them from the inductive forces originating from permanent dipoles. Examples of molecular materials in which dispersive forces play a dominant role in crystal formation are poly-cycles like anthracene or pentacene, since in these molecules no polar side-group is present. The dependence of the resulting potential energy on the distance r and the polarizability α is:

$$V_{disp} = -\frac{1}{4\pi\epsilon_0}\frac{A^{''}\alpha^2}{r^6} \tag{2.3}$$

In Eq. 2.3, ϵ_0 is the dielectric constant in vacuum and $A^{''}$ is a parameter which accounts for the actual anisotropy of the charge distribution, including *quadrupolar* and higher-order moments.

Overall, charge distributions induced by permanent or fluctuating dipoles of the form of Eq. 2.3 represent an attractive (or negative) contribution to the total potential energy (Fig. 2.3a). However, for a complete expression of the intermolecular potential, positive contributions to the total energy must also be taken into account. They arise mostly from repulsive forces between the electronic charges and by the Pauli exclusion principle, avoiding the collapse of the solid structure. A common approximation is to account for such repulsive forces as function of the distance r through a power-law dependence r^{-12}, such that the *total* energy assumes the form of a Lennard-Jones potential:

$$V_{tot} = -\frac{A}{r^6} + \frac{B}{r^{12}} \tag{2.4}$$

The constants A and B are supposed take into account several factors like anisotropy. Solving $\partial V_{tot}/\partial r = 0$ in Eq. 2.4 allows to find the equilibrium distance, r_0, and the minimum energy as function of A and B, as shown in Fig. 2.3a. In a real molecular crystal, the equilibrium distance will depend on the crystal direction considered, which can be qualitatively explained by different values of A in Eq. 2.4 depending on the crystallographic axis and on the relative orientation of the molecules within the unit cell, as it is shown in Fig. 2.3b.

At this point it is necessary to stress that the prediction of crystal structures in molecular solids is a complicated task. One aspect of this complication is the already mentioned interaction anisotropy. Another aspect concerns the small differences in free energy between different crystal structures of the same compound, which gives rise to a phenomenon known as polymorphism [76]. The different crystal structures of the same compound are thus called *polymorphs*, and we will touch upon this topic further below. In general, as the molecular structure becomes more complicated and acquires degrees of freedom, the accurate prediction of the equilibrium crystal structure(s) becomes hardly possible [76]. However, recently important progresses have been made in the field of crystal structure prediction [77].

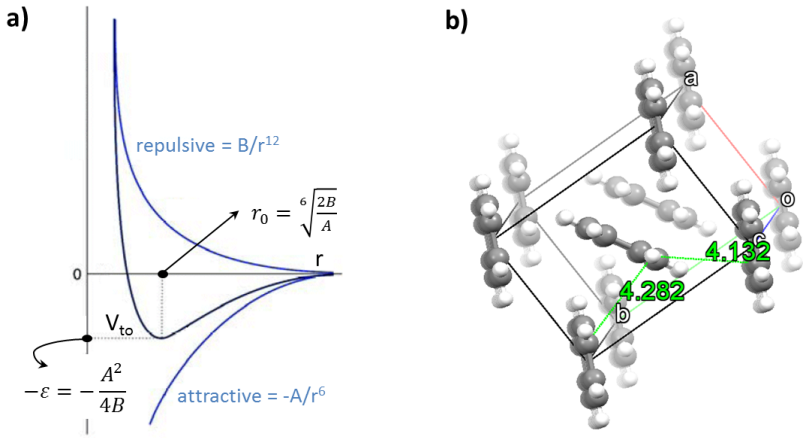

Figure 2.3: **a)** Lennard-Jones potential curve with attractive and repulsive contributions shown. **b)** View of pentacene unit cell with the peculiar herring-bone arrangement (crystal structure from Ref. [78]), where the equilibrium distances in Å between one terminal H atom and two C atoms belonging to different molecules are shown.

2.1.2.2 Contribution of quadrupoles to molecular packing

How the π-conjugation of electrons in OSCs determines their solid-state packing can be also understood by considering the quadrupolar moment of a π-conjugated molecule. In the case of benzene examined in detail above (Fig. 2.1d), but also for many other conjugated hydrocarbons, the delocalization of the negatively charged electron cloud in the "shared" π orbital leaves a volume of compensating positive charge (Fig. 2.4a). This means that, despite benzene does not have any dipole moment, it possesses a quadrupolar moment due to the deviations of its charge distribution from spherical isotropy [79, 80]. This argument can be easily extended to many other hydrocarbons exhibiting a conjugated π system. The most energetically favorable configuration for the many molecular objects building up a crystal is the so called *herringbone* packing (Fig. 2.4a), i.e. an edge-on-face configuration in which the edges bearing an overall negative charge point towards the positive faces. This is, indeed, the configuration of like electric quadrupole moments that minimizes repulsive interactions and maximizes attractive contributions, and is a quite common pattern for conjugated, polycyclic hydrocarbons like tetracene, pentacene, diindenoperylene. Interestingly, more and more relevance has been given in the literature to the role of quadrupolar interactions for the formation and stabilization of structures in biological systems [81, 82].

Perfluorination of benzene to give hexafluorobenzene, C_6F_6, leads to the inversion of the charge distribution landscape of the molecule. As a consequence, the molecular packing of a benzene-perfluorobenzene *co-crystal* is very different from that of pristine benzene, as shown in Fig. 2.4b. The molecular arrangement of the C_6H_6/C_6F_6 co-crystal in this case features a linear stack of quadrupoles of the same sign facing a line of opposite quadrupoles. In such way, slipped piles of face-to-face C_6H_6/C_6F_6 dimers stack adjacent to each other [80]. It is tempting to use the argument of the quadrupole moment inversion to predict a face-to-face molecular arrangement for another arene-perfluoroarene system, pentacene:perfluoropentacene (PEN:PFP) [61, 62]. However, one has to be careful since PEN and PFP are polycycles and have a lower symmetry than benzene and hexafluorobenzene. Indeed, to date such an arrangement has not been clearly documented for PEN:PFP.

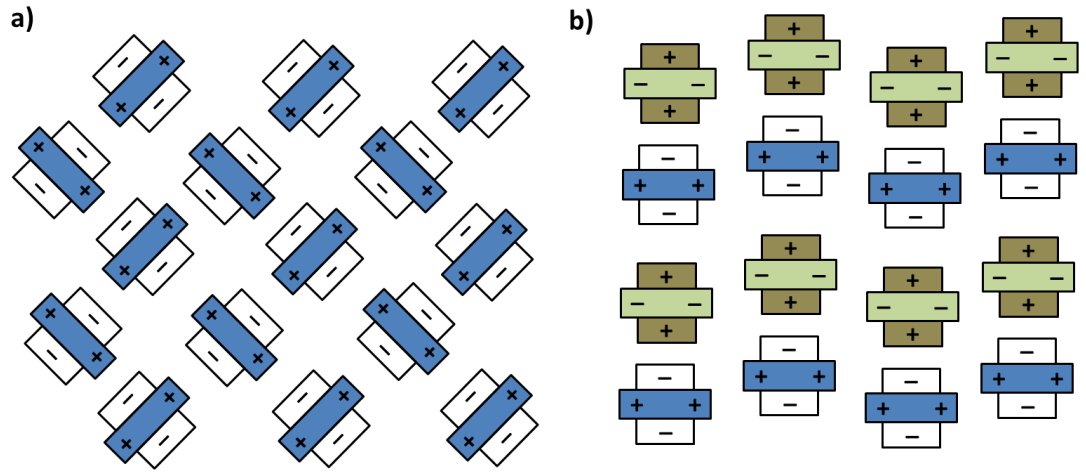

Figure 2.4: Schematics of equilibrium crystal structures resulting from the balance between attractive and repulsive quadrupolar forces. **a)** Herringbone or edge-to-face crystal packing of a single-component molecular crystal. **b)** Linear or face-to-face crystal packing in a bi-component co-crystal, e.g. a D:A co-crystal. Adapted from [80] with inverted signs for the electrostatic potential.

2.1.2.3 Molecular packing in D:A co-crystals

One important type of binary crystals are D:A co-crystals. In such systems, the molecular structure of D and A, respectively, can be totally different, therefore prediction of crystal packing based on electrostatic arguments becomes very difficult. Additionally, the energy alignment of the donor HOMO with the acceptor LUMO ad the efficient orbital overlap between the two may induce a partial CT from the donor to the acceptor. This transfer of electron density may induce a dipole within a D:A dimer, such that the additional Coulomb forces increase the overall cohesion energy of the solid compared to the pristine compounds. This was demonstrated for mixed thin films of OSCs as PEN:PFP [83], or picene(PIC):PFP [64] by their improved thermal stability to annealing in vacuum.

A large variety of systems commonly denominated "organic CT salts" has been studied. In these compounds it is possible to observe a transition from a neutral to a nearly ionic state of the D:A dimer [84]. Organic CT salts can be distinguished into two types [85, 86] depending on the packing of the D:A moieties: the first type features mixed [$D^{\delta+}A^{\delta-}$ ····· $D^{\delta+}A^{\delta-}$] stacks (Fig. 2.5a), the second type segregated [$D^{+}D^{+}$ ····· $D^{+}D^{+}$] and [$A^{-}A^{-}$ ····· $A^{-}A^{-}$] stacks (Fig. 2.5b). The strength of CT interactions in these two classes, respectively, can be sharply distinguished [87]. Compounds belonging to the first class (mixed stacks) form CT complexes, are neutral in their ground state and exhibit semiconducting properties. Compounds belonging to the second class (segregated stacks) form radical-ion salts and their ground state consists of positively and negatively charged stacks of ions, which give rise to high conductivities in the direction parallel to the stacks themselves. The most famous example belonging to this second class is probably the tetrathiafulvalene:tetracyano-quinodimethane (TTF:TCNQ) D:A co-crystal, TTF:TCNQ, whose single crystals can exhibit charge carrier conductivities as high as $\sim 10^2$ Ω/cm.

One may argue that, as soon as the molecular weight of D and A increases, due to the possibly increasing flexibility and number of degrees of freedom of the molecular units the probability to form stable segregated D:A stacks becomes lower. This generalization seems in agreement with the fact that for radical-ion salts forming segregated D and A moieties the D and A units are highly planar [87]. Notice that, in thin film growth, the formation of D:A stacks might be further hindered by kinetic factors despite an overall negative energy balance of the reaction $D^0 + A^0 \rightarrow D^{\delta+}{:}A^{\delta-}$.

For the material combinations investigated in thesis, structural and spectroscopic investigations give strong hints for the formation of CT complexes in polycrystalline thin films. However,

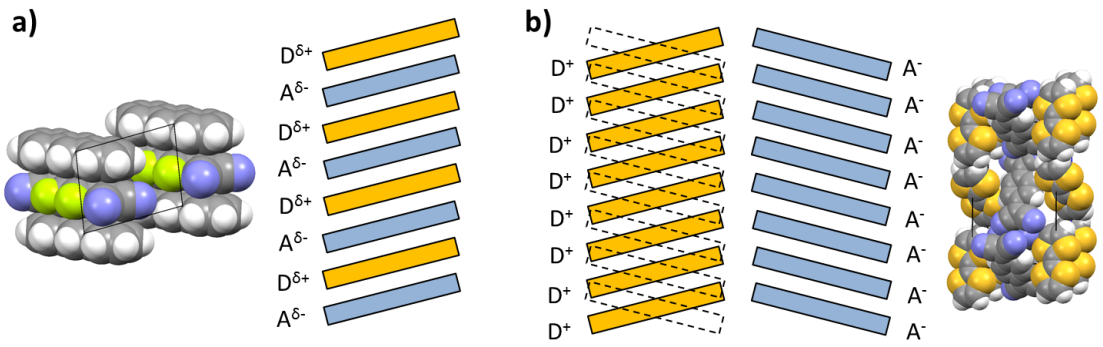

Figure 2.5: **a)** [LEFT] Unit cell of tetracene (TET):F4TCNQ co-crystal exhibiting mixed D:A stacks; [RIGHT] illustration of a mixed D:A stack with the donors bearing a partial positive charge, $\delta+$, and the acceptors a partial negative charge, $\delta-$. **b)** [LEFT] illustration of segregated D and A stacks with the donors bearing a full positive charge, +, and the acceptors bearing a full negative charge, -, where the spatial arrangement of two adjacent stacks is shown by the dashed lines; [RIGHT] Unit cell of the "organic metal" tetrathiafulvalene (TTF):TCNQ co-crystal. The schematics are adapted from Ref. [75]. The experimental crystal structures are taken from Ref. [88] (TET:F4TCNQ) and Ref. [89] (TTF:TCNQ).

determination of the kind of D:A stacking motif and the relative orientation of the inequivalent stacks is beyond the scope of this thesis. Nevertheless, mostly by the thorough comparison with similar D:A co-crystals from the literature and by qualitative evaluation of the strength of CT interactions in the ground-state, we can reasonably assume a nature of mixed stacks for all the D:A pairs investigated here. As mentioned in the Introduction, mixed D:A systems and their structure in thin films are the focus of this thesis. In the following paragraph we will consider some energetic arguments which are useful for predicting the equilibrium mixing configuration of *binary mixtures*.

2.1.3 Binary mixtures[4]

In the previous paragraphs we have considered the Lennard-Jones expression of the potential energy (Eq. 2.4) and we have presented two examples of crystal packing motifs, i.e. mixed and segregated stacks. Here we report useful expressions for the calculation of the free energy of a lattice composed by two materials, A and B. This will help understanding better the mixing behavior of the D:A mixtures studied in this thesis, as illustrated by the examples reported.

2.1.3.1 Thermodynamics of regular solutions

In order to explain solid state properties of materials (not only OSCs), defects are of great importance. In order to work a useful expression for the free energy of a binary mixture A:B, it is useful here to include the presence of a defect or "impurity" B in concentration x in the lattice of a perfect crystal A. In general, a lattice of $N = N_A + N_B$ particles has a configurational entropy S given by the Boltzmann expression:

$$\begin{aligned} S = k_B \ln \Omega = k_B \ln \frac{N!}{N_A! N_B!} = k_B (\ln N! - \ln N_A! - \ln N_B!) \approx \\ \approx k_B (N \ln N - N_A \ln N_A - N_B \ln N_B) \end{aligned} \tag{2.5}$$

where k_B is the Boltzmann constant and we used the Stirling approximation. The argument of the logarithm is the number of permutations of N objects excluding the equivalent permutations of the N_A and N_B objects. Since N_A and N_A are linked *via* the total number of particles N, it is

[4]Most of the contents of this paragraph are adapted form the books of Kitajgorodskij [90, 91]. Other references are indicated.

convenient to divide Eq. 2.5 by N and define $N_B/N = x \Rightarrow N_A/N = 1 - x$, which allows to use only the variable x.

Apart from the entropy contribution contained in Eq. 2.5, inclusion of a species B in the lattice of A involves also a different interaction potential, ΔV. We assume to have a lattice of mixed spherical particles A and B and we consider only nearest-neighbor interactions. One needs to take into account a "homo-particle" potentials, V_{AA} and V_{BB}, and "hetero-particle" potential, V_{AB}, and include the coordination number per particle, Z, to obtain the total interaction potential, W:

$$\chi = Z\frac{W}{k_BT} = \frac{Z}{k_BT}(V_{AA} + V_{BB} - 2V_{AB}) \tag{2.6}$$

In Eq. 2.6, χ is the normalized interaction potential. The Helmholtz free energy of mixing, F, is then obtained by summing the two contributions related to the configurational entropy (Eq. 2.5) and the interaction energy (Eq. 2.6), respectively:

$$F = k_BT(\chi x(1-x) + x\ln x + (1-x)\ln(1-x)) \tag{2.7}$$

The expression $\chi x(1-x)$ in Eq. 2.7 is the mixing energy or mixing *heat*. The different signs of the homo-particle and hetero-particle potentials in Eq. 2.6 account for the fact that mixing, i.e. more favorable A-B interactions, competes with de-mixing, i.e. more favorable A-A or B-B interactions.

In Fig. 2.6 we illustrate the dependence of F on the molar ratio x and the homo-particle interaction parameter V_{AA}. The values for Z, V_{BB}, V_{AB} and T are reported in the figure caption.

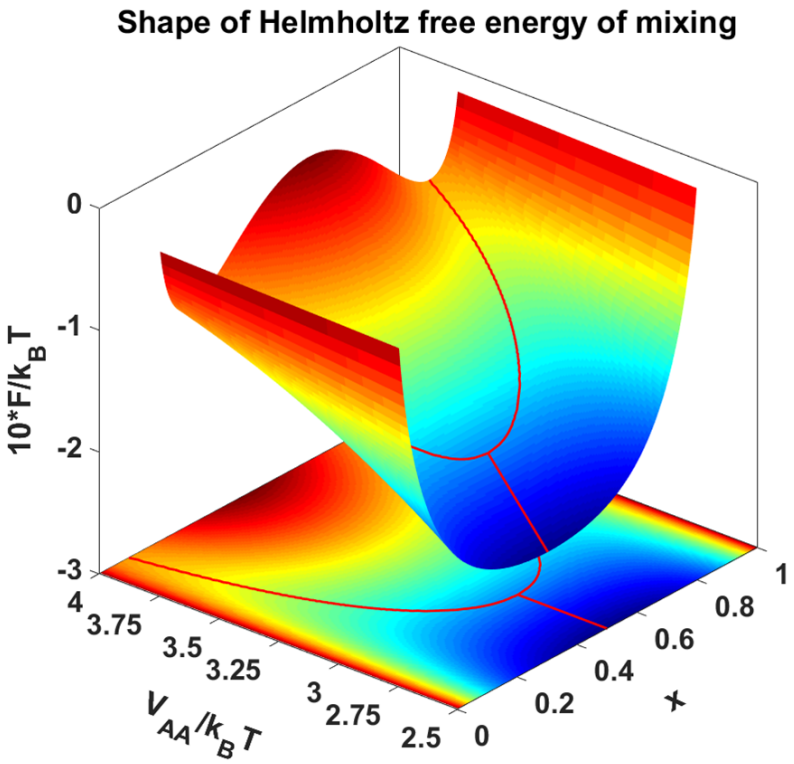

Figure 2.6: Example of variation of the Helmholtz free energy of mixing as function of the molar ratio of "impurities", x, and the inter-particle interaction potential for homologous particles, V_{AA}. The curve was simulated from Eq. 2.7 setting $Z = 1$, $V_{BB} = 3k_BT$, $V_{AB} = 2k_BT$, $T = 298K$, which leads to $\chi > 2$ for $V_{AA} > 3k_BT$ (Eq. 2.6). The red lines correspond to the local minima as function of the inter-particle potential.

The shape of F can be rationalized as follows [37] (Fig. 2.7). At high T the logarithmic entropy term will dominate the free energy, which can be regarded as a vanishing χ term in Eq. 2.6. In

this case the energy curve exhibits only one minimum at $x = 0.5$, which can be interpreted as an unlimited ability of the A and B particles to mix in any molar ratio, i.e. the system is a solid solution.

Lowering T may give origin to three different scenarios, since in this T range the entropy of mixing does not dominate anymore.

- If $\chi < 0$, the interactions between hetero-particles dominates, which can be interpreted as a favorable formation of an A:B complex. In this case, assuming that the A:B complex has a 1:1 stoichiometry, it can be expected that the excess amount of either A or B, which does not participate to the complex, precipitates in pristine domains.
- If $\chi \approx 0$, there is no clear dominance of homo- or hetero-particle interactions, and the system the system is a solid solution with the components A and B being able to mix in any proportion.
- If $\chi > 2$, the free-energy curve assumes a shape in which two local minima appear at symmetric positions, respectively $x = x_m$ and $x = 1 - x_m$, about the local maximum located at at $x = 0.5$. The two local minima are indicative of a *phase-separation* occurring within the binary mixture, i.e., the two compounds A and B segregate in pristine domains with macroscopic phase boundaries.

The latter case can be observed in Fig. 2.6 for $V_{AA} > 3k_BT$. As V_{AA} decreases from its maximum value, the minima approach $x = 0.5$ and, for $V_{AA} = 3k_BT$, they converge to the central value. For $V_{AA} \leq 3k_BT$, due to overall weakened interactions, there are no more phase boundaries in the binary mixture and the miscibility is complete.

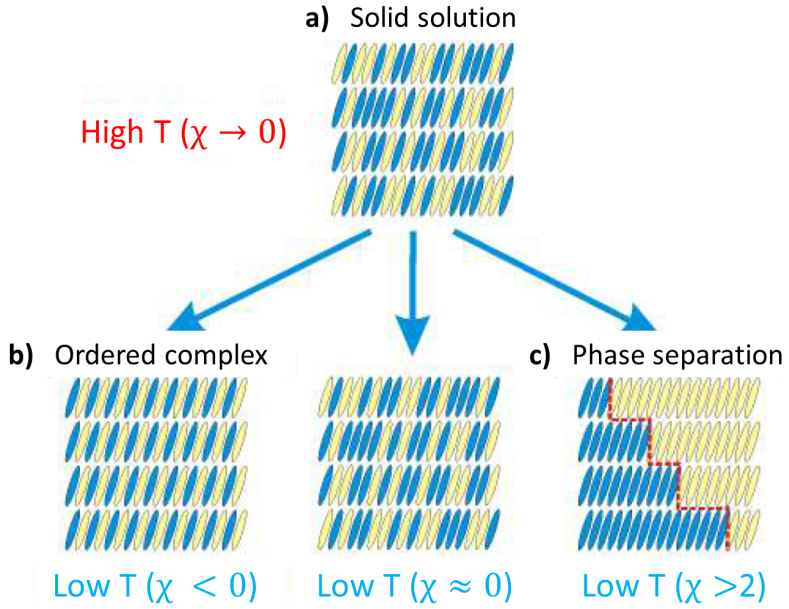

Figure 2.7: Simplified mixing scenarios for binary mixtures as function of T and of the total interaction potential χ (Eq. 2.6). Adapted from Ref. [37].

2.1.3.2 Examples for molecular materials

The above discussion of the Helmholtz free energy of mixing relies on the approximation of spherical particles exhibiting isotropic nearest-neighbor interactions. However, often OSCs consist of rod-shaped molecules which grow in a layered fashion when deposited in thin films on a substrate. It is possible to include anisotropy of the in-plane (i.e., parallel to the substrate) *vs.* the out-of-plane component (i.e., perpendicular to the substrate) of the inter-molecular potential in a

molecular mixture. In Ref. [92], a general modification of Eq. 2.7 for the free energy of mixing to account for anisotropic interactions as well stress terms due to size mismatch of the two molecular components in a layered system has been presented. The molecular blends in different mixing ratios investigated in Ref. [92] were constituted of DIP and PEN, which by virtue of their similar size exhibited unlimited miscibility both parallel and perpendicular to the substrate, as inferred from X-ray scattering.

The basic principles of phase behavior in regular solutions of isotropic particles illustrated above have proven helpful in rationalizing the mixing behavior in thin films of DIP:PFP *vs.* DIP:PEN mixtures [92–94], and similarly for PEN:PFP [37, 38, 62] grown by OMBD. For instance, the phase-separation observed for DIP:C_{60} [95] and sexithiophene (6T):C_{60} [96] mixtures seems fairly justified by the very different molecular structure of the rod-shaped DIP and 6T compared to the spherical C_{60}.

Experimental phase diagrams of mixtures of low molecular weight-materials have also been traced (see [91] and references therein). Such phase diagrams become quite complicated already for relatively small molecular components with a limited number of degrees of freedom, and are therefore expected to become even more complicated as the conformational degrees of freedom of the molecular components increase [97]. Indeed, the conformational energy explicitly enters the free energy of mixing (Eq. 2.7).

As final remark for this section, one should always bear in mind that thin film growth is a non-equilibrium process where kinetic factors may have a bigger impact on the mixing behavior than thermodynamic arguments. In the next paragraph we therefore review some concepts related to growth of thin films which are relevant for this thesis. A careful balance of equilibrium arguments and kinetic factors should be able to shed light on a wide panorama of mixing scenarios.

2.1.4 Growth of molecular materials [5]

As outlined in the Introduction, vacuum deposition techniques, in particular OMBD, enable a high degree of control of the self-assembly processes involved in thin film growth on surfaces. This is largely due to the absence of a solvent, which allows to restrict the attention exclusively to the molecule-molecule and molecule-substrate interactions. Vacuum deposition techniques provide therefore a valuable tool for the controlled fabrication of several heterostructure architectures [37] and their implementation in devices [101].

In vacuum deposition, OSCs are sublimated from a source, impinge a substrate with high kinetic energy and condensate onto its surface due to to van der Waals interactions, i.e. there are no chemical bonds forming. For the systems studied in this thesis, there is a "quasi-epitaxial" relationship between substrate and OSC molecules. This terminology means that there is no commensurate relationship between the lattice of the substrate and of the molecular material, although there can be a specific orientation relationship between them. For the systems studied here, the substrate is an amorphous Si oxide surface and the orientational relationship with the molecular material corresponds to the thin film texture.

Molecular materials, among which OSCs, possess orientational and conformational degrees of freedom (Fig. 2.8) which render the understanding and the control of their self-assembly processes on surfaces more difficult than for atomic systems. In other words, the intrinsic anisotropy of OSCs renders their interactions in the solid state orientation-dependent.

The processes following the impinging of molecules on a surface are sketched in Fig. 2.8 and explained in caption. Not included in the sketch are desorption, insertion and local annealing processes [102]. Not shown are also the (inevitable) impurity adsorbates on the substrate surface, which can affect inter-molecular interactions. Further complications arise when two different materials are co-evaporated, as it is the case for D:A mixtures. For example, concerning downhill diffusion occurring on top of a molecular terrace (Fig. 2.8e), one has to distinguish which phase constitutes the terrace, i.e. pristine donor, pristine acceptor or, possibly, D:A co-crystal phase.

[5] The main sources for this section are the review article of Forrest (Ref. [98]), the book of Markov ([99]) and the article of Kowarik et al. (Ref. [100]). Other references are explicitly cited.

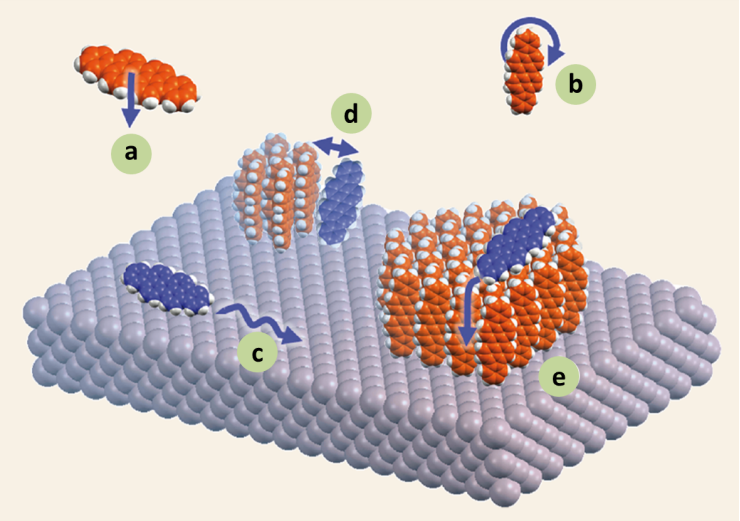

Figure 2.8: Illustration of the processes occurring for vacuum deposited molecular OSCs on a surface: **a)** arrival of one molecule sublimated from a hot source; **b)** rotational and vibrational degrees of freedom; **c)** diffusion of a molecule along the substrate potential; **d)** cluster formation; **e)** downhill diffusion from a molecular terrace. Adapted from Ref. [100].

2.1.4.1 Classification of growth modes

Despite the substantial complication of growth processes for molecular materials compared to atomic systems, "classical" arguments like the critical nucleus size [102, 103] and the scaling laws for film roughness and in-plane correlation lengths [104–107] still apply to some extent.

For epitaxial atomic systems, thin film growth modes can be classified based on the balance between desorption energy and variation of the chemical potential from the gas to the condensed phase for the adsorbate species. Another classification is based on classical wetting theory of non-volatile liquids, and involves the balance between surface energies of the supporting solid, the liquid droplet and the atmosphere [108]. The formalism employed to describe epitaxial growth is better suited as starting point for grasping some fundamental aspects of the quasi-epitaxial growth of molecular systems and it can be extended in order to include the misfit energy (or "stress") between the adsorbate species and the surface underneath. Indeed, stress can be observed also for quasi-epitaxial systems. One example is represented by the growth of DIP on native Si oxide, whose unit cell parameters continuously change during growth, converging to the thin film phase after a threshold thickness of three monolayers [109].

In Fig. 2.9 we illustrate the three growth modes classified for epitaxial systems in which the substrate material is different from the adsorbate material (hetero-epitaxy).

- In the *Volmer-Weber* growth mode, a strong de-wetting of the adsorbate is observed as a consequence of weaker interactions with the substrate then within the bulk adsorbate material itself. The surface exhibits an island-like morphology. The islands can come in contact with each other as a consequence of their lateral growth.

- In the *Stranski-Krastanov* growth mode, an initial layer-by-layer wetting stage of the adsorbate on the substrate is followed by a de-wetting/roughening stage. The onset of roughening is related to thickness-dependent strain energy.

- In the *Frank-van der Merwe* growth mode, a layer-by-layer growth fashion proceeds independently of film thickness. This is typically observed for homo-epitaxy as a special case of hetero-epitaxy.

For OSCs it might be problematic to unambiguously define the growth mode solely from post-growth surface morphology analysis due to possible de-wetting effects of the as-grown film, which can happen on several timescales depending on the material. However, the growth mode for several

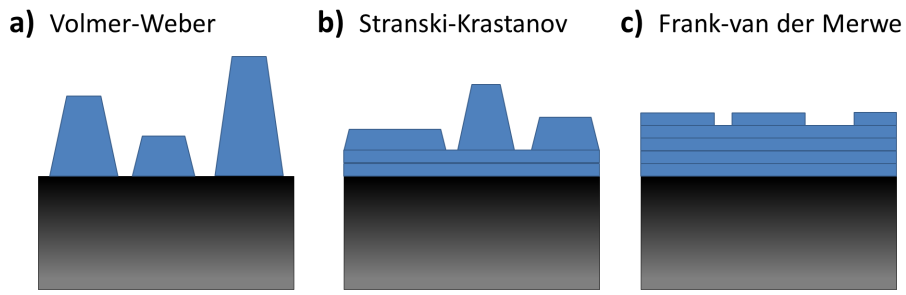

Figure 2.9: Growth modes in epitaxial growth. **a)** Volmer-Weber (pure island growth); **b)** Stranski-Krastanov (layer-by-layer + island growth); **c)** Frank-van der Merwe (pure layer-by-layer growth). Adapted from Ref. [100].

OSCs is now quite established thanks to *in situ* analyses during growth. The most common scenario is that an initial layer-by-layer growth is followed by rapid roughening (Stranski-Krastanov), as e.g. in the case of DIP [110]. The mechanisms leading to roughening can be several, for instance difference in the vertical growth rate of adjacent grains or orientational transition of the molecular units. Complete de-wetting (Volmer-Weber) can be deduced from the surface morphology of several OSCs, including the acceptor materials TCNNQ and F6TCNNQ employed in this thesis [111].

2.1.4.2 Energetic parameters of diffusion processes

There exist energy barriers associated with the processes occurring on the surface of a growing film [112] (Fig. 2.10), which we briefly describe below.

- The binding energy, E_B, is the energy for the formation of an aggregate of particles and therefore determines the critical nucleus size of an island (Fig. 2.10d).
- The intra-layer diffusion barrier, E_D, is the energy that a particle has to overcome in order to diffuse across the surface potential of a given layer or terrace (Fig. 2.10a,b).
- The Ehrlich-Schwöbel barrier, E_{ES}, is the energy associated with inter-layer transport, i.e. it is the energy barrier that the particle has to overcome in order to diffuse one layer downwards. The presence of such barrier is related to the lack of nearest-neighbor interactions that the particle experiences in proximity of a step edge (Fig. 2.10c). A lower ES barrier implies enhanced inter-layer transport and is usually connected to a more pronounced layer-by-layer growth fashion, which in turn causes thin films to be smoother (compare Fig. 2.9a,b with Fig. 2.9c).

The three energy parameters, E_B, E_D and E_{ES} have been obtained simultaneously by kinetic Monte Carlo growth simulations for isotropic particles and compared with real-time experiments for the growth of C_{60} thin films [112]. This comparison is particularly suited because of the nearly spherical shape of C_{60}, which renders the coarse-grained approach of the simulation closer to the experiment. The simulations in Ref. [112] led to the following values: $E_B = 0.13$ eV, $E_D = 0.11$ eV, $E_{ES} = 0.54$ eV. Additional parameters that enter the description of growth processes are the deposition rate and the temperature. Together with the energy terms described above, they determine film morphology in terms of island nucleation, lateral growth, and interlayer transport.

In real systems, a further complication may arise from the fact that the exact shape of the surface potential represented in Fig. 2.10 depends in general on the crystal facet on top of which the diffusion process takes place. For single-component thin films of OSCs exhibiting a 2D-powder-like crystalline texture, the crystal plane in contact with the substrate is well defined and the anisotropy of the interaction potential can be neglected, leading to one set of energy parameters to describe the growth. As outlined above, more complicated situations in which multiple sets E_B^i, E_D^i and E_{ES}^i need to be defined are: a) single-component OSC thin films exhibiting a high mosaicity, i.e. a broad distribution of the orientation of the single crystallites, involving that the

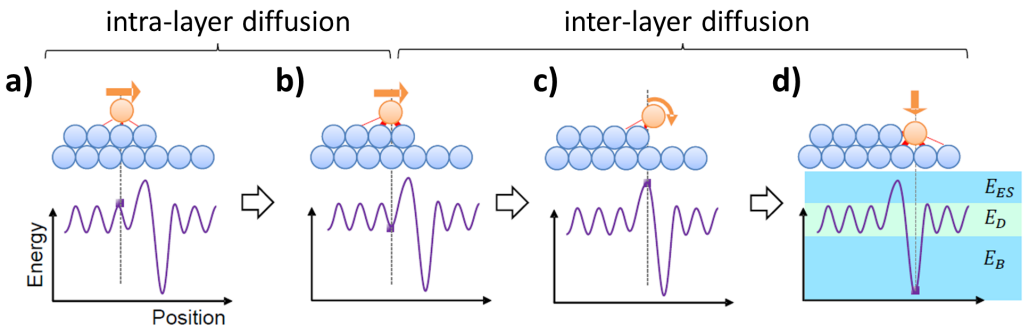

Figure 2.10: Intra- and inter-layer diffusion processes involved in thin film growth. The top schematics illustrate the location of a particle with respect to a lattice underneath during diffusion processes. The bottom plots indicate the surface potential at the given location. **a)** "Top" position corresponds to a local maximum of the surface potential (local minimum of nearest-neighbour interactions); **b)** "bridge" position corresponds to a local minimum of the surface potential (local maximum of nearest-neighbour interactions); **c)** "edge" position corresponds to an absolute minimum of the surface potential (absolute minimum of nearest-neighbour interactions); **d)** "step" position corresponds to an absolute minimum of the surface potential (absolute maximum of nearest-neighbour interactions). The relative magnitudes of the energy barriers are sketched, which are different from those obtained in Ref. [112]. Adapted from Ref. [113].

contact plane with the substrate is not well defined; b) binary mixtures with crystal mosaicity and/or phase heterogeneity.

2.1.4.3 Orientation transition for anisotropic molecules

For anisotropic particles like the OSCs used in this work (see Materials section 3.1), the energy barriers described above depend on the relative orientation of the molecules and therefore the description of inter- and intra-layer diffusion processes becomes more complicated. In particular, orientational transitions may happen during the early growth stages. To illustrate this phenomenon, we show an example of molecular dynamics (MD) simulations of the growth of PEN on amorphous Si oxide surfaces taken from Ref. [114] (Fig. 2.11).

The molecules impinge the substrate and remain adsorbed due to van der Waals interactions. The strength of these molecule-substrate interactions per molecule/rod are maximized for a face-on orientation (Fig. 2.11a). As the surface coverage increases, a cluster forms. The size of this molecular cluster, defined by the number of molecules incorporated in the cluster itself, increases accordingly. Up to a critical cluster size, the long axis of the constituting molecules remains nearly parallel to the surface. Beyond this critical size, an orientational transition of the molecules in the cluster sets in, and addition of further molecules leads to a gradual increase of the average molecular tilt angle (Fig. 2.11b). The same mechanism has been obtained from MD simulations of PEN deposited on an ordered C_{60} lattice [115].

Notice that the coexistence of lying-down and upright-standing molecular domains in the submonolayer regime has been experimentally proved for sexithiophene (6T) deposited on thermally grown Si oxide [116]. Lowering of the substrate temperature generally favors the nucleation of molecular domains exhibiting lying-down orientation, as it has been extensively shown for DIP [109, 117–119].

Including the anisotropy of the interaction potential in modeling of diffusion and nucleation processes increases the complexity of the system. However, it allows to gain further insights into the mechanisms of thin film growth and into the ways these can be affected by changing several experimental parameters. This is a fundamental prerequisite for the rational design of functional molecular layers in optoelectronic devices.

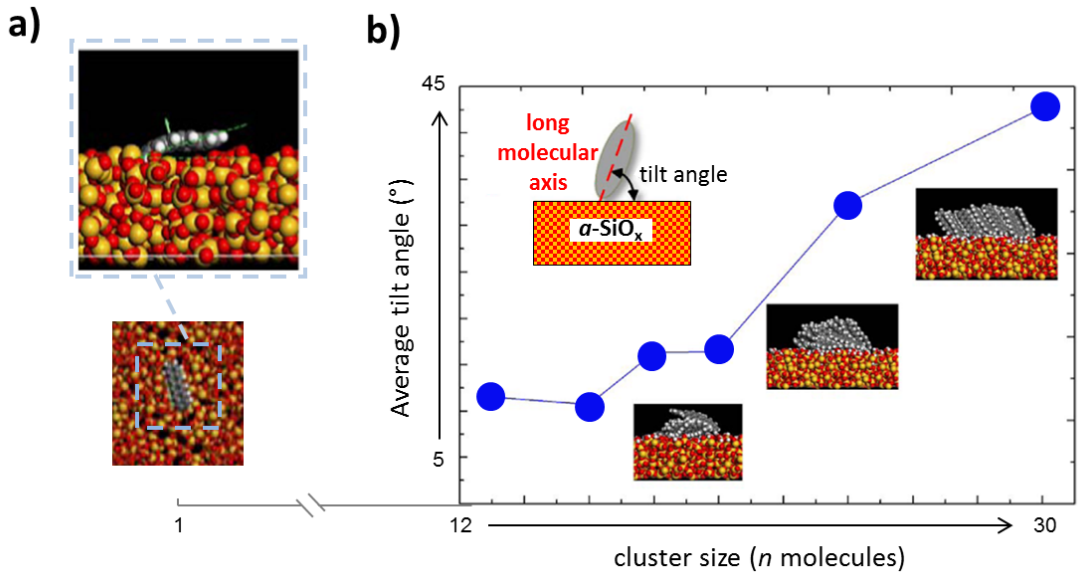

Figure 2.11: Molecular dynamics simulations of cluster size-dependent orientational transition of PEN molecules on amorphous Si oxide (a-SiO_x). **a)** One single molecule diffuses on the surface maintaining a face-on configuration in order to maximize van der Waals interactions. **b)** After a critical cluster size of n=11 molecules, a gradual orientational transition occurs, with the long molecular axis assuming in average a more upright-standing orientation. Adapted from Ref. [114].

2.1.5 Polymorphism

The occurrence of different crystal structures for the same molecular material or materials combination is called polymorphism. It is a topic of paramount importance for drug design [120] and is in general a very common issue in the growth of organic molecular crystals. Indeed, for what concerns crystals and co-crystals prepared from solution, the resulting polymorphic forms are strongly affected by nature of the solvent, temperature of the solution and, for bi-component systems, by the mixing ratio [121–123]. The appearance of different crystal polymorphs for molecular materials is related to equilibrium arguments as well as to growth dynamics. Indeed, equilibrium crystal structures might differ only very slightly in their free energy, therefore a minimal change of the growth conditions can trigger the nucleation of one polymorph rather than the other, or more polymorphs can coexhist within a crystal.

The most common small-molecular OSCs often exhibit polymorphism in single crystals, as it is the case for DIP [124], PEN [125, 126], α-6T [127, 128] and dibenzo-tetrathiafulvalene (DBTTF) [129], just to cite some examples. Also for D:A CT salts containing differently functionalized TTF as donor unit and TCNQ as acceptor unit, different polymorphic forms have been identified [130, 131]. The definition of polymorphism implies that, for a given bi-component system, the presence of several crystal structures exhibiting different stoichiometries are also classified as polymorphs, as it is the case e.g. for the D:A co-crystals of perylene:TCNQ [131].

A very common case of polymorphism is encountered when comparing the crystal structures of OSCs deposited on substrates with their bulk structures. Deposition of thin films of given compounds often leads to the formation of crystal structures which are different from those one would observe by growing bulk crystals by, e.g., solvent evaporation or vapor sublimation. The new polymorphs are observed as result of a) the dynamic processes involved in thin-film growth, b) the energetic landscape of the substrate surface. They are therefore denominated thin-film phases or substrate-induced phases (SIPs) [132]. Thin-film and bulk phases can coexist in the same film, with their relative abundance depending on film thickness [96]. In other cases, the thin-film phase might be present only in the first few monolayer, subsequently evolving in the bulk phase in a more abrupt way. In either case, one can expect that the thicker the film gets, the more its structure tends to transform into a bulk polymorph. Interestingly, it is possible to “manipulate”

the occurrence of different polymorphs by changing the growth parameters. Examples have been shown involving manipulation of the substrate temperature duriing growth [118] and irradiation with monocromatic light [133].

The study of SIPs is of special importance for OFETs since it has been observed that charge transport in the organic channel occurs only within the first ~ 2 monolayers [134]. Simulations of charge transport processes can benefit by the experimental knowledge of inter-molecular distances within the unit cell since they allow the calculation of transfer integrals. Therefore, the recognition and the precise structural solution of thin-film phases are of paramount importance [135, 136]. In the Materials section 3.1, we will discuss more in detail some cases of polymorphic forms of OSCs which are most relevant for this thesis.

2.1.6 Charge transport [6]

In this paragraph we summarize some fundamental aspects of charge transport in OSCs, which will support the data analysis of the electrical conductivity data shown the Results section 4.5.

In atomic semiconducting solids like Si, the coupling between electronic states and lattice vibrations (phonons) is negligible. Conversely, such coupling is fundamental for transport phenomena in OSCs. This leads to the definition of a quasi-particle, the *polaron*, which can be viewed as if the "electronic charge is dressed by a phonon cloud" [60]. One generally talks about polarons when considering an electrically charged molecule. Therefore, charge transport in molecular solids can be regarded as migration of polarons from a lattice site to another. Notice that that carrier diffusion can happen as local displacement around an average position *and* as a drift of this average position. In devices based on organic materials, drift diffusion dominates over local diffusion.

The parameter which expresses the intrinsic ability of a charge to diffuse in a solid matrix is the mobility, μ. Disorder obviously affects μ. The contribution of disorder to transport phenomena needs to be taken into account especially in systems like non-single crystalline, small-molecular OSCs. For such systems, the simplest expression relating the mobility to the charge drift velocity v_d and the electric field F, $v_d = \mu F$, is not valid [87]. Experimental results show that the dependence of μ on temperature depends on the degree of disorder of an organic solid [75]. In polycrystalline thin films of OSCs, the migration of a charge from one molecule to another proceeds mostly *via* hopping, which is greatly favored by a good inter-molecular overlap of the π-orbitals. Since this is a thermally activated process, in general increasing temperature favors transport in such systems. The approach of Bässler and co-workers to disorder [59] consists in assuming a Gaussian broadening Δ of the site energy, which is physically justified only by the shape of absorption bands in disordered organic materials.

In general, μ will depend on the temperature T, the energetic disorder Δ and the electric field E, the latter lowering the energetic barrier for carrier release from trap states. It has been proven experimentally that μ depends also on charge carrier density n due to filling of trap states. Therefore, the mobility can be expressed as:

$$\mu \equiv \mu(T, \Delta, F, n) \tag{2.8}$$

Eq. 2.8 implicitly relates charge carrier mobility to thin film crystalline structure and morphology *via* the disorder-induced energy broadening, Δ. For instance, a grain boundary broadens the distribution of site energy and thus affects the mobility, which can be particularly dramatic at hetero-interfaces between different materials. In this case, the difference in orbital energy between the materials constituting the grains might represent a further barrier to charge hopping. This argument explains the recognized requirements for thin film structure and morphology in solar cells, namely, that a certain degree of phase separation is needed in order to create D:A interfaces for exciton dissociation, but a path for the photo-generated carriers should be ensured through pristine D or A domains reaching to the contacts [27, 65]. Grain boundaries are also viewed as privileged sites where traps might be located.

The relationship between μ and the conductivity σ is [58]:

$$\sigma = 1/\rho = en\mu(T, \Delta, F, n) \tag{2.9}$$

[6] Most of the contents of this section are taken from the review article of Coropceanu et al. (Ref. [60]), when not differently specified.

where ρ is the film resistivity, e is the elementary charge, and it is assumed that only one kind of carrier is present. In general, the conductivity σ is related to the electrical field $\mathbf{E}$ and the conduction current density $\mathbf{J}$ *via*:

$$\mathbf{J} = \sigma \mathbf{E} \tag{2.10}$$

Note that we have inserted Eq. 2.8 in Eq. 2.9 to show all parameters affecting μ. As outlined in the introduction, in optoelectronic devices one aims at optimizing layer conductivity, which is often achieved by means of molecular doping. An implication of Eq. 2.9 is that a conductivity measurement will always lead a value in which the contributions of μ and n, respectively, are not resolved.This thesis contains indeed data of σ *vs.* D:A mixing ratio. Reasonable assumptions on the dependence of μ and n on the mixing ratio can be made based on the data obtained by complementary experimental techniques like X-ray scattering and UV-vis-NIR absorption spectroscopy, as illustrated in the Results section 4.5.

2.2 Description of radiation-matter interactions [7]

Solution of the Maxwell equations in absence of a static electric charge leads to the description of a transverse plane wave $\mathbf{E}(\mathbf{r}, t)$ propagating in an energy-absorbing medium:

$$\mathbf{E}(\mathbf{r}, t) = \mathbf{E}_0 \exp\left(i\frac{\omega}{c}\mathbf{n}\cdot\mathbf{r} - i\omega t\right)\left[\exp\left(-\frac{\omega}{c}\mathbf{k}\cdot\mathbf{r}\right)\right] \tag{2.11}$$

Here, ω is the frequency of the monochromatic light and c is the speed of light in vacuum. The first exponential factor describes the propagation of the periodic wave, where $\mathbf{n}$ is the *refractive index*. The second exponential factor describes the attenuation of the field inside the medium, with $\mathbf{k}$ being the *extinction coefficient*. The functions $\mathbf{n}$ and $\mathbf{k}$ represent, respectively, the real and imaginary part of the complex refractive index $\tilde{\mathbf{n}}$:

$$\tilde{n} = n + ik \tag{2.12}$$

Notice that Eq. 2.12 is the scalar representation of $\tilde{\mathbf{n}}$, and in the following we shall mostly use this representation. The extinction coefficient k is related to the absorption coefficient, α, *via*:

$$\alpha = \frac{2\omega k}{c} = \frac{4\pi k}{\lambda} \tag{2.13}$$

where λ is the wavelength.
The complex refractive index $\tilde{\epsilon}$ is defined as a function of $\tilde{n}$ for non-magnetic materials as:

$$\tilde{\epsilon} = \epsilon_1 + i\epsilon_2 = \tilde{n}^2 \tag{2.14}$$

The imaginary part of $\tilde{\epsilon}$, ϵ_2, describes optical excitations in a solid.
The real and imaginary parts of $\tilde{n}$ and $\tilde{\epsilon}$ are therefore related *via*:

$$\epsilon_1 = n^2 - k^2 \tag{2.15a}$$
$$\epsilon_2 = 2nk \tag{2.15b}$$

The system of Eq. 2.15 can be inverted in order to express n and k as a function of ϵ_1 and ϵ_2:

$$n = \left\{\frac{1}{2}\left[\sqrt{(\epsilon_1^2 + \epsilon_2^2)} + \epsilon_1\right]\right\}^{1/2} \tag{2.16a}$$
$$k = \left\{\frac{1}{2}\left[\sqrt{(\epsilon_1^2 + \epsilon_2^2)} - \epsilon_1\right]\right\}^{1/2} \tag{2.16b}$$

[7] The first part of this section is mostly taken from the book of Wooten [137]. The paragraph dealing with the Fresnel coefficients is mostly taken from the Woollam VASE manual [138]. The paragraphs concerning optical excitations in molecular solids are mostly taken from Refs. [75, 87, 139].

If the material is not isotropic, the optical functions in Eqs. 2.15, 2.16 become tensors.

The quantum mechanical treatment of a monochromatic perturbation of energy $\hbar\omega$ periodic in time allows to express $\epsilon_2(\omega)$ as a function of the transition probability from an electronic state ϕ_i to a state ϕ_j if the perturbation matches an energy gap of the system, $\mathcal{E}_{ij}$. In particular, ϵ_2 is proportional to the square modulus of the matrix element V_{ji}:

$$V_{ji} = \int \phi_j^* V(\mathbf{r}) \phi_i d\mathbf{r} \tag{2.17}$$

where $V(\mathbf{r})$ is the potential operator of the perturbation.

A consequence of Eq. 2.17 is that, in general, it is not possible to get unambiguous information on ground electronic states by means of optical absorption spectroscopy. Indeed, in first order perturbation theory the intensity of the observed absorption features is proportional to $|V_{ji}|^2$, where the contributions from *both* the initial and the final state are convoluted. However, occasionally strong CT interactions between a donor and an acceptor molecule can lead in the ground-state to an ionization process that causes formation of a positive and a negative polaron, respectively, as observed for P3HT doped with F4TCNQ [140]. In this case, it is possible to recognize in UV-vis-NIR absorption spectra the "fingerprints" of the polaronic species. This allows to draw quite solid conclusions about the ionization process that occurred in the ground state.

2.2.1 The Lorentz oscillator model

In order to be able to model $\epsilon_2(\omega)$ to study the optical properties of thin films, a convenient approximation is the Lorentz oscillator, for which the dynamical equation is written as:

$$m\frac{d^2\mathbf{r}}{dt^2} + m\Gamma\frac{d\mathbf{r}}{dt} + m\omega_0^2\mathbf{r} = -e\mathbf{E}_{loc} \tag{2.18}$$

Eq. 2.18 describes an attenuated forced oscillator, which can be used to model a system such as an electron bound to a nucleus (see caption of Fig. 2.12 for the explanation of the single terms).The form of Eq. 2.18 is quite general and allows to include in this description also inter-atomic vibration, which fall in the infrared range of the spectrum. In this case, the electron mass m has to be replaced with the *reduced mass* of the atoms involved in the vibration.

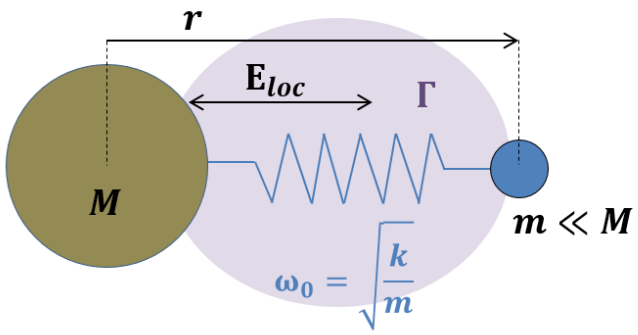

Figure 2.12: Representation of an electron bound to a nucleus in the Lorentz oscillator model. The mass m of the electron, which is located at the coordinate $\mathbf{r}$ with respect to the center of the nucleus, is much smaller than the mass M of the nucleus itself, which allows to circumvent the use of the reduced mass in Eq. 2.18. The electron is bound to the nucleus *via* the spring having the characteristic frequency $\omega_0 = \sqrt{\frac{k}{m}}$, where k is the spring constant. $\mathbf{E}_{loc}$ is the microscopic electric field experienced by the electron. The parameter Γ governs the magnitude of the viscous damping of the oscillator and accounts for energy-loss processes.

An analytical expression for $\epsilon_1(\omega)$ and $\epsilon_2(\omega)$ in non-magnetic materials can be derived:

$$\epsilon_1 = 1 + \frac{4\pi N \mathrm{e}^2}{m} + \frac{(\omega_0^2 - \omega^2)}{(\omega_0^2 - \omega^2)^2 + \Gamma^2\omega^2} \tag{2.19a}$$

$$\epsilon_2 = \frac{4\pi N \mathrm{e}^2}{m} + \frac{\Gamma\omega}{(\omega_0^2 - \omega^2)^2 + \Gamma^2\omega^2} \tag{2.19b}$$

In Eqs. 2.20, N is the number of electrons per unit volume. Including the possibility of multiple electronic transitions between atomic states separated by the energy $\hbar\omega_j$, where the probability of each transition is weighted by the corresponding oscillator strength f_j, a quantum-mechanical expression for the complex $\tilde{\epsilon}$ can be written:

$$\tilde{\epsilon} = 1 + \frac{4\pi N \mathrm{e}^2}{m} + \sum_j \frac{N f_j}{(\omega_j^2 - \omega^2) - i\Gamma_j\omega} \tag{2.20}$$

Expressing $\epsilon_1(\omega)$ and $\epsilon_2(\omega)$ from Eq. 2.20 does not obviously change their form compared to Eq. 2.19, apart from the inclusion of the summation over multiple transitions. If $\epsilon_1(\omega)$ and $\epsilon_2(\omega)$ are known, calculation of n and k is straightforward (Eq. 2.16).

The shape of $\tilde{\epsilon}$ is a complex Lorentzian. In the vicinity of a transition, i.e. when $\omega \approx \omega_j$, $\epsilon_2(\omega)$ also behaves similarly to a Lorentzian curve. Therefore, often simple Lorentzian functions (or sums of them) are used to fit optical absorption bands if broadening effects due to the solid state environment are neglected. In other words, in the simplest approximation, absorption bands are intrinsically Lorentzian in shape.

2.2.2 Response function and Kramers-Krönig relations

Dispersion relations like the dependence of the refractive index n on ω (Eqs. 2.12-2.16) follow from the *causality* requirement. For a causal system, the response X in frequency space depends on the stimulus f and the response function G according to:

$$X(\omega) = G(\omega) f(\omega) \tag{2.21}$$

Notice that $X(\omega)$, $G(\omega)$ and $f(\omega)$ are complex quantities. A practical application of Eq. 2.21 is that, in frequency space, the electric field $\mathbf{E}$ inside of a material depends on the external electric field $\mathbf{E}_{ext}$ *via* the dielectric function $\tilde{\epsilon}$ (2.14) as:

$$\mathbf{E}(\omega) = \frac{1}{\tilde{\epsilon}(\omega)} \mathbf{E}_{ext}(\omega) \tag{2.22}$$

Comparing Eq. 2.22 with Eq. 2.21, it is obvious that $1/\tilde{\epsilon}$ is the response function. From Eq. 2.21 one can show that the response function has a singularity at $\omega = \omega_0$, where ω_0 is a resonance mode of the system, which can be an electronic transition or the excitation of a molecular vibration. Taking into account these singularities by integrating in the complex plane, it is possible to show that in a causal system the following relationships must hold:

$$\epsilon_1(\omega) = 1 + \frac{2}{\pi} \fint_0^\infty \frac{\omega' \epsilon_2(\omega')}{(\omega')^2 - \omega^2} d\omega' \tag{2.23a}$$

$$\epsilon_2(\omega) = -\frac{2\omega}{\pi} \fint_0^\infty \frac{\epsilon_1(\omega') - 1}{(\omega')^2 - \omega^2} d\omega' \tag{2.23b}$$

The integrals in Eq. 2.23 indicate the Cauchy principal value [141]. They are called Kramers-Krönig (KK) relations and follow from causality requirements. They state that there cannot be any output before the arrival of an input signal, but the output may be delayed with respect to the input. Another consequence of Eq. 2.23 is that the response function of a system cannot only

describe absorption, but has also to contain information on the phase shift of the non-absorbed components, i.e. it has to describe dispersion.

The KK relations are a fundamental tool to cross-check the validity of a given optical model. This is not always straightforward since *all* frequencies contribute to the reconstructed optical functions contained in Eq. 2.23, and elaborated mathematical procedures are necessary to ensure KK consistency of the calculated optical functions [142]. However, the dielectric functions $\epsilon_1(\omega)$ and $\epsilon_2(\omega)$ obtained with the Lorentz oscillator model (Eq. 2.19) are defined KK consistent and represent therefore a valid starting point to model optical spectra.

2.2.3 Fresnel coefficients at interfaces

We consider an electromagnetic wave traveling in an infinite medium of complex refractive index $\tilde{n}_1$ and impinging at an interface with an infinite medium of complex refractive index $\tilde{n}_2$, as in Fig. 2.13a.

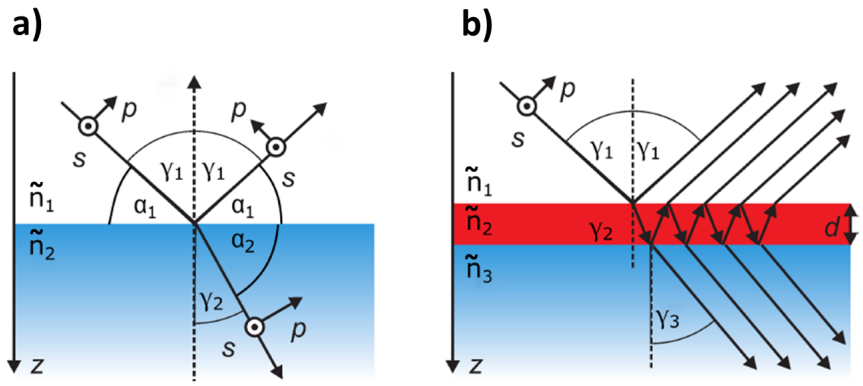

Figure 2.13: **a)** Single interface between infinite materials of refractive index $\tilde{n}_1$ and $\tilde{n}_2$, respectively. A wave with electric field components s and p impinges the interface at angle $\gamma_1 = 90° - \alpha_1$ from the normal. The angles γ and α refer to the convention for the angles in the visible/UV and X-ray region, respectively. A part of the wave is reflected at the same angle and travels back into material 1, whereas a part is transmitted inside material 2 at an angle $\gamma_2 < \gamma_1$. **b)** Double interface created by insertion of a thin film of finite thickness d and refractive index $\tilde{n}_3$. Multiple reflections inside the thin film need to be taken into account.

The Fresnel coefficients relate the complex amplitude of the incident electric field $\tilde{E}^{inc}$ with the reflected and transmitted fields at the interface, respectively $\tilde{E}^{refl}$and $\tilde{E}^{tr}$, according to:

$$\tilde{r}_{p/s} = \frac{\tilde{E}^{refl}_{p/s}}{\tilde{E}^{inc}_{p/s}}; \qquad \tilde{t}_{p/s} = \frac{\tilde{E}^{tr}_{p/s}}{\tilde{E}^{inc}_{p/s}} \tag{2.24}$$

The quantities $\tilde{r}$ and $\tilde{t}$ in Eq. 2.24 express the complex reflection and transmission coefficients, respectively, of $\tilde{E}^{inc}$ in either the p or s polarization state. The optical plane is defined by the plane in which the incident and reflected/transmitted waves propagate (Fig. 2.13). For practical use, what is actually measured is the *intensity* ratio between the reflected/transmitted part and the incident beam, $\left|\tilde{r}_{p/s}\right|^2 / \left|\tilde{t}_{p/s}\right|^2$. By imposing: a) continuity of the normal and tangential components of the fields, b) equality of the phase, one obtains for the transmitted part of the beam the well known Snell's law:

$$\tilde{n}_1 \sin(\gamma_1) = \tilde{n}_2 \sin(\gamma_2) \tag{2.25}$$

Notice that in general all quantities of Eq. 2.25 are complex, and angles γ are measured from the normal to the interface (Fig. 2.13). The Fresnel reflection coefficients of Eq. 2.24 can thus be

expressed as function of $\tilde{n}$ and γ:

$$\tilde{r_p} = \frac{\tilde{n}_2 \cos(\gamma_1) - \tilde{n}_1 \cos(\gamma_2)}{\tilde{n}_2 \cos(\gamma_1) + \tilde{n}_1 \cos(\gamma_2)}; \qquad \tilde{r_s} = \frac{\tilde{n}_1 \cos(\gamma_1) - \tilde{n}_2 \cos(\gamma_2)}{\tilde{n}_1 \cos(\gamma_1) + \tilde{n}_2 \cos(\gamma_2)} \tag{2.26}$$

Notice that Eq. 2.26 is valid for the case illustrated in Fig. 2.13a where the media 1 and 2 are infinite. In order to build an optical model for thin films, one or more additional slabs of material of finite thickness d between the infinite (or bulk) media have to be included (Fig. 2.13b). In this case, multiple reflections can take place within the thin film and the Fresnel coefficients for the reflected part of the beam, $\tilde{R}$, need to be re-defined as (see Ref. [143] and references therein):

$$\tilde{R}_{p/s} = \frac{\tilde{E}^{tot}_{p/s}}{\tilde{E}^{inc}_{p/s}} = \frac{\sum_i \tilde{E}^{refl}_{i,p/s}}{\tilde{E}^{inc}_{p/s}} = \frac{\tilde{r}_{01,p/s} + \tilde{r}_{12,p/s} \mathrm{e}^{-i2\beta}}{1 + \tilde{r}_{01,p/s} \tilde{r}_{12,p/s} \mathrm{e}^{-i2\beta}}, \tag{2.27a}$$

$$\beta = 2\pi \tilde{n}_2 \frac{d}{\lambda} \cos(\gamma_2) = 2\pi \frac{d}{\lambda} \sqrt{\tilde{n}_2^2 - \tilde{n}_1^2 \sin^2(\gamma_1)} \tag{2.27b}$$

Notice that the subscripts in Eq. 2.27 refer to the labeling of the different media as in Fig. 2.13b. The coefficients $\tilde{R}_{p/s}$ are called pseudo-Fresnel coefficients. In the third term from the left-hand side of Eq. 2.27a, the sum runs over all reflection events. The parameter β is the phase thickness of the film, with λ wavelength of the incident radiation.

Corresponding expressions can be obtained for the pseudo-Fresnel coefficients of the transmitted part of the beam in the visible and UV region electromagnetic region. Additionally, we anticipate here that the same formalism for scattering at interfaces holds for the X-ray region (see Methods section 3.3). However, for X-rays the angles are defined from the surface plane instead than from its normal, i.e. the angles α are used instead of γ in Fig. 2.13.

2.2.4 Effective medium approximations

If the composition of the thin film 2 in Fig. 2.13b is not homogeneous, an *effective* dielectric function, $\langle\tilde{\epsilon}\rangle$, can be defined. Several effective medium approximation (EMA) models are based on the inclusion of a given number of constituent materials j into a host material and can be jointly expressed as [144]:

$$\frac{\langle\tilde{\epsilon}\rangle - \tilde{\epsilon}_h}{\langle\tilde{\epsilon}\rangle + g\tilde{\epsilon}_h} = \sum_j x_j \frac{\tilde{\epsilon}_j - \tilde{\epsilon}_h}{\tilde{\epsilon}_j + g\tilde{\epsilon}_h} \tag{2.28}$$

where $\tilde{\epsilon}_h$ is the dielectric function of the host material, x_j is the fraction of the j^{th} constituent material and g is a screening and geometric factor.

In particular, the Bruggeman model consists in setting $\tilde{\epsilon}_h = \langle\tilde{\epsilon}\rangle$ and therefore does not make any assumption concerning the material with the highest constituent fraction, being self-consistent (see also [145] and references therein). In the Bruggeman model, Eq. 2.28 must be solved numerically and the correct solution branch needs to be chosen. Such model is the most appropriate to describe surface roughness of thin films whereby one of the constituent materials is set as void with x_{void} = 50% [144].

The Bruggeman model has particular relevance for this work and in general for works dealing with binary mixtures of OSCs [38, 93, 142] where surface roughness cannot be neglected. In this thesis, D:A equimolar mixtures are modeled by a single dielectric function and the Bruggeman model is exploited to account for surface roughness. Indeed, for well-mixing systems like DIP:F6TCNNQ (see Results section 4.1), only one homogenous phase of the D:A co-crystal is observed. This approximation is also used for systems like 6T:F6TCNNQ, in which partial phase-separation of the pristine materials is observed in equimolar mixtures (see Results section 4.1), and relies on the assumption that the characteristic length-scales for phase-separation are much smaller than the wavelength of the incident radiation. This avoids excessive complication of the optical model employed and allows to obtain quantitative information about the optical anisotropy of the system.

Some remarks must be made concerning the applicability of the EMA models above. All such models work within the dipole approximation, i.e. they assume that the $\lambda \gg a$, where a is a typical length scale of the constituent materials. If this is certainly true for nano-crystals or nanoscopic pores, it becomes much less accurate if one considers, e.g., large islands of a strongly de-wetted material, where the lateral and/or vertical length scales of the islands might well be of the same order of magnitude of the visible light, i.e. $\sim$ several hundreds nm. In this case, diffused scattering of the light becomes much more significant and the EMA models illustrated above fail.

2.2.5 The Franck-Condon principle

The oscillator formalism (Eq. 2.19) allows to qualitatively describe optical transitions in a wide energy range, from the microwave to the infrared, visible and UV [137]. Due to the KK-relations (Eq. 2.23), vibrations in a solid, which are located in the infrared region of the spectrum, also contribute to the dielectric function in the UV-vis region, but their effect is in general negligible. This is because the periods of vibration of the nuclei compared to electron motions are much longer, i.e. the nuclei are "immobile" over the timescale of an electronic transition. From a quantum-mechanical point of view, this involves that the total wave-function $\psi_{s\nu}$ containing the vibrational state ν and the electronic state s can be approximated as:

$$\psi_{s\nu} = \phi_\nu(\mathbf{R})\phi_s(\mathbf{R};\mathbf{r}) \tag{2.29}$$

Eq. 2.29 expresses the Born-Oppenheimer (or adiabatic) approximation for biatomic molecules. The variable $\mathbf{r}$ includes the coordinates of all electrons constituting the molecule. Here, ϕ_ν indicates the vibrational wave-function and uniquely depends on the nuclear coordinate $\mathbf{R}$, whereas $\phi_s(\mathbf{R};\mathbf{r})$ indicates the electronic wave-function and depends on both $\mathbf{r}$ and $\mathbf{R}$ [67]. The factorization of $\psi_{s\nu}$ in Eq. 2.29 allows to solve the Schrödinger equation for the electronic part at several fixed values of $\mathbf{R}$ in order to construct the curve describing $E_s(\mathbf{R})$ for a given electronic state s, which is then used as a potential to solve the Schrödinger equation for the nuclear part [67]. The typical shape of $E_s(\mathbf{R})$ is shown in Fig. 2.14. Notice that Eq. 2.29 can be considered also valid for complex molecules like OSCs, where $\mathbf{R}$ represents a general configuration coordinate.

A common approach to optical excitations in a wavelength range where $\lambda \gg d$, with d lattice parameter of the solid, is the *dipole approximation*. In this approximation, the spatial variations of the electric field $\mathbf{E}$ of an incoming wave across the atom (or molecule) are neglected, and the operator $V(\mathbf{r})$ in Eq. 2.17 for calculation of the transition probability is the electric dipole operator $\boldsymbol{\mu}$, which for a molecule is given by [67]:

$$V(\mathbf{r}) \equiv \boldsymbol{\mu} = \mu(\mathbf{r}) = e\left(\sum_i Z_i\mathbf{R}_i - \sum_j \mathbf{r}_j\right) \tag{2.30}$$

The sums in Eq. 2.30 extend over all nuclei i with total charge Z_i and electrons j constituting the molecule. The use of the operator $\boldsymbol{\mu}$ to calculate transition amplitudes is the common starting point for several derivations in optical spectroscopy. The corresponding matrix element is also commonly called *transition dipole moment* (TDM), often also indicated with $\boldsymbol{\mu}$ as the operator itself. Notice that, in general, the TDM is a vector.

Inserting Eq. 2.30 into Eq. 2.17 with the electronic-vibrational wave-function given in Eq. 2.29, it can be shown that the transition probability from an initial *vibronic* state characterized by the quantum numbers $s\nu$ to a final state $s'\nu'$ is proportional to the Franck-Condon factor $f_{\nu'\nu}$ [67, 147]. Using a different notation than in Eq. 2.17 we may write:

$$V_{ji} \equiv V_{s'\nu',s\nu} \propto f_{\nu'\nu} = \int_0^\infty \phi^*_{\nu'}\phi_\nu dR \tag{2.31}$$

The Franck-Condon factor in Eq. 2.31 is the overlap integral between two vibrational states belonging to different electronic states. The Franck-Condon principle states that an electronic transition is "vertical", i.e. it occurs at the same configurational coordinate $\mathbf{R}$ of the nuclei, and its probability is maximized when the overlap between the vibrational states is maximum, as illustrated in the diagram of Fig. 2.14.

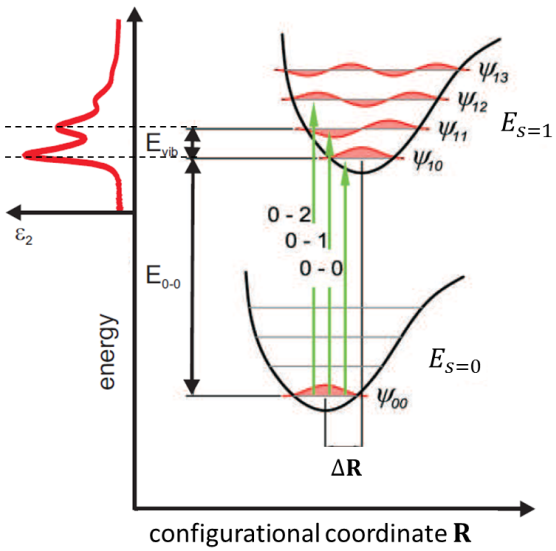

Figure 2.14: Illustration of the Franck-Condon principle. In abscissa, the configurational coordinate $\mathbf{R}$ represents the positions of all nuclei forming the molecule is shown. The potential curves $E_s(\mathbf{R})$ can be calculated solving the electronic part of the Schrödinger equation for the wave-function expressed in Eq. 2.29. The potential curves shift towards larger $\mathbf{R}$ for excited electronic states, which corresponds to the tendency of the molecule to dissociate for highly energetic excitations. $\mathbf{\Delta R}$ denotes the shift of the potential minimum. The vibronic transitions from the ground state ψ_{00} to the excited states $\psi_{1\nu'}$ are indicated. E_{0-0} indicates the energy gap between the electronic states in their respective lowest vibrational state, and E_{vib} is the difference in energy between two vibrational states ν and $\nu+1$. The top left plot shows an absorption spectrum of DIP in solution. Adapted from Ref. [146].

The top left plot of Fig. 2.14 shows an example of absorption spectrum of DIP in solution in terms of ϵ_2. The characteristic curve shape with multiple bands of different relative intensity (also called *vibronic progression*), often observed for OSCs, is an effect provoked by the different probabilities for the vibronic transitions. The spacing between the bands and their intensity distribution can give important information about the degree of coupling between electronic and vibrational states in terms of the Huang-Rhys parameter S [148].

2.2.6 Excitons in molecular solids

The theory illustrated above relating vibronic transitions to absorption spectra rigorously holds for a monomer, i.e. for an isolated molecule. In a molecular crystal, due to the relatively weak cohesive forces described in the Fundamentals section 2.1, the solid can be viewed as an "oriented gas" and the transitions of the monomer can still be observed, although intermolecular interactions lead to several differences between the spectra of the monomer and of the crystal, respectively. Such differences consist in splitting of the vibronic bands, change of their relative intensity and red shifts.

The effect of red-shift of the absorption spectrum is explained by the polarizability of the medium in a solid (or in a solution) compared to the isolated molecule (in a gas) [149, 150]. The excitations in the single molecule polarize the surrounding environment, which then acts on the molecule itself with a resulting field. Such field renders the ground state ψ_{00} less binding, i.e. decreases E_{0-0} (Fig. 2.14), which results in an overall red-shift of the absorption spectrum. Notice that, if E_{0-0} denotes the position of the lowest energy absorption peak as in Fig. 2.14, it typically holds $\mathrm{E}_{0-0,isol.mol.} > \mathrm{E}_{0-0,solution} > \mathrm{E}_{0-0,solid}$ since the polarization energy generally increases going from the gas to the molecule in solution and then in the molecular crystal.

In solids, electronic excitations from a ground state to an excited state lead to the formation

of coulombically bound electron-hole pairs called *excitons*. The theory described in the above sections does not take into account exciton formation. Treating for the bound electron-hole pair as a hydrogenoid atomic system immersed in a polarizable medium, one can write simple expressions for the exciton binding energy E_{ex}^{b} and characteristic exciton radius a_{ex} [151]:

$$E_{ex}^{b} = Ry\frac{\mu_{ex}}{m}\frac{\mu_1}{\epsilon^2} \tag{2.32a}$$

$$a_{ex} = a_B\frac{m}{\mu_{ex}}\epsilon \tag{2.32b}$$

In Eq. 2.32a, $Ry = 13.6$ eV is the Rydberg constant, μ_{ex} is the exciton reduced effective mass, m is the free electron mass and ϵ is the dielectric constant of the medium (analogous to ϵ_1 in Eqs. 2.14,2.15a). In Eq. 2.32b, $a_B = 0.529$Å is the classical Bohr radius of the hydrogen atom. Excitons can transport energy without transport of a net charge [151]. Three kinds of excitons exist, which we briefly describe in the following.

- For *Frenkel excitons* it holds $a_{ex} \ll d$, with d unit cell parameter of the molecular crystal, i.e. these excitations can be thought as localized on one molecular unit. However, they can move in the crystal *via* dipole interactions.
- For *Mott-Wannier excitons* it holds $a_{ex} \gg d$, i.e. these excitons have some degree of delocalization in the crystal. Due to their delocalized nature, these excitons have been observed mostly in semiconductor crystals of relatively high dielectric screening like Si or Ge, but they are difficult to obtain in molecular solids.
- For *CT excitons*, it holds $a_{ex} \approx d$. For example in OSCs, where often the crystal unit cell contains two inequivalent molecules, this means that a CT exciton can be delocalized on two molecular units.

The three kinds of molecular excitations above can describe at the microscopic level the relative intensity of the vibronic bands in a molecular solid. For example, for crystalline films of DIP exhibiting uniaxial anisotropy it has been shown that inclusion of both a Frenkel and a CT exciton can reproduce fairly well the out-of-plane component of ϵ_2 [148].

2.2.6.1 Davydov splitting

The exciton model has been described in detail by Davydov [152] and Kasha [139]. It is useful here to consider the case of exciton formation in a molecular *dimer*, which is of relevance for many OSCs containing two inequivalent molecules per unit cell. The assumption of this model is that the two monomeric units forming the dimer have a small electron overlap, which is the case for molecular materials. The expressions for the ground-state and excited state wave-functions, respectively Ψ_G and Ψ_E, are written as:

$$\Psi_G = \psi_u\psi_v \tag{2.33a}$$

$$\Psi_E = \frac{1}{\sqrt{2}}\left(\psi_u^{\dagger}\psi_v \pm \psi_u\psi_v^{\dagger}\right) \tag{2.33b}$$

In Eq. 2.33b, $\psi_{u(v)}$ represents the ground state wave function of molecule $u(v)$ in the dimer and $\psi_{u(v)}^{\dagger}$ represent the corresponding excited state wave functions. Two effects are obtained. First, a lowering of the dimer excited state energy compared to the monomer, ΔE_{vdW}, due to van der Waals interactions between the two excitations, each localized on one molecular unit. This is a binding contribution. Secondly, a resonance splitting of the excited levels, ΔE_{res}, which stems from the exchange of excitation energy between the two inequivalent molecules. It typically holds $\Delta E_{vdW} \ll \Delta E_{res}$.

Writing the splitting term ΔE_{res} as function of the TDM of the single molecules leads to different selection rules for the split levels depending on the relative orientation of the molecular TDMs. Illustration of several relevant cases can be found in Refs. [93, 139]. Here we focus on the case of molecular TDMs oriented obliquely to each other, which is of relevance for some OSCs studied in this work. In this case, transitions to both split excited levels are allowed and their energy separation is commonly denominated Davydov splitting, ΔE_{Dav}, as depicted in Fig. 2.15.

The excited state of the monomer is thus slightly red-shifted due to the van der Waals binding contribution and then split between two sub-bands, E' and E'', called the Davydov components of the fundamental transition $G \rightarrow E$. The low(high)-energy component results from the in(out-of)-phase interaction of the monomer TDMs. It follows that a change in the relative intensity of the Davydov components observed e.g. in absorption spectroscopy can originate either from a change in the strength of intermolecular interactions or from a change in the orientation of the dimer. We will see an interesting example of this in the Results section 4.3. Interestingly, a theoretical study by Beljonne et al. [153] shows that the Davydov splitting in PEN is modulated by the percentage of CT character of the fundamental transition, whose energy shifts with the intermolecular distance (see also Fig. 2.3).

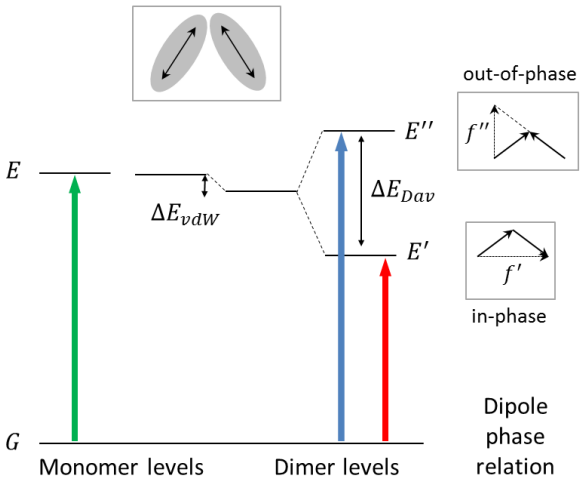

Figure 2.15: Exciton formation in a molecular homo-dimer with oblique orientation of the monomer TDM (top sketch). The TDM can be oriented along any molecular axis. The Davydov splitting of the energy levels is indicated as $= \Delta E_{Dav} = E'' - E'$. On the right, vector representation of the phase relation f of the two TDM. Adapted from Ref. [139].

Notice that Davydov splitting, changes of relative band intensity and red-shifts can be also observed considering vibrational transitions between ϕ_ν states (Eq. 2.29). For instance, in Ref. [154] Davydov splitting of a set of vibrational modes for the prototypical OSC PTCDA is shown, and in this thesis Davydov splitting is suggested for the C$\equiv$N stretching mode of F6TCNNQ (see Results section 4.4). Also, CT-type interactions can induce both a change in relative intensity of the vibrational bands as well as mode shifts to lower energies. Examples of CT interactions-induced relative intensity changes as well as mode shifts to lower energies can be found in the literature [42, 86, 155, 156] and in the Results section 4.4 of this thesis.

2.2.6.2 Charge transfer interactions

The dimer model of Kasha [139] can be conceptually extended to include a heterodimer, i.e. a dimer constituted of two different molecular species, for example a donor and an acceptor. In this case the energy level alignment, primarily of the donor HOMO with respect to the acceptor LUMO, might induce strong CT-type interactions with transfer of electron density from D to A. Therefore, the electronic coupling between the D and A monomers might be significant and the *ansatz* leading to Eq. 2.33b may not be applicable. Intermolecular D:A interactions that involve CT may give rise to different scenarios [157], which are schematically illustrated in Fig. 2.16. Below

we briefly describe these scenarios in a simplified way, i.e. neglecting the exciton binding energy [157, 158].

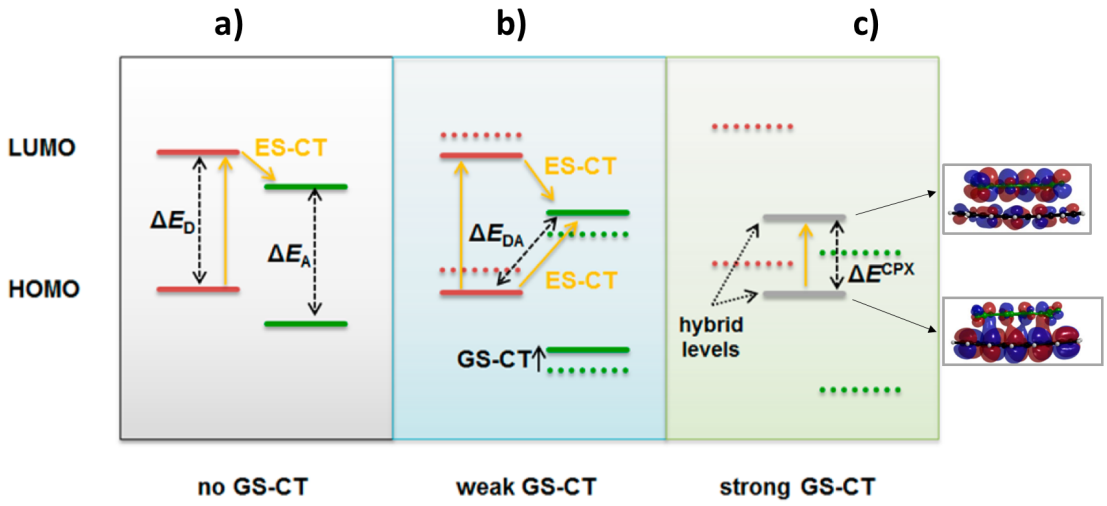

Figure 2.16: Simplified illustration of the different CT situations at a D:A interface. The HOMO-LUMO levels of the donor are in red, those of the acceptor in green. The different energy gaps are indicated as ΔE. The abbreviations GS- and ES-CT stand respectively for excited state and ground-state CT. Adapted from Ref. [157]. In **c)**, the DFT simulation of the hybrid levels in PEN:F4TCNQ is adapted from Ref. [54].

- Fig. 2.16a shows a situation in which the energy difference between the donor HOMO and the acceptor LUMO is large and there is no coupling in the ground-state (GS), i.e. CT from D to A can occur only after an excitation is provoked on the donor, with corresponding exciton formation, and the excited electron can be transferred from the donor LUMO to the acceptor LUMO. This is one way to induce excited state CT, or ES-CT, and is widely invoked as main mechanism to separate the exciton and extract charge carriers from organic solar cells [27, 159].
- In Fig. 2.16b, the GS-CT coupling is stronger than in the case of Fig. 2.16a, but still relatively weak and it is manly manifested in the shift of the energy levels due to exciton formation. Here, an additional ES-CT pathway is present which involves direct excitation of an electron from the donor HOMO to the acceptor LUMO, and allows to define a D-A gap, ΔE_{DA}, which can be estimated by optical spectroscopy as shown in Refs. [157, 160, 161].
- In the third case represented in Fig. 2.16c, the donor HOMO and acceptor LUMO lie close in energy and a strong coupling between them is expected with significant GS-CT. As already mentioned in the Introduction, recent works [47, 54] suggest that this GS-CT scenario is governed by hybridization of the frontier orbitals of donor and acceptor, which leads to the formation of a new supramolecular complex featuring new hybrid HOMO and LUMO levels (see also Fig. 1.2a). In the ground state, the hybrid HOMO is doubly occupied with the electrons coming from the donor HOMO and the hybrid LUMO is empty. The *character* of the new hybrid levels depends on how much of the monomer orbitals they retain, i.e., what is the magnitude of the coefficients for the linear combination of the donor HOMO and acceptor LUMO in the Hückel-like treatment of the isolated orbitals (see Introduction and Refs. [48, 55]). As a consequence of orbital hybridization a new bandgap is formed, ΔE^{CPX}, whose width depends on the intermolecular overlap integral [48, 55] and which is typically smaller than $\Delta E_{D,A}$ in Fig. 2.16a (see Ref. [162] and Results section 4.1).

From a spectroscopic point of view, the scenario of strong GS-CT with formation of a supramolecular complex (Fig. 2.16c) involves that the fundamental transition from the hybrid HOMO to the

hybrid LUMO in the complex can be observed at significantly lower energy than the fundamental transitions in the pristine donor and acceptor. In general, the use of complementary methods is required to obtain a comprehensive picture of the various CT scenarios [157].

To interpret the data contained in this work for the D:A combinations employed, we always assume that some degree of GS-CT occurs *via* complex formation (Fig. 2.16c). However, the detailed analysis of the various mechanisms illustrated in Fig. 2.16 goes beyond the scope of the thesis. For the material combinations studied here, formation of D:A co-crystals is also experimentally proved. The formation of D:A molecular crystals is directly related with the strong GS-CT within the supramolecular complex. However, in this thesis we do not explicitly discuss to which extent D:A intermolecular interactions within the dimer affect the overall cohesion of a D:A co-crystal, i.e. we do not isolate the electronic coupling between different dimers in the crystal from the van der Waals contributions.

The effect of GS-CT interactions on molecular vibrations is also a topic of this thesis. Apart from what anticipated in the Introduction, the effect of GS-CT on molecular vibrations becomes now clearer in a molecular picture considering the shape of the molecular orbitals in the case of strong GS-CT (Fig. 2.16c). The significant alteration of the ground-state of the D:A dimer involves a change in the shape of the corresponding potential curve *vs.* the configurational coordinate (Fig. 2.14). This, in turn, involves a change in the shape and energy spacing of the *vibrational* wavefunctions ϕ_ν (Eq. 2.29). Therefore, although optical absorption experiments do not allow to unambiguously discriminate between effects of ES- and GS-CT (Eq. 2.17), the study of molecular vibrations allows to overcome this difficulty and to quantify the degree of GS-CT, which is the topic of the Results section 4.4.

2.2.7 Scattering of X-rays [8]

We pass now to analyze the interactions with X-rays, whose typical wavelength is about 10^3 times shorter than that of UV-Vis radiation. Therefore, for treating interactions of X-rays with media on the typical length scales of organic molecular solids, the dipole approximation fails and it is necessary to take into account spatial variations of the electromagnetic field.

We start by considering the scattering of X-rays from a *free* electron. Classically, the periodic electric field of an incoming X-ray photon exerts a force on the electronic charge, which responds by oscillating and emitting electromagnetic radiation during its acceleration. This scattering process is called *elastic* when the energy of the outgoing photon is the same as the energy of the incoming photon; however, the direction of the momentum $\hbar\mathbf{k}$ may change. The X-ray scattering methods employed in this thesis are based on elastic scattering.

The differential scattering cross section of an electromagnetic wave scattered by a free electron is:

$$\left(\frac{d\sigma}{d\Omega}\right) = r_0^2 \left|\hat{\boldsymbol{\epsilon}} \cdot \hat{\boldsymbol{\epsilon}}'\right| \tag{2.34}$$

where Ω is the solid angle and σ is the cross section, $\hat{\boldsymbol{\epsilon}}$ is the polarization of the incident field and $\hat{\boldsymbol{\epsilon}}'$ that of the radiated field. In Eq. 2.34, the fundamental length scale of the scattering process, r_0, has been introduced:

$$r_0 = \left(\frac{e^2}{4\pi\epsilon_0 mc^2}\right) \tag{2.35}$$

From Eq. 2.35, r_0 amounts to 2.82×10^{-5} Å and is called the Thomson scattering length or electron scattering radius.

Elastic scattering from an atom involves that all the constituting electrons oscillate under the effect of the incoming photons. The phase shift between an electromagnetic wave of momentum $\mathbf{k}$ hitting an atom and being elastically scattered with momentum $\mathbf{k}'$ is $\Delta\phi = \mathbf{Q} \cdot \mathbf{r}$, with:

$$\mathbf{Q} = \mathbf{k} - \mathbf{k}' \tag{2.36}$$

[8] The contents of this section have been taken mostly from the book of Als-Nielsen [163], and other sources are explicitly cited.

being the total *momentum transfer*.

The distribution of all electrons within the atom needs to be taken into account, which leads to the definition of the atomic form factor $f^0(\mathbf{Q})$.

$$f^0(\mathbf{Q}) = \int \rho_e(\mathbf{r}) \mathrm{e}^{i\mathbf{Q}\cdot\mathbf{r}} d\mathbf{r} \tag{2.37}$$

The integration runs over the atomic volume and, mathematically, is equivalent to the Fourier transform of the electron density of the atom, $\rho_e(\mathbf{r})$. The form factor f^0 can be seen as a weighting factor for the scattering length of a single electron.

The exact $f^0(\mathbf{Q})$ can be approximated by a weighted sum of Gaussian curves [164], which is a monotonically decreasing function. It always results $f^0(\mathbf{Q}=0) = Z$, the atomic number, since all volume elements of the atom scatter in phase, and $f^0(\mathbf{Q}\to\infty) = 0$ since for increasing angles the volume elements tend to scatter out of phase.

2.2.7.1 General expression of the atomic form factor

Not all electrons of an atom will respond as free electrons to an external field. The electrons in the deepest energy levels, or K-shell electrons, are more bound than the electrons in the higher-lying L- or M-shells, therefore their response will deviate more significantly from that of a free electron. This is true for incoming photon energies $\hbar\omega$ smaller than the element-specific absorption edge. Above this energy threshold, the electrons respond as if they were free. The response of a bound electron to incoming photons can be assimilated to that of a forced harmonic oscillator [165], analogous to the Lorentz oscillator model (Eqs. 2.18-2.20).

In general, the scattering efficiency given by the atomic form factor of Eq. 2.37 is lowered by an amount f' due to the bound electrons. Including an additional term, f'' to take into account dissipation due to absorption processes, the form factor becomes $f(\mathbf{Q}, \hbar\omega)$:

$$f(\mathbf{Q}, \hbar\omega) = f^0(\mathbf{Q}) + f'(\hbar\omega) + if''(\hbar\omega) \tag{2.38}$$

Notice that f' and f'' are related to the behavior of tightly bound electrons, thus they do not appreciably depend on $\mathbf{Q}$. They vary strongly in proximity of an absorption edge, which is exploited in so-called "anomalous" X-ray scattering techniques.

Apart from elastic scattering, several processes involve *inelastic* scattering of X-rays, i.e., the energy of the incoming photon is absorbed. One of these processes is the *Compton scattering*, in which an incident photon transmits part of its energy to a quasi-free electron from an outer atomic shell, ejecting it, and is then scattered in another direction.

The absorption of X-rays from a core electron can lead to its ejection from the atomic K-shell. The emitted electron is denominated *photoelectron*, and a hole is created in the now unoccupied state. Two competing phenomena can occur to compensate the created hole, namely *fluorescence* and *Auger emission* of a second electron.

The processes described above lead in general to the attenuation of an X-ray beam traveling through a medium, although obviously each process has a different cross-section depending on the energy and the atomic number of the elements constituting the medium. In general, the transmittance of an X-ray beam can be phenomenologically described by the Lambert-Beer law (Eq. 3.20), which we report in relationship to optical absorption spectroscopy in the Methods section 3.3 further below (Eq. 3.20).

2.2.7.2 Diffraction from a crystal

When X-rays are elastically scattered from a crystal, the total scattering amplitude as function of $\mathbf{Q}$, $F^{cryst}(\mathbf{Q})$, can be calculated by performing a sum over the amplitude of the fields scattered from all atoms arranged in the *unit cells* of the crystal. The location of each atom in a given reference system can be written as $\mathfrak{R}_{n,j}$, where n run over all unit cells of the solid and j runs over all atoms inside the n^{th} unit cell. The symmetry properties of a crystal allow to write $\mathfrak{R}_{n,j} = \mathbf{R}_n + \mathbf{r}_j$

(Fig. 2.17) and factorize the sums over n and j, respectively, leading to the following expression:

$$F^{cryst}(\mathbf{Q}) \propto \sum_j \overbrace{\underbrace{f_j(\mathbf{Q})}_{\substack{\text{atomic}\\ \text{form factor}}} \mathrm{e}^{i\mathbf{Q}\cdot\mathbf{r}_j}}^{\substack{\text{structure}\\ \text{factor}}} \sum_n \overbrace{\mathrm{e}^{i\mathbf{Q}\cdot\mathbf{R}_n}}^{\text{lattice sum}} \tag{2.39}$$

The summation over the indexes n in Eq. 2.39 is the lattice sum and runs over all possible angles/directions along the unity circle in the complex plane. It is non-vanishing if the constructive interference condition is met, i.e. $\mathbf{Q} \cdot \mathbf{R}_n = 2\pi M$, with $M \in \mathbb{Z}$, for which the scattered field is amplified by a factor of the order of the number of unit cells in the sample. This simply states the somehow experimentally obvious fact that the larger is the illuminated area of the sample, the stronger the signal will be.

The vectors $\mathbf{R}_n$ belong to a Bravais lattice, i.e. a suitably defined, translationally invariant periodic structure. Overall, 7 kinds of Bravais lattices exist, which can be consulted on the International Tables for Crystallography [166]. Here we just notice that very often for molecular solids it is common to have the Bravais lattices of lowest symmetry like monoclinic or triclinic.

The vectors $\mathbf{R}_n$ can be always written in real space as a linear combination of the basis vectors $\mathbf{a}_1$, $\mathbf{a}_2$ and $\mathbf{a}_3$ with integer coefficients n_1, n_2 and n_3:

$$\mathbf{R}_n = n_1\mathbf{a}_1 + n_2\mathbf{a}_2 + n_3\mathbf{a}_3 \tag{2.40}$$

The basis vectors of Eq. 2.40 can be used to define a set of new basis vectors in the *reciprocal space*, called reciprocal basis vectors, which we write in the compact form:

$$\mathbf{a}_x^* = 2\pi\frac{\mathbf{a}_y \times \mathbf{a}_z}{V}, \quad \text{with } V = \mathbf{a}_1 \cdot (\mathbf{a}_2 \times \mathbf{a}_3) \tag{2.41}$$

where subscripts x, y, z define the three right-handed permutations of the subscripts in Eq. 2.40, and V is the unit cell volume. Any reciprocal space vector $\mathbf{G}$ can be defined as:

$$\mathbf{G} = h\mathbf{a}_1^* + k\mathbf{a}_2^* + l\mathbf{a}_3^* \tag{2.42}$$

The integer coefficients h, k, l in Eq. 2.40 are called Miller indices. Notice that a rotation by an angle ϕ in the direct lattice corresponds to a rotation of the same magnitude in the reciprocal lattice. The reciprocal lattice vectors in Eq. 2.41 are defined such that the product $\mathbf{G} \cdot \mathbf{R}_n$ can be easily worked out as:

$$\mathbf{G} \cdot \mathbf{R}_n = 2\pi\,(hn_1 + kn_2 + ln_3) = 2\pi \times M, \quad \text{with } M \in \mathbb{Z} \tag{2.43}$$

Looking now again at the lattice sum in Eq. 2.39, one obtains non-destructive interference only if the Laue condition is met:

$$\mathbf{Q} = \mathbf{G} \tag{2.44}$$

An formulation equivalent to Eq. 2.44 is the experimentally more intuitive Bragg's law, for which we refer to Fig. 2.17. We consider a crystal at which coherent X-ray photons of wavelength λ are specularly reflected from a given set of crystal planes characterized by a spacing d. The total path difference between two photons reflected from consecutive crystal planes is $2s$, which has to be equal to an integer multiple of λ in order to result in constructive interference. Expressing s as function of d and θ leads to:

$$n\lambda = 2d\sin(\theta) \tag{2.45}$$

The index $n \in \mathbb{N}$ denotes the *diffraction order* and expresses the fact that, for any fixed d, there exist several orders of the same reflection giving constructive interference which are located at approximately $n \times \theta$ (for small θ). As noted above, the Bragg's law (Eq. 2.45) and the Laue condition (Eq. 2.44) are equivalent since they express the condition for the coherent superposition of the elastically scattered waves.

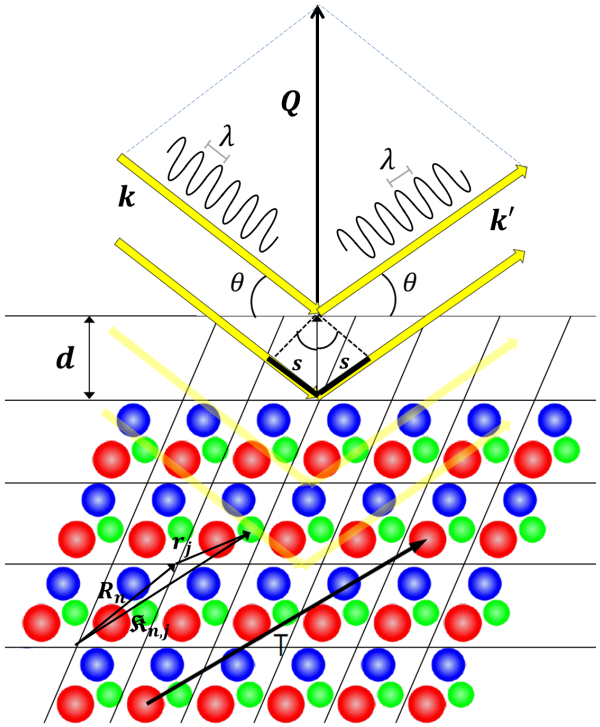

Figure 2.17: [LOWER part] Illustration of the definition of position vectors $\mathbf{R}_n$ and $\mathbf{r}_j$, respectively for unit cells and atoms within each unit cell. The vector $\mathbf{T}$ denotes the translational invariance of the Bravais lattice. [UPPER part] Specular scattering geometry which allows to deduce the Bragg's law, as described in the main text. The momentum transfer $\mathbf{Q}$ defined in Eq. 2.36 is also shown. Adapted from [165].

Here we add some comments on the summation over the indices j in Eq. 2.39, where we omitted the energy-dependence of the atomic complex form factor f_j. This summation is called *structure factor*. Generally, a basis set $\mathbf{r}_j$ needs to be superimposed to the Bravais lattice in order to describe all atomic positions, and the scattering contribution of each atom needs to be weighted by its respective form factor. For the applications elastic scattering which we exploit in this thesis the dependence of the atomic form factor on photon energy can be neglected and the form factor can be treated as a real quantity. The superposition of an additional basis set $\mathbf{r}_j$ leads to modulations of the total scattered amplitude compared to an ideal Bravais lattice. This may occasionally lead to destructive interference which causes systematic absences of given diffraction features. As it can be expected, for molecular solids the structure factor may become very complicated due to the presence of many atoms for each molecule. From Eq. 2.39 it follows that the unit cell parameters of a given molecular crystal can be calculated from a diffraction pattern by simply reproducing the *positions* of the diffraction maxima. In order to solve the full molecular structure, modeling of peak *intensity* through the structure factor is necessary [135, 136].

CHAPTER 3

MATERIALS AND METHODS

In this chapter we introduce the molecular materials that constitute the thin films produced and characterized in this work and the substrates used as support for the films. Subsequently we introduce the experimental methods which have been used for thin film characterization. We describe most extensively X-ray surface scattering techniques carried out at synchrotron facilities as the information that they provide on thin film structure represents often the starting point of further characterization. In combination with real-time X-ray reflectivity measurements we illustrate two models for thin film growth that assume the kinematical approximation, and further on we illustrate the exact recursive method of Parratt. We continue by describing optical spectroscopy methods, especially ellipsometry and infrared spectroscopy, and conclude with other characterization methods: transmission-absorption spectroscopy, atomic force microscopy and electrical conductivity measurements. Several examples of the application of these experimental methods for the characterization of thin films of OSCs are reported throughout the chapter.

3.1 Organic Semiconductors

Here we describe the molecular and crystal structure of the OSCs employed in this work, citing selected studies that feature their use. We divide them based on their donor or acceptor character. Whenever necessary, we stress the reported presence of different crystal polymorphs. The relative HOMO-LUMO energy level alignment is relevant for the discussion within the single Results sections and is therefore presented there. The chemical structure and the size of the molecules will be also shown in the pertaining Results sections.

3.1.1 Donors

3.1.1.1 Diindenoperylene

Diindenoperylene (DIP, Fig. 3.1a) was used as donor material throughout this thesis. This OSC exhibits in single crystals ambipolar transport with fairly high time-of-flight mobilities [167]. It has also been employed in organic solar cells in combination with C_{60}, achieving high fill factors and open-circuit voltages [168]. Several bulk crystal polymorphs are observed depending on the T at which the single crystals are held [124]. In particular, the polymorph observed at the highest T is the only one exhibiting a different symmetry of the unit cell compared to the others at lower T. It has been found that this polymorph (Fig. 3.1) closely resembles to the structure observed in DIP thin films grown at $T \approx 298$ K or higher on several substrates [124, 169, 170].

When DIP is evaporated on native Si oxide at 403 K, within the first 3 ML a gradual expansion of the a unit cell axis of $\sim 2.5\%$ is observed [109, 118] accompanied by a decrease in the tilting angle of the DIP molecules [171]. This could be explained a stress release mechanism. After the 3 monolayers thickness, the unit cell parameters matches that of the high-T bulk polymorph

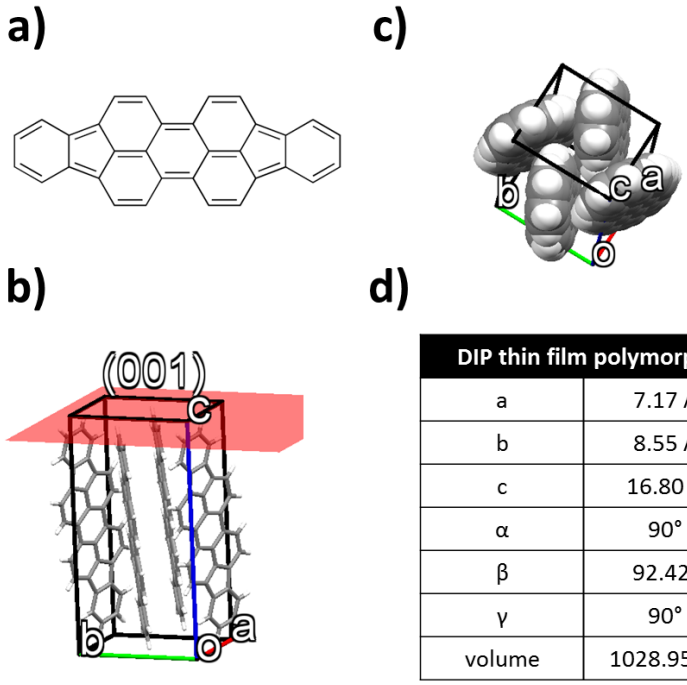

DIP thin film polymorph	
a	7.17 Å
b	8.55 Å
c	16.80 Å
α	90°
β	92.42°
γ	90°
volume	1028.95 Å^3

Figure 3.1: **a)** Molecular structure of DIP (H atoms not shown). **b)-d)** Unit cell of DIP thin film polymorph, or high-T bulk polymorph [124]. **b)** View along an axis nearly coplanar with the ab-plane or with the crystal plane of Miller indices $(hkl) = (001)$. **c)** View along an axis nearly parallel to the long molecular axis. **d)** Unit cell parameters and total volume. Color code for atoms: C (grey), H (white).

[124]. Interestingly, this structural transition to the high-T bulk crystal polymorph does not match with the onset of rapid roughening, which occurs around the 6^{th} total evaporated ML at 403 K [110]. This strongly suggests that roughening is not triggered by stress release. In Ref. [105] it was suggested that the growth rate of DIP grains on top of a formed DIP layer might depend on whether the new grain nucleates at a grain boundary or on a terrace.

The explanation of the roughening behavior of DIP deposited below $\sim$ room T or lower seems more immediately connected to the coexistence of different orientational domains during growth, namely of standing-up and lying-down molecules [109, 117]. Grains formed by lying-down molecules will exhibit a faster vertical growth rate than standing-up domains, leading to enhanced roughening [62].

The DIP stock used in this thesis was bought from PAH Research Institute (Greifenberg) and has undergone one purification cycle by gradient sublimation (thanks to Jens Pflaum).

3.1.1.2 α-Sexithiophene

Two single crystal structures could be identified for α-sexithiophene (6T, Fig. 3.2a): a) the so-called low-temperature (low-T) polymorph [127], b) the so-called high-temperature (high-T) polymorph [128]. A number of polymorphs has also been observed in vacuum sublimated films [172, 173], but their molecular structure has never been fully solved. The use of 6T in OFET architectures and the characterization of device transfer characteristics have been reported [174, 175] and show high charge carrier mobility of this OSC.

The possibility to use 6T-based OFETs for chemical sensing has also been demostrated [176] as well as its use as donor in combination with C_{60} in organic solar cells [177] or as templating layer for DIP [178]. Furthermore, the recent world-record efficiency for small-molecular OSCs-based organic solar cells of 13.2% established by Heliatek [179] has been achieved using a functionalized five-membered thiophene ring derivative in the functional organic layers. All these examples of applications demonstrate that functionalized multi-membered thiopenes, in particular 6T, have a

huge potential to become the standard OSC material for optoelectronic applications.

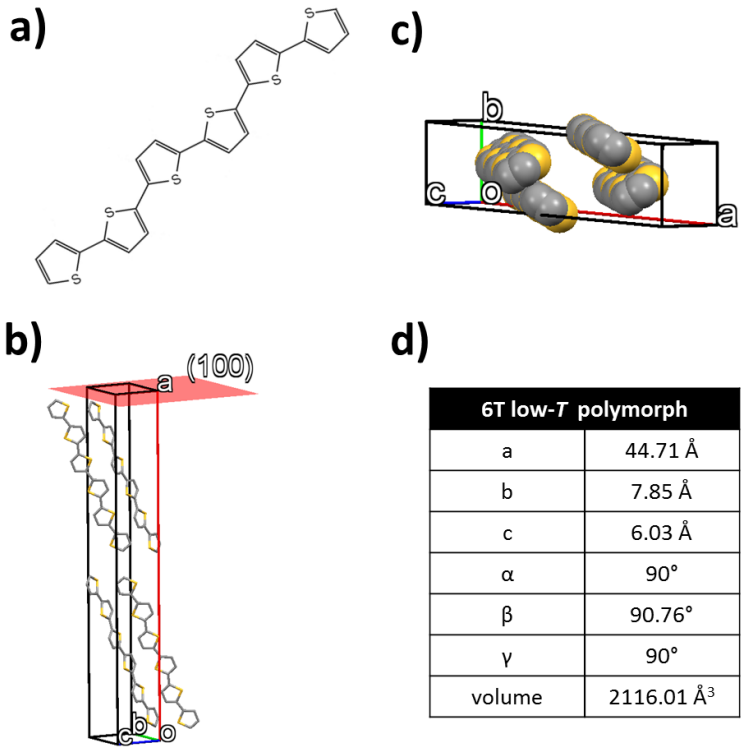

Figure 3.2: **a)** Molecular structure of 6T (H atoms not shown). **b)-d)**. Unit cell of 6T low-T bulk polymorph [127]. **b)** View along an axis nearly coplanar with the bc-plane or with the crystal plane of Miller indices $(hkl) = (100)$. **c)** View along an axis nearly parallel to the long molecular axis. **d)** Unit cell parameters and total volume. Color code for atoms: C (grey), S (yellow). Positions of H atoms not reported in the original crystal structure file.

In this thesis, two polymorphic forms of 6T found in thin films are most important: the low-T (Fig. 3.2) and the β-phase. The latter has been first clearly identified by Moser and co-workers [180] as a disordered layered phase present in vacuum-deposited thin films using growth parameters very similar to those employed here. Although its crystal structure could not be solved, it has been identified as a metastable structure induced by the interactions with the substrate and tends to transform to the bulk low-T phase for high film thicknesses and temperatures [96]. The coexistence of the low-T and β-phase in vacuum deposited films can be easily recognized by inspection of XRR profiles for thin films of upright-standing 6T molecules since their tilting with respect to the substrate normal is lower for the β-phase than for the low-T phase (see for instance Fig. 4.18)

The 6T stock used in this thesis was bought from Sigma Aldrich and purified twice by gradient sublimation (thanks to Jens Pflaum).

3.1.1.3 Pentacene

Pentacene (PEN, Fig. 3.3a) is one of the most thoroughly studied OSCs. Several polymorphs have been observed in thin films as well as in single crystals [125, 181]. Despite extensive studies, there is not yet a full understanding of the parameters governing the appearance of the different polymorphs. For PEN grown on amorphous Si oxide surfaces, one main thin-film polymorph [125, 182, 183] is commonly observed to coexist with another "bulk" polymorph. The relative amount of thin-film and bulk phase, respectively, depends on film thickness and substrate temperature [182]. As a general trend, higher substrate temperatures and film thicknesses favor the nucleation of the bulk phase. It is not clear to which of the reported single crystal structures the bulk phase observed in thin films belongs. Here we support Nabok and co-workers [135], who assign the bulk phase

to the structure reported by Campbell et al. [184] based on both XRR and GIXD data. Indeed, the lattice spacing d extracted from XRR data gives limited information concerning the unit cell parameters, and a cross-check with GIXD data provides a more accurate estimation. However, in principle more than one bulk polymorph can be present in the films, the relative amount depending on the details of film preparation.

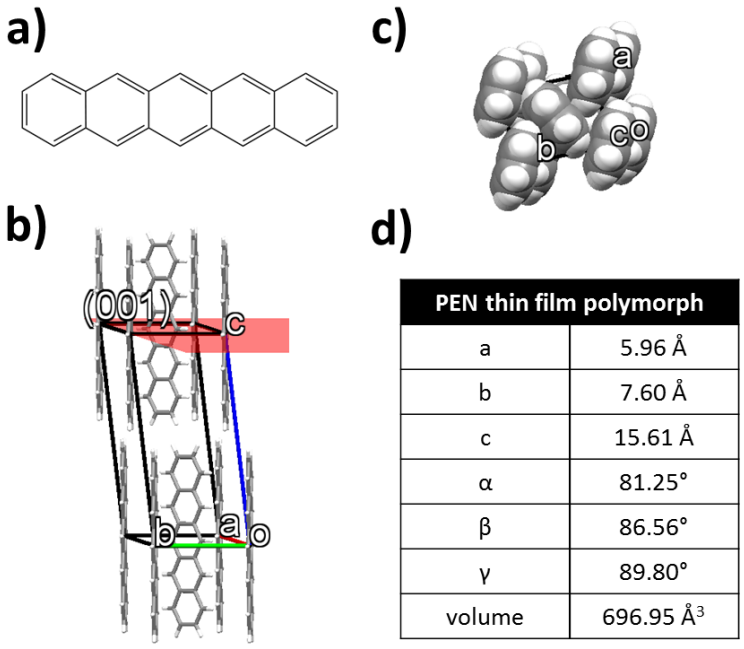

PEN thin film polymorph	
a	5.96 Å
b	7.60 Å
c	15.61 Å
α	81.25°
β	86.56°
γ	89.80°
volume	696.95 Å^3

Figure 3.3: **a)** Molecular structure of PEN (H atoms not shown). **b)-d)** Unit cell of PEN thin film polymorph [78]. **b**) View along an axis nearly coplanar with the *ab*-plane or with the crystal plane of Miller indices $(hkl) = (001)$. **c)** View along an axis nearly parallel to the long molecular axis. **d)** Unit cell parameters and total volume. Color code for atoms: C (grey), H (white).

For the growth parameters employed in this work, the thin-film polymorph is observed (Fig. 3.3b-d). A fundamental interest in solving the crystal structure of this phase is based on the applications of PEN as high-mobility OSC in OFET architectures [14, 185]. Applying different methods to analyze GIXD diffraction patterns measured on thin films, Schiefer and co-workers [78] as well as Nabok and co-workers [135] have solved the full structure of the thin-film polymorph.

The PEN stock used in this work was bought from Sigma Aldrich and used as received.

3.1.1.4 Dibenzo-tetrathiafulvalene

Dibenzo-tetrathiafulvalene (DBTTF, Fig. 3.4a) is a derivative of the better known tetrathiafulvalene (TTF), famous for forming a metallic salt with the acceptor tetracyano-naphtoquinodimethane (TCNQ) [186]. The salt becomes superconductive in a T range between ∼80 and ∼60 K [187].

The material has been employed in OFETs as single crystal [9] as well as thin film and shows room-T mobility of nearly 1 cm^2/Vs and 0.06 cm^2/Vs, respectively. Thanks to its ability to form thin films with good texture, it is a candidate for applications in optoelectronic devices.

Also for DBTTF, polymorphism has been reported. Several, slightly different single crystal structures fall under the denomination "α-polymorph", all of them exhibiting a monoclininc unit cell [188, 189] (Fig. 3.4b-d). A β-polymorph, also with a monoclinic unit cell, has been obtained by Brillante and co-workers [129] by means of re-crystallization in toluene. A single crystal structure having triclinic unit cell denominated "δ-polymorph" has been reported by Mamada and co-workers [190]. A fourth polymorph has been identified for films vacuum-sublimated on glass, called "γ-polymorph" [129], but no unit cell parameters have been provided. By comparison of our data with the data of Ref. [129] we conclude that this is the same thin-film polymorph observed by us

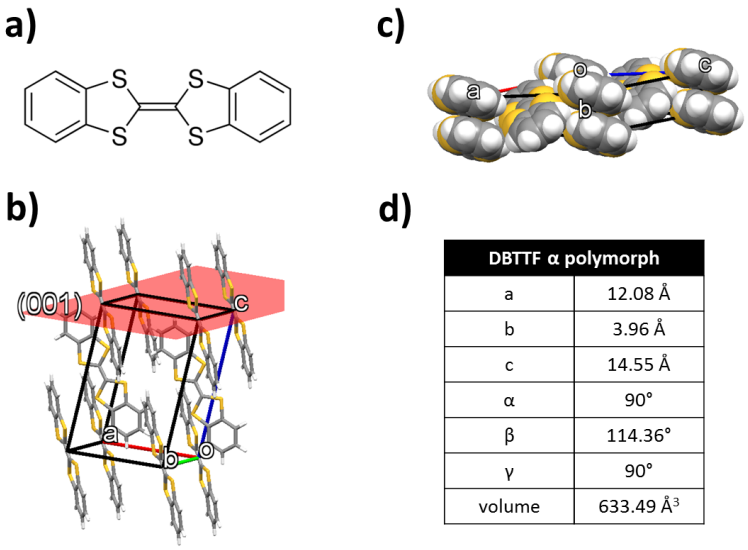

DBTTF α polymorph	
a	12.08 Å
b	3.96 Å
c	14.55 Å
α	90°
β	114.36°
γ	90°
volume	633.49 Å^3

Figure 3.4: **a)** Molecular structure of DBTTF (H atoms not shown). **b)-d)** Unit cell of DBTTF α-polymorph [188]. Notice that this polymorph does not correspond to the one we found in thin films (see Results section 4.5). **b**) View along an axis nearly coplanar with the ab-plane or with the crystal plane of Miller indices $(hkl) = (001)$. **c)** View along an axis nearly parallel to the long molecular axis. **d)** Unit cell parameters and total volume. Color code for atoms: C (grey), H (white), S (yellow).

(see Results section 4.5). Thanks to the strongly uniaxial texture of the DBTTF thin films studied here, we were able to fit the unit cell parameters (see Tab. 4.4).

The DBTTF stock used in this thesis was purchased from Sigma Aldrich and used as received.

3.1.1.5 Poly(3-hexylthiophene)

Poly(3-hexylthiophene) (P3HT, Fig. 3.5a) is the only polymeric OSC used in this work. The monomeric units are constituted by single thiophene rings functionalized with a hexa-membered linear alcane for improving the solubility. Due to the many degrees of freedom of the average polymeric chain and to the required deposition from solution, it is in general difficult to control the self assembly processes for this kind of materials. Nevertheless, so-called "regioregular" configurations can be obtained, which exhibit periodic stacks of rigid polymeric lamellae in the direction either parallel or perpendicular to the substrate surface. Such locally ordered configurations can greatly enhance charge-transport [3, 4].

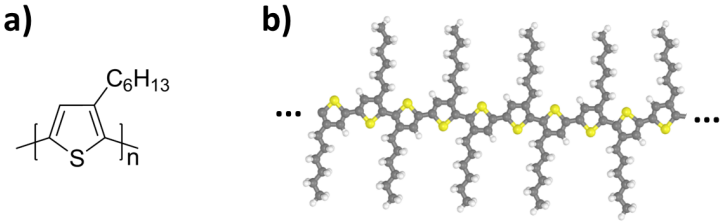

Figure 3.5: **a)** Molecular structure of the 3HT monomer (H atoms not shown). **b)** Extended P3HT chain. Color code for atoms: C (grey), H (white), S (yellow).

A very high number of publications demonstrate the use of P3HT as donor in blends with the acceptor [6,6]-phenyl-C61-butyric acid methyl ester (PCBM) for applications in organic solar cells [191]. In the context of this thesis the use of P3HT is interesting for the perspective of molecular

doping with strong acceptors [140, 192] and for purposes of comparison with small-molecular OSCs concerning the strength of CT interactions.

The P3HT stock used in this thesis was bought from Sigma Aldrich and used as received.

3.1.2 Acceptors

3.1.2.1 F6TCNNQ

The detailed steps for the synthesis of 1,3,4,5,7,8-hexafluoro-tetracyanonaphtoquinodimethane (F6TCNNQ or F6TNAP, Fig. 3.6a) has been first published by Koech and co-workers [193], although the use of this strong acceptor had been documented earlier in the patent literature [194, 195].

F6TCNNQ exhibits two main advantages compared to the smaller F4TCNQ commonly used for molecular doping: a) lower LUMO level, which makes it one of the strongest acceptors available to date [196]; b) lower diffusivity in organic matrices, which prevents the problem of dopant diffusion often encountered with F4TCNQ [52, 197].

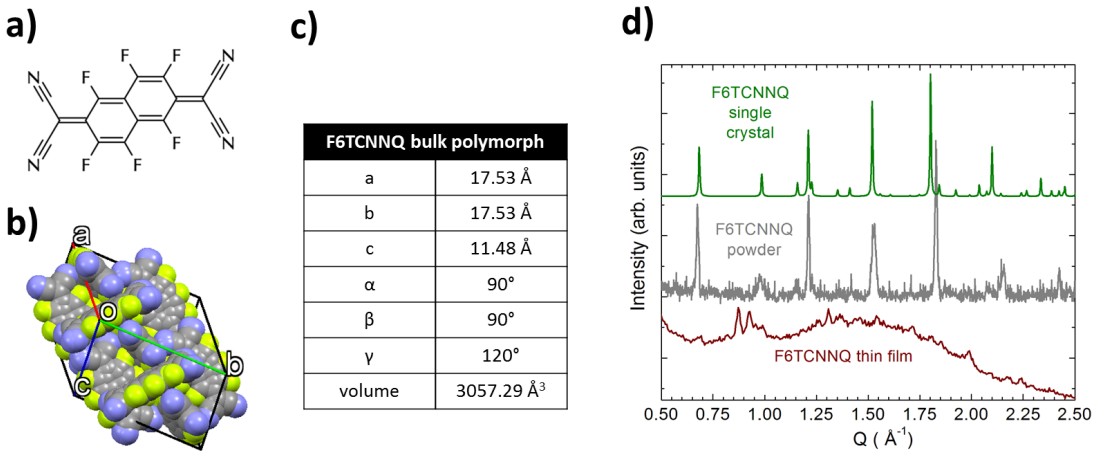

Figure 3.6: **a)** Molecular structure of F6TCNNQ. **b)** Unit cell of bulk polymorph [198]. **c)** Comparison of diffraction patterns demonstrating that the polymorph found in thin films is different from the bulk polymorph. The slight discrepancy between peak position of single crystal and powder for $Q >\sim 1.8$ Å^{-1} is probably due to erroneous atom positions in the crystal structure file. **d)** Unit cell parameters and total volume. Color code for atoms: C (grey), N (violet), F (green).

Between the first publication of a synthesis route for F6TCNNQ [193] and its recent growth and characterization as single crystal by Li and co-workers [198] nearly ten years have passed. At the same time, Hu and co-workers have published several single crystal structures where F6TCNNQ works as acceptor in co-crystals with the donors triphenylene, phenantrene, pyrene and naphtho[1,2-b:5,6-b′]dithiophene (NDT) [199]. Several degrees of GS-CT have been reported for these D:A co-crystals, the highest being found for NDT:F6TCNNQ. The unit cell of the published single-crystal structure of F6TCNNQ exhibits a hexagonal unit cell, which is quite exceptional for OSCs, and is unusually large because it contains 9 inequivalent molecules (Fig. 3.6b,c). The electron density of this material amounts to $\sim$ 0.45 Å^{-3} and is significantly higher than the electron density of, e.g., DIP ($\sim$ 0.37 Å^{-3}). This is likely due to a very close packing of the molecular units and the high electron density of the constituent elements.

The comparison of the diffraction patterns in Fig. 3.6d demonstrates that the polymorph present in thin films is different from the published crystal structure. We measured diffraction from the powder that we use as source material for sublimating F6TCNNQ and its structure matches very well the published bulk polymorph. Therefore, we proved that also for F6CNNQ a thin-film polymorph exists.

The molecular structure of F6TCNNQ (Fig. 3.6a) features a triple bond, C$\equiv$N, whose vibrational resonance frequency has been found to be sensitive to the GS-CT state of molecules

structurally similar to F6TCNNQ, like TCNQ [155] and F4TCNQ [86]. The sensitivity of this bond to CT interactions derives by its involvement in the quinoid-to-benzenoid molecular deformation upon ionization [200].

The F6TCNNQ stock used in this work was purchased from Novaled [1].

3.1.2.2 TCNNQ

The interest in obtaining F6TCNNQ as single crystals is probably not mirrored for its non-fluorinated version, tetracyano-naphthoquinodimethane (TCNNQ or TNAP, Fig. 3.7). Indeed, up to date no single crystal structure of TCNNQ has been published.

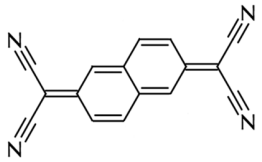

Figure 3.7: Molecular structure of TCNNQ (H atoms not shown).

Several reports show the successful growth of D:A co-crystals featuring TCNNQ as acceptor [201, 202]. One study has focused on the electronic structure of TCNNQ adsorbed on different metal surfaces and on its different ionization states upon K-doping[203]. Among the published single D:A crystal structures with TCNNQ, one features TTF as donor [204]. Recently, formation of a D:A supramolecular complex with DBTTF as donor in thin films has been shown based on optical spectroscopy data [111]. In this thesis we present X-ray scattering data that proves the formation of DBTTF:TCNNQ co-crystallites with 2D-powder texture in thin films.

The TCNNQ used in this thesis was purchased from Sigma Aldrich and used as received.

3.2 Substrates

Here we describe the materials employed as substrates for the deposition of the thin films studied in this thesis. The chemical nature of the substrate surface is in all cases mostly Si dioxide, which we refer to as "Si oxide" for simplicity. The use of different substrates is related to the particular investigation tool employed for the characterization of the thin film deposited atop, as described further below. All substrates exhibit an amorphous surface structure.

3.2.1 Native, thermally grown Si oxide and glass

For most of the thin films prepared in the course of this thesis, amorphous Si oxide was used as substrate. The choice relies on several factors. Amorphous Si oxide is commonly used as gate dielectric in OFETs and it is often passivated with an organic compound in order to reduce the density of surface traps [12, 205]. It is established that the vast majority of OSCs interact more weakly with this kind surface than with metal surfaces or single-crystalline surfaces of other oxides. The most notable exception to this behavior is probably 3,4,9,10-perylene tetracarboxylic dianhydride (PTCDA), which exhibits relatively strong interactions also with amorphous Si oxide due to its chemical functionalization, [206, 207]. In the context of quasi-epitaxy (see Ref. [98] and Fundamentals section 2.1), for the OSCs employed in this thesis, growth and self-assembly processes are not expected to be "templated" by the amorphous Si oxide surfaces during growth at room T. However, lowering the substrate T during growth affects growth dynamics and leads to a change of the quasi-epitaxial relationship between molecular orientation and substrate plane, as detailed in the Results section 4.3.

Another factor concerns the suitability of Si substrates for the thin film characterization methods employed in this work, for instance surface X-ray scattering (Methods section 3.3). Furthermore, Si wafers with different oxide thickness can be used for purposes of multi-sample analysis

[1] Thanks to Dr. Andreas Opitz (Humboldt Universität zu Berlin) for shipping of the F6TCNNQ stock.

of ellipsometry data [208, 209] (Fig. 3.8), as explained further below in the Methods section 3.3. In particular, we use native and thermally grown Si oxide surfaces on Si substrates. The native oxide forms naturally due to exposure of a clean Si surface to standard atmosphere with consequent diffusion of O_2 into the surface. The thickness of this native oxide layer is ∼2 nm and its composition varies with the distance from the Si surface, from stoichiometric SiO_2 in the topmost layers to a stoichiometry with lower O_2 content near the Si substrate [210]. The surface roughness is in the order of few Å [38]. Thicker Si oxide layers can be artificially grown by heating the Si substrates up to ∼ 1300 K in a O_2-rich atmosphere. The oxide growth rate depends on the substrate T and on the O_2 partial pressure. The topmost layers of the oxides produced thereby are amorphous [211–213]. We will denote both native and thermally grown Si oxide substrates mostly as "SiO_x". Glass slides were also used as substrates, mostly for the purpose of absorption spectroscopy measurements in transmission geometry (Fig. 3.8) in a spectral range from ∼0.6 eV to ∼6 eV.

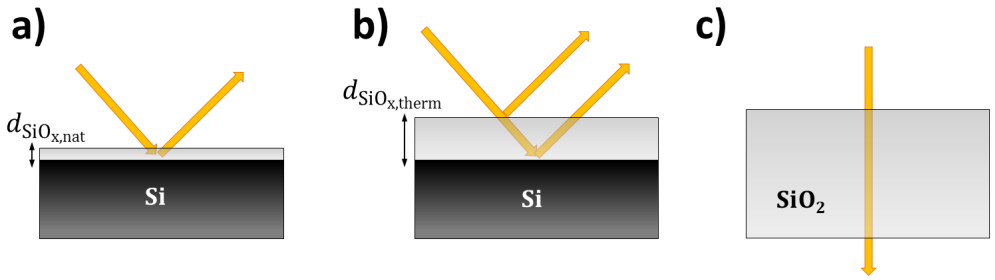

Figure 3.8: Substrates employed in this thesis for the growth of thin films of OSCs. **a)** Si with amorphous native Si oxide layer ($d_{SiO_x,nat} \approx 2$ nm). **b)** Si with amorphous thermally grown Si oxide layer ($d_{SiO_x,therm} \approx$ 100-150 nm). **c)** Amorphous glass slide (slide thickness ∼0.5 cm). The arrows depict light beams following different paths and represent the use of these substrates for optical spectroscopy in different geometries: **a)**,**b)** ellipsometry in reflection, **c)** ellipsometry or absorption spectroscopy in transmission.

The glasses employed are amorphous with a surface roughness ≤ 1 nm [214, 215], therefore their surface properties are expected to be similar to those of native and thermally grown SiO_x. This typically leads to a nearly identical crystal structure and morphology for thin films of OSCs deposited simultaneously on these substrates. However, occasionally the morphology exhibited by the thin films grown on SiO_x and glass, respectively, is different. This may be due to the slightly different relative abundance of siloxane bridges and silanol terminations [216] on the surface of the two kinds of oxides, which leads to an overall different surface potential which might have a different impact on growth and self-assembly processes depending on the molecular system under study.

In the course of this work, p-doped Si(001) wafers with a native oxide layer were used as substrate material, from which slides of several sizes were cut, ranging from 5×10 mm^2 up to ∼15×15 mm^2. Si slides of 5×10 mm^2 with a thermally grown Si oxide layer of thickness 100-150 nm were also used. Borosilicate glass (Borofloat® from Schott) and fused silica glasses (UQG Optics) were also as glass substrates.

3.2.2 Si oxide on Au

Si wafers coated with 5 nm Ti adhesion layer and 200 nm polycrystalline Au (∼10x15 mm^2) were used as substrates for the deposition of SiO_x. Prior to deposition, the Au substrates were cleaned first with acetone and then with isopropanol in an ultrasonic bath and subsequently dried under a gentle stream of N_2. The layers that constitute the substrates after coating with SiO_x are sketched in Fig. 3.9. The Au slides were then transferred into a Plasmalab 800Plus (Oxford Instruments) for deposition of the oxide layer *via* plasma-enhanced chemical vapor deposition (PECVD) [2].

[2]Thanks to Tanja Martin, University of Tübingen, for assistance during the preparation of the Si oxide coatings.

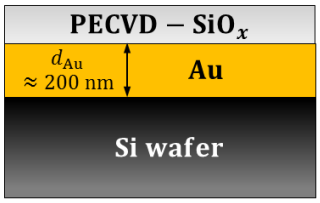

Figure 3.9: Schematics of the layers constituting of the SiO_x-coated Au substrates. For simplicity, the Ti adhesion layer between the Si wafer and the Au film is not shown.

During deposition of the SiO_x film, the substrates have been kept at 573 K. We used a plasma power of 30 W and a gas mixture of 16% SiH_4 and 25% N_2O in a N_2 carrier gas flow. The total pressure in the reaction chamber was 1 Torr. These parameters are very similar to those reported in Ref. [217]. Since the thickness of the oxide layer can be controlled by the duration of the deposition, we tested five different combinations of plasma power and total deposition time. We then characterized [3] the produced layers using atomic force microscopy (AFM), optical microscopy and ellipsometry. The several characterizations performed on the substrates are explained in the caption of Fig. 3.10.

The SiO_x layers for subsequent deposition of OSC films need to exhibit a homogeneous Si oxide surface while being as thin as possible in order not to lower the reflectivity from the metal substrate. We therefore chose the parameters of the plasma which deliver an oxide thickness of $\sim$ 12 nm, this representing the best compromise between thickness and layer homogeneity (Fig. 3.10c, circled data-point).

Concerning the use of these substrates for surface X-ray scattering experiments, one has to carefully choose the photon energy in order to avoid being close to an absorption edge of Au. For instance, an energy in the range of $\sim$12-14 keV as employed for samples on Si/SiO_x is not recommended since the L_1-edge of Au is at $\sim$14.35 keV and one has high probability to damage the organic layer with the Au photoelectrons. Going towards lower energies is also not recommended due to the lower-energy absorption edges. However, the K-edge is located at $\sim$80.73 keV, therefore an energy slightly above $\sim$20 keV can be chosen.

[3] Thanks to Ronny Löffler, University of Tübingen and Lisa$^+$, for the selective etching of the substrates.

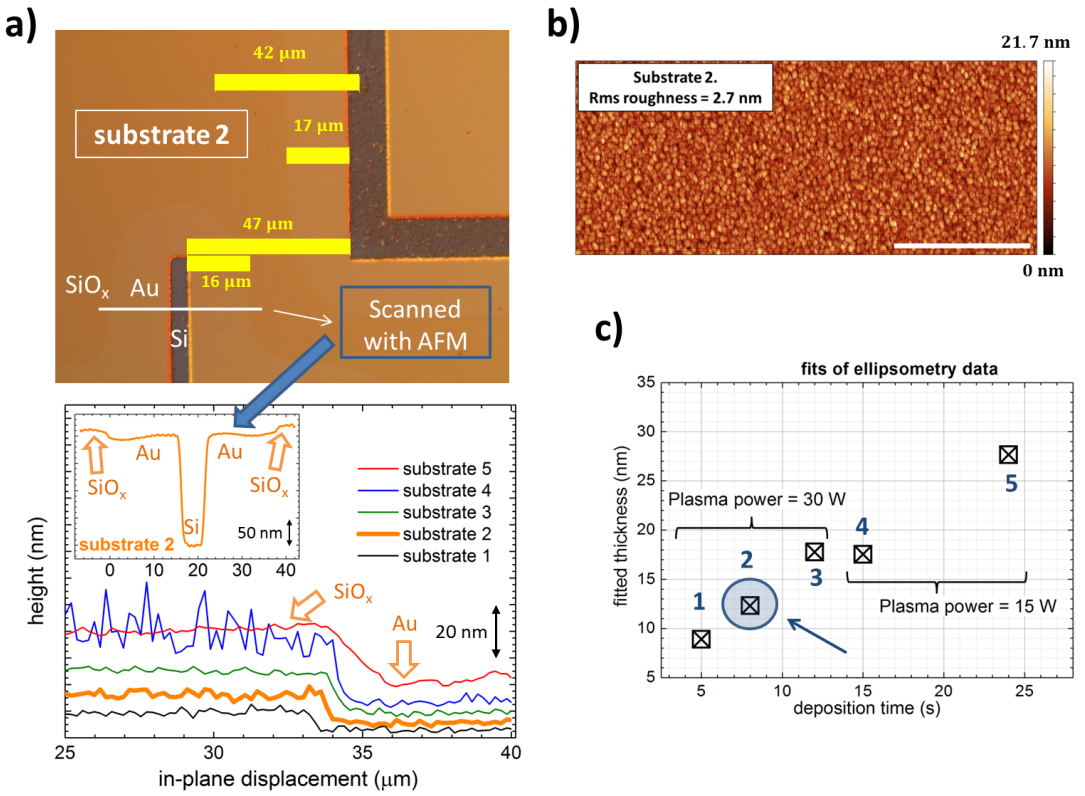

Figure 3.10: Characterization of five PECVD-SiO_x layers produced with different plasma powers and deposition times. **a)** [TOP] Optical microscope image of the test substrate 2 (plasma power: 30 W, deposition time: 8 s, estimated Si oxide thickness: 12 nm). The dark brown areas were selectively etched using a mask in order to reach the layer below the Au coating. The Si oxide layer was selectively etched along a contour 16-17 μm wide around these dark areas. The white-highlighted line was further scanned under the AFM, as shown in the inset of the figure below. [BOTTOM] AFM scans of all test substrates 1-5, where the SiO_x layer has been removed in order to show the SiO_x-to-Au step (orange arrows). All AFM scans were analyzed using the software Gwiddion [218]. Clearly the oxide thickness increases with deposition time and plasma power. Notice that for substrate 4 the deposition parameters do not allow a homogeneous coverage of the oxide surface. The inset shows a line scan along the surface of the test substrate 2 including the SiO_x-to-Au step (orange arrows) and the etched Au channel, from which a thickness of 200 nm of the Au film can be seen. **b)** AFM scan of the homogeneous SiO_x surface of the test substrate 2 with calculated roughness. The inset scale bar corresponds to 2 μm. **c)** Thickness values obtained from the fits of the ellipsometry data on the test SiO_x/Au substrates. The thickness values match very well the profiles shown in **a)**. A simple optical model was used consisting of a SiO_2 layer on top of an Au substrate. The circled data-point indicates the chosen deposition parameters.

3.3 Experimental methods

Here, the main experimental methods employed in the course of this thesis are described. The section is obviously not intended to provide an exhaustive description of each technique, but rather gives an overview of the working principle and of some aspects directly related with the "hands-on" operation of the devices.

3.3.1 Organic Molecular Beam Deposition [4]

Vacuum deposition techniques are particularly suited for tailoring heterostructures in the direction perpendicular to the substrate [98]. In the course of this thesis we use organic molecular beam deposition (OMBD) to produce thin films of OSCs. This technique is based on the thermal sublimation of the organic source material, which is in the form of a powder, onto a target substrate under vacuum conditions. A drawback of OMBD is that, due to the thermal sublimation process involved, it is suited only for those organic materials which are stable upon evaporation. Organic materials with a much larger molecular weight will decompose before reaching the sublimation point. Therefore, OMBD cannot be employed to deposit polymeric films. For this class of OSCs, deposition from solution is the most diffused for the production of thin films.

3.3.1.1 Importance of vacuum

Vacuum conditions of several orders of magnitude below atmospheric pressure can be reached inside suitably equipped vacuum chambers. The degree of vacuum for our thin film deposition experiments lies in the range of "very high vacuum", based on the definitions reported in Ref. [220]. For ease of reading we will refer to it as "high vacuum" (HV), with a base pressure P in the order of $\sim 1\times10^{-8}$ mbar ($\sim 1\times10^{-6}$ Pa, or $\sim 0.75\times10^{-8}$ Torr).

Vacuum is of primary importance for general surface physics. This becomes obvious considering surface analysis techniques like, e.g., those involving photoemission of electrons, which require "ultra-high vacuum" (UHV) conditions with $P < 10^{-9}$ mbar in order to achieve a reasonable sensitivity. For OMBD, vacuum also allows to minimize the amount of contaminants on the substrate and in the film during the deposition process. Contaminants include organic residuals of organic solvents on the substrate surface as well as residual gas species in the chamber. Vacuum reduces the interaction probability of the sublimed organic material with these "background" gases and further avoids interactions between the organic molecules themselves in the vapor phase. To see this, a useful parameter is the mean free path, $\Lambda_{m.f.}$, of a gas molecule of diameter d_0 with a background gas density n (in molecules/m^3):

$$\Lambda_{m.f.} = \left(\sqrt{2}\pi d_0^2 n\right)^{-1} \tag{3.1}$$

The quantity Λ in Eq. 3.1 has units of cm and defines the straight distance which a molecule can travel before undergoing a collision. It depends implicitly on gas pressure and temperature *via* the gas density. For the typical pressures employed for OMBD in this thesis, Λ is in the order of $\sim$ 6 Km, obvously much larger than the size of a vacuum chamber. Thus, considering only the plume of material sublimed from the source (Fig. 3.11), the molecules do not interact with each other before encountering a surface, i.e. they are said to fly "ballistically" onto the substrate. This aspect greatly eases the understanding of growth processes since, in practice, inter-molecular interactions in the vapor phase can be neglected, i.e. cluster formation occurs only after molecules start diffusing on the substrate.

To reduce the impact of contaminants, a good practice is to carry out an "outgassing" of potentially contaminated surfaces. This is typically achieved by heating up substrate, chamber walls and organic source materials after reaching sufficient vacuum conditions. The suitable final temperature for the outgassing depends on the component considered. Typically, the substrate can be heated up to $\sim$ 700 K. During the outgassing of the chamber walls, commonly referred to as "baking", care should be taken in order to minimize the thermal shocks between the chamber walls and the windows (Fig. 3.11), and the walls should not be heated to more than some degrees

[4] The contents of this section have been mostly taken by the books of Weston [219] and O'Hanlon [220]. Other sources are explicitly cited.

above 373 K mainly with the aim of water removal. The organic source material in form of powder should also undergo outgassing for removal of possible traces of water, with the outgassing T kept well below the sublimation point in order to prevent undesired loss of material.

Outgassing and baking the several components of a vacuum chamber allows to minimize the presence of undesired gaseous contaminants. However, the total density contaminants on a surface is ultimately determined by the minimal pressure achieved. From the kinetic theory of gases, the time for the formation of a monolayer of contaminant molecules of mass m on a surface kept at temperature T is [98]:

$$\tau = \frac{N_s \zeta \sqrt{2\pi m k_B T}}{P} \tag{3.2}$$

where N_s is the surface density for completion of a monolayer and ζ is related to the *sticking probability*, which in general depends inversely on T. Lowering the substrate T leads to shorter times for a surface to be covered by residual gases in the vacuum chamber. Concerning the dependence of τ on P in Eq. 3.2, reducing P by one order of magnitude leads to a 10-fold increase of the surface contamination time. At the typical background P employed in this thesis, τ is in the order of few minutes at room T, which is in the same order of the formation time of a molecular monolayer at the growth rates employed in this thesis, suggesting that some inclusions of residual gas species must be present in our films. Although it is known that inclusion of gas impurities in a matrix of the OSC picene can affect the OFET transport properties [221], it has been also found that the thin film crystal structure of picene is not affected by post-growth exposure of an as-grown film to atmosphere [222]. Overall, very similar film growth conditions were used for the sample series of each comparative study presented in this thesis. Therefore, it can be safely assumed that the conclusions drawn here are not affected by the degree of surface contamination.

3.3.1.2 Main components

In this section we describe the main parts of the equipment for the growth of thin films of OSCs by means of OMBD. We refer to the schematics depicted in Fig. 3.11.

- A *vacuum chamber* provides the "clean" environment in which OMBD is performed. The walls of a vacuum chamber have to withstand an external load due to the atmospheric pressure as high as nearly $\sim 10^3$ Kg/m^2. Therefore, they are commonly fabricated in stainless steel, which is a resistant, highly vacuum-compatible material with low outgassing rates and offers wide possibilities for joint-welding of extensions. Typically, a vacuum chamber will host one or more transparent windows that, one one side, enable visual inspection of the internal parts, and on the other side offer the possibility to perform *in situ* optical spectroscopy. In the course of this thesis we have also used a portable vacuum chamber [223] which hosts a cylindrical Be window for *in situ* X-ray scattering experiments (Fig. 3.16a). The chamber walls can undergo baking procedures but, due to the insertion of these additional ceramic components in its stainless steel structure, special care must be taken to avoid thermal shocks.

- Several kinds of *pumps* need to be employed simultaneously in order to produce HV. The basic pumping unit is called *pre-vacuum* pump or, somehow in laboratory-slang, "roughening pump" since it creates an initial, "rough" vacuum. A pre-vacuum pump alone allows to evacuate the system only down to $\sim 10^{-3}$ mbar. Several types of pre-vacuum pumps exist, two examples of which are oil pumps (one- and two-stages) and membrane pumps. In order to reach pressures in the HV range, a *turbomolecular pump* (TMP) needs to be attached in series to a pre-vacuum pump. The pumping mechanism in this pressure range, where the molecular flow regime sets in, is based on the transfer of kinetic energy from a series of rotating turbines to the residual gas molecules. The shape of the turbine blades causes the impacted gas molecules to diffuse away from the chamber environment, which is at pressure P, and to be compressed downstream at pressure $P_1 > P$. The compressed gas can be then pumped away by the pre-vacuum pump. The *compression ratio* gives information about the quantity P_1/P. Notice that gas species of higher molecular weight are pumped more efficiently. In general, lower pressures can be reached by pumping the system for longer. However, the lowest attainable pressure is ultimately determined by the construction parameters of the setup and by the characteristics of the materials employed. The pumps

are connected between them and to the vacuum chamber by means of valves. The correct operation of these valves is important to avoid potential damage to the pumps and/or to avoid compromising the vacuum conditions inside the main chamber.

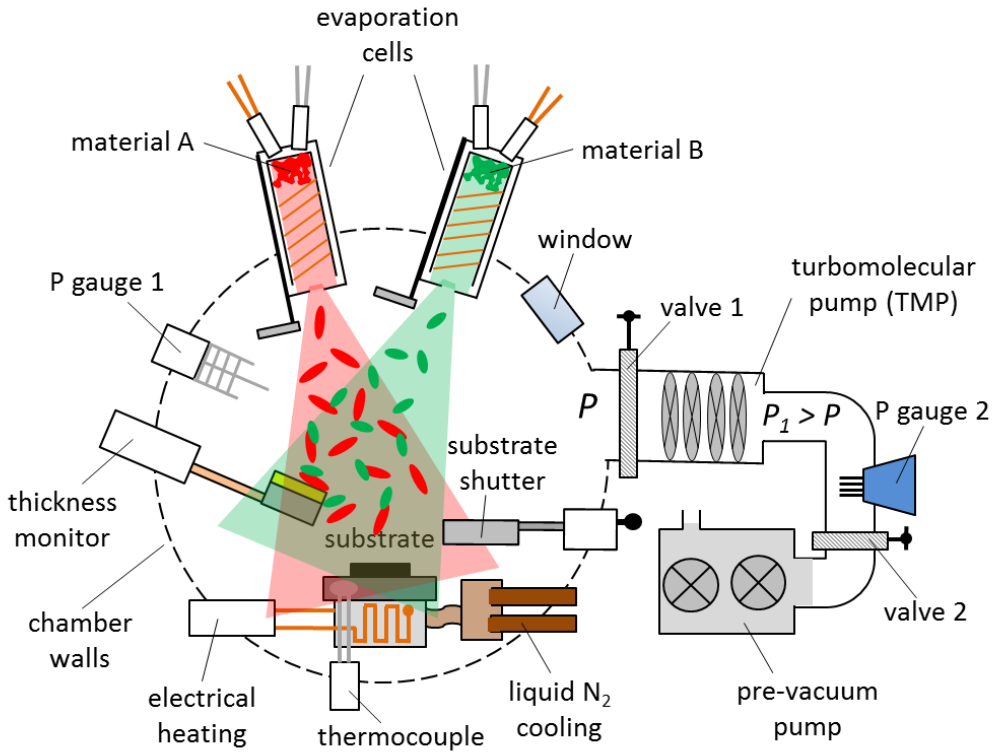

Figure 3.11: Typical setup for OMBD. All the components illustrated are described in the text. Notice that the disposition shown here is schematic.

- Several types of *pressure sensors* (or "gauges") exist to measure the pressure in the system. Often, it is desirable to measure both the pressure in the chamber, P, and the backing pressure, P_1. Since they differ by several orders of magnitude, we use two different pressure gauges. By monitoring the pressure in the chamber we can understand if the target pressure for starting the thin film growth has been reached. For measuring P during the growth of the thin films studied in this thesis, ionization gauges have been used. These types of sensors are based on the ionization of the residual gas molecules that occurs between two electrodes. The value of P is measured indirectly by the amount of current generated in this ionization process. The measurement of the backing pressure, P_1, has been carried out by means of a Pirani gauge. This type sensor works based on the variation of the electrical resistivity of a heated wire by heat transfer with the residual gas. The heated wire represents one resistive element inserted in a Wheatstone bridge to increase the sensitivity. The readings of these pressure gauges give information on the drop rate of P and are therefore diagnostic for possible leaks in the vacuum system.

- The organic powder is placed inside an Al_2O_3 crucible of an *evaporation cell* in order to generate a plume of molecular material flying onto the substrate. A Ta sheet in contact with the crucible and welded to thermocouple wires allows for measurement of the temperature in the crucible. The crucible is placed inside a larger Al_2O_3 cylinder. Electrical heating is provided by a resistive coil wrapped around the larger cylinder. The coil is further wrapped in two layers of Ta foils. Cells built according to a special design are denominated Knudsen cells and allow to minimize heat losses, keep the temperature of the crucible constant and avoid gradients along its walls, which might cause undesired condensation of the evaporated

material. Once the sublimation point of the organic powder is reached, the evaporation rate can be controlled by the cell T. Calibration curves are typically traced for each new material inserted in a cell. The latter aspect is particularly important for the growth of binary mixtures in a bulk heterojunction architecture, for which two materials are evaporated simultaneously and their molar ratio needs to be determined precisely. The molecular flux on the substrate can be interrupted or restored quickly thanks to shutters covering the orifice of the evaporation cells. Through this fine control of the evaporation rates, a number of different film architectures can be realized.

- A *thickness monitor* allows to monitor the deposition rate of a material sublimed from a cell. This device contains crystal which is electrically driven to oscillate at a frequency in the order of $\sim 10^4$-10^5 Hz. A thin Au disc is placed in contact with the oscillator since this noble metal favors the sticking of molecules. As the evaporated molecules hit the Au disc, its total mass changes. Such change modifies the resonance frequency of the oscillator, which is compensated by the external circuit. Thickness monitors are very sensitive but, in order to give quantitative information on the effective amount of deposited organic material, they need to be calibrated by means of complementary methods for the estimation of the real film thickness. The "scale factor" so obtained depends on the orientation and distance of the thickness monitor with respect to the evaporation cells and the target substrate. For the majority of the D:A mixtures studied here, two separate thickness monitors were used, one for the donor and one for the acceptor, allowing to minimize errors in the D:A mixing ratio.
- The *sample holder* allows to grow organic thin films one a single substrate or on multiple substrates simultaneously, which is a great advantage for some of the characterization methods used in this thesis. The sample holder can be electrically heated up to $\sim$ 800 K, for instance for the desorption of a previously deposited film. Therefore, materials with minimal outgassing rate at this T need to be chosen. Often, the choice falls on Mo. Additional to the resistive heating, the OMBD setups we used also feature a custom-built cooling system in which liquid N_2 can be let flow and exhausted into an open circuit. The flowing N_2 gradually starts filling a small recipient which is in thermal contact with the sample holder. A substrate T as low as $\sim$115 K can be thereby attained. Notice that the substrate T represents one of the main parameters that influence growth and structure formation in thin films of OSCs, and it is also relatively easy to control. The substrate can be additionally covered by means of a translational shutter, which prevents exposure to the molecular flux. The construction parameters of the sample holder, in particular its height from the bottom of the chamber, is fundamental for X-ray scattering experiments at synchrotron facilities for the correct alignment of the sample.

For the sake of brevity, the above list of components covers only the most important ones. As mentioned above, portable vacuum chambers can be built which integrate all these components and at the same time allow *in situ* experiments [224, 225].

3.3.2 Synchrotron radiation and equipment [5]

X-ray scattering represents a major tool of investigation employed throughout this thesis. All the results presented rely on the preliminary characterization of thin film structural properties by means of X-ray scattering (Fig. 1.3). The information obtained provides a solid basis for the interpretation of further spectroscopic or transport data. This general approach, in which X-ray scattering plays a major role, would not have been possible without access to synchrotron facilities, which can provide X-ray radiation with very high fluxes. External users who wish to use synchrotron radiation need to submit an application and, in case of acceptance, can have access to the facility.

3.3.2.1 Production of synchrotron radiation

Synchrotron facilities exploit the radiative properties of a current of electrons maintained on a closed path in vacuum and accelerated at relativistic speeds. As the tangential velocity v of the

[5] The contents of this paragraph are mostly taken from the book of Willmott [165]. Other sources are explicitly cited.

relativistic electrons is changed due to a centripetal acceleration a, they emit electromagnetic radiation with a very sharp angular distribution in the forward direction, while the backward emission is highly suppressed (Fig. 3.12).

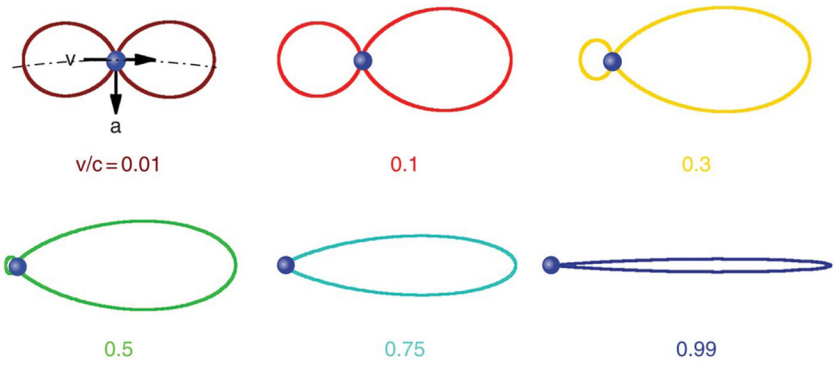

Figure 3.12: Field lines of a radiating electron traveling at a speed v which experiences a centripetal acceleration a. The fraction of the electron velocity with respect to the speed of light c is indicated. Adapted from Ref. [165].

The main components of a synchrotron are illustrated in Fig. 3.13. Electrons are initially generated by the heated filament of an electron gun and they undergo two acceleration stages, first inside a linear accelerator (LINAC) and subsequently inside a booster ring. Afterward, they are inserted into the storage ring, a series of straight segments connected such that the electrons are kept transiting along a closed path. Bending magnets (BM) located at the connections of the straight segments change the direction of v and cause the electrons to radiate tangentially to the curvature radius (Fig. 3.12). Other arrays of magnets, called insertion devices, are located instead at the straight segments of the storage ring and also cause the electrons to radiate by means of periodic oscillations. In order to compensate possible radiative energy losses of the traveling electrons, radio-frequency (RF) cavities are present along the storage ring (Fig. 3.13). In order to exploit the radiation produced by the bending of the electron trajectory, experimental stations called "beamlines" are annexed to the storage ring by means of a beam-defining aperture followed by a port called "front end". Before entering these experimental stations, the beam of radiation is passed through a series of optical elements which shape, monochromatize and focus it onto the sample held in the "experimental hutch" (Fig. 3.13).

The quantity $\mathcal{E} = mc^2/\sqrt{1-(v/c)^2}$, where v is the actual velocity of the electrons and c is the speed of light, defines the total energy of each electron circulating in the storage ring and usually amounts to some GeV. The ratio between this energy and the energy of an electron at rest is the Lorentz factor, $\gamma = \mathcal{E}/\left(mc^2\right)$. However, the parameter that best describes the performances of a synchrotron and is therefore used as figure of merit is the *brilliance*, defined as the flux of the generated cone of radiation normalized by its emittance. The flux is defined as the number of photons per second normalized by the 0.1% of the spectral bandwidth (BW). The emittance takes into account the finite size of the point source where synchrotron radiation is generated and its angular divergence, and it has units of (mrad^2 mm^2). The units for the brilliance are therefore (ph/s)/(0.1%BW mm^2 mrad^2):

$$\text{Brilliance} = \frac{\text{photons/second}}{0.1\%\text{BW mrad}^2\text{mm}^2} \tag{3.3}$$

The introduction of advanced insertion devices called "undulators" around the year 2000 have led to 3^{rd} generation synchrotrons, with brilliances as high as $\sim 10^{20}$ (ph/s)/(0.1%BW mm^2 mrad^2). In parallel, free electron lasers (FEL) have been developed, with nowadays reach brilliances as high as $\sim 10^{30}$ (ph/s)/(0.1%BW mm^2 mrad^2). Currently, several synchrotrons around the world are undergoing an upgrade to gain a further ~ 2 orders of magnitude in brilliance, mainly by reducing the emittance, and become 4^{th} generation sources, or diffraction-limited storage rings (DLSR).

The $\sim$12 order of magnitudes higher brilliance of synchrotron sources compared to laboratory sources is one of the main reasons for the interest in their use. High brilliance becomes especially

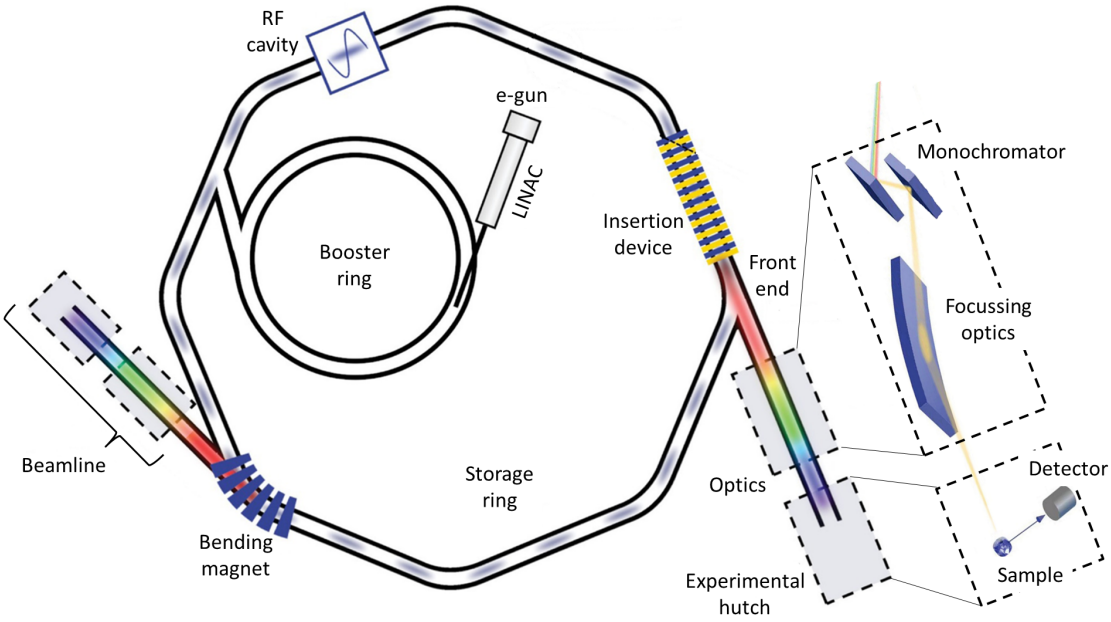

Figure 3.13: Schematic view of the main parts of a synchrotron facility. Each component is explained in the text. Adapted from Ref. [165].

important for surface scattering experiments on organic films, where the systems under study are in a thickness range of ∼10-100 nm of a weakly scattering material like C. It further allows real-time measurements during film growth with very short acquisition times, high dynamic range of the data and very good signal-to-noise. An occasional drawback of having a high brilliance source is that the organic films may be affected by radiation damage. However, a careful choice of sample environment and beam energy allows to avoid these damages. Indeed, the possibility to finely tune the beam energy is another advantage of synchrotron sources.

3.3.2.2 Beamline components

For the investigation of organic thin films by means of elastic scattering of X-rays, the high-brilliance beam needs to be monochromatized and focussed on the sample. To absolve this tasks, several optical elements are located between the sample in the experimental hutch and the front end, which are thus usually few tens meters apart from each other. The *ensemble* of optical elements, the components in the experimental hutch and control room is commonly denominated "beamline" (Fig. 3.13). For the sake of brevity, we group these "primary" optical components into two categories.

- *Focusing elements* have the function to reduce the incoming beam of radiation to a smaller spot-size and at the same time minimize intensity losses. These optical components can be divided into mirrors and lenses. Both kinds can be crafted in suitable shapes depending on the beam properties. In particular for mirrors, in order to achieve beam focusing without dramatic loss of intensity, the principle of total external reflection at incident angles below the critical angle α_c is exploited. This principle can be used to avoid higher harmonics of the beam to come through the optics. Indeed, the spectrum generated from an insertion device has a broad band. For the particular case of undulators, the spectrum exhibits peaks of characteristic shape at even and odd harmonics, respectively. Thus, suitably tuning the mirror angle α with respect to the incident beam results in total external reflection only for the first harmonic at, say, $\hbar\omega = \hbar\omega_{n=1}$, such that $\alpha < \alpha_c\,(\hbar\omega_1)$. Since α_c is a decreasing function of photon energy (Eq. 3.5), for the higher harmonics $\hbar\omega_{n>1}$ it will be $\alpha > \alpha_c\,(\hbar\omega_n)$ and the associated reflectivity will drop fast (see the following Methods section).

- *Monochromators* are used to obtain a spectrally pure beam from the initially polycromatic

radiation. Several orders of magnitude of the radiation power generated in the storage ring is dissipated in correspondence these optical elements, and often they require liquid N_2 cooling to minimize thermal variations. Several types of monochromators exist depending on the spectral range of interest. Monochromators based on *gratings*, for instance, con be used for so-called "soft" X-rays, i.e. for energies up to ∼1 keV, i.e. wavelengths down to few nm. To this category belong Rowland circles which, thanks to their spherical concave shape, also possess to ability to focus diverging beams. Above this energy, the fabrication of gratings becomes technically impossible. Monochromators based on *single crystals* or *multilayers* are therefore employed for "hard" X-rays and are based on the Bragg's equation 2.45. An example of single crystal monochromator is Si(111), which allows to achieve a spectral width as low as 10^{-4}. Employing Si single crystals that expose higher-order facets (e.g. Si(222) or Si(333)) further reduces the spectral bandwidth thanks to the reduced Darwin width of the Bragg peaks. Multilayers, instead, represent a convenient way to bridge the gap in the characteristic spacing d between gratings and single crystals as they allow to tune the single layer thickness. They are generally build up of a bilayer sequence of a high- and low-Z material, respectively, the former having the role of "reflection" layer (e.g. Ru) and the latter that of "spacing" layer (e.g. B_4C). The surface roughness of these structures obviously needs to be minimized in order to maximize the reflectivity (see Eq. 3.9).

The above optical components are typically hosted in the so-called "optics hutch". After focussing and monochromatization, the beam enters the experimental hutch. In the following we briefly describe the main components of an experimental hutch for surface diffraction experiments. Before the X-ray beam encounters the sample, it typically goes through: a) beam defining slits, b) beam flux monitor, c) series of attenuators. The attenuators are typically made of single metal plates of precise thickness which can be combined together in many ways in order to attenuate by the desired factor the beam flux reaching the sample. Often, the user can choose to make the attenuators work in "automatic" mode. In this case, the flux measured by the detector after the sample is used as input to select the appropriate attenuators combination.

The sample is held into the geometrical center of a goniometer. Further downstream, i.e. more distant from the front end, a detector is placed. Often, 2D-detectors built of arrays of photon-counting chips (size of ∼100 μm) are employed, relevant examples being the PILATUS (Dectris) and the Maxipix (ESRF) detectors. Additional sets of slits can be placed between sample and detector in order to reduce spurious scattering. Several motors allow to rotate and translate the sample with respect to the incident beam. The detector can also be rotated along several circles, spanning a big portion of the spherical surface of the goniometer. The mechanical components of the goniometer, including the motors for detector and sample movement, constitute a *diffractometer*. Depending on the number of degrees of freedom of the sample with respect to the detector, diffractometers are denominated "n-circle diffractometers", where n is the number of degrees of freedom. In practice, a diffractometer allows the quantitative analysis of X-ray scattering data *via* the calculation of the momentum transfer (Eq. 3.6).

Several other components are presents, but for the sake of brevity we shall not go into their details here. Importantly, several beamlines feature diffractometers which can host a portable vacuum chamber and therefore allow to carry out *in situ* experiments during the growth of thin films. This possibility allows to exploit synchrotron radiation for real-time studies of molecular systems employing a setup for OMBD growth that has been calibrated at the home laboratory and subsequently transported to the beamline (see Appendix 6.5). This represents an enormous advantage in terms of time saving and allows to carry out comparative studies on several molecular systems during one experimental session (see Results section 4.2.

3.3.3 X-ray scattering from surfaces [6]

The most suitable geometry for a surface X-ray scattering experiment can be chosen if some important aspects of X-ray scattering at interfaces are considered. Analogously to the visible region, Snell's law holds (Eq. 2.25) and the Fresnel equations 2.26,2.27 are formally equivalent, provided proper re-definition of the angles, which for X-rays are measured from the interface

[6] This part is mostly taken from the books of Tolan [226], Als-Nielsen [163] and Willmott [165]. Other sources are explicitly cited.

and not from the normal to it (see Fig. 2.13). Analogous to the visible and UV part of the electromagnetic spectrum, a complex refractive index $\tilde{n}$ can be defined in the X-ray region:

$$\tilde{n} = 1 - \delta + i\beta, \quad \text{with } \delta = \frac{\lambda^2}{2\pi} r_0 \rho_e \ ; \ \beta = \frac{\lambda}{4\pi}\mu \tag{3.4}$$

In Eq. 3.4, the positive quantity δ is the refractive index decrement and is in the order of $\sim Z \times 10^{-7}$. For carbon-based materials it is therefore in the order of $\sim 10^{-6}$. It is proportional to the material electron density ρ_e and decreases with photon energy as $\propto (\hbar\omega)^{-2}$. It follows that the real part of $\tilde{n}$, $1 - \delta \equiv n < 1$, which involves that the phase velocity $v_p = \frac{c}{n}$ is larger than c. This is not unphysical since the group velocity, which matters for information and energy transport, is $v_g = cn < c$. The quantity β in Eq. 3.4 accounts for absorption processes, therefore it depends on the absorption coefficient μ and not on ρ_e. It decreases with energy as $\propto (\hbar\omega)^{-4}$ and for carbon-based materials it is in the order of $\sim 10^{-8}$. In this thesis, considerations regarding β come into play concerning the choice of the best energy for X-ray scattering experiments in order to avoid the emission of photoelectrons from the substrate, which might damage the organic film atop.

Concerning the X-ray region, we will refer in the following to the schematics in Fig. 3.14.

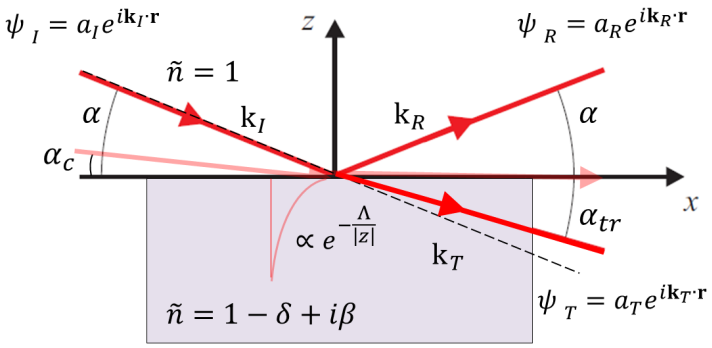

Figure 3.14: Schematics of reflection and transmission of an incident X-ray beam ψ_I with momentum $\mathbf{k}_I$ at an angle α. The reflected beam has momentum $\mathbf{k}_R$, the beam transmitted at an angle $\alpha_{tr} < \alpha$ has momentum $\mathbf{k}_T$. It follows that for $\alpha \leq \alpha_c$ one observes total external reflection. Here, the medium in which the X-rays initially propagate is vacuum, therefore $\tilde{n} = 1$. The evanescent wave decaying exponentially into the medium for $\alpha \leq \alpha_c$ is represented, with $|\Lambda|$ being the penetration depth. Adapted from [163, 226].

Due to the refraction correction, an X-ray traveling in vacuum and encountering an interface is transmitted through the medium at an angle $\alpha_{tr} < \alpha$. Therefore, a *critical angle* α_c exists such that for $\alpha \leq \alpha_c$ there is total external reflection of the incident wave. Imposing α_{tr} in the Snell's law for X-rays, since $\delta \ll 1$ one can write:

$$\alpha_c \approx \lambda \sqrt{\frac{r_0 \rho_e}{\pi}} \tag{3.5}$$

The dependence of α_c on the electron density ρ_e renders it material-specific. Notice that Eq. 3.5 is written for the case of the X-rays initially propagating is vacuum, for which $\rho_{e,vac} = 0$. Writing the transmitted angle α_{tr} in its complex form leads to the result that, for $\alpha \leq \alpha_c$, there has to exist a wave propagating parallel to the interface and whose amplitude decays exponentially with depth in the medium. Such an evanescent field is attenuated by a factor e at the *penetration depth* Λ, which depends on α and on the absorption coefficient μ (Eq. 3.4) [163]. In the limit $\alpha \to 0$, the penetration depth is independent from angle and energy, and is of the order of ~ 50 Å, which for OSCs corresponds to only few molecular monolayers. The fact that total reflection can be obtained is of fundamental importance for the study of the crystal structure of weakly scattering organic materials in thin films, where the signal from the investigated sample needs to be maximized.

The definitions of the momentum transfer **Q** (Eq. 2.36) depending on the laboratory reference system are given in Eq. 3.6 [227, 228] and refer to the geometry depicted in Fig. 3.21. The unit of **Q** is an inverse length.

$$Q_x = \frac{2\pi}{\lambda}\cos(\alpha')\sin(2\phi); \tag{3.6a}$$

$$Q_y = \frac{2\pi}{\lambda}\left[\cos(\alpha')\cos(2\phi) - \cos(\alpha)\right]; \tag{3.6b}$$

$$Q_{||} = \sqrt{Q_x^2 + Q_y^2}; \tag{3.6c}$$

$$Q_z = \frac{2\pi}{\lambda}\left[\sin(\alpha) + \sin(\alpha')\right] \tag{3.6d}$$

Typically, the texture of thin films of OSCs resembles a 2D-powder, i.e. one has a random orientation of single nano-crystallites in the substrate plane, in contrast to a uniaxial orientation of the molecular units in the out-of-plane direction. For such film texture one cannot distinguish between Q_x and Q_y since all families of parallel crystal planes are randomly distributed around the z-axis (Fig. 3.21). The total in-plane momentum transfer $Q_{||}$ (Eq. 3.6c) represents therefore the most convenient independent variable to quantify the scattering vector in a diffraction experiment for 2D powders. For specular geometry, i.e. $2\phi = 0$ and $\alpha' = \alpha$ in Fig. 3.21a, one has $Q_{||} = 0$ Å^{-1}, and only the momentum transfer parallel to the substrate plane, Q_z, is probed. Expressing the independent variable as momentum transfer renders different datasets comparable even for different photon energies, i.e. different values of λ in Eq. 3.6. In the following we consider two particular geometries for X-ray scattering experiments on thin films.

3.3.3.1 X-ray reflectivity

The use of X-ray reflectivity (XRR) allows to study the electron density profile of a sample in the direction perpendicular to the substrate. A *specular* geometry (Fig. 3.15a) is used to measure XRR, with $2\phi = 0$ in Fig. 3.21a. In this geometry, the out-of-plane momentum transfer Q_z (Eq. 3.6a) is probed. Notice that, in general, the reflectivity does not coincide with the Fresnel reflectivity, which we indicate $\left|\tilde{r}^2\right|$ using the same notation as in Eq. 2.24. This is due to the fact that the latter assumes perfectly flat interfaces, which is in practice never the case. If the interfaces are not perfectly flat, off-specular contributions to the reflectivity are present.

The Fresnel reflectivity decays quickly for angles above α_c. Using the same notation of Fig. 3.14 it can be shown that for $\alpha >\sim 3\alpha_c$ [226]:

$$|\tilde{r}|^2 \sim \left(\frac{\alpha_c}{2\alpha}\right)^4 \tag{3.7}$$

Eq. 3.7 implies that the Fresnel reflectivity decays approximately like Q_z^{-4} for angles above α_c. A typical XRR profile can be inspected in Fig. 3.15b, where the geometry for XRR measurements is also represented (Fig. 3.15a). In the following we briefly comment on the most important features of an XRR scan indicated in Fig. 3.15b.

- The *Kiessig fringes* (or *Kiessig oscillations*) arise from interference between the reflected waves at the film/air and film/substrate interfaces, respectively. Their amplitude increases with the contrast in ρ_e between the materials constituting the interfaces [229]. The occurrence of such fringes does not depend on the thin film having a crystalline texture and can be observed also for amorphous films. The spacing ΔQ_z between the Kiessig fringes allows an approximate calculation of the film thickness $D = 2\pi/\Delta Q_z$. Additionally, their damping provides a qualitative estimation of film roughness. For typical film thicknesses realized in this thesis, the Kiessig fringes typically vanish for a film roughness $>\sim 5$ nm. More accurate estimations of film thickness and roughness require modeling of the XRR curve including the electron density ρ_e.

- A *Bragg peak* arises from the coherent superposition of the waves scattered from families of molecular layers stacking in the out-of-plane direction when the Bragg condition (Eq. 2.45) is

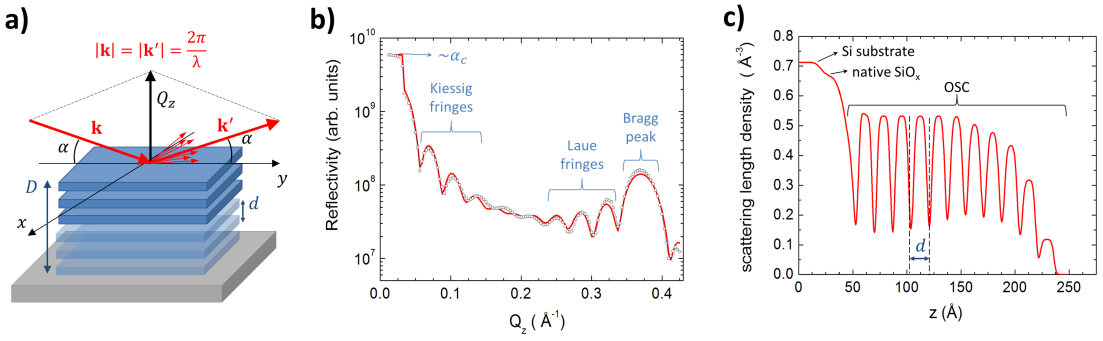

Figure 3.15: **a)** Schematic of XRR geometry. The molecular planes within the organic film with characteristic spacing d and total film thickness D are sketched in blue. The gray bottom plane represents the substrate. The smaller red arrows represent the off-specular contribution to the reflectivity. **b)** Example of a measured XRR profile on a DIP:F6TCNNQ mixed film in a 6:1 molar ratio (connected dots) and its simulation using the Parratt formalism (red line). The relevant features of an XRR curve are marked by the blue labels. Notice the independent variable in abscissa expressed as Q_z and the logarithmic scale in the ordinates. **c)** Scattering length density profile (SLD, in $Å^{-3}$) extracted from the simulation of the XRR curve in **b)**, where the layers of the different materials are indicated. Application of the Parratt formalism to simulate XRR curves is illustrated further below.

fulfilled. The position of Bragg peaks allows to calculate the inter-layer spacing d. For molecular materials this is particularly important since, due to the orientational degrees of freedom, a molecule can adopt several conformations on a substrate if its orientation is affected by some environmental parameter or if different crystalline polymorphs are present. Therefore, depending on the sample investigated, the presence of several Bragg peaks corresponding to different values of d can give a hint for the presence of different polymorphs and/or of different molecular orientations. Measuring the off-specular reflectivity (small red arrows in Fig. 3.15a) around a Bragg peak allows to obtain useful information on the mosaicity of the sample, i.e. the distribution of crystal orientations, by means of so-called rocking scans. All these kinds of preliminary information are valuable also considering that, in general, the use of synchrotron radiation to measure XRR is not strictly necessary.

- The *Laue Fringes* are interference fringes originating from crystals scattering coherently along the z direction. Their spacing gives information about the lenght scale of such coherence, D_{coh}. For OSCs exhibiting high structural order like DIP it may happen that the thin film scatters coherently for its entire thickness D, therefore $D_{coh} = D$ [169], i.e. the Kiessig and Laue fringes give the same information. For D:A binary mixtures of OSCs like those most investigated in this work, co-crystal nucleation with phase-separation of the excess material involves the co-existence of different crystalline phases which might be stacked on top of each other . In the latter case one additional interface is present, namely the one between the co-crystal and the pristine excess phase, which might shift the fringes as well as the Bragg peak due to interference [62].

3.3.3.2 Measuring X-ray reflectivity *in situ* and in real-time

In order to perform *in situ* X-ray scattering experiments, a portable vacuum chamber [223] was used, which is equipped with a Be window that allows the incident and scattered X-rays to be detected over an almost 360° wide field of view (Fig. 3.16). Measurement of sequential XRR scans during thin film growth allows to extract time-resolved information on the out-of-plane structure of a given system. A suitable time resolution needs to be chosen in order to gain sub-monolayer information and at the same time scan a suitable Q_z-range with a sufficient number of data points. Typically, a Q_z-range including first Bragg peak (Fig. 3.16b) allows the use of several theoretical approaches to model the growth process itself by fitting the real-time XRR data.

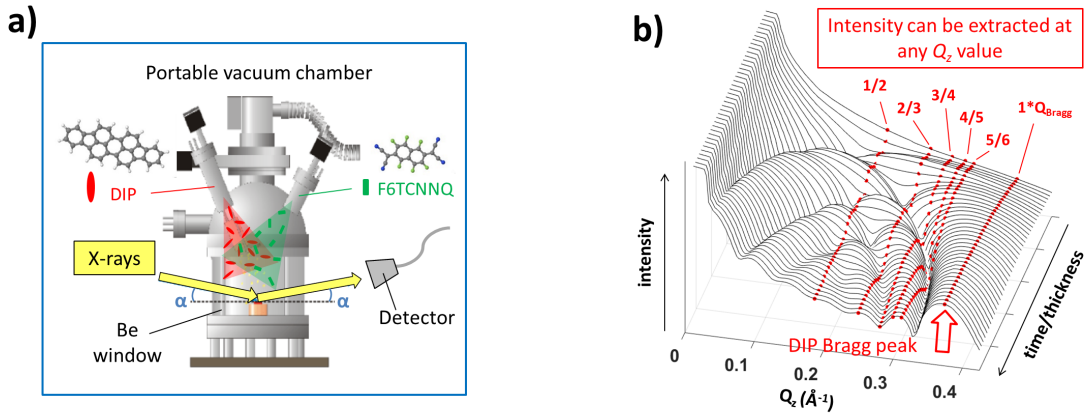

Figure 3.16: **a)** Schematic illustration of the experimental setup for *in situ* XRR measurements in real-time during the growth of co-evaporated DIP:F6TCNNQ films. A cylindrical Be window allows *in situ* experiments. The incoming angle α coincides with the exit angle in specular geometry. Adapted from Ref. [224]. **b)** Example of a dataset obtained by sequentially measuring XRR scans in a Q_z-range up to the first DIP Bragg peak to obtain information on film growth dynamics with sub-monolayer resolution. The reflectivity as function of time can be extracted at arbitrary points along the XRR curves.

3.3.3.3 Parratt formalism

The Parratt formalism [230] consists in a recursive approach which allows to treat the scattering of X-rays at multiple interfaces taking into account refraction and absorption effects. Thereby it is possible to simulate XRR curves (red line in Fig. 3.15b) and to model electron density profiles along the normal to the interfaces (Fig. 3.15c). This approach is exact for perfectly flat interfaces. The formalism reported here is taken from Ref. [226].

One considers the Fresnel reflection coefficient for X-rays at the interface between layer j and the layer $j+1$ beneath, $r_{j,j+1}$, which carries the information about the electron density *via* $\tilde{n}_j(\rho_{e,j})$. The Fresnel coefficient $r_{j,j+1}$ enters then the recursive formula:

$$X_j = \frac{R_j}{T_j} = \exp\left(-2ik_{z,j}z_j\right)\frac{r_{j,j+1} + X_{j+1}\exp\left(2ik_{z,j+1}z_j\right)}{1 + r_{j,j+1}X_{j+1}\exp\left(2ik_{z,j+1}z_j\right)} \tag{3.8}$$

where $k_{z,j} = k\sqrt{\tilde{n}_j^2 - \cos\left(\alpha\right)^2}$ is the component of the wave vector in layer j along the z direction, with $\tilde{n}_j = 1 - \delta_j + i\beta_j$ complex refractive index of the material constituting layer j (see Eq. 3.4) and carries the information about the electron density $\rho_{e,j}$. Eq. 3.8, describes the ratio between the total reflected and transmitted amplitudes, respectively R_j and T_j. Notice that the exponential factor describes the phase shift within layer j and is formally equivalent to the exponential factor of the pseudo-Fresnel coefficients (Eq. 2.27).

Inclusion of roughness for the interfaces between the different layers leads to an overall decrease of the reflectivity. A number of approaches to this problem have been suggested, the most important of which are summarized in Ref. [226]. Here we report the treatment suggested by Névot and Croce [231], which consists in multiplying the Fresnel coefficient $r_{j,j+1}$ by a Gaussian factor [7]:

$$\tilde{r}_{j,j+1} = r_{j,j+1}\exp\left(-2k_{z,j}k_{z,j+1}\sigma_j^2\right) \tag{3.9}$$

The parameter σ_j is the root mean square roughness at the interface between an upper layer j and a lower layer $j+1$, and it is therefore related to the distribution of z coordinates around a

[7] An accurate treatment of the scattering process at a rough interface employing the distorted wave Born approximation (DWBA) [232] demonstrates that the accuracy of the Névot-Croce factor in describing the interface roughness depends in general on the *lateral* structure of the sample. In particular, the Névot-Croce factor is strictly valid for small lateral correlation lengths ξ, or, in other words, for the "predominance of high spatial frequencies" [231]. However, as noticed by Tolan [226], the influence of the lateral structure on the treatment of the vertical roughness can be largely neglected above the critical angle, which is where our analysis is focused.

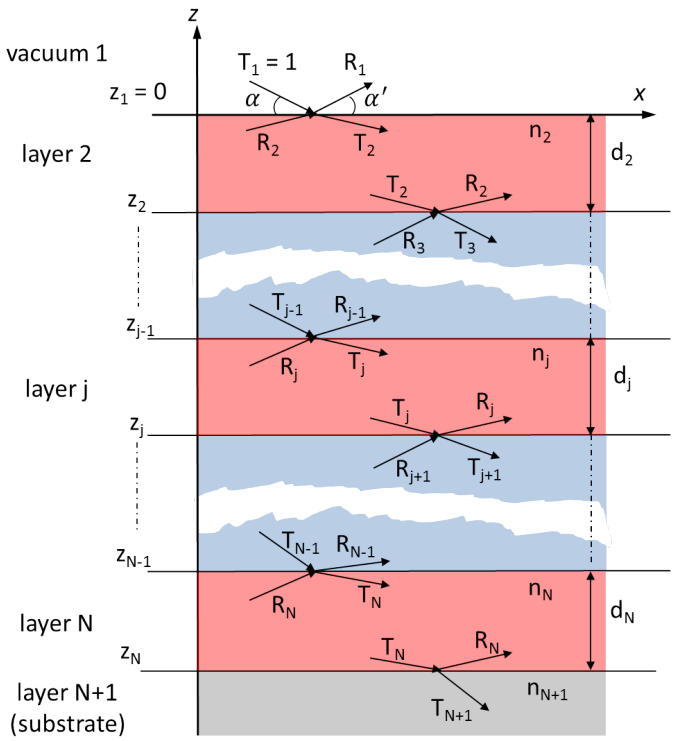

Figure 3.17: Sketch illustrating the parameters involved in the dynamical treatment of scattering from a multilayer system (Parratt formalism). For the scattering angles it holds $\alpha' = \alpha$. Notice that the transmitted beams will impinge the next interface at shallower angle due to refraction. The substrate is assumed to be much thicker than the penetration depth of the X-rays, therefore it holds $R_{N+1} = 0$. Adapted from Ref. [226].

mean value according to some (assumed) probability density [226].

3.3.3.4 Kinematical approximation

To model the scattering process in multilayer systems, a common approach consists in using the kinematical approximation, which consists in neglecting refraction and absorption effects of X-rays at interfaces during a scattering event. This approximation applies well to thin films (∼10 nm) of weakly scattering organic materials in a Q_z region well above α_c [163]. Notice that the Bragg's law (Eq. 2.45) is also obtained in kinematical approximation.

We write the expression for the reflected intensity as function of time, $I(t)$, as:

$$I(t) = \left| A(q) \cdot \mathrm{e}^{i\Phi(q)} + f(q) \sum_n \theta_n(t) \cdot \mathrm{e}^{inqd} \right|^2 \tag{3.10}$$

The form of Eq. 3.10 is the same as found in Ref. [110] and is in essence an expression of the total scattering amplitude from a bulk crystal (Eq. 2.39) adapted for a specular geometry assuming no refraction or absorption effects (see also Fig. 3.18). In Eq. 3.10, $A(q)$ and $\Phi(q)$ are the scattering amplitude and phase from the substrate, respectively, whereas $f(q)$ is the scattering amplitude from the *single* layers building up the thin film. The factor $\theta_n(t)$ is the time-dependent layer coverage for the n-th layer, and the summation runs over all the layers n composing the film.

The three parameters $A(q)$, $\Phi(q)$ and $f(q)$ need to be fitted for each chosen Q_z point of the reflectivity curve, but they are assumed time-independent. For the special case of the anti-Bragg point, i.e. $q = (1/2) \cdot Q_{Bragg}$, a system of algebraic equations to calculate these three parameters can be directly obtained, as explained in detail in Ref. [224]. In order to obtain the $\theta_n(t)$ for each layer in Eq. 3.10, a *growth model* needs to be assumed. We describe here two growth models: a)

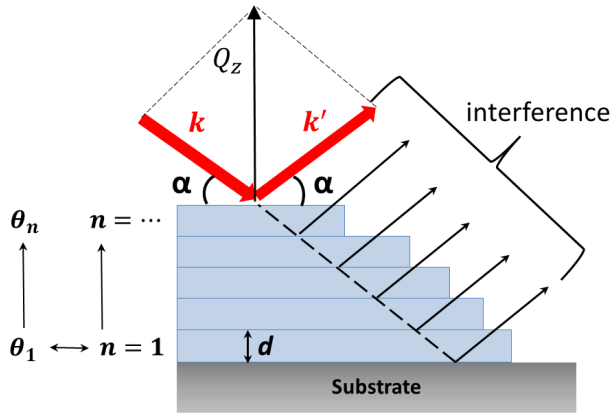

Figure 3.18: Sketch of the X-ray scattering process involving reflection from a multi-layered system according to the kinematical approximation. The incoming X-rays have a wave vector of magnitude $k = \frac{2\pi}{\lambda}$. In this geometry, the vector difference between the outgoing and the incoming wave vectors is the momentum transfer perpendicular to the substrate plane, Q_z. In this representation, Q_z corresponds to q in Eq. 3.10. The angle α represents the incident angle, which coincides with the exit angle in specular geometry, and determines the magnitude of the probed Q_z (Eq. 3.6d).

the "birth-death" model of Cohen [233] as in Refs. [110, 224], b) the Trofimov model [234] in its simplified version introduced by Woll [235] as in Refs. [113, 236, 237].

3.3.3.5 Growth model 1: Cohen

The Cohen model consists in a series of coupled differential equations for the layer coverages $\theta_n(t)$:

$$\frac{d\theta_n}{dt^*} = (\theta_{n-1} - \theta_n) + k_n(\theta_{n+1} - \theta_{n+2})(\theta_{n-1} - \theta_n) - \\ + k_n(\theta_{n-2} - \theta_{n-1})(\theta_n - \theta_{n+1}) \tag{3.11}$$

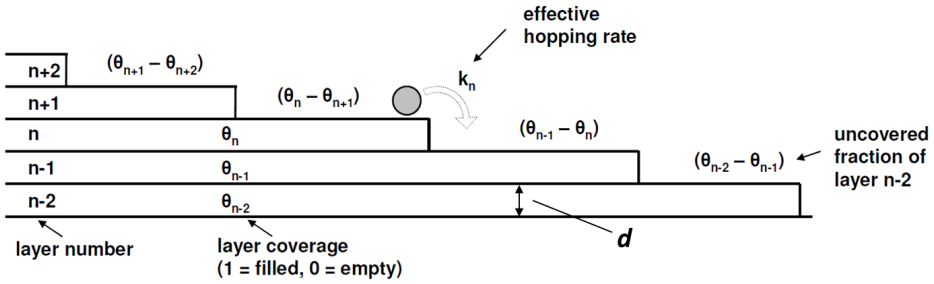

Figure 3.19: Sketch of growth dynamics of a multilayer system as described by the Cohen model. The parameter d represents the inter-layer spacing. For an explanation of the represented parameters, see main text. Adapted from Ref. [233]

The adimensional time t^* has been introduced in order to normalize by the completion time for one ML [110]. The time-dependence of the layer coverages θ_n has been omitted for clarity. The parameters k_n are the inter-layer jump rates and they are defined positive. Therefore, the first addendum multiplied by "$+k_n$" is proportional to the number of net jumps from $n+1$ to n, whereas the second addendum multiplied by "$-k_n$" is proportional to the number of net jumps from n to $n-1$. Eq. 3.11 couples up to five monolayers, from layer $n+2$ to layer $n-2$ (Fig. 3.19).

Numerical solution of the corresponding system of coupled equations allows to fit k_n and to obtain the time-evolution of the layer coverages.

3.3.3.6 Growth model 2: Trofimov

The Trofimov model features a system of coupled differential equations, which we write following Refs. [113, 236, 237]:

$$\frac{d\theta_n}{dt} = R_n(\xi_{n-1} - \theta_n) + R_{n+1}(\theta_n - \xi_n) \tag{3.12a}$$

$$\xi_n = \begin{cases} 1, & \text{if } n = 1 \\ 0, & \text{if } n > 1, \theta_n < \theta_{cr,n} \\ 1 - \mathrm{e}^{-\left(\sqrt{-\ln(1-\theta_n)} - \sqrt{-\ln(1-\theta_{cr,n})}\right)^2}, & \text{otherwise} \end{cases} \tag{3.12b}$$

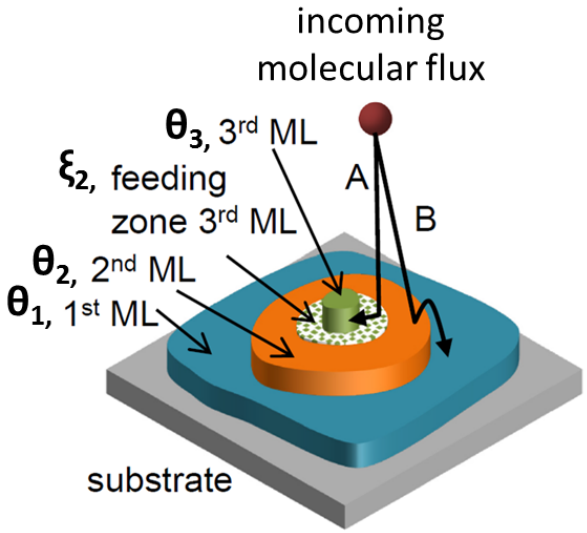

Figure 3.20: Sketch of growth dynamics of a multilayer system as described by the Trofimov model. For an explanation of the represented parameters, see main text. Adapted from Ref. [113].

In Eq. 3.12a, R_n is the *effective* deposition rate for the n^{th} layer and ξ_n describes the formation of a *feeding zone* (FZ) on top of layer n, i.e., the surface fraction sitting on the n^{th} ML that actually contributes to the growth of the n^{th}+1 ML. In the first layer, $\xi_{n-1} = \xi_0 = 1$, thus, all molecules sticking on the bare substrate are used to fill up the 1^{st} ML. The term $(\xi_{n-1} - \theta_n)$ describes the portion of the n^{th}-1 layer that is exposed to incoming molecules that contribute to the growth of the n^{th} layer. The term $(\theta_n - \xi_n)$ describes the portion of the n^{th} ML that contributes to the growth of the n^{th} ML itself instead of the n^{th}+1 ML. From these definitions it follows that the first term describes in-plane diffusion (path A in Fig. 3.20), whereas the second term describes inter-layer transport [237] (path B in Fig. 3.20).

The formation and time-evolution of the FZ is described by Eq. 3.12b, where the onset for the formation of a FZ is given by the layer-dependent critical layer coverage, $\theta_{cr,n}$. The fitting parameters are, therefore, R_n and $\theta_{cr,n}$. As noticed in Ref. [113], the inclusion of layer-dependent growth rates takes into account the physical observation that the landing molecules might exhibit a layer-dependent sticking coefficient, especially when comparing molecules landing directly on the bare substrate with those landing on an already formed organic surface.

3.3.3.7 Grazing-Incidence X-ray Diffraction

In grazing-incidence X-ray diffraction (GIXD) (Fig. 3.21) the incidence angle is kept below α_c in order to obtain total external reflection of the incoming photons, enabling structural studies of weakly scattering organic materials in thin films, where the signal from the investigated sample needs to be maximized. Furthermore, the dependence of the penetration depth Λ on the incident angle renders depth-resolved structural studies of thin films of OSCs possible [95, 238].

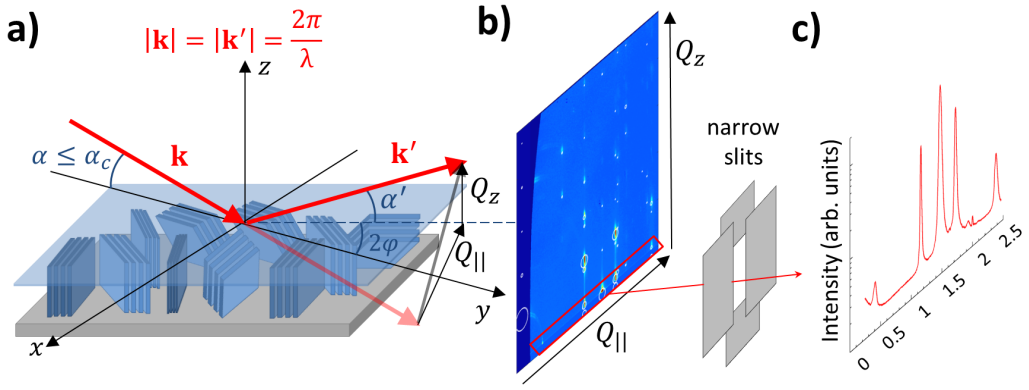

Figure 3.21: **a)** Grazing-incidence X-ray diffraction geometry (GIXD). The overall 2D powder-like film texture is sketched by the several crystalline planes having isotropic orientation in the substrate plane. Decomposition of the total momentum transfer in $Q_{||}$ and Q_z is indicated. **b)** Example of diffraction pattern (Q-map) measured with an area detector for a DIP film ($Q_{||}$-range $\sim 0-2.5$ Å^{-1}, Q_z-range $\sim 0-2.0$ Å^{-1}). The white circles superimposed to the experimental map represent a simulation of the position and intensity of the diffraction spots based on the known crystal structure of the thin film polymorph of DIP [124] (see below in the text). Notice that some simulated spots are also in the darker region, outside the measured Q-range. **c)** Example of GIXD scan for a DIP film obtained with closed slits in order to improve the signal-to-noise.

This procedure allows to measure diffraction patterns where the independent coordinates are $Q_{||}$ and Q_z, (Fig. 3.21). Since the thin films investigated in this work exhibit a 2D- or 3D-powder texture, i.e. they are respectively uniaxially anisotropic or isotropic, rotation of the sample around the z-axis does not change the intensity of the Bragg peaks seen in Fig. 3.21. In the course of this thesis, often the terms "GIXD scan" and "reciprocal space map" (or "Q-map") are used to indicate slightly different setups employed for measuring diffraction patterns in grazing-incidence geometry. In both kinds of setups, the incident angle α is fixed.

For a *GIXD scan*, the out-of-plane angle of the detector α', is kept at $\approx \alpha$ while it is moved in the xy-plane along a circle of which the sample represents the center (this is achieved by means of a goniometer, see Appendix 6.5). Two sets of slits, vertical and horizontal, are placed between the sample and the detector in order to improve the signal-to-noise. Optimization of the gap between the slits enables to use the 2D-detector as a point detector. Due to the low α' and to the closed slits settings, only the region in Q-space near the substrate reflection edge (i.e. $Q_z \approx 0$) is measured. The in-plane detector angle is varied and the intensity on the point-like region of the detector is integrated and plotted against $Q_{||}$ (Fig. 3.21c). Notice that the closed slit configuration leads to a convolution of the diffracted beam shape with the slits aperture [226], which sets a lower limit of peak width in GIXD scans.

Measurement of a *reciprocal space map* involves that also α' of the detector is changed. In this configuration, the slits are kept completely open and nearly the whole detector surface is illuminated. This leads to an overall worse signal-to-noise. Recently, a setup has been proposed to record Q-maps with very high signal-to-noise that consists in placing a custom-designed collimator between the sample and the detector [239]. Due to the limited size of the 2D detector, often several "shots" are needed to cover the desired Q-range. The number of images required will depend on sample-detector distance and detector size.

If the molecular film exhibits a high coherence in the out-of-plane direction, a diffraction pattern

can display several elongated diffraction spots along Q_z having the same value of $Q_{||}$. These elongated spots are called crystal truncation rods (CTRs) and arise as a consequence of the finite size of the crystalline film in the z direction, i.e. in this direction the diffraction spot has a size inversely proportional to the scattering volume [163]. Mathematically this corresponds a convolution of a theta function, representing the cleaved crystal, with the film electron density. Such convolution results in an intensity decaying as $1/Q_z^2$ from a given Bragg peak and leads therefore to the "smearing" of the diffraction spots. It is important to stress that such smearing is purely an effect of finite crystal size and should not be confused with the broadening of a diffraction spot along Debye-Scherrer rings due to film mosaicity.

In GIXD, due to the presence of a substrate, the Ewald sphere [240, 241] intersects the crystal truncation rods [242] in the upper half of the xy-plane (Fig. 3.22b). The radius of the Ewald sphere defines which is the maximum Q that is possible to measure.

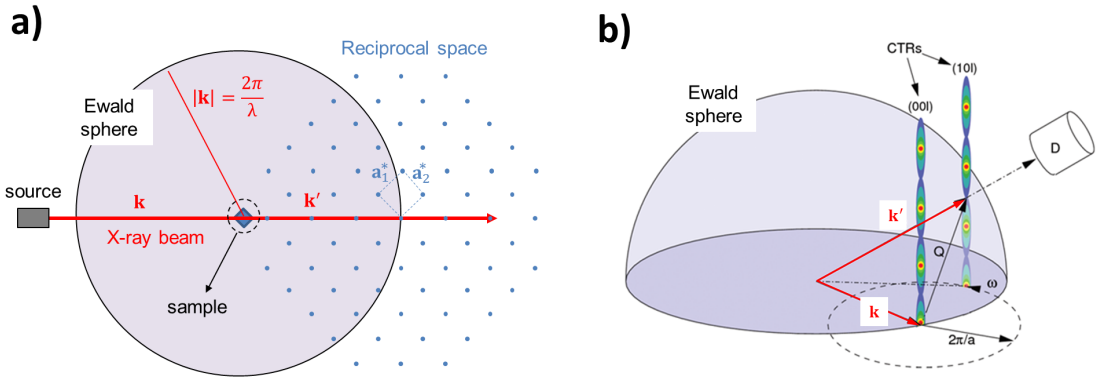

Figure 3.22: **a)** Ewald sphere construction in 2D. The radius of the Ewald sphere is, in the reciprocal space, $|\mathbf{k}| = \frac{2\pi}{\lambda}$. The lattice of blue dots represents the (infinite) reciprocal space constructed from the real-space lattice of the sample (in this case a single crystal), with the vectors a_i^* representing the basis vectors (Eq. 2.42). For the thin films studied in this thesis, the crystallites have a random in-plane orientation, which involves that the depicted reciprocal lattice adopts all possible in-plane orientations, therefore each reciprocal lattice point will intersect the contour of the Ewald sphere for certain angles. Adapted from Ref. [241]. **b)** 3D Ewald sphere construction in a surface scattering experiment. The upper half of the Ewald sphere intersects two crystal truncation rods (CTRs) separated by the reciprocal space vector $\frac{2\pi}{a}$, where e.g. $a = |\mathbf{a}_1^*|$ in reference to **a)**. The angle ω represents the in-plane rotation of the sample. Due to the in-plane isotropy of the film, all truncation rods will intersect the surface of the Ewald sphere. Adapted from [242].

Due to the in-plane isotropy of the crystallites constituting the film, the reciprocal lattice generated by the sample (Fig. 3.22a) and the CTRs at each lattice point will intersect the surface of the Ewald sphere, thereby allowing one to obtain information on the full crystal structure of the film and, by reproducing peak intensities, on the details of the molecular arrangement within the unit cell *via* simulation of the structure factor (Eq. 2.39) [135, 136]. It is to be recalled that a rotation of the real crystal lattice by an angle ϕ around a given axis corresponds to an analogous rotation of the reciprocal lattice. This implies that a collective change in molecular orientation in a crystalline film causes a corresponding "flipping" of the generated diffraction pattern, as we will see in the Results section 4.3.

3.3.3.8 Projection and rotation of a unit cell on a surface

If the thin film exhibits uniaxial anisotropy and if the crystal polymorph present in the film is known, or if a reasonable assumption can be made for it, a Q-map as the one shown in Fig. 3.21b allows to deduce the orientation of the unit cell of the OSC material, which in turn allows to determine the molecular orientation on the substrate. In order to do this, one uses as starting point the known crystal structure, which contains detailed information about the molecular packing and, therefore, the unit cell parameters. The unit cell parameters consist of the unit cell axes a, b, c

and the angles between them, α (angle between the b and c axes), β (angle between the a and c axes) and γ (angle between the a and b axes). The classification of the 7 Bravais lattices is based on the number of equal parameters.

As a first step, we transform the coordinate system of the crystal **a**, **b**, **c** in a Cartesian axis system **x**, **y**, **z**. If $\mathbf{w} = (w_a\ w_b\ w_c)$ is a vector expressed in crystal coordinates, then its transformation to a vector $\mathbf{v} = (v_x\ v_y\ v_z)$ in Cartesian coordinates is performed *via* the orthogonalization matrix matrix $\hat{\boldsymbol{O}}$ [243]. The expression for $\hat{\boldsymbol{O}}$ contained in Eq. 3.13 follows the convention that **x** is collinear with **a**, **y** is collinear with $\mathbf{a} \times \mathbf{b} \times \mathbf{x}$, **z** is collinear with the reciprocal axis $\mathbf{c}^* = \mathbf{a} \times \mathbf{b}$.

$$\mathbf{v} = \hat{\boldsymbol{O}}\mathbf{w}, \quad \text{with } \hat{\boldsymbol{O}} = \begin{pmatrix} a & b\cos(\gamma) & c\cos(\beta) \\ 0 & b\sin(\gamma) & c\left[\cos(\alpha) - \cos(\beta)\cos(\gamma)\right]/\sin(\gamma) \\ 0 & 0 & V/\left[a\,b\sin(\gamma)\right] \end{pmatrix} \tag{3.13}$$

In a second step, the so-obtained unit cell in Cartesian coordinates is rotated by an angle ϕ about either the x, y or z axis by means of the known rotation matrices $\hat{\boldsymbol{R}}_i$, where i is the rotation axis [244]). Once the desired orientation of the OSC unit cell is obtained, the Q_x, Q_y and Q_z values can be calculated using Eqs. 2.41-2.44 and the resulting Bragg peaks can be compared with the experimental ones having Q-coordinates given by Eq. 3.6. Subsequently, knowing the crystal structure, it is possible to deduce the molecular orientation on the substrate. For instance, the simulation shown in Fig. 3.21b is obtained for an upright-standing orientation of the unit cell of the thin-film phase of DIP. Further examples with rod-like OSCs are contained in the Results section 4.3.

3.3.4 Variable angle spectroscopic ellipsometry [8]

In this thesis, variable angle spectroscopic Ellipsometry (VASE) is employed to study the optical anisotropy of thin films of OSCs arising as a consequence of: a) the intrinsic anisotropy of many molecular OSCs, b) the structural anisotropy of the films. In particular, due to the typical 2D-powder texture, the in-plane component of the optical functions (i.e. in the xy plane) will differ from the out-of-plane component (i.e. along the z axis). Ellipsometry can also be employed to obtain information on other film properties, among which the most relevant for this thesis are film thickness and roughness.

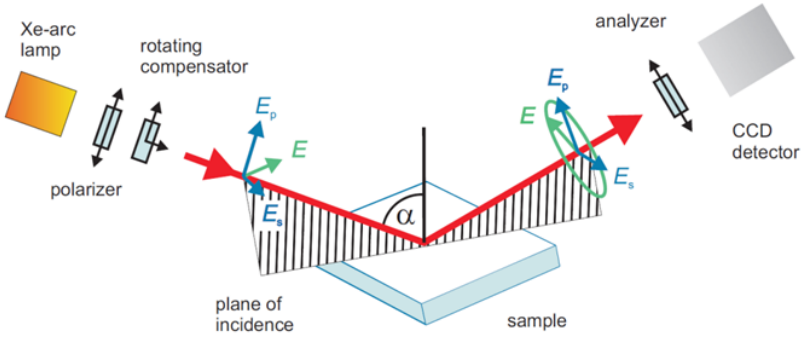

Figure 3.23: Schematic of an ellipsometry setup employing a rotating compensator. The s- and p-components of an arbitrarily oriented electric field **E** are shown. The description of the setup is contained in the text. Adapted from [146].

In general, the ellipsometric function $\tilde{\rho}$ is measured:

$$\tilde{\rho} = \frac{\tilde{R}_p}{\tilde{R}_s} = \tan(\psi)\mathrm{e}^{i\Delta} \tag{3.14}$$

[8] The contents of this paragraph have been taken mostly from the variable angle spectroscopic ellipsometry (VASE) manual [138].

where $\tilde{R}_{p/s}$ are the pseudo-Fresnel coefficients of Eq. 2.27. The ellipsometric equation involves that not only an intensity ratio is measured, but also a phase shift, which increases the sensitivity of the technique. Several optical components are employed for the experimental evaluation of $\tilde{\rho}$ in Eq. 3.14, as schematically shown in Fig. 3.23.

The several optical components involve a light source, a polarizer, a rotating compensator, an analyzer and a CCD detector. The light passes through a fixed polarizer, after which a rotating compensator is inserted which converts the light polarization from linear to elliptical. As the elliptically polarized light interacts with the sample, the s- and p-component of the electric field **E** experience different retardation and intensity variation, respectively, which changes the polarization state of the beam compared to its state before entering the sample. Such polarization change carries a lot of information about the anisotropy of the thin film optical properties. The analyzer consists in another fixed polarizer for measurement of the final state of light. In order to reduce disturbance from environmental light to improve the signal-to-noise, a stepper motor-driven light chopper is employed. Digital signal analysis filters noise sources at frequencies other than the chopping one. The beam enters then optical fibers and arrives to the spectrometer, where it is decomposed into its chromatic components by a grating. Each vavelength hits the pixel of a CCD detector, allowing simultaneous measurement of a wide wavelength range at once and fast acquisition of spectroscopic data.

Prior to a measurement, the absolute position of polarizer and analyzer axes as well as the relative attenuation of the chopped signal with respect to the continuous component need to be calibrated and the sample needs to be aligned. Subsequently, the procedure of data acquisition and analysis is illustrated in Fig. 3.24.

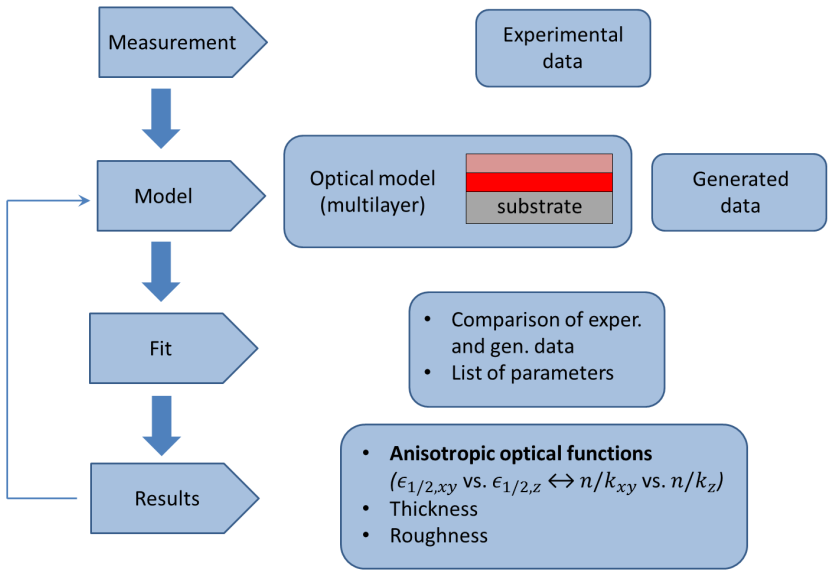

Figure 3.24: Diagram illustrating the data acquisition and fitting procedure in WVASE, explained in more detail in the text. Adapted from [138].

An optical model has to be built and used to simulate the optical properties of the sample. Notice that if an anisotropic optical model is employed, the dielectric function $\tilde{\epsilon}$ becomes a tensor. Data are then generated from such model and compared with the measurement. Comparison of the experimental and modeled $\tilde{\rho}$ is done by inverting Eq. 3.14 and choosing the right branch of solutions [146]. By adopting a "point-by-point" procedure, this operation can be performed such that at each single wavelength Eq. 3.14 is satisfied. Alternatively, "normal fitting" can be carried out, i.e. the optical constants can be simulated with analytical functions. The advantage of the point-by-point approach is that also a poor choice of the initial parameters will lead to convergence, whereas for the analytical approach a good initial guess is needed. Typically, a point-by-point fit is performed at the beginning and is then refined by performing a normal fit.

A multi-sample analysis of the same organic film deposited on different substrates allows to

reduce the correlations between fitted parameters and thereby improve the accuracy of the so-obtained optical functions [208]. Typically, the same optical model is employed for films deposited on similar surfaces like native and thermally grown Si oxide and glass. However, for some systems the surface morphology depends critically on the kind of oxide despite the crystal structure investigated by means of X-ray scattering does not show comparably large differences. The safest approach is to choose native and thermally grown Si oxide layers of different thickness [209] (see Materials section 3.2).

As outlined in the Fundamentals section 2.2, surface roughness can be modeled using EMA models. However, for ellipsometry data, EMA models can be applied within certain limits. The most important requirement is that roughness features should be at most ∼10% of the beam wavelength, otherwise diffuse scattering and de-polarization of the specular beam may occur. This means that for islands size comparable to the wavelength, EMA modeling fails.

Ellipsometry can be also performed in transmission, where the ellipsometric parameter is now defined as:

$$\tilde{\rho} = \frac{\tilde{T}_p}{\tilde{T}_s} \tag{3.15}$$

The procedure for data analysis and fitting is analogous to the description above. The steps to align the sample and choose the proper settings for beam intensity to avoid signal overload are also analogous and adapted to the transmission geometry.

Description of the setup used for VASE A Woollam M-2000 spectroscopic ellipsometer with rotating compensator and extended range in the NIR (676 wavelengths in total for a covered spectral range between 5 eV and 0.75 eV) was used to get information about the optical anisotropy of the films. The light source employed is a Xe arc lamp, which covers a wavelength range of 190 nm - 2 μm (∼6.5 eV - 0.6 eV). Two CCD detectors are needed to cover the full range, one with Si-based chips for the UV-vis range and one with InGaAs chips for the NIR range. The films were measured in both transmission and reflection geometry using the same nominal sample (i.e., same growth process) grown on Si with both a native and a thermal oxide layer and on borosilicate glass, allowing for a multi-sample analysis. For measurements in transmission, a custom-built stage with finely tunable rotational and translational degrees of freedom is employed [245]. Ellipsometric measurements in reflection were performed with incidence angles of 45° to 80° in steps of 5°, and in transmission between 0° and 70° in steps of 5° (angles are always with respect to the substrate normal). Data were analyzed using the software WVASE [138]. To account for the top roughness of the thin films in the ellipsometry fit, an EMA layer including a fixed 50%/50% void-to-full ratio with varying thickness was used. Data fitting has been performed employing the WVASE32 software from J. A. Woollam Co., Inc. [138].

3.3.5 Fourier-transform infrared spectroscopy [9]

Fourier-transform infrared spectroscopy (FTIR) is used in this thesis to study molecular vibrations in an energy range between ∼0.12-0.28 eV or, in the more practical wavenumber units for FTIR, ∼1000-2300 cm^{-1}. This wavenumber range contains the so-called "fingerprint" region (∼1200-1700 cm^{-1}), where a large number molecular vibrations appear, including stretching of conjugated C-C bonds and in-plane bending of C-H bonds. A much lower number of vibrations is located in the region ∼2000-2300 cm^{-1}. Therefore, it is much easier to study changes in molecular vibrations located in the latter region, which is advantageous for characterizing physical phenomena that affect them. A chapter of this thesis is, indeed, dedicated to the study of the C≡N stretching, a type of vibration normally located around ∼2200 cm^{-1} in molecular materials. Below we briefly illustrate the working principle of FTIR and later on we describe a particular setup.

3.3.5.1 Working principle of an FTIR spectrometer

A schematic view of an FTIR spectrometer is given in Fig. 3.25.

[9] The content of this section has been taken mostly from Ref. [246].

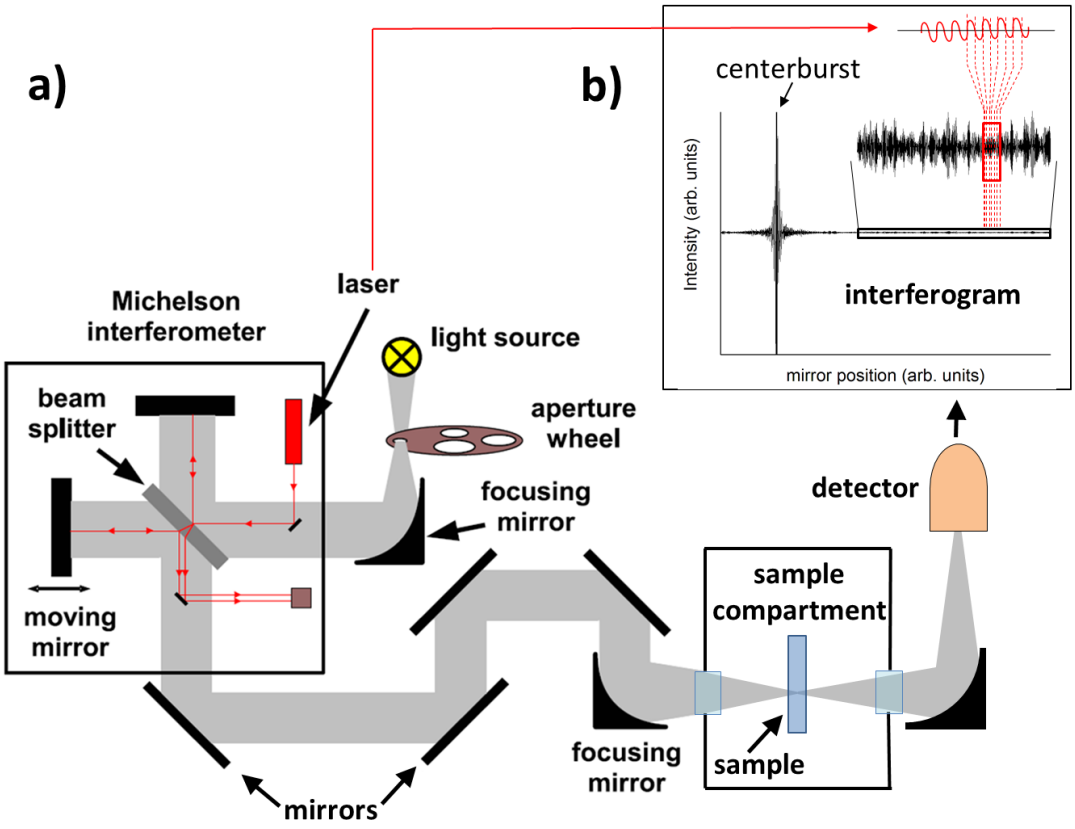

Figure 3.25: **a)** Schematics of an FTIR spectrometer based on a Michelson interferometer. **b)** Digitization of the interferogram $I(x)$ at the points of zero-crossing of the laser amplitude (see Eq. 3.16b). Description of the single parts is contained in the text. Adapted from Refs. [246, 247].

A Michelson interferometer is the heart of the instrument. An IR beam generated by a suitable source enters into the interferometer and is divided into two equally intense branches by means of a beam splitter. One branch of the beam is reflected from a fixed mirror and the other by a moving mirror, the latter continuously sweeping along its axis by a total distance L. The change in path length of the beam reflected at the moving mirror causes a phase shift with respect to the beam reflected at the fixed mirror. When the two branches recombine at the beam-splitter, they will have acquired a relative phase ϕ depending on the mirror displacement x:

$$\phi = \frac{2\pi}{\lambda} \cdot (2x) \rightarrow 2x = n\lambda \leftrightarrow x = \frac{n\lambda}{2} \tag{3.16a}$$

$$I(x) = S(\nu)\cos(2\pi\nu x), \quad \text{with} \quad \nu = \frac{1}{\lambda} \tag{3.16b}$$

The two most right-hand equations in Eq. 3.16a express the condition of constructive interference at the beam splitter, i.e. $\phi = 2\pi n$. After the interferometer, the IR beam is focused onto the sample and subsequently on the detector. A laser is used to precisely track the change in optical path difference due to the moving mirror. Indeed, the laser intensity is modulated many times during one sweep cycle of the moving mirror, as shown in Fig. 3.25b.

The raw data measured by the instrument consists in the interferogram $I(x)$ (Eq. 3.16b), which is digitized at the at the zero-crossing points of the modulated laser intensity (Fig. 3.25b). In Eq. 3.16b, the wavenumber ν has been introduced, and $S(\nu)$ is the Fourier component of $I(x)$ at ν. The sampling spacing in a spectrum is $\Delta\nu = 1/L = 1/(N\Delta x)$ with $N \in \mathbb{N}$ and Δx the sampling distance within the interferometer. Since Δx is extremely precise, the built-in resolution of an

FTIR spectrometer is in the order of 0.01 cm^{-1}. Therefore, compared to dispersive spectroscopy, FTIR spectroscopy has two main advantages: a) it possesses a very high built-in resolution, b) no monochromatization of the beam is present, which leads to high radiation throughput since all the frequencies impinge on the detector simultaneously.

Once the interferogram $I(x)$ has been measured, the spectrum in frequency space is obtained by numerically evaluating a *discrete* Fourier transform of the interferogram:

$$S(k\Delta\nu) = \sum_{n=0}^{N-1} I(n\Delta x)\mathrm{e}^{i(2\pi nk/N)} \tag{3.17}$$

N corresponds to the total number of equidistant sampling points. The feature of highest intensity in the interferogram is commonly referred to as "centerburst" (Fig. 3.25b). Mathematically it represents the inverse Fourier transform of $S(k\Delta\nu)$ calculated at $n = 0$. The centerburst is therefore proportional to the sum of all intensities divided by N and gives an indication of the total intensity on the detector. In frequency space, the centerburst translates into a broadband spectrum, and the details of the single molecular vibrations are contained in the much weaker wings, therefore the dynamic range of the data is typically high (Fig. 3.25b).

A number of mathematical operations need to be performed in order to avoid artifacts when carrying out the Fourier transformation in Eq. 3.17. Below we briefly mention them.

- The *zero-filling* interpolates the spectrum in order to avoid the so-called "picket-fence" effect. This happens if the sampling points $k\Delta\nu$ lie between effective absorption features of the substance under study. As a result of the picket-fence effect, peak intensity might appear reduced.
- *Aliasing* occurs because the Fourier transformation of the interferogram in Eq. 3.17 does not produce one single spectrum, but rather a periodic sequence of mirror-imaged interferograms in frequency space. Therefore, the interferogram with the correct scaling of the wavenumber axis needs to be chosen.
- *Undersampling* exploits the aliasing property illustrated above and allows to reduce the size of the measured interferogram.
- *Leakage* arises because of the truncation of the Fourier transform in Eq. 3.17 at a finite length $L = N\Delta x$, and translates into an instrumental broadening of the line shape. Several analytical functions can be convoluted with the measured interferogram in order to reduce this broadening. In other words, in FTIR spectroscopy the instrumental line-shape is not an intrinsic property of the spectrometer, but rather a mathematical function which can be appropriately chosen.
- *Phase correction* of the calculated interferogram is necessary in order to correctly calculate the real part of the complex Fourier transform in Eq. 3.17.

All the above aspects of the Fourier-transformation of the interferogram (Eq. 3.17) are taken into account by inserting the proper settings into the measurement software. The spectrum obtained after all necessary calculations is the so-called "single-channel" spectrum, which can be used for calculation of transmittance/absorbance spectra, etc.

It needs to be pointed out that, if the signal-to-noise ratio cannot be improved because the detection limit of the instrument is reached, or other noise sources cannot be reduced, a solution is to adopt polarization-modulation techniques. For reflection experiments with modulated light, the additional compartment PMA50 from Bruker has been used [248].

Description of the setup used for FTIR In this thesis, a Vertex 70 spectrometer (Bruker) was used. Sampling of the interferogram is achieved by letting a He-Ne laser ($\lambda = 633$ nm) travel into a Michelson interferometer equipped with a Ge-coated KBr crystal as beam-splitter. The light source is a U-shaped Si carbide piece (globar) that emits in the mid-IR. The beam size can be changed by means of circular apertures placed right after the source. Two detectors are available: a) a LaTGS detector for room T operation, b) a liquid N_2-cooled mercury cadmium telluride detector mounted on a goniometer for measurements in reflection geometry. The combination of

light source, beam splitter and detector determines the maximum spectral range that is possible to measure. Sample holders are provided which allow rotation of the sample around a vertical axis. The spectrometer as well as the sample compartment are purged with dry air. All data were analyzed using the software OPUS from Bruker [249].

3.3.5.2 Reflection geometry with polarization-modulation

Investigation of the fingerprint region of the IR spectrum might be complicated by the fact that the roto-vibrational spectrum of atmospheric water is found in the same wavenumber range. Despite the use of dry air purging of the sample compartment, residual humidity is readily detected. Since the amount of material in the organic thin film is still relatively low compared to that of atmospheric gases, only the strongest molecular resonances can be unambiguously identified. We use polarization-modulation infrared reflection-absorption spectroscopy (PMIRRAS) to improve the overall signal-to-noise and collect valuable signal even from very small amounts of material. Contributions from atmospheric gas species like H_2O and CO_2 are canceled out, allowing unambiguous investigation of the fingerprint region.

The setup for PMIRRAS is shown in Fig. 3.26.

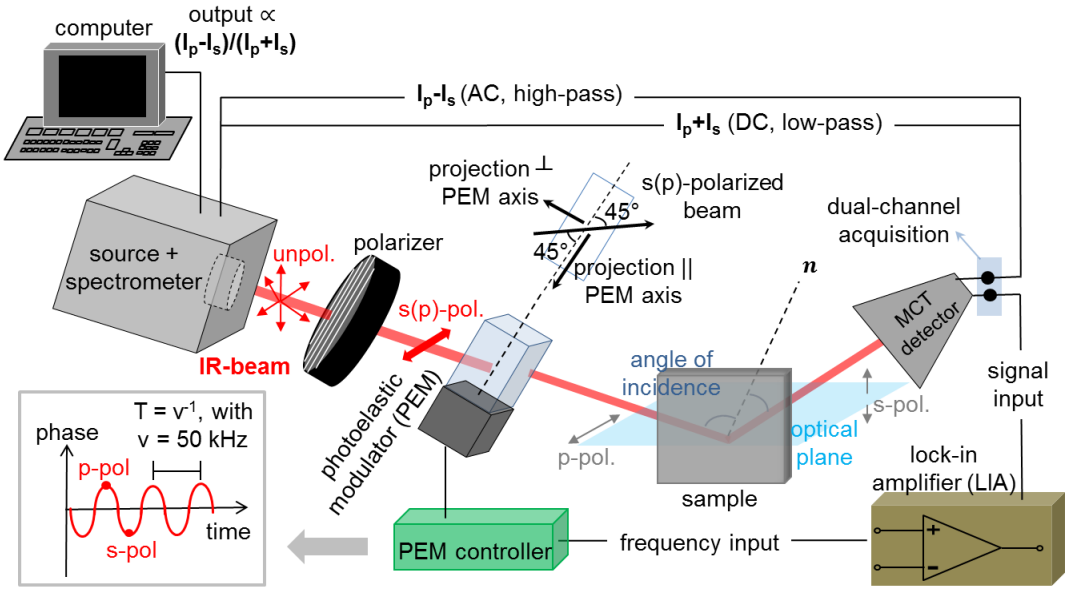

Figure 3.26: Schematics of setup for PMIRRAS. The source and spectrometer components belong to the Vertex 70 spectrometer described above. Description of the remaining components are detailed in the text. The optical plane is perpendicular to the plane of the sheet.

The initially unpolarized IR beam passes through a fixed polarizer. The polarization of the beam is then periodically changed by a mechanically-driven photoelastic modulator (PEM) whose optical axis is oriented at 45°. with respect to both the s- and p-components of the electric field. The working principle of a PEM consists in a dependence of the refractive index along the crystal axes x and y perpendicular to the beam propagation direction, n_x and n_y, on the deformation state of the crystal. This means that one of the components of the wave travels faster or slower than the other depending on the sign of the deformation of the corresponding crystal axis. If the crystal has a thickness z along the beam propagation axis, then the instantaneous phase difference, called the retardation $A(t)$, is given in length units by [250]:

$$A(t) = z\,(n_x(t) - n_y(t)) \tag{3.18}$$

Depending on the retardation $A(t)$ in Eq. 3.18, several polarization states can arise after the PEM. Setting a half-wave retardation of the slowest polarization component causes a rotation

by 90° of the linearly polarized electric field. In the setup we used, the polarization is switched between s- and p- at a frequency f, i.e. one has an s-(p-) polarized beam every $T = 2/f$ s.

Suitable substrates for the use of this technique are conductive surfaces like noble metals (Au, Ag or Cu). For such substrates one maximizes the difference $I_p - I_s$ between the intensity reflected with p- and s- polarization, respectively, if an incidence angle close to the Brewster angle is set. Another effect of the s- and p-polarization state of light regards the possibility to selectively excite a set of molecular vibrations and will be discussed shortly below.

A lock-in amplifier (LIA) allows to amplify the input signal, I_p - I_s, by setting an appropriate gain. The LIA generates a reference signal at the same frequency of the periodic driving voltage of the PEM, i.e. the LIA is "locked" at the PEM modulation frequency. The measured signal is proportional to $(\mathrm{I}_p - \mathrm{I}_s) / (\mathrm{I}_p + \mathrm{I}_s)$. The high-frequency, phase-corrected AC signal $\mathrm{I}_p - \mathrm{I}_s$ is separated from the DC average intensity $\mathrm{I}_p + \mathrm{I}_s$ by the LIA by means of high- and low-band pass filters [251]. Similarly to VASE illustrated in the previous section, this kind of "phase-sensitive" detection increases the sensitivity significantly. Modulation of the incoming beam by means of the PEM leads to a background line-shape superimposed to the "real" $\mathrm{I}_p - \mathrm{I}_s$. The intensity at the detector is proportional to the second-order Bessel function $J_2(\phi_0)$ [247, 252]:

$$\frac{\Delta I}{I} \propto \frac{\mathrm{I}_p - \mathrm{I}_s}{(\mathrm{I}_p + \mathrm{I}_s)} J_2(\phi_0) \tag{3.19}$$

The argument of J_2 is proportional to V_{PEM}/λ, where V_{PEM} is the driving voltage applied to the PEM to achieve a given deformation, and λ is the wavelength. Notice that the PEM retardation (Eq. 3.18) is well defined only for a fixed wavelength λ. Therefore, Eq. 3.19 is strictly valid only for the retardation wavelength set in the PEM. Since $J_2(\phi_0)$ depends on λ *via* ϕ_0, the measured differential reflectance will have a periodic shape of decaying amplitude (the Bessel function) with a spacing depending on the retardation wavelength.

Switching the beam polarization between s- and p- allows to exploit the *surface selection rule* for infrared spectroscopy on metal surfaces. For a given vibrational mode, only the component of the TDM perpendicular to the metal surface can be detected. Given the grazing incidence of the beam in a PMIRRAS experiment, only the p-polarized component of the incident light can couple efficiently with the TDM perpendicular to the substrate surface. The s-component of the incident light creates an instantaneous image dipole on the metal surface, therefore inhibiting the ability of the field to excite molecular vibrations. Notice that the surface selection rule is strictly valid for atoms bonded right at the metal surface. For increasing distances, the component of the electric field parallel to the surface (s-polarization in our case) will not be exactly zero [247]. Nevertheless, it has been shown that PMIRRAS can also be successfully applied to study self-assembled monolayers on metal oxide surfaces [217, 253] as well as D:A mixed thin films of OSCs on Au [57]. The relaxation of the surface selection rule for these systems does not affect the discussions presented in the Results section 4.4.

Description of the setup used for PMIRRAS PMIRRAS measurements were performed on a Vertex 70 infrared spectrometer equipped with a PMA 50 unit (Bruker) that allows measurements in reflection geometry. A half-wave retardation of 2200 cm^{-1} was set for the PEM to match the spectral region where the $\mathrm{C}\equiv\mathrm{N}$ stretching resonances are located (see Results section 4.4). The same retardation was used to analyze the data in the fingerprint region. To maximize the differential reflectance, the angle of incidence was set to 80° as a compromise between the Brewster angle for Au (∼85°) and a reduced beam footprint on the sample. Spectra were measured with 4 cm^{-1} resolution averaging 10^3 scans, allowing the measuring chamber to be purged with dry air for 15 min prior to starting the measurement. The infrared beam was initially p-polarized by a grid polarizer (Specac) and the polarization was modulated with a frequency of 50 kHz by a ZnSe photoelastic modulator (Hinds Instruments). The AC and DC components of the differential reflectance (Eq. 3.19) were measured using a SR830 DSP LIA (Stanford Instruments). The Bessel background arising from the polarization modulation was subtracted using the software OPUS from Bruker.

3.3.6 Other methods

In the following we describe additional experimental techniques employed in the course of this thesis. It is to be noticed that other characterization methods have been used apart from these described here, namely Raman and photoluminescence spectroscopy. However, the data measured with these methods are not contained in the Results chapter 4, therefore here we do not describe these two spectroscopic techniques.

3.3.6.1 Optical absorption spectroscopy in transmission

As outlined above, the possibility to deposit a thin film simultaneously on several substrates allows to carry out different kinds of optical spectroscopy on the samples produces during the same growth experiment. This, in turn, increases the comparability of the results. Typically, in the course of this thesis thin films have been grown on three substrates simultaneously (Fig. 3.8). In particular, the films grown on glass slides were used most often for UV-vis-NIR absorption spectroscopy measurements in transmission.

The advantage of transmission measurements is that they represent a fast and relatively uncomplicated characterization tool. The data obtained contain *averaged* information about the system under study and they do not require any optical model. The drawback is that only semi-quantitative information about the extinction coefficient k (Eq. 2.12) of thin films can be obtained. We adopted a simple transmission geometry with a non-polarized beam in normal incidence and without the use of an integrating sphere. Hence, neither back- and diffused scattering of the incident radiation is taken into account.

Due to the normal incidence of the beam, only information about the component of the TDM *parallel* to the substrate surface con be obtained (Fig. 3.27). This involves that only the in-plane component of k, k_{xy}, can be measured. Thus, if the organic film exhibits a defined 2D texture and if the overall molecular orientation is known, it is possible to deduce the orientation of the TDM for the observed optical transitions with respect to the molecular axes. Alternatively, if the orientation of the TDM with respect to the molecular axes is known, information about the orientation of the molecules on the substrate is obtained.

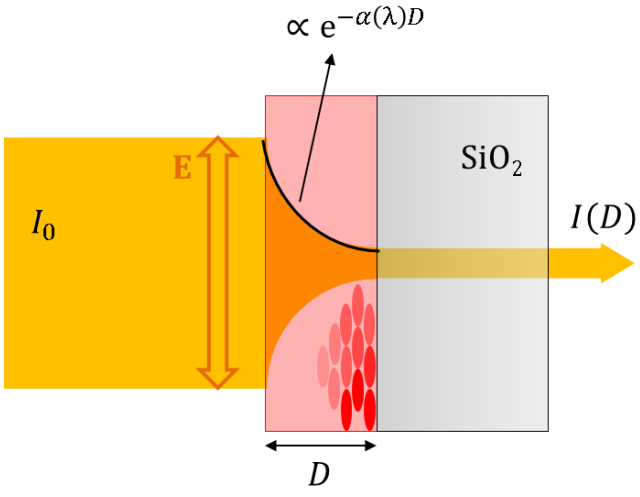

Figure 3.27: Sketch of absorption spectroscopy in transmission geometry. The electric field vector **E** of an unpolarized beam of intensity I_0 is parallel to the sample surface. The beam is attenuated inside the organic film of thickness D according to the Lambert-Beer law (Eq. 3.20). A possible orientation of the OSC molecules constituting the film is shown. No scattering of the beam at the interfaces with the SiO_2 substrate is depicted.

If an incident beam with intensity I_0 is shone through a sample and the transmitted portion reaches the detector with intensity I, then the measured transmittance is $T = I/I_0$ (Fig. 3.27).

The measured T can be related to the film absorption coefficient α and film thickness D by means of the Lambert-Beer law, valid for a monochromatic radiation of wavelength λ:

$$I(\lambda, D) = I_0 \mathrm{e}^{-\alpha(\lambda)D} \quad \rightarrow \quad \ln T = -\alpha(\lambda) D \quad \leftrightarrow \quad \alpha(\lambda) = -\ln T/D \tag{3.20}$$

Notice that the form of Eq. 3.20 is quite general an can be used also to quantify the attenuation of X-rays when passing through a medium [163]. The film thickness D can be estimated in a meaningful way by complementary methods such as XRR and ellipsometry. Once this is achieved, k can be calculated from α obtained with Eq.3.20 using Eq. 2.13:

$$k \equiv k_{xy}(\lambda) = \frac{\lambda \cdot \alpha(\lambda)}{4\pi} \tag{3.21}$$

where we explicitly indicated that only k_{xy} is measured in this normal incidence geometry. As mentioned above, all scattering effects at the glass interfaces are neglected. In order to minimize their impact on the calculation of k_{xy}, and to take into account possible fluctuations in the beam intensity, it is always a good practice to measure a blank glass slide as reference. For the transmission measurements performed in this thesis, we have always adopted the following procedure: a) measurement of the empty beam-path (air), which is kept stored in the memory of the machine as reference; b) measurement of a blank glass slide against the reference; c) measurement of the organic films on glass against the reference; d) subtraction of T of the glass from T of the film and calculation of k.

Overall, absorption spectroscopy is a useful and relatively easy tool for the semi-quantitative estimation of the extinction coefficient, $k_{xy}(\lambda)$, of organic thin films. Additionally, a careful cross-comparison of $k_{xy}(\lambda)$ fitted from high-sensitivity VASE data with the "raw" data obtained by absorption spectroscopy can give strong hints towards the validation of the optical model employed in VASE.

Description of the setup used for absorption spectroscopy UV-vis-NIR absorption data were collected using two different instruments in transmission geometry. A Cary 50 UV-Vis spectrophotometer (Varian), equipped with a Xe lamp as light source, was used for measurements with photon energy down to 1.25 eV. A Cary 5000 UV-Vis-NIR spectrophotometer (Varian), equipped with a deuterium lamp as light source, was used for measurements with photon energy down to 0.375 eV. In the latter case, due to absorption of the glass [254] information about the organic films can be extracted only above ∼0.5 eV. Both instrument are based on dispersive optics and moving slits for wavelength selection.

3.3.6.2 Atomic Force Microscopy [10]

The "soft" interactions in molecular thin films can be exploited to obtain information on film morphology if a suitable probe is used. To achieve this, the atomic force microscope (AFM, Fig. 3.28) has been first introduced by Binnig and co-workers in 1986 [256]. Compared to the scanning tunneling microscope (STM) introduced by Binnig and co-workers shortly before [257], this scanning probe microscopy technique does not require conductive or metalized samples since it is based on the short range interaction forces arising between the analyzed surface and an (ideally) atomically sharp tip. The strength of these interactions can be in the order of van der Waals forces or of atomic bonds [256].

The main components of an AFM system are the tip, which represents the probe, and the cantilever to which it is attached (Fig. 3.28b). The tip is few μm long and shaped like a pyramid or a cone, typically made of Si. The radius and angle of the tip determines the final lateral resolution. The cantilever is a micro precision-machined piece of Si or Si nitride (Si_3N_4) ∼100 μm long and held by a chip. In several scanning modes (Fig. 3.28d), the cantilever oscillates under the action of a piezoelectric element driven by a periodic voltage, and its response can be described by a forced oscillator. The *resonance frequency* $f_r = \frac{1}{2\pi}\sqrt{\frac{k}{m}}$ of a cantilever depends on its construction parameters *via* the spring constant k. The latter can be determined by the displacement s that the cantilever experiences when it interacts with a surface with a force F (Fig. 3.28c) according

[10] The contents of this paragraph are mostly taken from Ref. [255]

to the Hooke's law , $F = -kx$. Therefore, the cantilever displacement is proportional to the attractive or repulsive force of the tip with the surface. In general, tips of different k are required depending on the nature of the surface to scan and on the scanning mode chosen. The dependence of the cantilever displacement on the interaction force is exploited to measure *height profiles* of the surface, i.e. $z(x, y)$, when the tip is scanned across it. Notice that the z-resolution on the final approaching distance of the tip to the surface.

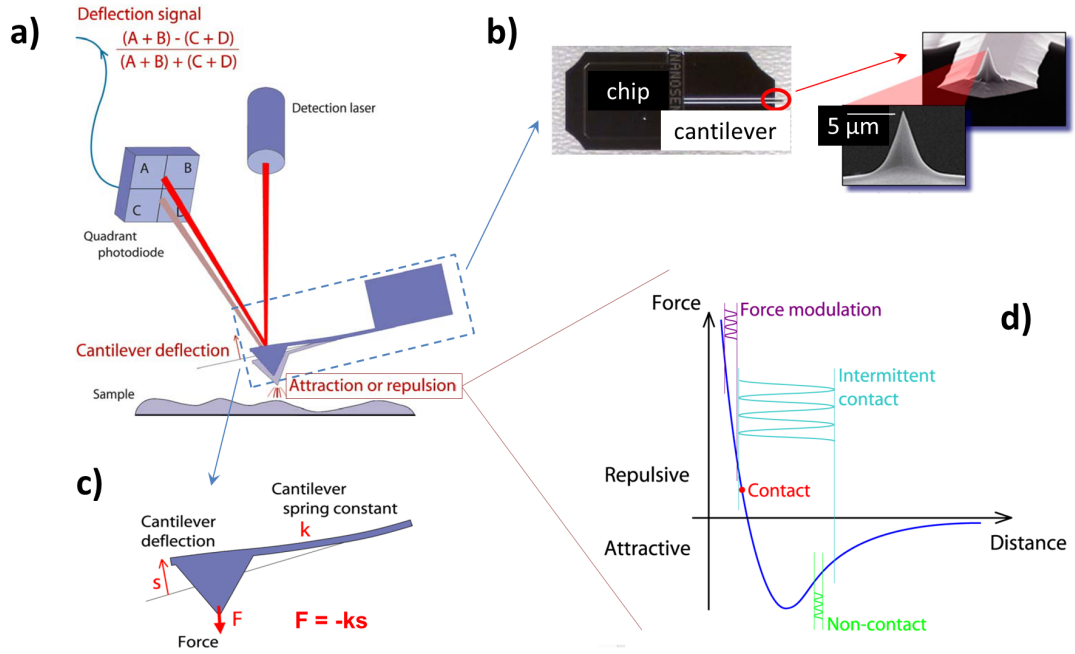

Figure 3.28: **a)** Schematic view of the detection principle of an AFM setup, with the definition of the laser deflection signal on the photodiode array. **b)** Microscope pictures of a cantilever to which a $\sim$5 μm long conical tip is attached. **c)** Definition of the displacement s and the elastic constant k depending on the force F between substrate and tip. **d)** Typical curve representing a Lennard-Jones interaction potential (Eq. 2.4) and the tip-surface interaction ranges used in each imaging mode. The intermittent contact mode is briefly described in the text. For the other imaging modes, please consult Ref. [255], from which the figure was adapted.

In order to accurately measure the cantilever displacement, the principle of the optical lever is used. Cantilevers have a metallic coating, typically of Ag, on their back surface, so that a laser can be shone on this coated area and reflected onto a detector (Fig. 3.28a). The total optical path of the reflected beam is long enough so that also small cantilever displacements translate into sufficiently large deviations of the laser position on the detector. The most common detection system consists in an array of four photodiodes arranged so that the laser spot position can be calculated in two directions.

Measurement of surface profiles can be performed by means of several scanning modes. They differentiate from each other based on the range of the tip-surface interaction potential within which they work. The most widely used scanning mode for soft materials, like molecular films, is called intermittent contact mode, or "tapping" mode (Fig. 3.28d). The cantilever oscillates at a given frequency between the attractive and the repulsive portion of the potential. In other words, the tip is periodically driven in contact with the film surface (repulsive potential) and dragged away from it (attractive potential). A target amplitude of this oscillation is set in the instrument and the deflections of the cantilever, resulting from interactions of the tip with the surface, are compensated for by a voltage signal generated in a feedback loop. The AFM signal giving the surface profile $z(x, y)$ is given by the amount of compensating voltage. This scanning mode minimizes the time the "hard" tip is in contact with the "soft" surface, thereby reducing the probability to damage the film as the tip is swept across the surface while keeping high sensitivity. In intermittent contact

mode, the height of molecular monolayers, d, can be resolved [62, 63], with $d >\sim 1$ nm.

Generally, several technical difficulties can be encountered during measurements. *Vibrations* due to thermal noise or to the environment may render the imaging unstable. Several settings of the instrument can be changed in order to optimize the measurement. Additionally, anti-vibration tables are commonly coupled to AFM systems to minimize the impact of environmental noise. *Humidity* in form of a water film is generally present on the film during imaging in environmental conditions, even for highly hydrophobic surfaces. This might cause problems during the approaching stage of the tip towards the film, in the worst case rendering it impossible. Carefully blowing the inter-space between tip and film with N_2 may solve the problem. *Artifacts* in the images may arise due to a damaged or contaminated tip. Indeed, the surface height profiles $z(x, y)$ always result from a convolution of the tip shape with the real surface morphology. Inappropriate scanning settings, like a fast sweeping frequency of the tip of a very rough surface, may quickly lead to deterioration of the image quality, broadening of the surface features or even visible transfer of material from one area of the surface to another (grafting).

As concluding remark, we notice that the signal generated by the cantilever deflection contains a number of information which is not limited to the height profiles. Importantly, the *phase shift* of the cantilever signal with respect to the drive signal is sensitive to the mechanical properties of the surface. For instance, exploiting phase-imaging mode can give information about the film domains constituted by different material phases [258]. An interesting example of the of the application of phase-imaging is shown in Fig. 6.18 of the Appendix.

Description of the AFM setup A Nanowizard-II AFM system was used (JPK-Bruker). The cantilevers (AppNano) were of rectangular shape and their size was always in the order of $\sim$120 μm length, $\sim$30 μm width, $\sim$5 μm thickness. The tips were 14-16 μm high with a tip radius < 10 nm, an elastic constant $\sim 15 < k < 80$ N/m and a resonance frequency $200 < f_r < 400$ kHz. The head of the AFM was placed on top of a Micro 40 anti-vibration table (Halcyonics).

3.3.6.3 Electrical Conductivity [11]

Electrical conductivity of thin films of OSCs has been measured using the setup illustrated in Fig.3.29b has been employed. It consists in a array of $n = 10$ conductive channels connected in parallel by inter-digitated ITO indium tin oxide (ITO) contacts patterned on a quartz glass substrate. The organic material was deposited on the entire patterned area and therefore covers both the ITO contacts and the glass substrate.

Due to the parallel contact geometry, the *total* resistance, R_{tot} if reduced by a factor n with respect to R, the *channel* resistance (Fig.3.29a). Applying a voltage U and measuring the external current I, one obtains $R_{tot} = U/I$. The electrical conductivity of a thin film contained in a channel can thus be calculated using Eq. 2.9 and expressing the resistivity ρ as function of R_{tot}, and of the construction parameters of the channels (Fig.3.29b and caption):

$$\sigma = \frac{L}{nRWd} \tag{3.22}$$

Notice that in Eq. 3.22, the resistance at the interface between organic material and ITO contacts is assumed negligible. The calibration for estimation of the channel thickness d was performed separately by means of AFM as described in Ref. [259].

[11] The deposition of the organic films and the measurements of their electrical conductivity have been performed by Paul Beyer and Tino Meisel, Humboldt Universität zu Berlin.

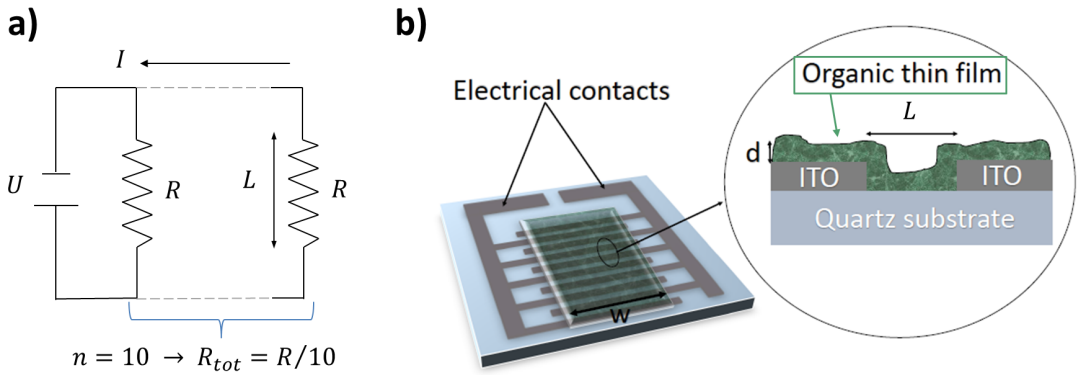

Figure 3.29: **a)** Equivalent circuit for film resistivity measurements: U, applied voltage; I, total current; R, resistance of single channels; L, channel length. **b)** Actual setup: W, channel width; d, film thickness. Adapted from Ref. [259].

Description of the setup used for conductivity measurements For additional details on the setup used for conductivity measurements, please refer to Ref. [111].

CHAPTER 4

RESULTS AND DISCUSSIONS

4.1 Thin film texture and optical properties of D:A mixtures. DIP:F6TCNNQ *vs.* 6T:F6TCNNQ [1]

First, we briefly recall some concepts outlined in the Introduction. Vacuum-deposited thin films of OSCs offer a wide range of possibilities for structural control [20, 98, 260], e.g. heterostructures can be tailored in several manners in order to obtain the desired material properties [37, 261]. One application of the heterostructure concept is the so called "molecular electrical doping", namely, an organic semiconducting matrix is doped with another OSC with the aim of increasing layer electrical conductivity [14] by means of charge-transfer (CT) between two types of OSCs, namely, a donor and an acceptor. Despite the numerous studies already carried out, to date only a limited number of systems has been studied, therefore it is useful to extend the spectrum of investigated material combinations in order to shed more light on the microscopic mechanisms occurring within molecular D:A systems.

In the study presented here, thin films were grown via vacuum deposition of two D:A pairs with varying mixing ratio in a bulk heterojunction architecture in order to maximize the theoretical number of donor-acceptor interfaces. For both combinations we employed the recently studied F6TCNNQ (Refs. [53, 193] and Fig. 3.6a) as acceptor. The donor compounds are DIP (Refs. [124, 167, 169] and Fig. 3.1a) and 6T (Refs. [127, 172, 173] and Fig. 3.2a). The materials employed exhibit a planar and elongated shape and differ significantly in length. The donor molecules were chosen such that it is expected for them to have different conformational degrees of freedom, namely, the molecular structure of DIP is "stiffer" than that of 6T and allows for less intra-molecular conformations. Additionally, due to the relative alignment of the donor HOMO to the acceptor LUMO, an energetically favored CT from the donors to the acceptor is expected (Fig. 4.1).

We introduce the idea that a larger number of conformational degrees of freedom of the molecular donor leads to an enhancement of the 3D (isotropic) character of thin-film texture as well as to partial phase-separation between donor and acceptor. Remarkably, due to the strong D:A interactions, we observe for both systems the formation of a D:A complex with corresponding segregation of D:A co-crystallites, although they mostly lack long-range order. The formation of D:A co-crystals is deduced by structural analysis and confirmed by optical spectroscopy, the latter showing new absorption bands from electronic transitions in the mixtures related to D:A CT-interactions within the co-crystals. These bands are located at energies specific to the material combination and below the optical gap of the pristine materials. Finally, correlation of the optical anisotropy of the new CT transitions with the orientation of the co-crystallites on the substrate allows one to conclude that the TDM associated with the new transitions is oriented perpendicularly to the π-conjugated planes of the face-to-face stacked donor and acceptor molecules within the complex.

The results presented in this section are organized as follows. We first compare X-ray scattering

[1] This section is based on Ref. [162].

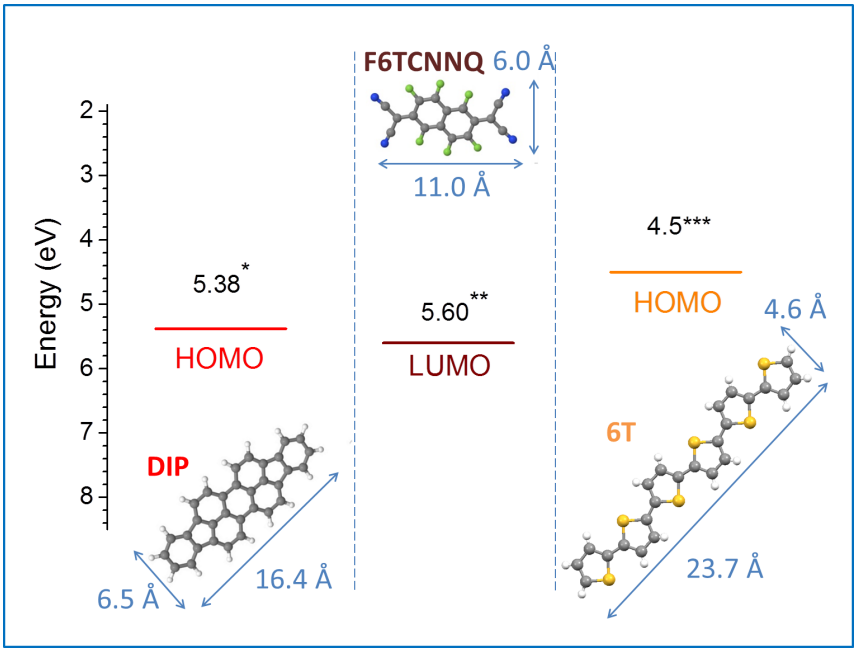

Figure 4.1: Energy levels of frontier orbitals and molecular structure of DIP, 6T and F6TCNNQ. The HOMO and LUMO values were obtained by means of photoelectron spectroscopy for samples in solid films: * Ref. [262], from UPS measurements for standing-up molecules; ** Ref. [53], from IPES measurements; *** from Ref. [263], from UPS measurements for standing-up molecules. All values given as peak onsets.

data for DIP:F6TCNNQ and 6T:F6TCNNQ mixtures, respectively, with focus on the mixtures in 1:1 molar ratio. We then compare optical absorption spectroscopy data for these 1:1 mixtures with data for the pristine compounds and finally we focus on the optical anisotropy of the equimolar mixtures.

4.1.1 Film deposition and experiments performed

We deposited films of the pristine compounds as well as DIP:F6TCNNQ and 6T:F6TCNNQ mixtures in different mixing ratios by means of OMBD. The substrates used were native Si oxide and borosilicate glass (Borofloat®) kept at room temperature. In the mixed films the molar ratio of one species with respect to the other was varied by adjusting the relative growth rates, keeping the total growth rate between 0.15 nm/min and 0.3 nm/min. The growth rates were monitored with two separate quartz crystal microbalances (for donor and acceptor material, respectively) calibrated by X-ray reflectivity for DIP and 6T, and by Atomic Force Microscopy for F6TCNNQ. The error on the mixing ratios is estimated ± 10%.

X-ray surface scattering measurements were carried out at synchrotron facilities. The data presented were acquired *ex situ* at the I07 beamline [264] of the Diamond Light Source (DLS, Oxford, United Kingdom) and at the ID03 beamline of the European Synchrotron Research Facility (ESRF, Grenoble, France). XRR and GIXD geometries (see Methods section 3.3) were used in order to investigate the film structure in the direction perpendicular (Q_z) and parallel ($Q_{||}$) to the substrate, respectively. The scattered intensity was measured by means of 2D detectors: a Pilatus 100K [242] at the I07 beamline and a Maxipix 2x2 at the ID03 beamline. The beam energy was 13 keV at I07 and 18 keV at ID03.

UV-vis-NIR absorption spectroscopy was carried out in transmission geometry. Thin films with different D:A mixing ratio were measured down to 1.25 eV (see Appendix 6.1). Thin films in a mixing ratio of 1:1 as well as the pristine compounds were measured down to 0.5 eV in order to show also the lowest energy transitions.

4.1.2 Structural characterization

In Fig. 4.2-4.3 X-ray scattering data of DIP:F6TCNNQ and 6T:F6TCNNQ mixtures on native Si oxide are shown. We distinguish Bragg peaks from the pristine compounds and Bragg peaks in the mixtures that stem presumably from a D:A co-crystal. We first focus on the results for the DIP:F6TCNNQ series, then we illustrate the results for the 6T:F6TCNNQ series. Bragg peaks found in XRR and GIXD scans are summarized in Tab. 6.1 and 6.2 of the Appendix 6.1.

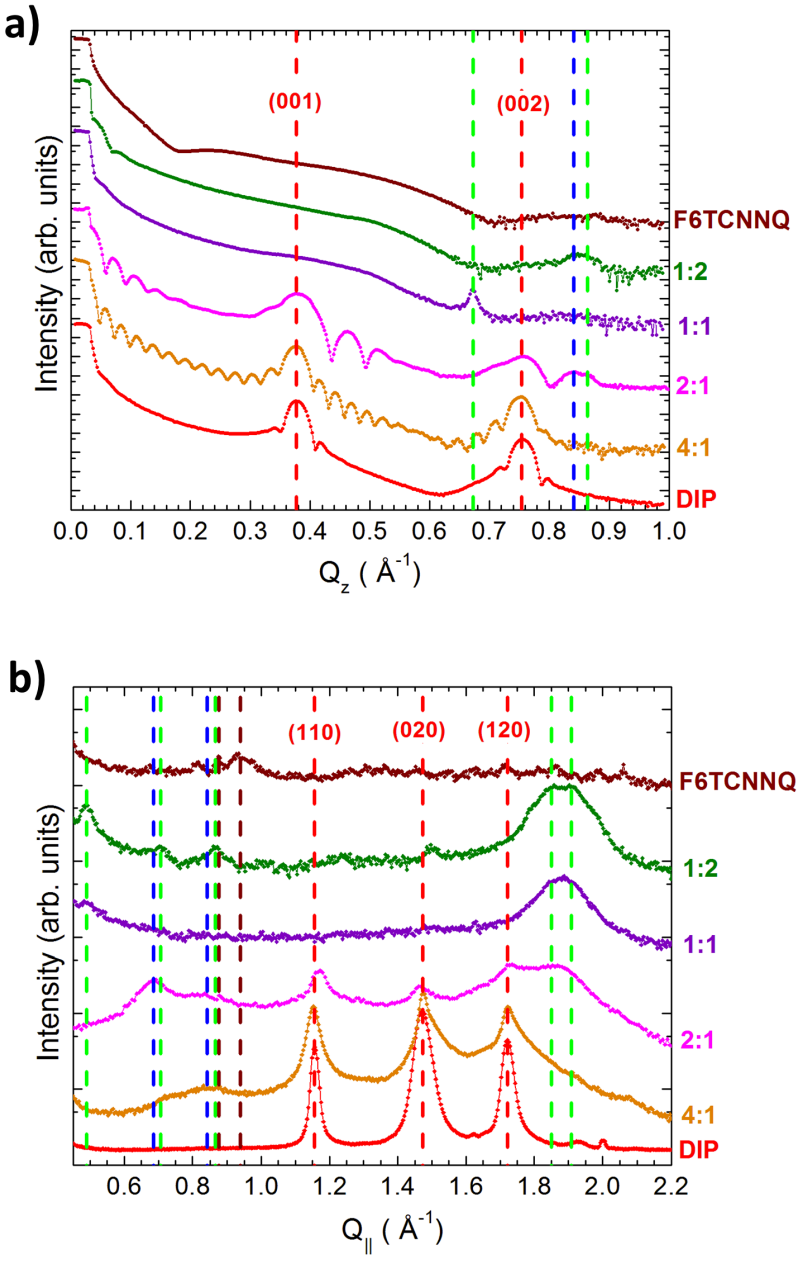

Figure 4.2: **a)** XRR and **b)** GIXD scans for D:A mixtures with DIP as donor and F6TCNNQ as acceptor in different molar ratios. Vertical dashed lines show the peak assignment: DIP thin film polymorph (red), DIP low-T or other polymorph (blue), F6TCNNQ (brown), DIP:F6TCNNQ D:A co-crystal (green). The Miller indices of the Bragg peaks for the DIP thin film polymorph are shown. The film thickness is 23 nm (pristine DIP), 30 nm (4:1), 30 nm (2:1), 14 nm (1:1), 22 nm (1:2), 31 nm (pristine F6TCNNQ).

From the XRR scans of the DIP:F6TCNNQ series (Fig. 4.2a) we see that Bragg peaks characteristic of a standing-up (σ) orientation of DIP [124] are broadening and then disappearing as the relative amount of the acceptor F6TCNNQ increases in the films. At the same time, new Bragg peaks arise which do not belong to pristine DIP. Pristine F6TCNNQ does not exhibit any significant out-of-plane order, therefore it is unlikely that the new peaks stem from segregated F6TCNNQ domains. The new peaks are attributed to a DIP:F6TCNNQ co-crystal. In particular, the peak at $Q_z = 0.67$ Å^{-1} for the 1:1 mixture (corresponding to a distance of ~ 9.4 Å in real space) could stem from a highly tilted edge-on orientation of the D:A stacks within the new co-crystal unit cell, similar to what observed for a Naphtho[1,2-b:5,6-b′]dithiophene (NDT):F6TCNNQ D:A co-crystal introduced recently in Ref. [199]. For the mixtures with excess DIP, one clearly observes a smoothing effect compared to the pristine DIP, denoted by enhanced Kiessig oscillations at low Q_z values (see also Fig. 3.15b), as already observed ,for instance, in DIP:C_{60} mixtures [95, 265]. As the amount of F6TCNNQ increases, the films get rougher, although some weak Kiessig oscillations are still visible. For pristine F6TCNNQ the Kiessig oscillations at low Q_z are absent but the reflectivity curve exhibits a very broad hump, which might indicate the presence of a wetting F6TCNNQ monolayer on the Si oxide surface.

From the GIXD profiles (Fig. 4.2b) we observe marked changes as the relative amount of F6TCNNQ in the films increases. The peaks stemming from σ-DIP tend to broaden and then disappear in the mixtures with higher relative amount of F6TCNNQ. At the same time, new features appear in the scans. The most pronounced changes consist of the relatively broad peaks arising between 1.80 and 1.95 Å^{-1} in $Q_{||}$. A new, pronounced peak appears also at 0.49 Å^{-1}. We attribute all these new features to a D:A DIP:F6TCNNQ co-crystal. The peak at 0.49 Å^{-1}, for example, might stem from the distance between adjacent inequivalent D:A stacks [199]. A number of additional peaks appear in the region $0.6 - 1$ Å^{-1} for the mixed films. Although an obvious attribution could not be found, an assignment was attempted. For the arguments on which these assignments are made, we address the reader to the corresponding section in the Supporting Information (SI) of Ref. [162].

We consider now the XRR and GIXD scans (Fig. 4.3a and b, respectively) for the 6T:F6TCNNQ series. Similarly to the XRR of the DIP:F6TCNNQ series, the Bragg peaks of standing-up 6T, which is present in both the low-temperature (LT) and the β phase [96, 180], broaden and then disappear with increasing relative amount of F6TCNNQ. The tendency to randomization of the orientation of the crystalline domains in the mixtures with excess F6TCNNQ is therefore a common feature of both D:A systems. In the films with excess 6T, though, we do not observe any smoothing. The GIXD profiles of the mixtures from 3:1 to 1:1 show that the (41-1) Bragg peak becomes stronger. Also, in the GIXD of the 1:1 mixture the (400) peak of the 6T LT phase appears. The presence of these features in the in-plane scans indicates that, even in the equimolar blend, 6T tends to segregate in crystalline domains that have a more random orientation compared to pristine 6T films as the content of F6TCNNQ increases, an effect which was not observed in the DIP:F6TCNNQ series. In 6T:F6TCNNQ, as for DIP:F6TCNNQ, it is possible to observe the development of new peaks in the region $Q_{||} = 1.80 - 1.95$ Å^{-1}, together with a new peak at 0.67 Å^{-1}. Therefore, for 6T:F6TCNNQ one can also deduce the formation of a D:A co-crystal structure.

The new features in the GIXD scans appearing at similar values of $Q_{||}$ between 1.80 and 1.95 Å^{-1} for both series of mixtures likely stem from crystallographic directions vicinal to or coincident with the π-π donor-acceptor stacking direction, as illustrated by the comparison of some GIXD scans with the powder diffraction patterns of known D:A compounds (see Figs. 6.1 and 6.2 in Appendix 6.1). We therefore suggest that both DIP:F6TCNNQ and 6T:F6TCNNQ pairs form mixed D:A stacks (see also Fig. 2.5a), which usually results in partial CT in the ground-state, as observed for other D:A pairs [56, 88, 200, 266].

In Fig. 4.4 we show the reciprocal space maps, i.e. full diffraction patterns, measured for DIP:F6TCNNQ (100 nm) and 6T:F6TCNNQ (72 nm) 1:1 mixtures. Overall, the diffracted intensity from the D:A co-crystal features appears in the Q-space as either elongated spots with some angular distribution, or as uniform Debye-Scherrer rings. For DIP:F6TCNNQ (Fig. 4.4a), the elongated spots indicate a mostly uniaxial arrangement of the molecular D:A crystalline domains (i.e. in the fashion of a 2D textured powder) although with some mosaicity in the order of $\pm$ 20°. The intensity of the diffraction features with $Q_{||} = 1.80 - 1.95$ Å^{-1} (corresponding in

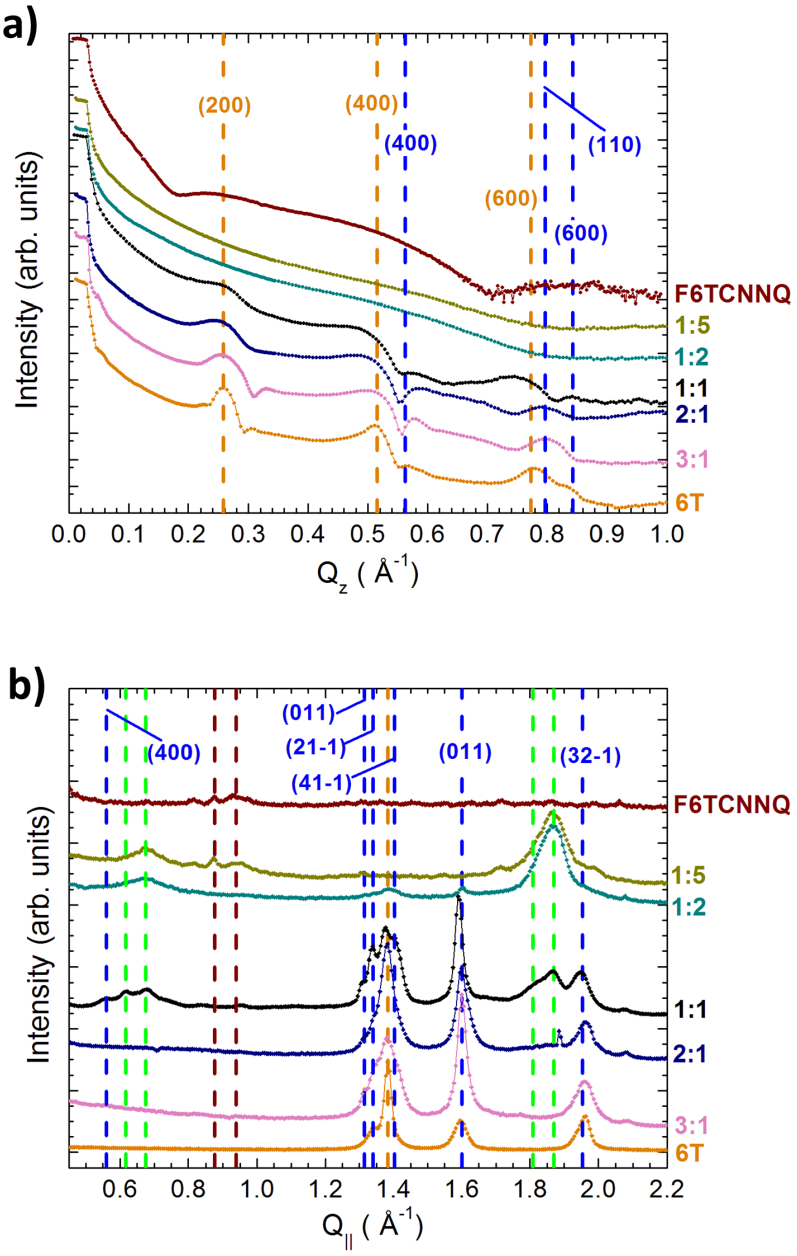

Figure 4.3: **a)** XRR and **b)** GIXD scans for D:A mixtures with 6T as donor and F6TCNNQ as acceptor mixed in different molar ratios. Vertical dashed lines show the peak attribution: 6T β polymorph (orange), 6T low-T polymorph (blue), F6TCNNQ (brown), 6T:F6TCNNQ D:A co-crystal (green). The Miller indices of the Bragg peaks for the 6T low-T polymorph are shown. The film thickness is 24 nm (pristine 6T), 27 nm (3:1), 25 nm (2:1), 72 nm (1:1), 23 nm (1:2), 27 nm (1:5), 31 nm (pristine F6TCNNQ).

real space to a π-π stacking distance of $3.5 - 3.2$ Å) is mostly concentrated in the region below $Q_z \approx 0.5$ Å^{-1}. This indicates that the direction of the π-π stacking of the D:A molecular components is roughly parallel to the substrate plane. For 6T:F6TCNNQ (Fig. 4.4b) the diffraction features with $Q_{||} = 1.80{-}1.95$ Å^{-1} appear as diffraction rings of uniform intensity, therefore it is not possible to deduce a preferred orientation of the π-stacking direction with respect to the substrate plane for this system. However, the elongated spot at $Q_{||} \approx 0.73$ Å^{-1}, $Q_z \approx 0.62$ Å^{-1} assigned to the co-crystal (marked with "CC") still indicates some preferred orientation. Due to the lack

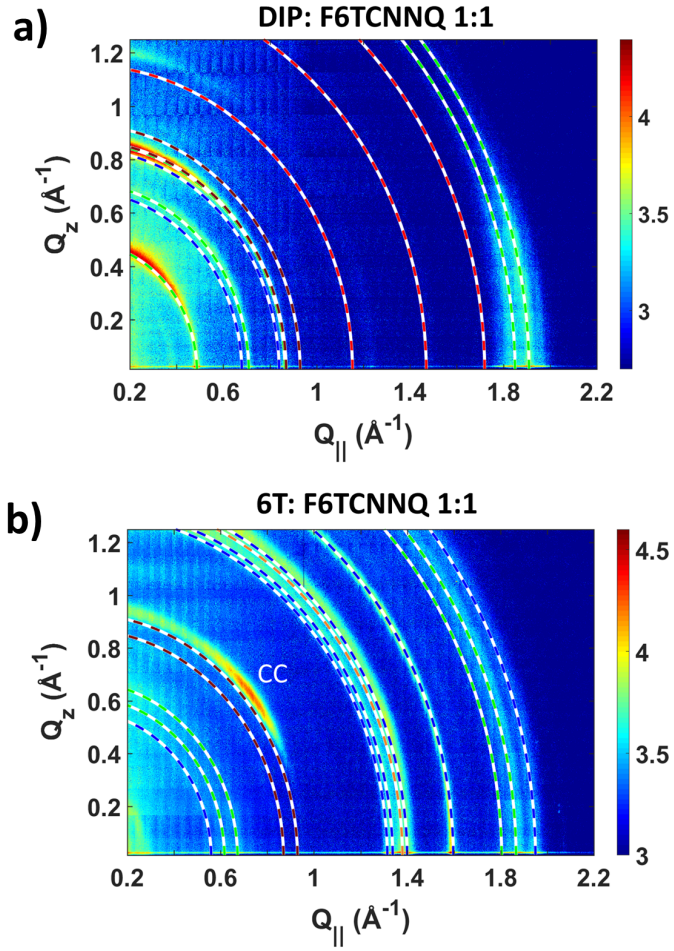

Figure 4.4: Reciprocal space maps of **a)** DIP:F6TCNNQ (thickness: 100 nm) and **b)** 6T:F6TCNNQ (thickness: 72 nm) 1:1 mixtures grown on native Si oxide. Color bars in logarithmic scale. Dashed lines indicate Debye-Scherrer rings whose total Q corresponds to the GIXD peaks in Fig. 4.2b and Fig. 4.3b respecting the same color code. For the 6T:F6TCNNQ 1:1 mixture, the diffraction feature exhibiting a maximum at $Q_{||} \approx 0.73$ Å^{-1}, $Q_z \approx 0.62$ Å^{-1} and marked "CC" is also assigned to the co-crystal, but its component along the $Q_z = 0$ Å^{-1} direction is too weak and therefore it is not marked in the corresponding GIXD scan of Fig. 4.3b.

of knowledge about the exact crystal structure of the two D:A complexes, indexing of the Bragg peaks is prohibitively difficult. Overall, we conclude that DIP:F6TCNNQ co-crystallites have a tendency for 2D powder-like texture with large mosaicity, whereas 6T:F6TCNNQ co-crystallites have a tendency for 3D powder arrangement. We tentatively explain this effect invoking the additional degrees of freedom of the longer 6T molecule, like flexibility as in the case simulated for para-sexiphenyl [267] or inter-annular torsion angles [268], compared to the shorter and stiffer DIP. This might involve a high concentration of defects incorporated in a growing 6T:F6TCNNQ molecular layer, rendering the growth of the subsequent layers more disordered and isotropic. Note that this mechanism can explain also the absence of film smoothing for the 6T:F6TCNNQ mixtures with nominal excess of 6T compared to the DIP:F6TCNNQ mixtures with nominal excess of DIP (Fig. 4.2a and 4.3a). However, such explanation is still on the level of hypothesis, which is intrinsically hard to proof.

Diffraction features belonging to crystallites of the pristine donor DIP are virtually absent in the reciprocal space map of the DIP:F6TCNNQ 1:1 mixture, whereas for the 6T:F6TCNNQ 1:1 mixture one can clearly recognize the features of pristine 6T crystallites. F6TCNNQ in pristine films is only weakly crystalline and we do not observe diffraction stemming from segregated F6TCNNQ

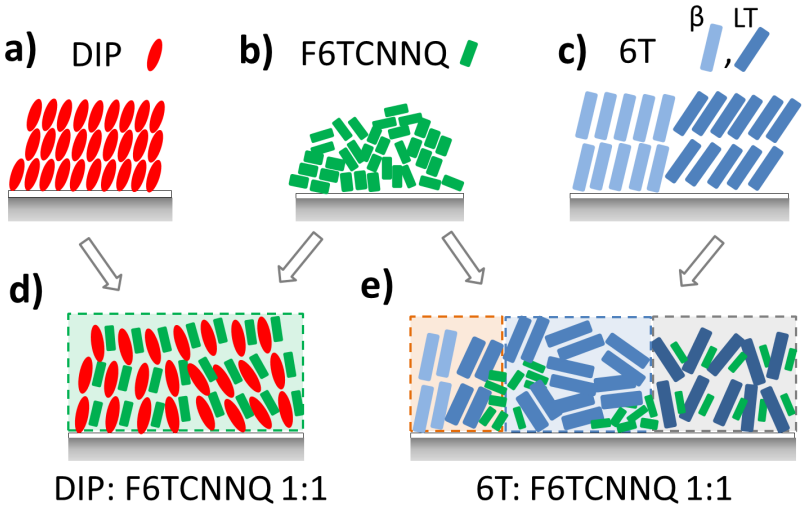

Figure 4.5: Sketches of the structure of the pristine compounds and D:A mixtures in thin films on native Si oxide. **a)** DIP, standing-up. **b)** F6TCNNQ, neither long-range crystalline order nor defined molecular orientation. **c)** 6T, standing up, with β phase and low-T phase exhibiting different tilt angle with respect to the substrate plane. **d)** DIP:F6TCNNQ 1:1, homogeneous distribution of D:A co-crystals with some mosaicity. **e)** 6T:F6TCNNQ 1:1, pronounced 3D powder-like texture (gray box); partial phase separation of pristine 6T and F6TCNNQ (orange and blue boxes) and randomly oriented 6T domains (blue box).

domains in the mixed films closer to a 1:1 mixing ratio. We speculate that, for 6T:F6TCNNQ, the difference in free energy between D:A co-crystallites and phase-separated domains of the pristine compounds is rather small due to the conformational degrees of freedom of 6T as highlighted above. Therefore kinetic effects [95] and inhomogeneities in the surface potential landscape, e.g. defects, might play a dominant role in determining which phase nucleates locally. The deduced structure and mixing behavior in the D:A mixtures of the compounds studied here are sketched in Fig. 4.5.

4.1.3 Optical characterization

From X-ray scattering data, an overall 2D-texture of the D:A co-crystallites in the equimolar mixtures of DIP and F6TCNNQ was deduced, whereas for 6T:F6TCNNQ 1:1 a more pronounced tendency to a 3D-texture was shown. Here, we show by means of UV-vis-NIR absorption spectroscopy the new, low-energy optical transitions appearing in the D:A mixtures , as well as their uniaxial anisotropy using spectroscopic ellipsometry.

4.1.3.1 New charge-transfer transitions

In Figure 4.6 we show the in-plane extinction coefficient k_{xy} obtained from transmission measurements in the UV-Vis-NIR region for the pristine compounds as well as for 1:1 mixtures grown on glass. We recall that, due to the normal incidence of the beam, only the in-plane component of k is probed (see Fig. 3.27).

The optical spectra of both equimolar mixtures exhibit highly convoluted profiles in the region above $\sim$ 2 eV, which cannot be trivially reproduced by a linear combination of the spectra of the pristine compounds. For DIP:F6TCNNQ 1:1, the maximum is located around 2.4 eV, whereas for 6T:F6TCNNQ 1:1 it is located approximately at 2.8 eV. Both types of mixtures exhibit new absorption bands that lie energetically below the optical gap of the pristine materials, the gap considered here as first absorption maximum. The position and integrated intensity of all new absorption bands for both material combinations are summarized in Tab. 4.1. It is possible to fit three new peaks for the DIP:F6TCNNQ 1:1 mixture and four for the 6T:F6TCNNQ 1:1 mixture

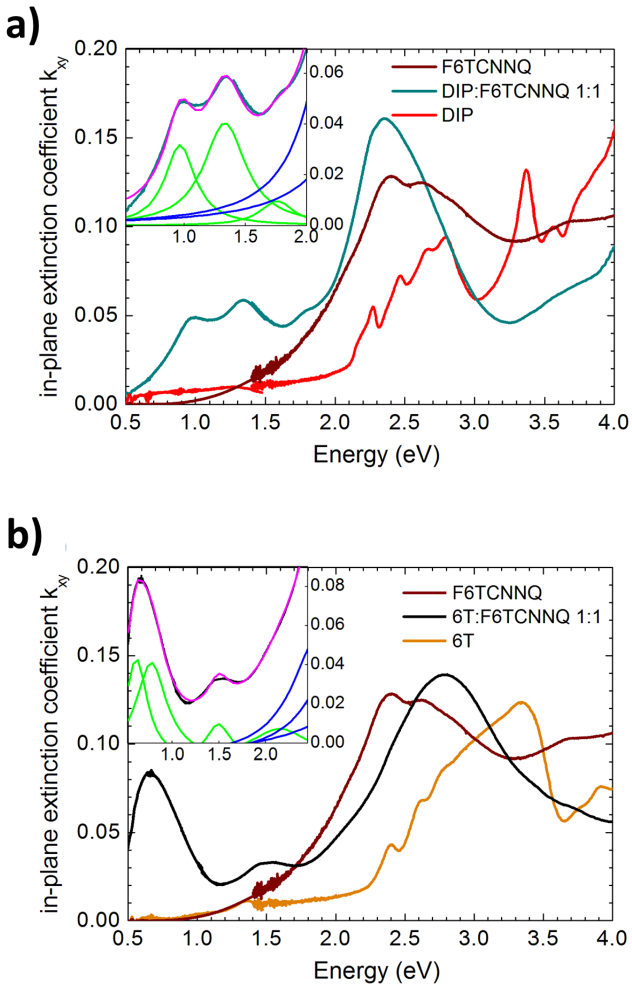

Figure 4.6: In-plane extinction coefficient of **a)** DIP (25 nm), F6TCNNQ (13 nm) and DIP:F6TCNNQ 1:1 (103 nm) and **b)** 6T (24 nm), F6TCNNQ (13 nm) and 6T:F6TCNNQ 1:1 (23 nm), all samples grown on borosilicate glass. The insets show Lorentzian fits to the new CT transitions in the 1:1 mixturesaccording to the following color-code: sub-bandgap transitions (green), transitions above the gap of the pristine materials (blue), global fit (magenta). The spectral portions measured with two different instruments are reported with some overlap around 1.5 eV. The downward bending of the spectral profiles of the pristine donor films around 1.5 eV is an artifact due to the grating and detector changeover in the spectrometer. Notice that the magnitude of k_{xy} for DIP [63, 269] and for 6T [270, 271] compares well with the literature.

arising below the bandgap of the pristine compounds. The shape, position and relative cross sections of the new sub-bandgap absorption features are specific to the respective D:A system. We assume that all these new transitions are related to excited state CT interactions. There is usually a close relationship between CT interactions in the excited state, as probed by UV-Vis-NIR absorption, and ground-state CT interactions. In order to quantify the degree of CT in the ground-state in D:A co-crystals, vibrational spectroscopy like Raman scattering [131, 272–274] or FTIR can be used. A quantitative determination of the degree of CT for DIP:F6TCNNQ using on FTIR spectroscopy is reported further in this thesis (see Results section 4.4). However, a detailed explanation of the mechanisms that govern D:A interactions as well as a quantitative determination of the degree of CT for both D:A pairs are beyond the scope of this section. Some general considerations may nevertheless help understanding qualitatively the observed spectral features.

Table 4.1: Energy position and integrated intensity of the new sub-bandgap absorption peaks in DIP:F6TCNNQ and 6T:F6TCNNQ 1:1 mixtures. The data were fitted using a sum of Lorentzian curves (Fig. 4.6a,b).

mixture	**energy [eV]**	**integr. intensity [10^{-2}]**
DIP:F6TCNNQ	0.97	1.5
	1.33	2.7
	1.76	0.5
6T:F6TCNNQ	0.61	1.5
	0.78	2.0
	1.49	0.5
	2.15	1.2

In general, upon formation of a D:A complex, the molecular orbitals of the isolated donor and acceptor are coupled to each other to some extent and therefore experience a perturbation in their shape and energy. Signatures of this coupling in optical spectra are: a) changes of the spectral profile above the optical gap of the pristine materials which cannot be reproduced by combination of the optical functions of pristine donor and acceptor according to effective medium models [160]; b) appearance of new transitions located below the optical bandgap of the pristine materials [48, 54, 57, 160]. For the two D:A systems studied in this work, case b) is evident. Keeping the acceptor material fixed (F6TCNNQ in our case), the characteristics of the new transitions depend on the energy and shape of the donor orbitals and on the details of the D:A coupling. These features differ significantly in DIP:F6TCNNQ compared to 6T:F6TCNNQ. As seen from Fig. 4.1, DIP is ∼30% longer than that of F6TCNNQ, whereas 6T is roughly twice the length of F6TCNNQ. Some DFT studies [192, 275] of the free energy of isolated CT complexes as a function of the interaction geometry including, e.g., relative shifts along the molecular backbone, showed that there is only one absolute conformational minimum, although several local minima are calculated. In our study, the 6T:F6TCNNQ complex might be present in more than one conformation due to non-equilibrium kinetic effects. Additionally, in Ref. [275] it is reported that the coupling of the 6T-HOMO with the F4TCNQ-LUMO determines the HOMO-LUMO gap for the minimum-energy conformation of the 6T:F4TCNQ CT complex. The nearly isotropic texture of the 6T:F6TCNNQ crystallites and the sub-structure of the strong lowest-energy optical transition in the 1:1 mixture (inset Fig. 4.6b) seem to agree with the presence of several conformations of the D:A complex.

Despite the intrinsic complexity of electronic coupling mechanisms in D:A pairs of molecular materials, in the framework of molecular doping we conclude that the origin of the lowest energy absorption features observed for the DIP:F6TCNNQ (0.97 eV) and the 6T:F6TCNNQ (0.61 and 0.78 eV) 1:1 mixtures resides in the transition of one electron from a strongly hybridized HOMO to a strongly hybridized LUMO of the new D:A supramolecular complex [48, 54]. We assume that the new transitions observed for these two D:A couples do not stem from fully ionized donor and acceptor species since there are no clear spectral signatures of the DIP cation (see SI of Ref. [162]) or 6T cation [276] together with the F6TCNNQ anion [53]. Therefore, the two material combinations studied here seem to belong to the category of D:A pairs of molecular semiconductors exhibiting partial CT in the ground state.

4.1.3.2 Anisotropy of the new transitions

In Fig. 4.7 we show the results obtained by means of VASE for the in-plane and out-of-plane component of the extinction coefficient, respectively k_{xy} and k_z, for the DIP:F6TCNNQ and 6T:F6TCNNQ 1:1 mixtures. Due to the experimental setup, the spectral range of VASE measurements is more restricted than for optical absorption measurements. To characterize the DIP:F6TCNNQ 1:1 sample we used the films deposited on native and thermal Si oxide. For the 6T:F6TCNNQ 1:1 sample we used the films deposited on native Si oxide and borosilicate glass. Reflection and transmission ellipsometry was carried out on the samples on Si oxide and glass, respectively. For the latter substrate, simple transmittance measurements with polarized light were also performed in order to increase the robustness of the fits. The roughness of the organic film is accounted for by including an EMA layer. The choice of the model was guided by AFM scans of

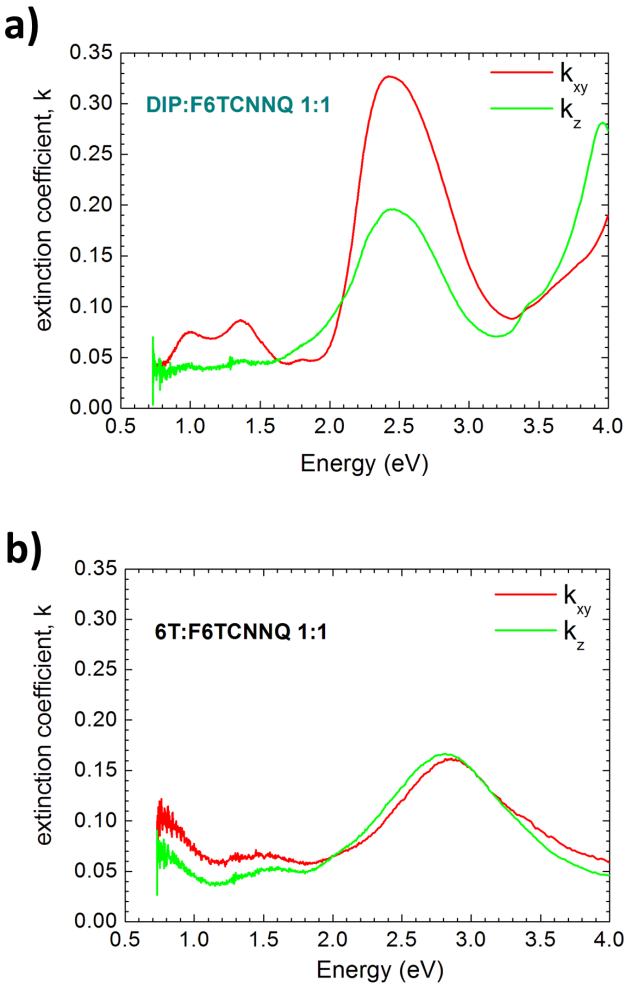

Figure 4.7: In-plane (k_{xy}) and out-of-plane (k_z) component of the extinction coefficient for **a)** DIP:F6TCNNQ 1:1 (103 nm) and **b)** 6T:F6TCNNQ 1:1 (23 nm) mixed films grown on Si oxide.

the film surface (see Fig. 6.4 in Appendix 6.1).

From Fig. 4.7, the anisotropy of the optical transitions can be inspected. In the region above ∼2 eV, the relative magnitude between k_{xy} and k_z is different for the two D:A systems, respectively. For the DIP:F6TCNNQ 1:1 film the in-plane component is stronger across almost the whole spectrum. For the 6T:F6TCNNQ 1:1 film in the same spectral region there is barely any difference between the two components. In the region where the new CT transitions are more clearly visible (i.e. below 2 eV) the in-plane component is stronger than the out-of-plane component for both mixtures, an exception being the weak band of DIP:F6TCNNQ at 1.76 eV. However, in the 6T:F6TCNNQ 1:1 mixture, the spectral shapes of the two components are very similar down to the lowest-energy transition, which is only partly visible. Conversely, k_{xy} in the DIP:F6TCNNQ 1:1 mixture exhibits pronounced maxima, whereas k_z is nearly flat. Overall, the optical anisotropy in the DIP:F6TCNNQ 1:1 mixture is more pronounced than in the 6T:F6TCNNQ 1:1 mixture, in agreement with the conclusions from X-ray scattering. The results for DIP:F6TCNNQ 1:1 on glass are in general agreement with the UV-Vis-NIR absorption measurements (see SI of Ref. [162]).

For the more uniaxially anisotropic DIP:F6TCNNQ 1:1 mixture, from X-ray scattering we concluded that the direction of the D:A π-stacking within the co-crystallites is roughly parallel to the substrate plane. In the present section we saw that the in-plane component of the new CT transitions is stronger than the out-of-plane component for this mixture. Therefore, we conclude that the TDM associated with CT transitions must be parallel to the π-stacking direction (Fig. 4.8),

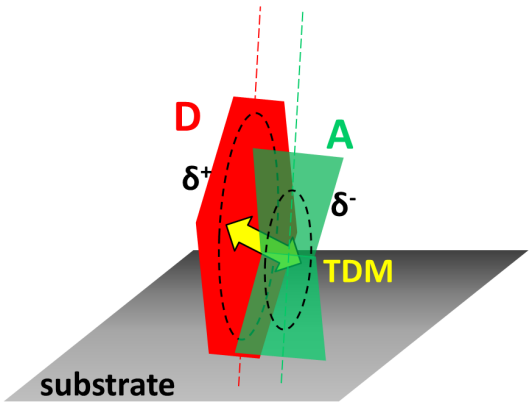

Figure 4.8: Sketch of the donor(D):acceptor(A) π-stacking direction and CT-TDM (yellow arrow) oriented parallel to the substrate for edge-on orientation. The "δ +/−" depict the partial CT in form of partial donation of an electron from the donor to the acceptor in the ground state. The dashed ellipsoids drawn inside the molecules represent the π-conjugation. The vertical dashed lines indicate the long molecular axis.

as already suggested for the D:A couple DIP:PDIR-CN_2 exhibiting only weak partial CT in the ground-state [157] (see also Fig. 2.16). This can be qualitatively explained by the strong CT between donor and acceptor molecule, that allows strong dipoles along the π-stacking direction in both the ground state and the excited state. Although the 6T:F6TCNNQ 1:1 mixture does not exhibit a degree of structural anisotropy that allows one to make conclusions about the direction of the D:A π-stacking with respect to the substrate plane, an analogous picture for the orientation of the TDM seems likely.

4.1.4 Summary of the results and possible applications

In conclusion, we studied two novel D:A systems of small-molecular OSCs, namely DIP:F6TCNNQ and 6T:F6TCNNQ. We speculate that the differences in crystalline texture and phase-composition between DIP:F6TCNNQ and 6T:F6TCNNQ equimolar mixtures, respectively, can be ascribed to the different conformational degrees of freedom of the donors. Formation of a D:A co-crystal is observed for both systems. One main driving force for co-crystal formation is the strong CT interaction between donor and acceptor due to the energy difference between HOMO and LUMO levels. The strength of the CT interaction for these systems is further evidenced by optical absorption measurements that reveal pronounced low-energy absorption features in the D:A 1:1 mixtures, which are absent in the pristine compounds.

For the more uniaxially ordered DIP:F6TCNNQ equimolar film, study of the optical anisotropy reveals that the in-plane component of the extinction coefficient of the new CT absorptions is stronger than the out-of-plane component. For the 6T:F6TCNNQ 1:1 mixture exhibiting a mostly 3D powder-like texture, the optical anisotropy is less pronounced. This supports a picture in which the CT transition dipole moment is oriented along the D:A π-stacking direction. We suggest such a scenario to be rather general for D:A pairs of planar molecular semiconductors forming supramolecular complexes. Therefore, the two D:A pairs studied here constitute an example of CT complexes with strong coupling that, by virtue of their low-energy transitions might be employed as light-harvesting functional materials in NIR detectors.

4.2 Roughness evolution in DIP:F6TCNNQ mixtures. An *in situ*, real-time study using X-ray reflectivity [2]

Binary D:A mixtures of molecular semiconductors represent technologically important systems. The knowledge of surface roughness during film growth as function of thickness *and* D:A mixing ratio is relevant for devices due to: a) possible thickness-dependent structural transitions [109, 236], b) the requirement to tune the extent of the interface area between different materials, c) the possibility to realize multilayer films with minimized interface roughness, d) the fact that, in OFETs, the conducting channel extends only in the first two monolayers of the organic layer [134]. These all represent important technological aspects which determine the optimal film thickness and D:A mixing ratio for the given application.

In several works on thin films of OSCs, XRR curves have been measured in real-time during film growth in order to fit the reflectivity at multiple points beyond the more conventional anti-Bragg point [110, 171, 236]. By doing so, information about the dependence of surface roughness on film thickness is gained. In one work dealing with mixtures of DIP with the Buckminster-fullerene (C_{60}), the time-evolution of the anti-Bragg oscillations together with the diffused scattering at low angle have been measured, and from the latter the inter-island distance as function of time has been calculated [265]. There, however, no quantitative evaluation of the film roughness as function of time has been carried out. In another work [62], the roughness evolution of equimolar PEN:PFP mixtures has been calculated by fitting real-time XRR data using the Parratt formalism. To the best of our knowledge, this represents the only quantitative real-time XRR study carried out on binary mixtures of OSCs.

4.2.1 Deposition of DIP:F6TCNNQ mixtures with DIP excess

In this work, we intend to expand the space of explored material combinations and mixing ratios. Therefore, we grow D:A mixtures with DIP as donor and F6TCNNQ as acceptor *via* OMBD in a portable vacuum chamber which allows to carry out *in situ* experiments at synchrotron beamlines [223] (Fig. 3.16a). We base on the results obtained post-growth in the previous Results section 4.1 which show that, for DIP:F6TCNNQ mixtures with DIP excess in a thickness range around 10-20 nm, the smoothest films can be prepared. We therefore grow mixtures with systematic excess of DIP in order to: a) be able to follow the evolution of nearly undamped Kiessig oscillations, b) identify the first Bragg peak of the excess DIP phase, which would otherwise disappear in mixtures with equimolar or higher F6TCNNQ content (see Fig. 4.2a).

X-ray reflectivity scans were measured *in situ* and in real-time during the growth of three DIP:F6TCNNQ mixtures with a molar ratio of 6:1, 4:1 and 2:1, respectively, on native Si oxide substrates kept at 40°C. The total film thickness and growth rate for these films were 17.5 nm and 0.14 nm/min, 14.0 nm and 0.14 nm/min, 17.5 nm and 0.18 nm/min. For each mixing ratio, the equivalent deposited amount DIP is easily calculated using the measured growth rate. The growth rates were measured by means of a carefully calibrated QCM. The materials were calibrated separately, DIP by means of XRR and F6TCNNQ by means of AFM. Measurement of each XRR curve took 150 s, which means that an average of ~ 4 XRR scans are measured for each equivalent DIP monolayer (ML), allowing for sub-ML resolution of the growth processes.

4.2.2 Fits of real-time data of binary systems

We carried out a quantitative fit of the real-time XRR curves using two different approaches. The first approach consists in analyzing the evolution of the reflectivity as function of time at several Q_z points. The reflectivity profiles so extracted exhibit peculiar "growth oscillations" which arise from the nucleation and gradual filling of new layers. These growth oscillations at fixed Q_z have been fitted by means of the Cohen [233] and Trofimov [234] growth models, respectively, combined with the kinematical approximation to treat the scattering of X-rays (see Methods section 3.3). The second approach consists in fitting each XRR curve measured during film growth using the Parratt formalism (see Methods section 3.3).

[2] Based on G. Duva et al., in preparation

One aim of this work is to test the reliability of the above models for treating relatively complicated systems such as D:A mixtures in which co-crystal formation is observed with phase separation of the excess phase, as it is the case for DIP:F6TCNNQ with excess DIP. Once their reliability in delivering the same qualitative information is assessed, we choose the model which represents the best compromise in terms of accuracy, on one side, and simplicity of implementation on the other. We then carry out a further analysis of film surface roughness evolution and growth mechanisms as function of D:A mixing ratio using the chosen model.

The Cohen model was used as first, simple approach. It was implemented using a set of custom-written Matlab scripts. Unfortunately, a global fit employing the Cohen model does not allow to obtain a reasonable agreement to the data in the entire thickness regime. This is possibly due to a gradual structural reorganization of the DIP unit cell during the growth of the first three monolayers [109, 118, 171]. To be able to reproduce the data, we reduced the fitted range only up to the third equivalent DIP ML (low-thickness regime). Note that, for the growth of OSCs, this thickness regime is of particular interest due to possible structural changes, as mentioned above for DIP, or also to re-orientation of the molecular units [263, 277]. The Trofimov model was implemented using the software *Trofit* [278] adapted for fitting multiple Q_z points simultaneously [3]. The Trofimov model allows to fit the data in the entire thickness regime, as discussed further below.

The Parratt formalism was implemented using the software *Motofit* [279] for the IgorPro package (WaveMetrics Inc.), which makes use of the Abeles matrix formalism for stratified media and assumes the Névot-Croce factor to treat interface roughness (Eq. 3.9). The Parratt and Abeles recursive algorithms lead to identical results [163, 226]. In the following, we will therefore refer to "Parratt formalism" as it represents the most common denomination. The Parratt formalism for treating multiple scattering in stratified media allows to fit an arbitrary XRR profile and obtain the corresponding electron density as function of film thickness, $\rho_e(z)$ (see also Fig. 3.15c). The total coverage of each layer was calculated from the ratio between the maximum electron density of a given layer, $\rho_{e,n}$, and the maximum electron density of the first layer, $\rho_{e,n=1}$, the latter taken from the fully grown film.

The fits carried out with the methods outlined above deliver qualitatively similar results, although quantitative differences emerge. We first illustrate the results obtained using the different methods. We then discuss the reasons for the differences between the results and, finally, we choose a model to guide the interpretation of the roughness evolution as function of DIP:F6TCNNQ mixing ratio.

4.2.2.1 Results for all models

The data analysis carried out in this work involves several steps, which in the end led to the choice of the Trofimov model for the further discussion of roughness evolution and other aspects of film growth. To illustrate this, we show in Fig. 4.9a a typical data-set of XRR scans measured *in situ* and in real time during the growth of the DIP:F6TCNNQ 4:1 mixture. The same kind of data-sets for all DIP:F6TCNNQ mixtures are reported in Fig. 6.5 of Appendix 6.2. The lateral axis of the upper plot in Fig. 4.9a indicates the number of equivalent DIP monolayers grown considering the DIP:F6TCNNQ molar ratio together with the measured total growth rate. In Fig. 4.9b, the extracted reflectivity-*vs.*-time profiles are plotted against the number of *total* growing ML, which at the anti-Bragg point allows to visually follow the filling of each molecular layer [110]. Already by visual inspection of the fits for the low-thickness regime we see that the Trofimov model is more capable of reproducing the experimental trend of the reflectivity *vs.* total layer thickness.

[3] The fits were performed by Linus Pithan, European Synchrotron Research Facility (ESRF)

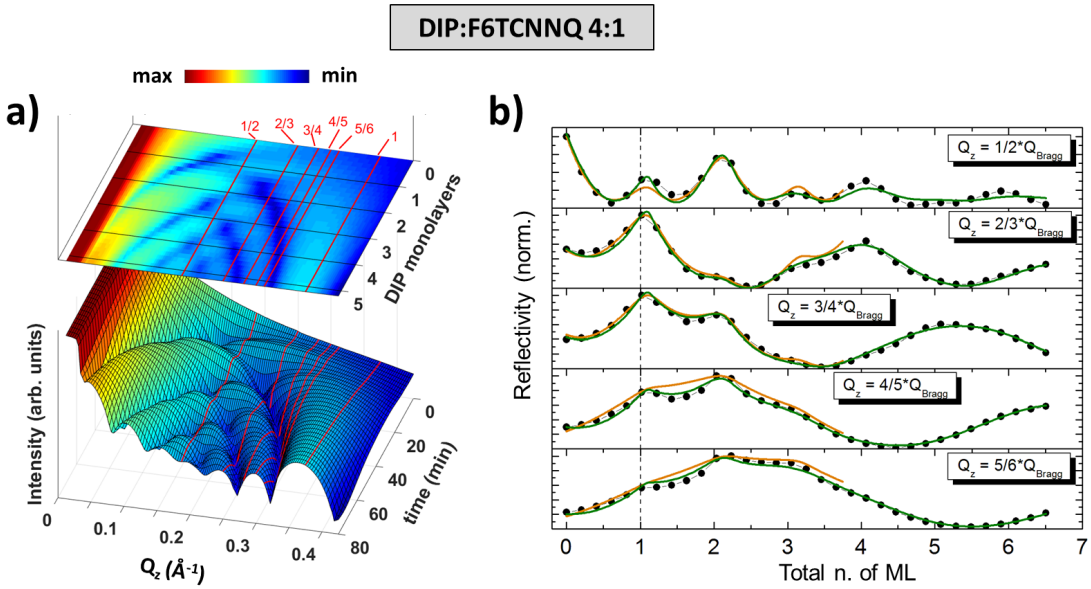

Figure 4.9: *In situ*, real-time XRR data for the DIP:F6TCNNQ 4:1 mixture. **a)** Time evolution of the reflectivity profile. The red lines indicate the fractional points in units of $Q_{z,Bragg}$ at which the time-evolution of the reflectivity has been extracted. A value for $Q_{z,Bragg} = 0.375$ Å^{-1} is used. The curve at time "0" corresponds to the first curve measured after exposing the substrate to the molecular flux. In the lower 3D plot, each "pixel" along the time axis corresponds to one experimentally measured curve. **b)** Extracted profiles at the anti-Bragg point ($Q_z = 1/2 \cdot Q_{Bragg}$) and other fractions of $Q_{z,Bragg}$, as indicated in the plots. The fits are superimposed to the experimental data: Cohen fits in the low-thickness regime (orange), Trofimov fits in the full range (green). Fits of the monotonically increasing intensity of the Bragg peak ($Q_z = Q_{Bragg}$) are not shown. The vertical dashed line corresponds to the first total grown ML measured with the thickness monitor.

The real-time XRR data presented in Fig. 4.9a were additionally fitted using the Parratt formalism (Fig. 4.10a). A multi-layer model was set up in order to reproduce the data (see Fig. 6.7 in Appendix 6.2). To minimize the number of free parameters, we impose boundary conditions for the electron density, the inter-layer roughness and the monolayer thickness. The fits allow to extract the electron density, ρ_e, as function of z for each experimental XRR curve (Fig. 4.10b). The complete set of Parratt fits for each experimental XRR curve for all three DIP:F6TCNNQ mixtures are reported in Fig. 6.8 of Appendix 6.2.

The average ρ_e has the following values expressed in scattering length density (electron density): 9.5×10^{-6}Å^{-2} (0.337 Å^{-3}) for the 6:1 mixture, 8.85×10^{-6}Å^{-2} (0.314 Å^{-3}) for the 4:1 mixture (see Fig. 4.10b) and 9.55×10^{-6}Å^{-2} (0.339 Å^{-3}) for the 2:1 mixture. The non-monotonic trend of the average ρ_e as function of mixing ratio seems the result of two competing effects: a) increasing out-of-plane film disorder with increasing amount of F6TCNNQ which leads to a less compact film and thus lower ρ_e; b) higher ρ_e of the F6TCNNQ units containing F and N atoms, compared to DIP containing only C and H.

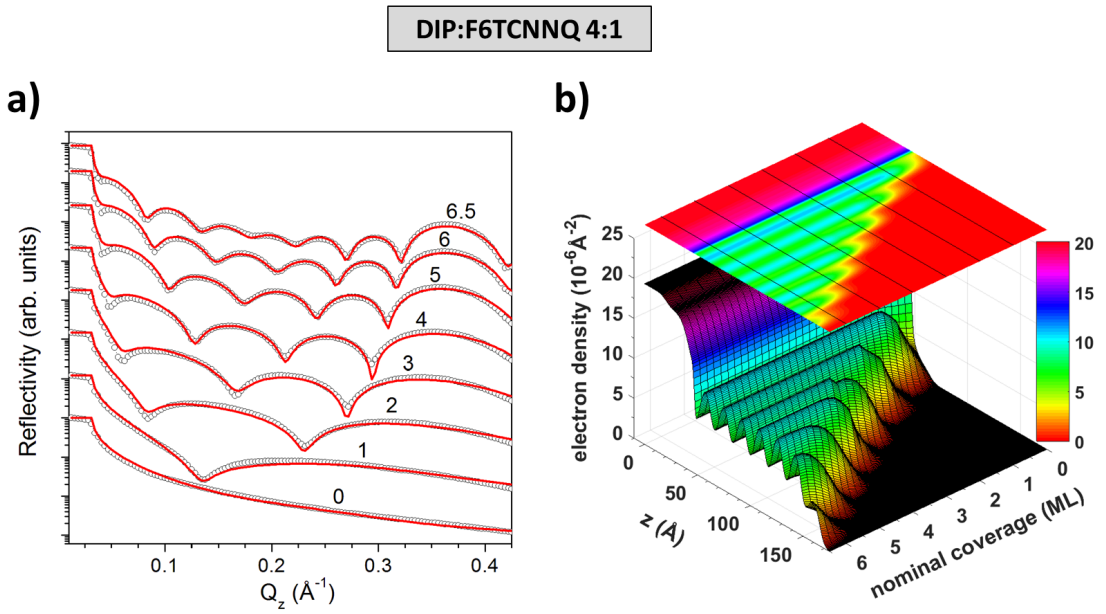

Figure 4.10: **a)** Selected experimental XRR scans (black dotted profiles) and Parratt fits (red profiles) for the DIP:F6TCNNQ 4:1 mixture. The curves were vertically shifted for clarity. Each experimental XRR profile corresponds to the nominal layer coverage indicated. **b)** Electron density as function of the z-coordinate perpendicular to the substrate and of the nominal layer coverage. Note the color scale for the electron density. The Si substrate is located at $z = 0$.

The layer coverages extracted with the Cohen and Trofimov models, and with the Parratt formalism, respectively, for the 4:1 mixture are shown in Fig. 4.11a. Modeling of the layer coverages $\theta_n(t)$ allows to calculate the interface roughness (or root mean-square roughness, RMS) as function of time, RMS(t), *via* the relationship [113, 235]:

$$\mathrm{RMS}(t) = \sqrt{\sum_{i=1}^{\infty}(\theta_i - \theta_{i+1})(i - C_{tot})^2} \tag{4.1a}$$

$$C_{tot} = \sum_{i=1}^{\infty}\theta_i \tag{4.1b}$$

The quantity C_{tot} in Eq. 4.1 is the time-dependent total layer coverage. The adimensional RMS(t) obtained with Eq. 4.1 is expressed in units of the ML thickness of DIP, d_{DIP}. As pointed out above, RMS(t) is relevant for material interfaces in organic heterostructures embedded in optoelectronic devices. Extrapolation of the interface roughness as function of time *and* D:A mixing ratio represents, therefore, the main result of this work. As it can be seen from Fig. 4.11a, the θ_n extracted with the different models match well with each other. The curves $\theta_{n=2-5}$ obtained from the Parratt fits saturate slightly above 0.9 instead of 1, which is due to the molecular layer in contact with the substrate having a slightly higher electron density than the upper layers (Fig. 4.10b).

The interface roughness calculated for the 4:1 mixture by means of Eq. 4.1 with all models is shown in Fig. 4.11b. Up to a nominal coverage of 2.5 ML, all models are in substantial agreement. In this thickness range, the main difference is that the "dip" in the RMS around completion of the 2^{nd} ML is more pronounced in the Cohen and Trofimov fits than in the Parratt fit. Concerning the differences between the two growth models between 2.5 and 3.5 nominal ML, the Cohen model exhibits an additional dip around completion of the 3^{rd} ML, which is absent in the Trofimov model. Such discrepancy can be explained by the fact that the Cohen fits are less accurate towards the end of the fitted range due to the artificially restricted dataset. The curves start to deviate substantially starting from the $\sim 3^{rd}$ ML, with the RMS from the Parratt fits being significantly larger, up to

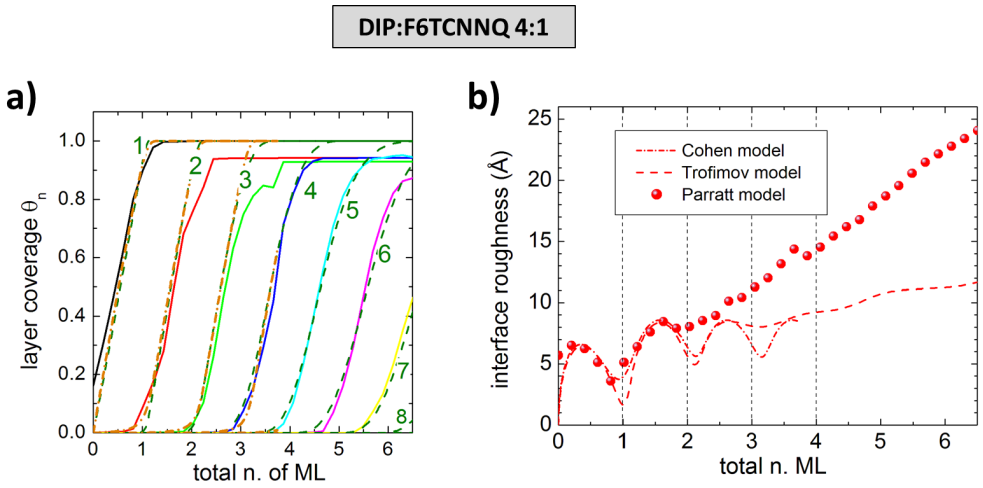

Figure 4.11: **a)** Layer coverage and **b)** interface roughness calculated with the Cohen, Trofimov and Parratt models. respectively. In **a)**, the curves obtained from the Cohen fits are orange dash-dotted lines, those from the Trofimov fits are green dashed lines with the layer indexes n indicated, those from the Parratt fits are continuous colored lines. In **b)**, the vertical lines correspond to the deposition of the first 4 nominal ML.

double the RMS from the Trofimov fits for the largest nominal coverage. This large discrepancy has two origins. In part, it is provoked by the saturation of layer filling at 0.9 for $\theta_{n=2-5}$ as discussed above (Fig. 4.11b). Another reason is that the growth models and the Parratt fits, respectively, are sensitive to different portions of the XRR curves. In particular, the Parratt fits include the Q_z region where the Kiessig oscillations appear (see also Fig. 3.15b), therefore they are expected to represent more closely the roughness of the *entire* film.

Very similar results are obtained for the 6:1 and the 2:1 DIP:F6TCNNQ mixtures (see Fig. 6.10 in Appendix 6.2). Overall, there is good quantitative agreement between all models up to a nominal coverage of ∼2.5 ML. Significant deviations start from the 3^{rd} ML, with the roughness being larger for the Parratt fits than the Cohen and Trofimov fits. Despite the quantitative discrepancies in this thickness regime, close qualitative similarities in the trends of the RMS curves as function of D:A mixing ratio are recognized. This gives a strong hint that systematic errors, arising from the assumptions within each model, do not affect the general conclusions of this work. This allows to carry out a comparative study between the films with different D:A mixing ratio.

4.2.2.2 Reasons for the differences between the fits

We start by discussing the differences between the fits using the Cohen and the Trofimov model, respectively. Compared to the Cohen model, the Trofimov model can better reproduce the entire dataset (see Fig. 6.5 in Appendix 6.2). It is a question, whether the improved fits are due to the number of parameters involved or to the better ability of the Trofimov model to capture growth processes [235]. We note that, to judge the latter aspect, a comparison with *ex situ* AFM data of film morphology to calculate layer coverages might be misleading due to the observed de-wetting behavior of DIP [280].

We further consider statistical aspects of the fits, namely, the number of free parameters *per ML* involved in the fits. The Cohen model features one free parameter, k_n, for the first molecular ML in direct contact with the substrate ($n = 1$) as well as for each subsequently deposited ML (Eq. 3.11). The Trofimov model features three parameters for the first ML ($n = 1$), namely R_1, R_2 and $\theta_{cr,1}$ (Eq. 3.12). In the Trofimov model we imposed $R_n = R_{n+1}$ for $n > 1$, in practice distinguishing only between molecules landing on the bare substrate and on an already formed organic layer. Therefore, already for the second ML ($n = 2$), the only free parameter not coupled to any previously defined parameter is $\theta_{cr,2}$, and this holds for each subsequent ML. A full statistical analysis evaluating the effect of the different coupling of layer coverages and kinetic parameters in

the systems of differential equations (Eqs. 3.11 and 3.12) exceeds the purposes of this work. Overall, the number of fitting parameters for the Trofimov model is clearly higher only for what concerns the first ML. This seems in part to explain the better agreement to the data in the low-thickness regime. For larger film coverages, there are no major difference with the Cohen model for what concerns the number of free parameters per ML. Therefore, we suggest that the Trofimov model is more able to capture the interplay between itra- and inter-layer molecular transport [113, 237] that determines nucleation rates and lateral island growth.

Here we focus on the differences between the results obtained with the kinematical approximation combined with the growth models, and the Parratt exact method, respectively. The presence of two different phases within a growing film, namely, pristine DIP crystals and D:A co-crystals, has a different impact on the measured reflectivity depending on the Q_z-region considered. In the region at lower Q_z, say, approximately between the total reflection edge and the anti-Bragg point, the Kiessig oscillations dominate the reflectivity signal, therefore the data are more sensitive to the spatial distribution of pristine DIP and co-crystal domains and are representative of the *average* reflectivity from the different phases. In the Q_z region between the anti-Bragg point and the first DIP Bragg peak, the Laue oscillations and the Bragg peak itself are given only by the isolated DIP domains scattering in a coherent fashion [169]. This implies that the Parratt fits are more sensitive to the phase heterogeneity of the D:A mixtures than the fits employing the kinematical approximation.

The above outlined differences in the models employed explain the quantitative deviations in the results obtained. However, the results for the RMS as function of D:A mixing ratio exhibit the same trends independent of the method. This allows to choose the Trofimov model to discuss the different behaviors of the RMS as function of D:A mixing ratio in the films. Indeed, such model represents the best compromise to keep the number of parameters reasonably low, allows ease of implementation and offers insights into the kinetics of film growth in both the in-plane and out-of-plane directions [237].

4.2.2.3 Roughness evolution *vs.* D:A mixing ratio

The Trofimov model is used to extract information about the growth mechanisms for the three DIP:F6TCNNQ mixtures studied here. In Fig. 4.12, we compare the results for the critical layer coverage, θ_{cr}, and the interface roughness (Eq. 4.1), which provide a description of inter-layer transport phenomena. The roughness evolution of a pristine DIP film obtained in Ref. [281] using the Parratt formalism is also shown in Fig. 4.12 for comparison.

Overall, $\theta_{cr,n}$ exhibits a decreasing trend with increasing film thickness. The 2:1 film exhibits the highest $\theta_{cr,n=1,2}$, which then becomes lower than the 6:1 and 4:1 films for $n > 2$. We recall that a value of θ_{cr} close to 1 indicates that one layer is nearly totally full before the one on top starts forming. Therefore, in a simplified view, having $\theta_{cr} \approx 1$ is equivalent to having a low ES barrier and consequently efficient inter-layer transport. This denotes an enhanced layer-by-layer growth character for the first two ML in the 2:1 mixture. Instead, from the 2^{nd} ML on, the 4:1 and 6:1 mixtures exhibit a more pronounced layer-by-layer growth behavior compared to the 2:1. This trend of $\theta_{cr,n}$ reflects in the behavior of the RMS, which, in the region below 2 ML, shows dips reaching the lowest roughness values for the 2:1 mixture, thus indicating the highest layer-filling ability. In this thickness range, the worst layer-filling ability is found for the 6:1 mixture, i.e. the mixture with the highest DIP content, where the dips indicative of a layer-by-layer growth fashion are the least pronounced. For all mixtures, the layer filling efficiency starts to decrease already from the 2^{nd} monolayer, as indicated by the less pronounced dip around 2 ML compared to the dip at 1 ML.

As it can be seen from Fig. 4.12, the films start to roughen pronouncedly from the $\sim 2^{nd}$ ML on. The absolute RMS values stay similar for all three mixtures until a total film thickness of ~ 6 ML is reached. Within this thickness range, only the RMS for the 4:1 mixture clearly exhibits further oscillations, although they are damped. The 6:1 mixture also shows such modulations, but they are damped out earlier compared to the 4:1 mixture. The 2:1 mixture does not show RMS oscillations after completion of the 2^{nd} ML. These trends indicate that a growth fashion resembling layer-by-layer persists only for the 4:1 mixture, at least up to the largest thickness investigated in our work for this sample. Interestingly, extrapolating the RMS of the 4:1 mixture up to a total thickness of 8 ML, the 2:1 shows in the end the highest roughness. The pronounced layer-by-layer

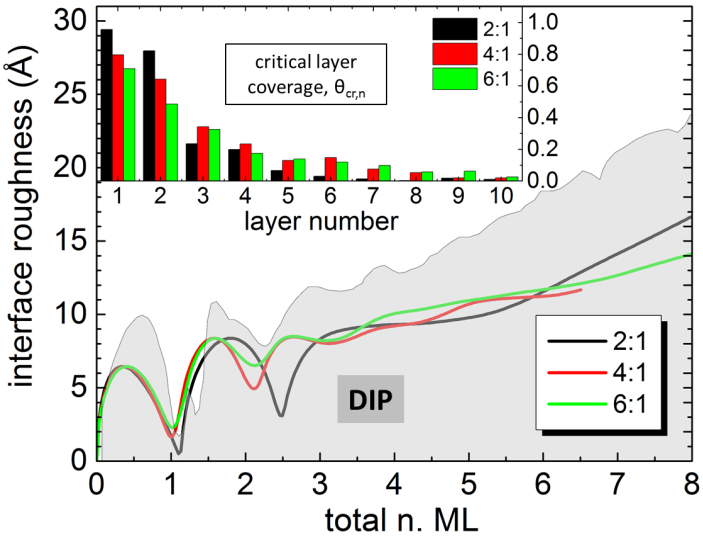

Figure 4.12: Evolution of interface roughness calculated with the Trofimov model as function of nominal layer coverage. The inset shows the critical layer coverages extracted from the fits (see Eq. 3.12). The gray-filled curve has been reproduced from Ref. [281] and was obtained from the Parratt fit of XRR curves for a pristine DIP film grown in very similar conditions.

growth fashion exhibited in the earlier growth stages is therefore completely "lost" after a thickness threshold of ∼6 ML.

Remarkably, all the mixtures of DIP with F6TCNNQ studied in this work are smoother than pristine DIP grown in very similar conditions (Fig. 4.12). Notice that, although the RMS for DIP shown in Fig. 4.12 has been obtained from fits employing the Parratt formalism, deviations from the Trofimov model are expected to be less significant for pristine films [236]. Refs. [95, 282] contain additional examples of mixing-induced film smoothing in D:A bulk heterojunuctions in presence of excess donor species. In these works, however, the mixed donor and acceptor exhibited phase separation. The fact that, in our work, the same smoothing effect is observed *also* in mixtures of strongly interacting D:A pairs for which co-crystal formation is observed, might help to shed more light on the actual mechanisms that lead to smoothing.

4.2.3 Growth scenarios in heterogeneous crystalline systems

We propose two possible mechanisms to explain our observations for the mixed films studied here. In particular, we try to explain the observation that the mixture with the highest F6TCNNQ content exhibits the most pronounced layer-by-layer growth mode in the early growth stages, but the highest roughness in the later growth stages.

We first suggest the following scenario. In the mixed films, F6TCNNQ molecules located at the edges of DIP terraces act as "defects" [267, 283], lowering the ES barrier for inter-layer diffusion (Fig. 4.13) and thereby leading to enhanced layer-by-layer growth. Notice that F6TCNNQ molecules are only "temporarily" included as defects before a favorable conformation for the nucleation of the DIP:F6TCNNQ co-crystal is found. This picture explains both the overall lower surface roughness of the mixtures compared to pristine DIP (Fig. 4.12) and the trend of roughness evolution *vs.* mixing ratio in the low-thickness regime. However, this mechanism alone does not provide a solid explanation for the trend inversion at higher thicknesses.

In order to shed more light on the mechanisms underlying the roughness evolution as function of thickness and D:A mixing ratio, one has to take into account the following effects connected with the increasing amount of F6TCNNQ in the mixtures (Fig. 6.11 in Appendix 6.2): a) increase of the relative amount of co-crystal compared to pristine DIP, b) reduction of the coherent size of the pristine DIP crystallites. We therefore suggest a mechanism that takes into account these

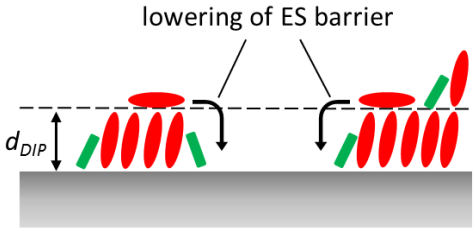

Figure 4.13: Sketch of the inclusion of F6TCNNQ molecules at the step-edges of pristine DIP crystallites in DIP:F6TCNNQ mixed films, which causes lowering of the ES barrier. The F6TCNNQ molecules act as "defects" until a conformation for nucleation of the DIP:F6TCNNQ co-crystal is found. The thickness of a DIP ML, d_{DIP}, is shown.

observations (Fig. 4.14). We consider the simplest scenario in which D:A co-crystals nucleate only on top of the bare substrate and not on already formed DIP terraces.

One has to consider the different rate at which a pristine DIP (r_z^{DIP}) and a DIP:F6TCNNQ crystal (r_z^{CC}), respectively, grow in the z direction. When co-evaporating DIP and F6TCNNQ, we assume that D:A co-crystallites nucleate at a later stage in the confined spaces between DIP crystallites. This is consistent with the mechanism suggested above for the initial inclusion of F6TCNNQ molecules at step-edges and consequent lowering of the ES barrier. Therefore, in the sub-ML regime, the DIP molecules that land on top of already formed grains or terraces in layer 1 diffuse downwards with high probability due to the presence of F6TCNNQ molecules at the step-edges (Fig. 4.13). A fraction of the landing molecules will not diffuse downwards and will thereby contribute to increase the coverage of layer 2. At this stage, a D:A co-crystal nucleates in the confined interstices between DIP crystallites.

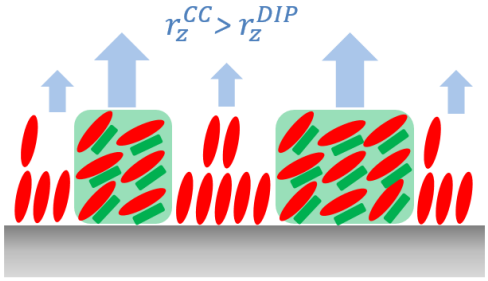

Figure 4.14: Illustration of the proposed smoothing mechanism during the initial growth stages of D:A mixtures where co-crystal formation is observed. The D:A co-crystals nucleate in the interstices between DIP grains. This nucleation of co-crystal is assumed to happen at a delayed stage compared to the nucleation of DIP grains. The vertical blue arrows represent the growth rate of the DIP and D:A co-crystal grains in the direction perpendicular to the substrate surface, respectively r_z^{DIP} and r_z^{CC}, with $r_z^{CC} > r_z^{DIP}$. The slightly different orientations of the single D:A complexes represent the higher mosaicity of the co-crystals compared to DIP crystallites [162]. The delayed nucleation of the co-crystal and the different vertical growth rates between the two crystalline phases can explain the observed trend of interface roughness as function of D:A mixing ratio, where a higher F6TCNNQ content leads to a higher amount of co-crystal and to a smaller lateral coherent size of the DIP grains.

The lateral growth of the pristine DIP domains is faster compared to their vertical growth due to the enhanced inter-layer transport by F6TCNNQ admixing (Fig. 4.13). The vertical growth of the D:A co-crystal might be considerably faster than that of DIP due to the characteristics of the surface potential of the exposed crystal facets, respectively. Overall, a D:A co-crystal grows in the z direction *faster* than the pristine DIP crystals, i.e.for the vertical growth rates r_z it holds $r_z^{CC} > r_z^{DIP}$. With the assumption of a delayed co-crystal nucleation, the proposed mechanism is

consistent with the increasing amount of D:A co-crystals and the concomitant reduction of coherent grain size of DIP as the amount of F6TCNNQ in the mixtures increases (Fig. 6.11 in Appendix 6.2).

The smoothing mechanism here proposed might be similar to the "filling" mechanism proposed for planar heterostructures of PFP on DIP and PEN on PFP [281]. However, in our case the filling mechanism works only at low coverages because at some point the vertical growth rate of the co-crystal takes over and causes the film in 2:1 molar ratio to roughen faster than the films with lower F6TCNNQ content. This scenario seems confirmed by inspection of the morphology of ∼20 nm thick DIP:F6TCNNQ mixtures on SiO_x-coated Au (see Fig. 6.17 in Appendix 6.4). The corresponding AFM scans for the 2:1 mixture show some tall islands "sticking out" of a smooth, homogeneous background, where the taller islands contain D:A co-crystals with pronounced mosaicity. Instead, the surface morphology of the 4:1 mixture completely resembles the smooth background of the 2:1 mixture, with no taller islands visible.

We speculate that the mechanism outlined above is rather general for 2D-textured, polycrystalline films where two different crystalline materials, or the same material but exposing different facets in the z direction, nucleate and grow in the vertical direction with different rates due to a different surface potential of the growing crystallites.

4.2.4 Summary of the results and possible applications

In summary, we have carried out a systematic study on bulk heterostructures featuring DIP as donor and F6TCNNQ as acceptor in three different D:A mixing ratios, namely, 6:1, 4:1 and 2:1. This material combination features formation of a D:A co-crystal with phase separation of the excess DIP [162]. The study includes real-time X-ray scattering experiments carried out *in situ* during film growth to elucidate the dependence of film roughness on thickness *and* D:A mixing ratio.

Several theoretical approaches have been combined to extract the interface roughness, or RMS, from the full data-set of time-dependent XRR curves measured for each D:A mixing ratio. In particular, the Cohen and Trofimov growth models within the framework of the kinematical approximation, and the Parratt formalism, respectively, have been employed. The sensitivity of each method to different portions of the XRR spectra leads to quantitative differences in the roughness evolution. However, a similar trend of the roughness as function of film thickness is observed, independently of the model used. This allows us to carry out a comparative study among the three DIP:F6TCNNQ mixing ratios employing the Trofimov model to simultaneously fit the reflectivity along several Q_z points. Indeed, although this model is not sensitive to the entire XRR curves, it represents a simple tool with a reduced number of parameters compared to the Parratt formalism, and it is easy to extend to numerous systems for comparative studies.

Despite the complicated nature of the systems studied here, where phase separation of a D:A crystal is observed aside of the dominant phase of pristine DIP, the combined approaches outlined above allow to draw some general conclusions about the trend of the RMS as function of D:A mixing ratio. All mixtures investigated are smoother than pristine DIP. Interestingly, the 2:1 mixture exhibits the lowest RMS values about integer nominal ML up to a total film thickness $\sim$ 2 ML, i.e. the mechanisms that lead to a layer-by-layer growth are most effective for the highest F6TCNNQ content in this thickness regime. For the 6:1 mixture with lowest F6TCNNQ content, the layer-by-layer growth is least pronounced. In an intermediate thickness regime between $\sim$ 3 and $\sim$ 6 ML the RMS is very similar for all films, but only the 4:1 mixture clearly shows persisting smoothness oscillations. In a thickness regime above $\sim$ 6 ML the 2:1 mixture is the roughest. The obtained trends show that the 2:1 mixture exhibits the largest relative changes in RMS going from the earlier growth stages to the later ones. This behavior has been tentatively explained by considering two relevant phenomena that occur for increasing amounts of F6TCNNQ, namely, lowering of the ES barrier and formation of D:A co-crystals.

This study is of fundamental interest for device architectures. Indeed, it is a common observation that for thin films of OSCs several phenomena exhibit a dependence on film thickness, like the occurrence of a different crystal polymorph or the onset of film roughening. Moreover, the mixing ratio between donor and acceptor might affect charge mobility through simultaneous change in film texture and doping efficiency (see last Results section 4.5).

4.3 Template-free control of molecular orientation of rod-like organic semiconductors in polycrystalline films [4]

In the previous Results sections 4.1 and 4.2 we have presented studies of mixed D:A systems. In the present section we demonstrate that for the technologically relevant, rod-shaped OSCs DIP, PEN and 6T (Figs. 3.1-3.3) deposited on amorphous Si oxide surfaces it is possible to prepare polycrystalline thin films in which the long axis of the moloecular units is oriented parallel to the substrate plane in a template-free fashion. In films grown by OMBD at room temperature (RT) or higher, the molecules are oriented upright standing (σ-orientation). Instead, the here-presented growth at low temperature followed by slow thermal annealing up to a temperature near molecular desorption has the effect of "freezing" the molecules with their long axis oriented parallel to the substrate plane (λ-orientation) while conferring them crystalline long-range order. We discuss the huge impact on the optical anisotropy of the films observed as a consequence of the orientation transition. We also propose a mechanism for explaining the achieved λ-orientation, which is stable under environmental conditions. Finally, we show that by applying the same protocol for film preparation it is also possible to select the orientation of the DIP:F6TCNNQ co-crystal (see Results section 4.1), and we discuss possible implications of the achieved orientation control for the study of charge-transfer phenomena.

4.3.1 Manipulating the structure of thin films of molecular OSCs

The efficiency of optoelectronic devices based on thin layers of OSCs [34] can be substantially improved by controlling thin film structure and molecular orientation. Although this has been achieved for polymers to some extent [4, 285], the high molecular weight and inherent high number of degrees of freedom of these materials render the self-assembly processes highly dependent on the preparation method. Employing small-molecular OSCs allows a superior control over thin film structure due to the reduced degrees of freedom of the molecular components. Additionally, the use of OMBD (Fig. 3.11) allows to rule out solvent effects on intermolecular interactions and structure-formation processes compared to deposition from solution.

4.3.1.1 Affecting the growth mode of molecular materials

Employing OMBD to grow thin films of OSCs [66, 260, 286] allows to exploit several strategies to affect the growth itself. For instance, illumination with polarized monochromatic light during the growth of the OSC tetracene has been recently shown to induce a biaxially anisotropic alignment of the crystalline domains [287]. More common approaches that have been explored to some extent include changes of the growth rate [171, 288, 289] and substrate temperature [118, 290], interrupted growth, [291] and combinations of them [292]. In all cases, the relevant parameters are manipulated *during* the growth processes.

It is important to stress here the role of molecule-molecule and molecule-substrate interactions responsible for crystallization processes during the growth of thin films of OSCs. For a given material, such interactions render a substrate-independent control of molecular orientation in crystalline films very difficult. Indeed, apart from possible re-orientation effects [170, 293], the crystal packing of the initial nuclei determines to a large extent the structure and molecular orientation of the subsequent layers. In fact, several examples show that a λ-orientation of molecular OSCs in crystalline films can be obtained by suitable choice of the chemical structure of the molecular material *or* of a "templating" substrate to affect the growth mode of the OSC atop. Relevant examples include the use of single-crystalline metal or metal-oxide surfaces, graphene monolayers and functionalizations of the molecular backbones to enhance molecule-substrate interactions [170, 207, 263, 294–307].

Specifically for DIP, some *in situ* investigations have shown that by deposition *via* OMBD on amorphous Si oxide at $T \leq 300$ K it is possible to obtain crystalline domains with λ-orientation [109, 117–119], although a coexistence with crystalline domains in σ-orientation was always observed. For PEN grown on Si oxide at T_{sub}=210 K, a recent work [308] demonstrates the growth of thin

[4] Based on Ref. [284]. The here described growth procedure to induce a stable horizontal molecular orientation in polycrystalline films has been submitted for patenting on the 15^{th} of August 2018 with the application number 102018213756.0.

films in which the molecular domains exhibit both σ- and λ-orientation. Furthermore, for non-crystalline systems of OSCs known as "anisotropic organic glasses" [309] the average molecular orientation in vapor-deposited films can be tuned to some extent. In particular, for rod-shaped molecules lowering of the deposition temperature leads to a reduction of the average tilt angle between the long molecular axis and the substrate [310, 311].

4.3.1.2 *Post*-growth treatments

Various strategies for *post*-growth manipulation of polycrystalline films of OSCs have also been exploited. For instance, solvent-vapor annealing can promote further film crystallization and improve the performance of optoelectronic components [312, 313]. The effects on thin film morphology can be quite dramatic, with strong de-wetting of the material on the substrate surface and a possible change of the average molecular orientation [313–315]. Thermal annealing, in turn, can be conveniently carried out *in situ* on as-grown films in order to improve their degree of crystallinity in the direction perpendicular to the substrate surface [282, 316]. However, the overall effect of possible structural reorganizations on charge transport properties depends critically on temperature and duration of the thermal annealing treatment [317, 318]. Interestingly, post-growth thermal annealing can also induce crystallization of amorphous layers of OSCs [319]. This suggests that, if the molecules exhibit a preferred orientation already in a poorly ordered film, providing thermal energy to the system can promote crystallization and turn the solid into a polycrystalline, uniaxially ordered film in which the molecular orientation is inherited from the disordered material. The possibility to use annealing to turn a disordered into a polycrystalline solid exhibiting a molecular orientation "locked" in the as-grown film has obviously important consequences on its optical properties.

4.3.1.3 Molecular orientation and anisotropy of the optical properties

The use of small-molecular OSCs as light-harvesters in solar cells calls for maximization of the absorption in the direction parallel to the bottom/top substrates working as contacts, where often ITO [320] or other transparent conductive oxides are used as electrodes. Similar requirements for the orientation of molecular emitters apply to OLEDs. Due to the typically strong intrinsic anisotropy of molecular semiconductors, the efficiency of light absorption/emission in a given direction depends on the orientation of the absorber/emitter [20, 321]. For uniaxially ordered thin films of small molecules this has the obvious consequence that spatial decomposition of the extinction coefficient, k, in the directions parallel (k_{xy}) and perpendicular (k_z) to the substrate plane, respectively, shows pronounced anisotropy. This was illustrated, e.g., for polycrystalline thin films of the molecular semiconductor diindenoperylene (DIP) exhibiting an upright standing orientation (σ-orientation): the HOMO-LUMO transition dipole moment (TDM) of DIP is oriented parallel to the long molecular axis, therefore in-plane absorption is much lower than the out-of-plane absorption [148]. In the Results section 4.1 (Fig. 4.7a) we also showed pronounced optical anisotropy of the low-energy CT-transitions for the DIP:F6TCNNQ co-crystal.

4.3.2 Inducing a stable λ-orientation in polycrystalline films - effects on their optical properties

We deposited thin films of three rod-shaped OSCs: DIP, PEN and 6T. For each material, deposition was carried out simultaneously on Si wafers with a native and 121 nm-thick thermally grown oxide layer employing a portable vacuum chamber [223] which allows to control the sample holder temperature by liquid N_2 cooling as well as resistive heating. For all three materials the substrates were cooled down to 123 K and their temperature (T_{sub}) was kept at 123 K during the deposition. The base pressure before starting the cooling was 5×10^{-8} mbar. The growth rate was around 0.3 nm/min for a total film thickness set to 20 nm on the thickness monitor. After growth, all films were annealed at a rate of $\sim$ 2 K/min up to a temperature compatible with their thermal stability, namely, 413 K for DIP, 353 K for PEN and 393 K for 6T. The final temperature was then kept for $\sim$ 90 minutes. The described film preparation protocol is sketched in Fig. 4.15.

For all three materials we carried out *ex situ* X-ray scattering experiments. For DIP the experiments were also carried out *in situ*. *In situ* and *ex situ* X-ray scattering measurements were

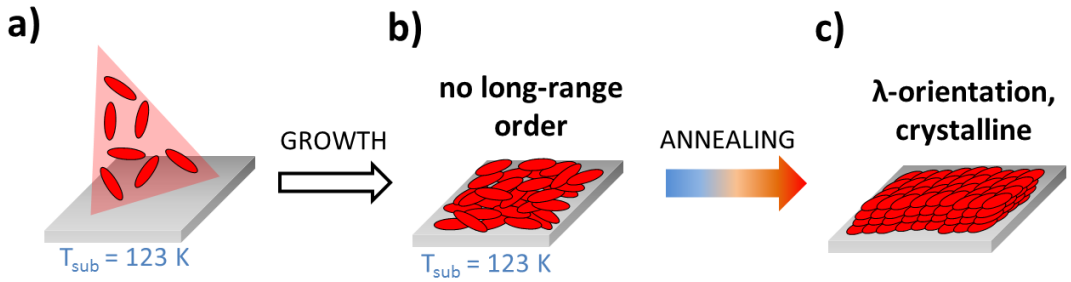

Figure 4.15: Description of the preparation procedure of thin films of rod-like OSCs in order to obtain a λ-orientation stable in atmospheric conditions. **a)** Vacuum deposition of the organic material on the substrate held at 123 K; **b)** after deposition up to the desired thickness, the thin film is constituted of disordered molecular aggregates, i.e. no long-range order is recognizable; **c)** thermal annealing in vacuum up to a temperature close to the film desorption causes crystallization of the material, which inherits the molecular λ-orientation from the as-deposited film.

carried out at the ID03 beamline (European Synchrotron Research Facility, ESRF) with a beam energy of 12.5 keV (0.992 Å) using a Maxipix 2×2 detector. For GIXD experiments, an incident angle of 0.11° was set, which is below the critical angle of Si ($\sim$ 0.14° at this energy) but roughly coincides with the critical angle of DIP assuming a material density of 1.3 g/cm^3. Therefore, the whole film thickness is probed by the incoming beam. In the following we first focus on the results obtained for DIP; subsequently, we summarize the results for PEN and 6T, highlighting similarities and differences with DIP.

4.3.2.1 Results for DIP

Q-maps measured *in situ* for a DIP film right after film deposition on native Si oxide at $T_{sub} = 123$ K are reported in Fig. 6.12 of Appendix 6.3. They show a diffraction feature from weakly ordered DIP domains, corresponding to molecules exhibiting their long axis roughly parallel to the substrate plane. Therefore, even at this low temperature (LT), some nuclei with short-range order are formed having a lateral coherent grain size of ~4.5 nm, which corresponds approximately to the length of three molecules in λ-orientation.

X-ray scattering and VASE experiments were further carried out *ex situ*. A DIP film grown at RT is compared with a film grown at LT (123 K). Both samples were annealed up to 413 K and then cooled down to RT. The X-ray diffraction patterns measured in both grazing incidence and specular geometry measured *ex situ* for the film grown at RT are shown in Fig. 4.16a and are compared with the corresponding data for the LT film (Fig. 4.16c). The X-ray diffraction pattern of the RT film matches the well-known thin film phase with molecules standing nearly upright [118]. The weak diffraction ring at $Q_{tot} = 0.375$ Å^{-1} stems from some DIP domains exhibiting a nearly random orientation [117]. Correspondingly, $k_z > k_{xy}$ in the visible range up to 3 eV (Fig. 4.16b). The situation is very different in the case of the LT film. Here, the DIP unit cell is tilted by 90° around the crystallographic a-axis with the (020) plane parallel to the substrate (Fig. 4.16c). The long molecular axis is then also parallel to the substrate plane, and the molecules exhibit a tilted edge-on configuration (inset Fig. 4.16c). From the position of the strong Bragg reflection at $Q_{||} = 0$ Å^{-1} and $Q_z \approx 1.5$ Å^{-1} it is evident that the (020) plane is parallel to the substrate. Note that there is no trace of the σ-orientation of DIP in the diffraction pattern.

The appearance of the two truncation rods $(1k0)$ and $(1k1)$ at $Q_{||} = 0.88$ Å^{-1} and $Q_{||} = 0.97$ Å^{-1}, respectively, for the LT film in Fig. 4.16c is an indication of the overall high coherence length of the crystallites in the direction perpendicular to the substrate. A broader distribution of crystallite orientations for the LT film than for the RT film is evident by the comparably broader Bragg peaks, i.e. the LT film exhibits a higher mosaicity than the RT film. The mosaicity calculated from the Bragg peaks belonging to the $(1k1)$ truncation rod is ± 7°. Remarkably, the presence of the $(00l)$ series of sharp Bragg peaks along $Q_{||}$ at $Q_z = 0$ Å^{-1} indicates a high coherence of the crystallites in the direction parallel to the substrate surface, with a coherent grain size of $\sim$ 50 nm

estimated from the width of the (001) peak (see Fig. 6.13 in Appendix 6.3).

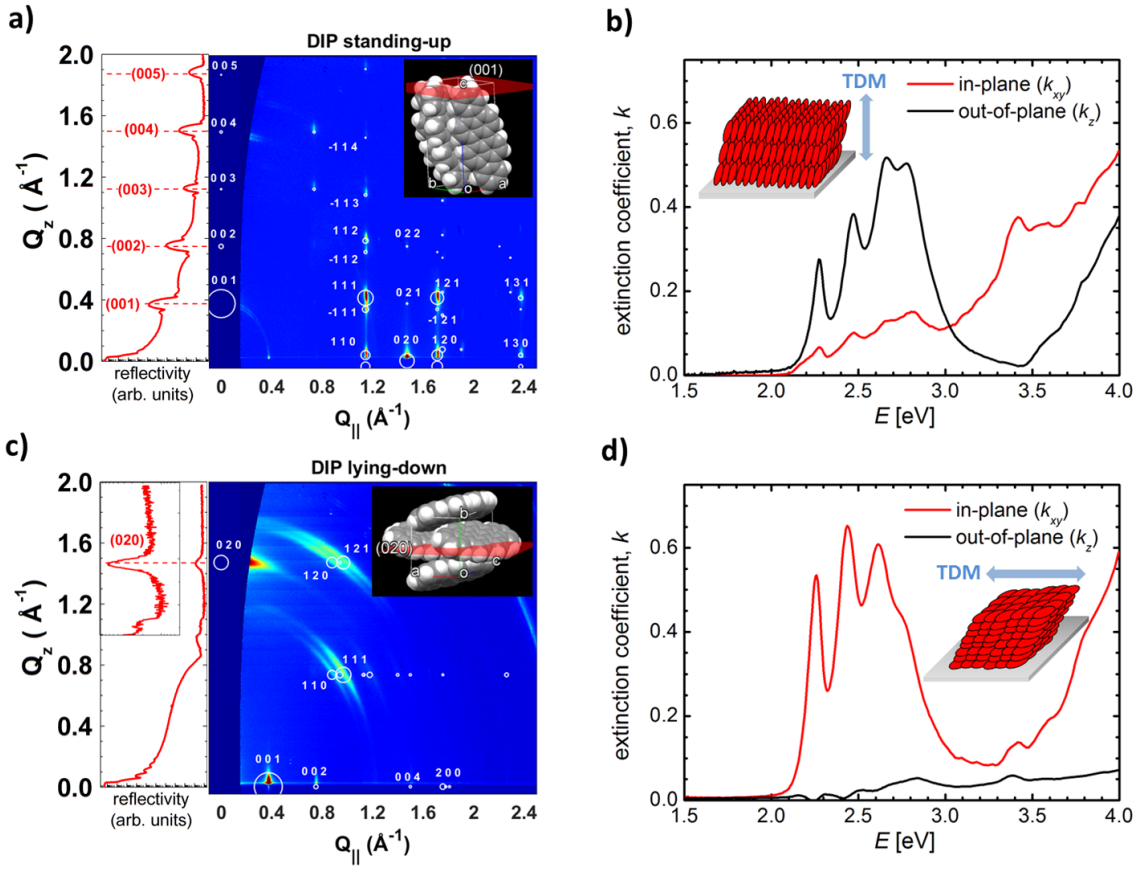

Figure 4.16: **a),c)** *Ex situ* X-ray diffraction patterns measured in grazing incidence (right panel) and specular geometry (left panel) for uniaxially oriented, polycrystalline DIP films in **a)** σ- and **c)** λ-orientation, both on a native Si oxide substrate. The expected positions of the Bragg peaks were simulated using the unit cell of the 423 K polymorph of DIP from Ref. [124], which matches well its thin-film phase. The Miller indices of the strongest Bragg peaks are shown, with the circles having a diameter proportional to the expected intensity. The insets illustrate the different orientations of the DIP unit cell and the contact plane with the substrate used to reproduce the measured diffraction patterns. **b),d)** Extinction coefficient obtained using VASE on the same DIP films as in **a)** and **c)**. Sketches illustrating the overall orientation of the molecules and of the TDM are shown.

In agreement with the molecular tilt, the in-plane absorption of DIP in λ-orientation is much stronger than the out-of-plane absorption, i.e., $k_{xy} \gg k_z$ (Fig. 4.16d). The long range order of the DIP crystallites in λ-orientation is further supported by the VASE data in Fig. 4.16d. Indeed, the highest-energy mode around 2.8 eV has been assigned to the combination of localized as well as delocalized excitations, and its intensity relative to the other transitions indicates intermolecular interactions in structurally ordered aggregates [148, 322].

To summarize this first part, we have shown that vacuum-deposition of DIP films lacking long-range order followed by thermal annealing to induce crystallization is an efficient method to obtain a molecular λ-orientation in the polycrystalline films. Consequently, selecting the orientation of DIP between σ and λ consequently allows the thin film optical absorption to be inverted between the in-plane and out-of-plane directions, respectively (Fig. 4.16a-d).

4.3.2.2 Results for PEN and 6T

To demonstrate that the above presented growth scheme allows for the fabrication of thin films with molecular λ-orientation for other technologically relevant OSCs, we present results also on

PEN and 6T.

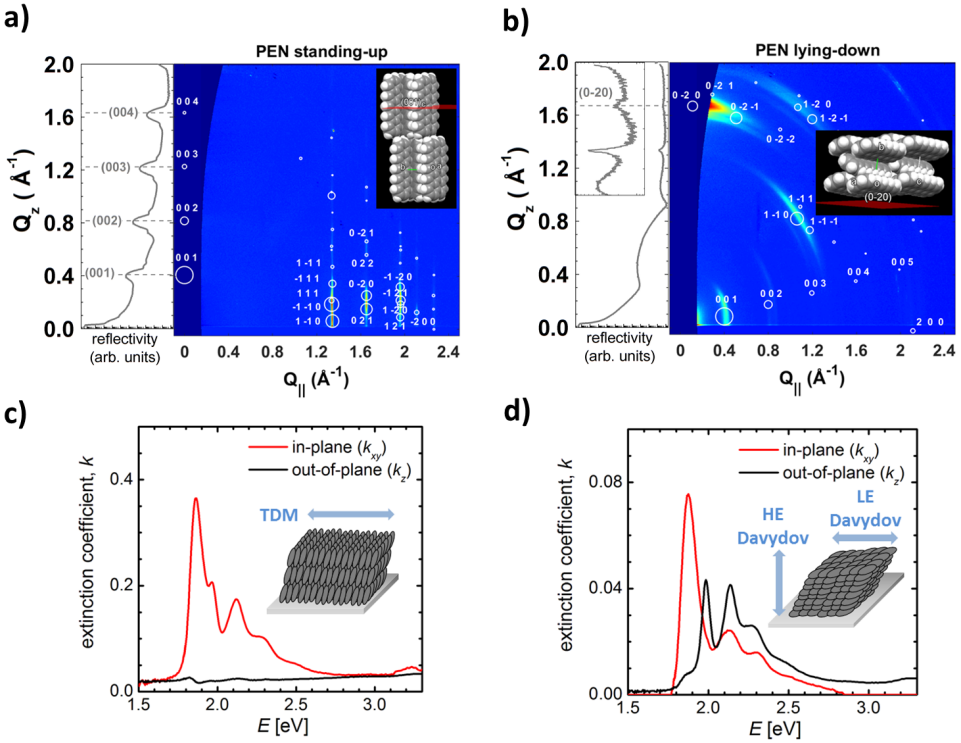

Figure 4.17: **a),b)** *Ex situ* X-ray diffraction patterns in specular (left) and grazing incidence (right) geometry. **c),d)** Extinction coefficient for PEN films in σ- and λ-orientation, respectively. The symbols and Miller indices overlaid to the diffraction patterns belong to the PEN substrate-induced polymorph (Ref. [78]). The sketches reported for the k data summarize the thin film optical properties, as detailed in the text.

The diffraction pattern of a PEN film in σ-orientation (Fig. 4.17a) differs strongly from that of a PEN film in λ-orientation (Fig. 4.17b) prepared with the growth procedure illustrated previously. An upright-standing orientation of the substrate-induced (or thin-film) polymorph of PEN [78] allows to reproduce very closely the position and relative intensity of the diffraction features in Fig. 4.17a. The diffraction pattern of PEN in λ-orientation (Fig. 4.17b) could be indexed by tilting the unit cell of the PEN thin-film polymorph by 77.5° around the crystallographic a-axis, thereby bringing the (0-20) plane nearly parallel to the substrate, similar to previous observations for PEN on graphene [307, 323]. Although the match is not perfect and the presence of some weak additional diffraction features points towards the presence of more than one polymorph, our guess gives clear evidence that environmentally stable polycrystalline PEN films in λ-orientation can be produced on amorphous Si oxide surfaces.

The HOMO-LUMO TDM of PEN is parallel to the short molecular axis, therefore $k_{xy} \gg k_z$ in thin films of PEN in σ-orientation (Fig. 4.17c and Ref. [183]). For the PEN film in λ-orientation, k_{xy} and k_z have similar strength. Interestingly, one observes that the low-energy (LE) Davydov component of the fundamental HOMO-LUMO transition [324] at ∼1.88 eV is oriented mostly in-plane, whereas the high-energy (HE) Davydov component at ∼1.99 eV is oriented mostly out-of-plane (Fig. 4.17d). The spatial decomposition of the Davydov components has already been observed in PEN single crystals [325] and in our polycrystalline film it is a direct consequence of the particular orientation of the herringbone stacking relative to the substrate.

For 6T, results similar to DIP and PEN are obtained. Notice that the Q-map shown in Fig. 4.18a has been measured for a non-annealed sample. The thin film in σ-orientation shows diffraction features from the low-temperature (low-T) bulk polymorph [127] (Fig. 4.18a). The vertical rod at $Q_z = 0$ Å^{-1}, $Q_{||} \approx 1.38$ Å^{-1} stems from a layered disordered phase of 6T denominated β-phase [180]. The coexistence of the β and low-T phases [96] explains the splitting of the (h00) series of Bragg peaks, which are also visible in the Q-map due to film mosaicity. The remaining diffraction

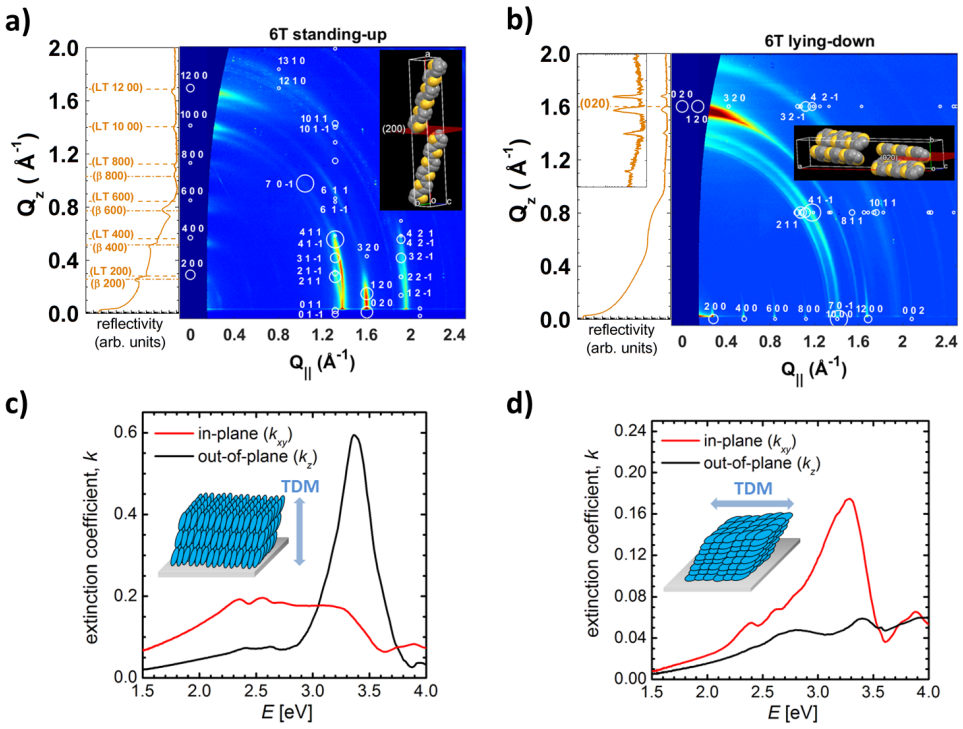

Figure 4.18: **a)**,**b)** *Ex situ* X-ray diffraction patterns in specular (left) and grazing incidence (right) geometry. **c)**,**d)** Extinction coefficient for 6T films in σ- and λ-orientation, respectively. The symbols and Miller indices overlaid to the diffraction patterns belong to the 6T low-temperature bulk polymorph (Ref. [127]). In the XRR scan of σ-6T, Bragg peaks of the β-phase are also reported. The sketches reported for the k data summarize the thin film optical properties, as detailed in the text.

features stem from an orientation of the low-T 6T unit cell exhibiting the (-411) plane as contact plane with the substrate [180, 301].

The diffraction pattern of the 6T film in λ-orientation (Fig. 4.18b) has been indexed by tilting the 6T unit cell by 90° around the c-axis in order to bring the (020) plane parallel to the substrate. The mosaicity of this film is higher than for DIP and PEN in λ-orientation, as it can be seen by the nearly ring-like diffraction features having $Q_{tot} \geq 1.35$ Å^{-1}. However, the (h00) series of sharp in-plane Bragg reflections and the pronounced (020) Bragg peak at $Q_z \approx 1.6$ Å^{-1}, $Q_{||} = 0$ Å^{-1} denote a strongly preferred λ-orientation. The presence of several ring-like diffraction features and, at the same time, the (h00) series of Bragg peaks quite localized around the sample horizon denotes that the high mosaicity regards only crystal directions approximately perpendicular to the long cell axis/long molecular axis, whereas the 6T molecules exhibit a well defined stacking in the direction parallel to the substrate.

The optical properties of 6T in σ-orientation have been measured for an annealed film, which shows a pronounced island-like morphology (see Fig. 6.15a,c in Appendix 6.3). The pronounced island-like morphology of the annealed 6T films in both σ- and λ-orientation renders the quantification of the optical anisotropy difficult due to the strong scattering background generated (see Fig. 6.16c in Appendix 6.3). The data reported in Fig. 4.18c,d represents nevertheless a qualitative estimation of the optical anisotropy. Since the HOMO-LUMO TDM of 6T is parallel to the long molecular axis, k_z is larger than k_{xy} for the 6T film in σ-orientation up to 3 eV [271] and *vice versa* for the 6T film in σ-orientation. However, the optical anisotropy for the 6T film in λ-orientation is weaker than for the DIP film in λ-orientation, an observation that we ascribe to the higher mosaicity in 6T.

4.3.2.3 Results for the DIP:F6TCNNQ co-crystal

We show here results that demonstrate the possibility to control the molecular orientation also in D:A mixtures of OSCs. In particular, unpublished data for the DIP:F6TCNNQ co-crystal in λ-orientation are presented here. In Fig. 4.19 we show the same data for the DIP:F6TCNNQ 1:1 mixture as shown in Fig. 4.4a in the Results section 4.2 (Fig. 4.19a). This sample is denominated "standing-up" since it was grown at RT. The data for the standing-up film are compared with the data for a DIP:F6TCNNQ 1:1 mixture grown at LT and slowly annealed up to 413 K, which is therefore denominated "lying-down". Both films were deposited on native Si oxide.

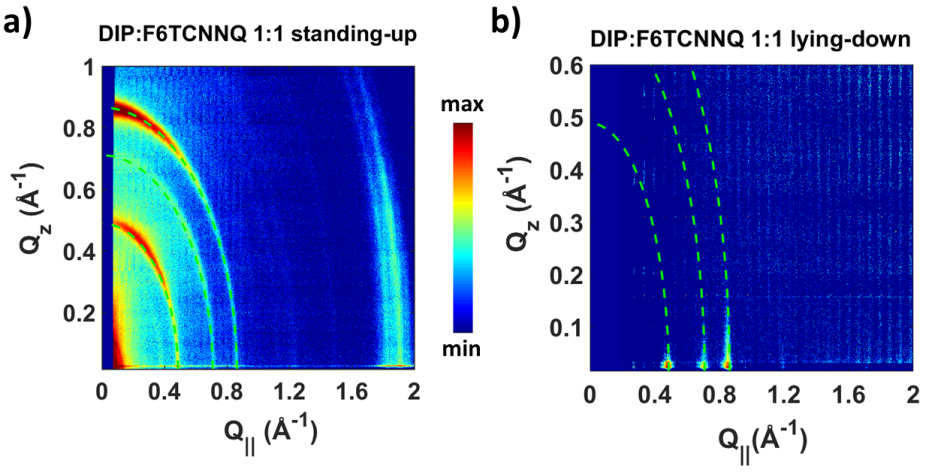

Figure 4.19: **a)** *Ex situ* and **b)** *In situ* X-ray diffraction patterns of DIP:F6TCNNQ mixtures in 1:1 molar ratio. The film thickness is $\sim$ 100 nm for **a)** and $\sim$ 20 nm for **b)**. The data in **a)** are the same shown in Fig. 4.4a and were measured for a film labeled "standing-up" since it has been deposited at RT. The data in **b)** were measured on a film labeled "lying-down" since it was deposited at $\sim$123 K and subsequently annealed up to 413 K. The dashed green circles mark diffraction features stemming from the DIP:F6TCNNQ co-crystal and have Q_{tot} of 0.49, 0.71 and 0.86 Å^{-1}, respectively. Notice the different scale of the Q_z-axis. The color scale is logarithmic.

The strong co-crystal diffraction features having Q_{tot}= 0.49, 0.71 and 0.86 Å^{-1} are marked with green dashed circles. The higher mosaicity of the standing-up film compared to the lying-down film is due to the higher thickness of the former ($\sim$ 100 nm) compared to the latter ($\sim$ 20 nm) and, likely, to the fact that the former sample has not been annealed. Apart from the different mosaicity, it is clear that the intensity of the marked diffraction features is mostly concentrated close to $Q_{||} \approx 0$ for the standing-up film. For the lying-down film, the intensity of the diffraction spots having the same Q_{tot} as the marked lines is concentrated at $Q_z \approx 0$. The remaining diffraction features $Q_{||}$ = 1.80 - 1.95 Å^{-1} for the standing up sample stem from crystal directions nearly coincident with the π-stacking direction of the D:A moieties. Such diffraction features disappear in the Q-map of the lying-down sample.

An attempt to assign the observed diffraction features has been made based on the published structure of the bulk D:A co-crystal NDT:F6TCNNQ [199]. The choice of this reference system is based on the fact that the powder diffraction pattern simulated with Mercury [326] shows the five strongest diffraction peaks (not shown) located at similar Q-positions as the five strongest diffraction features for the DIP:F6TCNNQ co-crystal. Interestingly, the unit cell of the NDT:F6TCNNQ co-crystal is monoclinic, which in general reduces the number of strong reflections compared to a crystal of triclinic symmetry. This gives a strong hint that the DIP:F6TCNNQ co-crystal unit cell has also a monoclinic symmetry. Differences in peak position and relative intensity between the NDT:F6TCNNQ and the DIP:F6TCNNQ co-crystal are obviously expected due to the different molecular structure of the donor. However, the arrangement of the donor relative to the acceptor, as well as the arrangement of the D:A stacks in the two co-crystals might be similar. This seems not unlikely also considering that the degree of CT interactions for the two D:A pairs is similar

(compare the next Results section 4.4 with Ref. [199]).

In Fig. 4.20 we show a comparison of two different orientations for the unit cell of the NDT:F6-TCNNQ co-crystal. In Fig. 4.20a, the unit cell is oriented such that the mixed D:A stacks assume an edge-on orientation (here also denominated "standing-up" orientation). In Fig. 4.20b the unit cell is oriented such that the mixed D:A stacks assume a face-on orientation (here also denominated "lying-down" orientation).

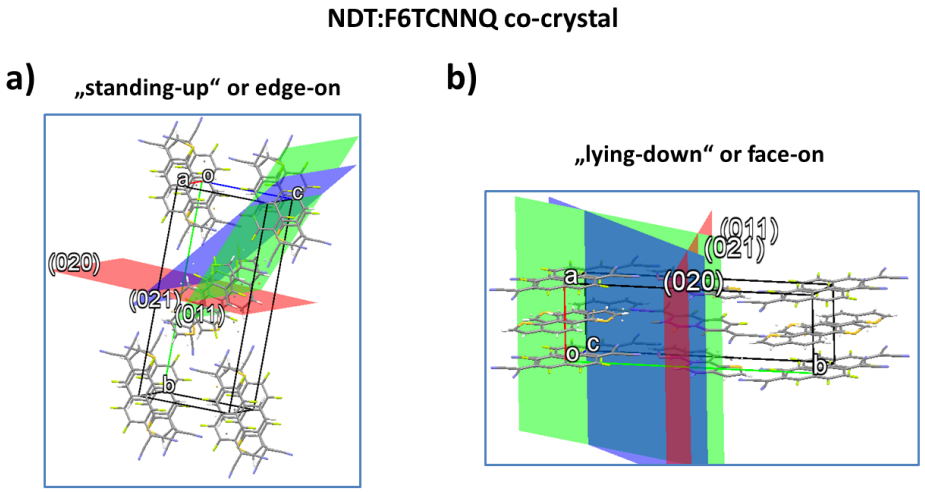

Figure 4.20: Unit cell of NDT:F6TCNNQ co-crystal from Ref. [199] in two different orientations: **a)** edge-on orientation of the mixed DA-stacks, which for this compound represents a "standing-up" orientation; **b)** face-on orientation of the mixed DA-stacks, which for this compound represents a "lying-down" orientation. Selected crystal planes are drawn and the corresponding Miller indices are indicated.

The crystal planes associated to the three strongest diffraction peaks having $Q_{tot} <\sim 1$ Å^{-1} are shown in Fig. 4.20. Within our crude approximation concerning the similarity of the two co-crystal structures, the assignment of the observed diffraction features with $Q_{tot} <\sim 1$ Å^{-1} for the DIP:F6TCNNQ co-crystal is summarized in Tab. 4.2.

Table 4.2: Indexing of the three strongest diffraction features for the DIP:F6TCNNQ co-crystal.

Q_{tot} (Å^{-1})	**cryst. direction (*hkl*)**
0.49	(020)
0.71	(011)
0.86	(021)

From the assignment in Tab. 4.2 it follows that the observed diffraction features for the standing-up DIP:F6TCNNQ co-crystal (Fig. 4.19a) can be explained by two possible edge-on orientations of the D:A moieties. In the first kind of edge-on orientation, the long molecular axis of both donor and acceptor is roughly perpendicular to the substrate plane (Fig. 4.20a). Rotating this unit cell by approximately 90° around the crystallographic a-axis leads to another edge-on orientation in which the long molecular axes are roughly parallel to the substrate plane. Conversely, the diffraction features for the lying-down DIP:F6TCNNQ co-crystal (Fig. 4.19b) can be described by a face-on orientation of the D:A moieties, which can be obtained rotating the standing-up unit cell (Fig. 4.20a) by 90°around the crystallographic c-axis (Fig. 4.20b).

The described rotations can also explain the disappearance of the diffraction features having $Q_{||} = 1.80 - 1.95$Å^{-1} from the Q-map of the lying-down DIP:F6TCNNQ co-crystal. Indeed, the corresponding Bragg peaks are now expected to be located in the out-of-plane direction, i.e. at $Q_{||} \approx 0$ and $Q_z = 1.80 - 1.95$Å^{-1}, but the measured Q_z-range is not large enough to render them visible.

4.3.2.4 A mechanism to explain a λ-orientation in crystalline films of OSCs

The mechanism that explains the results we obtained seems to primarily involve suppression of molecular dynamics. The single molecules landing on the bare substrate initially adopt a λ-orientation in order to maximize the van der Waals interactions with the Si oxide surface. However, due to the low T_{sub}, they lack the necessary thermal energy for a collective transition to a σ-orientation [114, 327], which would allow to maximize the total number of interactions per unit area. The same scenario holds for molecules landing on top of an already formed organic layer. The molecules within "buried" layers additionally experience hindrance to motion from the material deposited on top. In the end, the molecular aggregates in the as-deposited film exhibit an overall λ-orientation with no long-range order.

Upon film annealing, the molecular units receive enough thermal energy such that crystallization processes are triggered, which seemingly occur *via* minimal structural reorganization thanks to the initial "compact" (though disordered) packing of the film. When cooling down to RT, the formed crystallites are already kinetically trapped in the λ-orientation, which does not change further upon exposure to atmospheric conditions.

4.3.3 Summary of the results and possible applications

In summary, we have shown that vacuum deposition of the three rod-like OSCs DIP, PEN and 6T at T_{sub}=123 K followed by annealing in vacuum leads to the formation of uniaxially aligned films where the crystalline domains consist of molecules exclusively oriented with their long axis parallel to the substrate. The films are mostly polycrystalline with long range order, although some material-dependent differences in film texture are recognized. The optical properties of the thin films change according to the molecular orientation. In particular, for materials having their HOMO-LUMO TDM parallel to the long molecular axis, light absorption efficiency in the direction parallel to the substrate plane is greatly enhanced. Importantly, the horizontal molecular orientation and crystallinity of the films are conserved after exposure to atmospheric conditions. The possibility to induce a stable horizontal molecular orientation has been demonstrated also for the DIP:F6TCNNQ co-crystal. The alignment of the long molecular axis of rod-shaped OSCs parallel to the substrate plane on Si oxide without the use of specific templating surfaces, together with the pronounced crystalline coherence of the uniaxially anisotropic thin films had so far, to the best of our knowledge, not been achieved. Furthermore, although in this thesis results for three materials on amorphous Si oxide are shown, the above outlined mechanism is general for rod-shaped OSCs on a variety of substrates.

Such combination of properties has great potential for optoelectronic devices where, in general, high light-harvesting efficiency and high charge carrier mobility are demanded. For examples, the results shown for DIP and 6T envisage the use of rod-like molecular materials selectively grown in λ-orientation in order to maximize light absorption and increase the efficiency of organic solar cells. The recent demonstration of a Si Si-based solar cell sensitized with a tetracene thin film [328] demonstrates an additional direction of application, namely hybrid photovoltaic, where OSCs can compensate with their high absorptivity the portion of sun spectrum that is not efficiently harvested by the inorganic Si cell. Within this new application direction, detailed analysis of the hybrid interface between the organic material and the inorganic substrate is required [329, 330] in order to quantify, *inter alia*, energetic barriers for charge carrier injection. To this regard, an additional parameter that needs to be considered for OSCs is the dependence of the ionization potential/electron affinity on molecular orientation [263, 303]. Overall, the film preparation protocol presented here allows a high flexibility in the choice of the material-substrate combination since the requirement of strong molecule-surface interactions to induce a λ-orientation can be circumvented.

4.4 Study of CT-sensitive vibrations in DIP:F6TCNNQ and P3HT:F6TCNNQ mixtures [5]

In the Results section 4.1 we characterized the structural and optical properties of the D:A complex formed by DIP and F6TCNNQ. There, based on optical absorption data and assuming the model of orbital hybridization [54] we suggested that strong ground-state charge-transfer (GS-CT) takes place for this system. Here, we provide data that support this picture and allow to quantify the degree of GS-CT. Additionally, we compare the system DIP:F6TCNNQ to another system featuring the same acceptor but where the donor is replaced by the polymer P3HT (Fig. 3.5). The contents of this section are summarized in the following.

We investigate blends of the two donors DIP and P3HT, respectively, with the strong acceptor F6TCNNQ using FTIR spectroscopy in PMIRRAS configuration (see Methods section 3.3). To perform PMIRRAS, all samples were grown on Au substrates coated with $\sim$ 12 nm Si oxide deposited by plasma-enhanced chemical vapor deposition (PECVD). In the Results section 4.1, native Si oxide was used as substrate for the structural characterization of DIP:F6TCNNQ mixtures. Due to possible chemical and morphological differences between the PECVD-deposited Si oxide and the native Si oxide surfaces, here a detailed study of the thin film structure as function of the D:A mixing ratio on the new substrate is carried out, which serves to guide the analysis of the PMIRRAS spectra.

For the analysis of the PMIRRAS data, we initially consider the spectral range in which the strongest C=C stretching/C—H in-plane bending for DIP and C=C stretching for F6TCNNQ are located. In particular, we recognize a red-shift of the strongest C=C stretching modes of F6TCNNQ related to the formation of a D:A co-crystal with DIP with consequent GS-CT interactions. Subsequently, we analyze the position and relative intensity of the C$\equiv$N stretching modes of F6TCNNQ as function of the mixing ratio with DIP. In this region we carefully assign the observed vibrational features and we identify the CT-affected mode. By its red shift we calculate a partial CT, ρ, of 0.77$\pm$0.09 e.

Additionally, we observe that the CT-affected C$\equiv$N stretching peak in DIP:F6TCNNQ and P3HT:F6TCNNQ, respectively, exhibits nearly the same red-shift. This seems to point towards a very similar GS-CT strength for the two systems. However, comparison of the resonance strength of the C$\equiv$N relative to the C=C stretching modes for F6TCNNQ in the mixtures with DIP and P3HT, respectively, rather points towards much stronger, integer CT-type polymer-dopant interactions, which better matches optical spectroscopy data available from the literature [53, 140, 192]. Our findings show that a simultaneous analysis of both kinds of CT-sensitive vibrations in quinoid systems like F6TCNNQ (but likely also F4TCNQ) is necessary to get a reliable picture of the nature of GS-CT interactions.

4.4.1 Study of molecular vibrations to quantify GS-CT

For both polymeric and small-molecular OSCs, molecular electrical doping (MED) has been realized, namely, admixture of small percentages of a molecular material to an organic host matrix, typically not more than 10% in molar ratio, in order to increase electrical conductivity *via* doping [20]. Knowledge of the details of intermolecular interactions allows therefore to design and choose suitable material combinations in order to achieve the desired doping efficiency [47].

As outlined in the Fundamentals section 2.2, formation of a D:A complex involves some degree of CT interactions between donor and acceptor material already in the GS. In Ref. [155], it was shown that for several TCNQ salts there is a linear relationship between the position of the highest-frequency infrared-active C$\equiv$N-stretching mode of TCNQ and the degree of GS-CT of the salts, which had been independently estimated with complementary methods. This relationship is used to trace a calibration curve for the quantification of the GS-CT degree for several other TCNQ salts. Other vibrational modes of TCNQ-derived compounds associated with hexo-cyclic C=C stretching have been shown to be sensitive to the degree of GS-CT since they are also strongly involved in the quinoid-to-benzenoid molecular deformation that accompanies the ionization process [200, 332] which might result from the interaction with a donor compound. This approach based on FTIR spectroscopy has been used to study several other CT salts in form of macroscopic single crystals

[5] Based on Ref. [156]

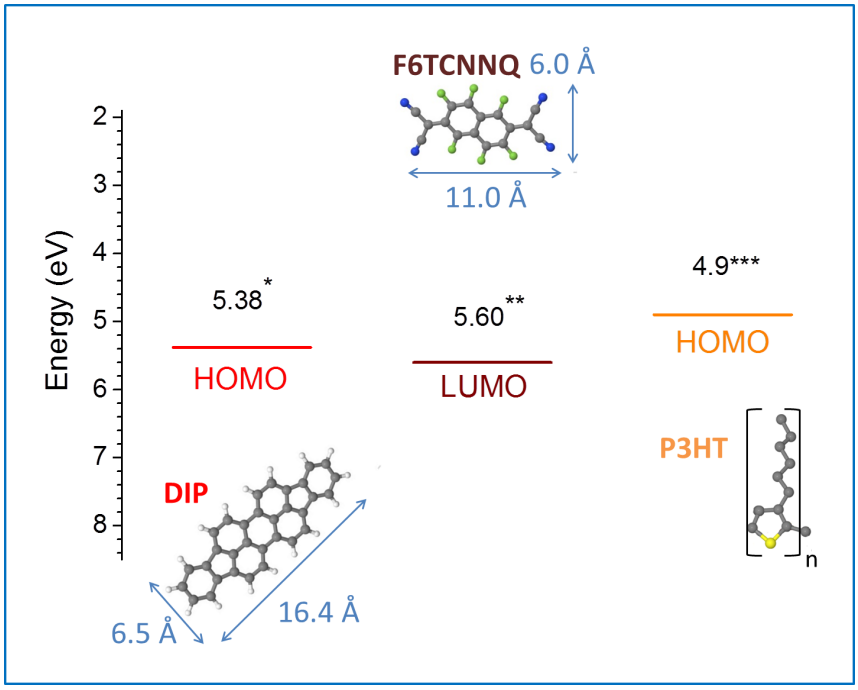

Figure 4.21: Molecular structure and energy levels of the compounds used in this work. The HOMO and LUMO values were obtained from different references: * from Ref. [262]; ** from Ref. [53]; *** from Ref. [331]. For the size of the 3HT monomer, please refer to Fig. 4.1.

[56, 86, 88, 131, 199, 333–335]. A prerequisite is the knowledge of the CT-affected peak position in the zero-CT (neutral) and the integer-CT (ionized) states, respectively.

Measurement of the GS-CT degree by FTIR spectroscopy, often with the aid of density-functionall theory (DFT) calculations, has been extended to thin films of OSCs, where polymers [51, 192, 336, 337] as well as molecular semiconductors [48, 57, 157, 338, 339] have been blended with other small-molecular components acting as dopants with donor or acceptor character. In the present section, we investigate thin films of OSCs with thickness between ∼10 and 20 nm, containing DIP or P3HT as donors and F6TCNNQ as acceptor. These are two representative D:A systems for which a driving force for GS-CT is expected according to the relative energy level alignment (Fig. 4.21). We use PMIRRAS to quantify the degree of GS-CT in DIP:F6TCNNQ and P3HT:F6TCNNQ. This technique allows to have excellent signal-to-noise ratio and to avoid signal from atmospheric gases. We study the structure of DIP:F6TCNNQ blends in different mixing ratios as a guide to the unambiguous identification of the effects of GS-CT interactions on the spectral shape and position of the CT-sensitive vibrations for F6TCNNQ. Finally, we show a comparison between the CT-sensitive modes of DIP:F6TCNNQ and P3HT:F6TCNNQ blends.

4.4.2 Sample and substrate preparation

To ensure high reflectance of the infrared radiation and to exploit the surface selection rules for infrared spectroscopy on metals in reflection geometry (see Methods section 3.3), Si wafers covered by a ∼200 nm thick Au layer were used, on which an additional Si oxide (SiO_x) layer of ∼12 nm thickness has been deposited by PECVD, similarly to Refs. [217, 340]. We coated the Au substrates with SiO_x in order to prevent interaction of the molecular components with the Au surface, which might induce a change in molecular orientation [170] as well as perturb the electronic structure at the metal-organic interface [341]. The Si oxide coating is thin enough to still ensure high reflectance from the metal substrate and conservation of the surface selection rules [340], but also thick enough to ensure its homogeneity. Additional details on the substrate preparation and characterization are reported in the Materials section 3.2 (Fig. 3.10).

Binary D:A mixtures with DIP as donor and F6TCNNQ as acceptor were grown on the Au/SiO_x substrates *via* OMBD in a vacuum chamber with a base pressure of 3×10^{-8} mbar. Prior to growth

of the organic films, the substrates were cleaned first with acetone and isopropanol in an ultrasonic bath and dried under N_2. The substrates were subsequently heated up to ∼500 K for 2 hours in vacuum in order to remove possible solvent residuals. Films of the pristine compounds as well as DIP:F6TCNNQ mixtures in different mixing ratios were grown by co-evaporation up to a thickness around 20 nm at a substrate temperature of 300 K. The total growth rate was kept between 0.1 nm/min and 0.3 nm/min for all samples. The growth rates were monitored with two separate quartz crystal microbalances for donor and acceptor material, respectively, calibrated by X-ray reflectivity for DIP and by AFM for F6TCNNQ, both on native Si oxide, with an error on the mixing ratios of ± 10%.

A pristine P3HT film as well as P3HT:F6TCNNQ blends were prepared by spin coating on the Au/SiO_x substrates [6]. Both compounds were dissolved in chloroform, where 10.4 mg P3HT and 2.3 mg of F6TCNNQ, respectively, were added to 3.5 ml of solvent. The F6TCNNQ solution was stirred at 55-60°C for at least 24 hours. Two solutions in 5:1 P3HT:F6TCNNQ molar ratio were prepared. The first solution was mixed 30 minutes before the spin-coating process, whereas the second was mixed 72 hours. Another solution in molar ratio 2:1 was prepared and mixed 30 minutes prior to spin-coating. Note that the molar ratios are defined as [moles of thiophene monomers]:[moles of F6TCNNQ molecules]. For thin film deposition, 50 μl of the desired solution were spin-coated at 800 rpm for 40 s, which resulted in less than 10 nm thickness of the organic films.

X-ray scattering experiments in GIXD geometry were carried out at the ID10 beamline of the European Synchrotron Research Facility (ESRF, Grenoble, France). A relatively beam energy of 22 keV and short exposure times avoid beam-damage due to the photoelectrons from the Au substrate. For PMIRRAS measurements, the setup described in the Methods section 3.3 was used.

4.4.3 Structural characterization of DIP:F6TCNNQ mixtures

It is important to first analyze the structure of the thin films as function of the DIP:F6TCNNQ mixing ratio in order to investigate the formation of a D:A complex and possible changes in molecular orientation in the mixtures with respect to the pristine films [62].

In Fig. 4.22 we show reciprocal space maps of the different DIP:F6TCNNQ mixtures and of the pristine films. From Fig. 4.22a (pristine DIP) diffraction features stemming from the DIP thin-film phase in an upright-standing (σ) orientation can be seen, as marked by the small white circles. These features fade away and gradually disappear as the relative amount of F6TCNNQ in the blends increases. The uniaxial alignment of the DIP crystallites in the pristine film is less pronounced than for films grown on native Si oxide [118], an effect that can be attributed to the substrate roughness [342] (see Fig. 3.10 in the Materials section 3.2).

Going from Fig. 4.22b (4:1 mixture) to Fig. 4.22e (1:2 mixture) several observations can be made. First, it is possible to recognize a ring-like diffraction feature (white dashed circle) having Q_{tot} ∼0.38 Å^{-1} corresponding to the (001) Bragg peak of nearly random oriented DIP crystallites, in which a significant portion of the molecules exhibit their long molecular axis roughly parallel to the substrate surface, i.e. they tend to a lying-down (λ) orientation. Additionally, new diffraction features arise in the maps that we assign to the DIP:F6TCNNQ co-crystal [162] (green dashed circles). Obviously, the degree of long-range order of the co-crystal varies considerably depending on the D:A mixing ratio. In particular, the features indicating a crystalline phase become clearer only starting from the 1:1 film towards increasing F6TCNNQ content.

For the 1:4 mixture in Fig. 4.22f, the diffraction features from the co-crystal are strongest. This seems to point towards a complex phase-nucleation scenario in which exceeding F6TCNNQ is necessary to thermodinamically favor co-crystal nucleation, as it has been already observed for mixtures of organic conjugated molecules in solution [121]. The position and relative intensity of the co-crystal features match our findings for this D:A system on native Si oxide (see Results section 4.1), in particular with the diffraction features having $Q_{||} \sim 1.80 - 1.95$ Å^{-1} that stem from a $\pi - \pi$ stacking distance of 3.5-3.2 Å between the conjugated cores of DIP and F6TCNNQ. Therefore, a tilted edge-on orientation for the DIP:F6TCNNQ supramolecular complex on the substrate is deduced as in Ref [162]. The DIP:F6TCNNQ co-crystallites are overall uniaxially oriented, although with a pronounced mosaicity of $\sim \pm 15°$ estimated from the spread intensity of

[6] Thanks to Paul Beyer, Humboldt Universität zu Berlin

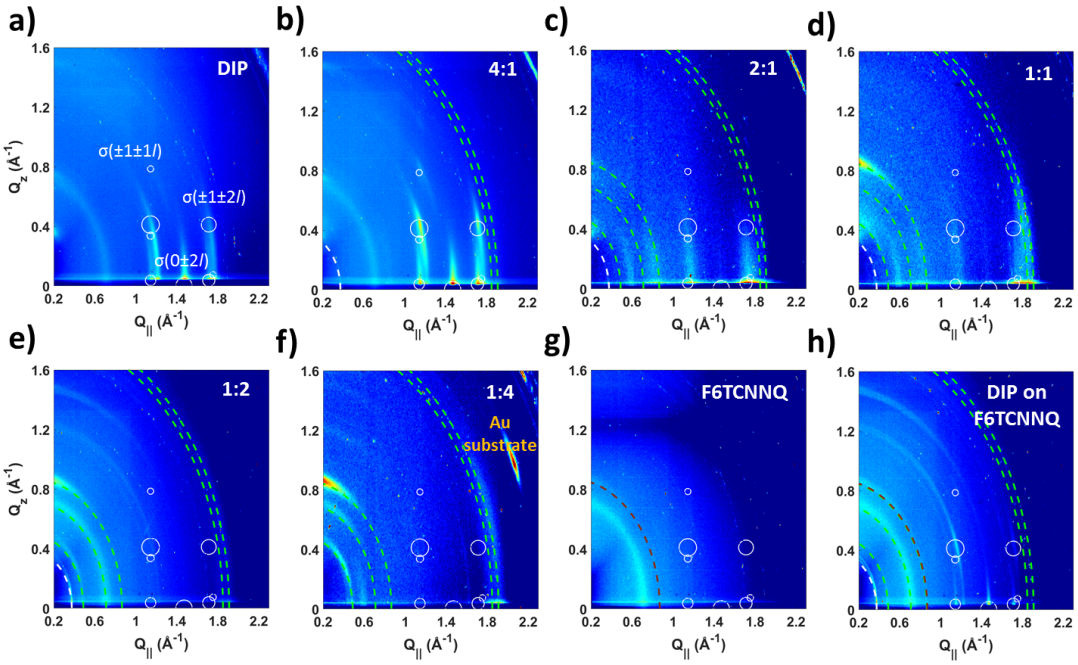

Figure 4.22: Reciprocal space maps of DIP:F6TCNNQ blends in varying mixing ratios grown on Au/SiO_x substrates. The diffraction features, that are expected to be most intense for the thin film phase of DIP in σ-orientation are indicated as white circles with a diameter proportional to the intensity. For pristine DIP, Miller indexes of the corresponding truncation rods according to Ref. [124] are shown. The dashed curved lines indicate specific diffraction features: (001) Bragg peak for the DIP thin film polymorph (white); pristine F6TCNNQ (brown); DIP:F6TCNNQ co-crystal (green). The uniform diffraction ring with a total Q value of 0.71 Å^{-1} comes from a Kapton window in the setup.

the strongest co-crystal diffraction feature along a Debye-Scherrer ring with $Q_{tot} \approx 0.86$ Å^{-1}. Note that the (001) diffraction ring of DIP in λ-orientation disappears due to the large molar excess of F6TCNNQ, that hinders nucleation of a sizable amount of DIP crystallites.

In pristine F6TCNNQ (Fig. 4.22g), only one weak diffraction feature having $Q_{tot} \approx 0.88$ Å^{-1} (brown dashed circle) is visible, pointing towards the coexistence of only few crystallites with amorphous domains. This feature does not match with any feature of the recently published single-crystal structure of F6TCNNQ [198], therefore it must stem from a thin-film phase of F6TCNNQ (see Fig. 3.6d). Notice that the weak diffraction ring might largely overlap with the broadened spot of the co-crystal at $Q_z \approx 0.86$ Å^{-1} in the mixtures with excess F6TCNNQ. Therefore, the presence of phase-separated F6TCNNQ domains in both crystalline and amorphous state in such mixtures seems likely.

We produced also a "planar" D:A interfaces by depositing DIP directly on top of the F6TCNNQ islands (this sample is denominated "DIP on F6TCNNQ", Fig. 4.22h). In contrast to blended films, this architecture allows to "artificially" obtain segregated DIP and F6TCNNQ domains, minimizing the number of interfaces between the two materials. For this sample, DIP exhibits a more random orientation compared to the pristine film, as evidenced by the several diffraction features with nearly ring-like shape. Correspondingly, the (001) diffraction ring having Q_{tot} ~0.38 Å^{-1} is fairly strong and the intensity of the diffraction ring having Q_{tot} ~1.5 Å^{-1} corresponding to the (0 ±2 0) reflection of DIP is higher near $Q_{||} \approx 0.2$ Å^{-1}. This indicates the presence of DIP domain exhibiting a nearly λ-orientation [284]. Only weak diffraction features of the co-crystal are recognizable, mainly the rings having $Q_{tot} \approx 0.48$ Å^{-1} and $Q_{tot} \approx 0.86$ Å^{-1}, the latter being probably overlapped with the stronger diffraction ring from pristine F6TCNNQ at $Q_{tot} \approx 0.88$ Å^{-1}. We conclude that for DIP on F6TCNNQ there are some D:A co-crystallites forming at the D:A interface but, due to the planar architecture, their relative amount is largely outweighed by the domains of the pristine

compounds.

4.4.4 PMIRRAS data for DIP:F6TCNNQ mixtures

Here, we analyze PMIRRAS spectra measured for the DIP:F6TCNNQ blends. We focus on D:A mixing ratio-dependent changes of relative peak intensity and their shifts. We discuss such observations in terms of three distinct factors. First, we point out the effect of molecular orientation. Second, we consider the effect of GS-CT interactions between DIP and F6TCNNQ. Third, we take into account solvent-shifts. We divide the discussion between two spectral ranges. First, we analyze the range ∼1350-1700 cm^{-1}, where the strongest modes are found including C═C stretching for both molecules and in-plane C—H bending for DIP. Secondly, we analyze the range ∼2180-2240 cm^{-1}, where the C≡N stretching modes for F6TCNNQ are found. Subsequently, we analyze the C≡N stretching region for F6TCNNQ in mixtures with P3HT and, finally, we show the spectra for P3HT:F6TCNNQ mixtures in a wider range from ∼1350 cm^{-1} to ∼2250 cm^{-1}.

4.4.4.1 C=C stretching and C-H in-plane bending region for DIP:F6TCNNQ

The PMIRRAS spectra are shown in Fig. 4.23 for the region 1300-1750 cm^{-1}, where vibrational modes are located including C═C stretching and C—H in-plane bending for DIP and endo- and hexo-skeletal C═C stretching for F6TCNNQ. It can be seen that, starting from pristine DIP, the spectra gradually change into the spectrum of pristine F6TCNNQ, which qualitatively confirms the nominal mixing ratios.

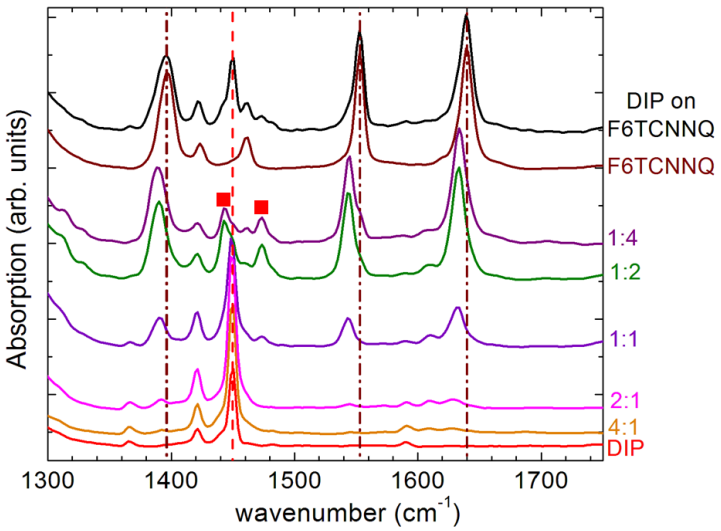

Figure 4.23: PMIRRAS spectra of DIP:F6TCNNQ mixed films and pristine compounds in the region of the skeletal C=C stretching and in-plane C-H bending modes. The brown(red) vertical lines mark the strongest modes of pristine F6TCNNQ(DIP) at 1396.5, 1553 and 1640(1449.5) cm^{-1}. The red squares mark two resonances stemming from DIP in a nearly λ-orientation.

The strongest DIP mode is located at 1449.5 cm^{-1} and is marked in Fig. 4.23 by a vertical dashed red line. According to our DFT calculations (see Fig. 6.22 in Appendix 6.4), this breathing mode has B_{1u} parity and consists only marginally of C═C stretching vibrations of the DIP skeleton; indeed it features mostly in-plane C—H bending of the hydrogen atoms located on the indeno-groups, and has a TDM parallel to the long molecular axis. The weak low-energy shoulder of this peak at 1442.0 cm^{-1} in pristine DIP is not expected from DFT calculations and is therefore attributed to a Davydov splitting of the strongest DIP mode at 1449.5 cm^{-1}. For the 1:2, 1:4 and DIP on F6TCNNQ samples, this shoulder gains oscillator strength relative to the component at 1449.5 cm^{-1}. In these mixtures, an additional peak at 1474.0 cm^{-1} appears, with its shoulder at 1482.5 cm^{-1}. Both features are predicted by DFT and mostly involve in-plane C—H bending of the bonds located on the indeno-groups as well as on the perylene core.

The low-energy Davydov component of the strongest DIP mode at 1449.5 cm^{-1} and the additional peak at 1474.0 cm^{-1} are marked by a red square in Fig. 4.23. These features become stronger relative to the others in the mixtures with F6TCNNQ due to a change in the average orientation of the DIP molecules (see Fig. 6.21 in Appendix 6.4). In the blended films, DIP is embedded either in pristine crystallites or in D:A co-crystallites with F6TCNNQ. From the GIXD data in Fig. 4.22, we have seen that the pristine DIP crystallites undergo an orientation-transition, with a sizable portion of DIP molecules exhibiting a nearly λ-orientation. For the DIP molecules embedded in the co-crystal unit cell, a possible edge-on configuration with a pronounced tilting towards the substrate [162] together with the mosaicity of the co-crystallites (Fig. 4.22f) imply that a high portion of DIP is oriented roughly parallel to the substrate surface. These scenarios, together with the surface selection rules for PMIRRAS, can fully explain the changes in relative intensities of the DIP vibrational modes discussed above.

Table 4.3: Position of F6TCNNQ FTIR peaks in the pristine film and in the mixtures, the latter expressed as DIP:F6TCNNQ molar ratio. All peak positions given in cm^{-1}.

F6TCNNQ	**1:4**	**1:2**	**1:1**	**2:1**	**4:1**
1553.0	1544.0	1544.0	1543.5	1544.0	1545.5
1640.0	1633.5	1633.5	1632.5	1629.0	1628.0
1396.5	1389.5	1390.0	1391.0	1391.0	1392.0

An important observation from Fig. 4.23 is the red-shift of the strongest F6TCNNQ modes when going from pristine F6TCNNQ (or DIP on F6TCNNQ) to the bulk heterostructures. The peak positions are summarized in Tab. 4.3. The weaker peaks at 1424 cm^{-1} and 1461 cm^{-1} in pristine F6TCNNQ do not shift significantly in the bulk mixtures, and the former peak almost overlaps with a resonance of DIP. The red-shift of the strongest F6TCNNQ resonance modes in the bulk mixtures can be rationalized as being induced by GS-CT interactions between the donor DIP and the acceptor F6TCNNQ. Indeed, for all these mixtures the presence of D:A co-crystallites is evidenced by X-ray diffraction (Fig. 4.22b-f). We recall that, in F_4TCNQ single crystals, the position of the peak corresponding to the hexo-skeletal C=C stretching has been found to be heavily affected by GS-CT interactions [332]. For F6TCNNQ, our DFT calculations suggest a different scenario. The three strongest modes indicated above at 1396.5 cm^{-1}, 1553 cm^{-1} and 1640 cm^{-1} are mostly constituted by endo-skeletal C=C stretching vibrations (see Fig. 6.23 in Appendix 6.4). The biggest contribution of the hexo-skeletal C=C bond is found for the resonance of the mode at 1553 cm^{-1} in pristine F6TCNNQ, which also exhibits the largest CT-induced red-shift. Therefore, though in F_4TCNQ mostly the hexo-skeletal C=C stretching is affected, in F6TCNNQ also the endo-skeletal C=C bonds are heavily affected by GS-CT interactions. This might indicate a more effective charge delocalization in the extended quinoid system of F6TCNNQ compared to the smaller F_4TCNQ.

A closer inspection of the data in Fig. 4.23 reveals a high-energy shoulder of the red-shifted F6TCNNQ modes in the bulk mixtures (see Fig. 6.20a,b Appendix 6.4). This shoulder originates from phase-separated F6TCNNQ domains and therefore resembles the position of the vibrations unaffected by CT. As noticed previously, exceeding F6TCNNQ seems to favor nucleation of the co-crystal. Since thin film growth is a non-equilibrium process, nucleation of the co-crystal might be partly suppressed if the amount of F6TCNNQ is insufficient. Therefore, spectral features of phase-separated F6TCNNQ are also observed in the mixtures with excess DIP. We notice that the AFM scans in lock-in phase-shift mode (Fig. 6.18 in Appendix 6.4), especially for the 2:1 film, clearly show the presence of phase-separated F6TCNNQ domains. Inspecting further the data for the DIP on F6TCNNQ sample in Fig. 4.23 reveals the presence of a weak low energy shoulder for some of the strongest C=C stretching modes (see Fig. 6.20c in Appendix 6.4). This shoulder stems from GS-CT interactions within the relatively small amount of D:A co-crystal formed at the interface between F6TCNNQ islands and DIP coating, in agreement with the results from X-ray scattering (Fig. 4.22h).

4.4.4.2 C≡N stretching region for DIP:F6TCNNQ

In Fig. 4.24a the spectral region 2170-2255 cm^{-1} is shown, where the C≡N stretching modes are located. Pristine DIP obviously does not exhibit such kind of vibration. Overall, four peaks are observed, which are numbered in decreasing energy. Already by qualitative inspection of Fig. 4.24 it is possible to notice a gradual red-shift of the resonance modes as function of D:A mixing ratio. We fitted peaks 1-4 with a sum of Lorentzian curves in order to accurately determine their position (see Tab. 6.3 in Appendix 6.4). In the following, we first consider the attribution of these four peaks in detail, then we provide an estimate for the degree of GS-CT in the DIP:F6TCNNQ complex.

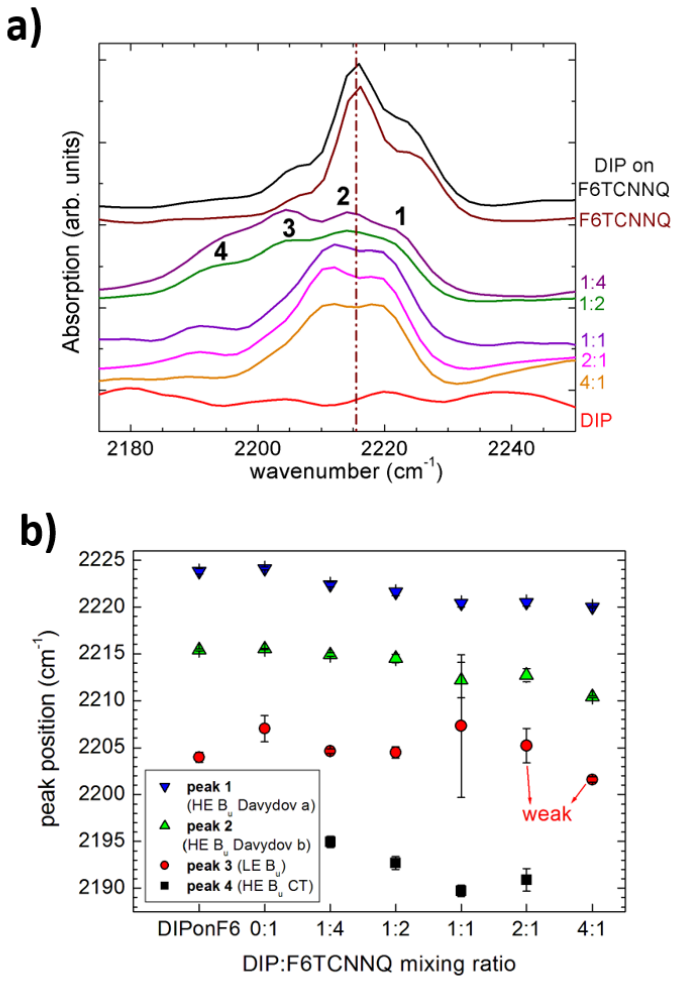

Figure 4.24: **a)** PMIRRAS spectra of DIP:F6TCNNQ mixtures and pristine compounds in the region of the C≡N stretching modes. The vertical dash-dotted line marks 2215.5 cm^{-1}, which corresponds to the strongest Davydov component of the high energy B_u mode in pristine F6TCNNQ. The data have been scaled for better comparability. The resolution of the spectra is 2 cm^{-1}. **b)** Fitted C≡N stretching peak positions. The error bars represent the statistical error of the fits. Abbreviations in the legend based on the DFT calculations for the single molecule: peak 1, Davydov component "a" of the high-energy B_u mode; peak 2, Davydov component "b" of the high-energy B_u mode; peak 3, low-energy B_u mode; peak 4, CT-affected high-energy B_u mode.

Peak assignment Our DFT calculations predict only two antisymmetric C≡N stretching modes for the isolated F6TCNNQ molecule (see Fig: 6.23 in Appendix 6.4). However, the spectrum of the pristine material shows three peaks, as already noticed in Ref. [192]. Based on DFT

calculations, we suggest that peak 1 and 2 are the Davydov components of the stronger high energy mode of B_u symmetry, whereas peak 3 is the weaker, low energy B_u mode. This interpretation is supported by considering the peak distance and width. Peak 1 and 2 are ≈ 7 cm^{-1} apart from each other, and their average position is ≈ 13 cm^{-1} apart from peak 3. This indicates the "finer" character of the Davydov splitting compared to the energy separation between the two modes. Additionally, peak 1 and 2 have nearly the same width in all mixtures.

The change in relative peak intensity of peaks 1-3 as function of D:A mixing ratio can be explained in terms of orientation change of the F6TCNNQ molecules when pristine F6TCNNQ crystallites coexist with DIP:F6TCNNQ co-crystallites. Our DFT calculations show that the two IR-active C$\equiv$N stretching modes in the isolated molecule have their respective transition dipole moment perpendicular to each other (see Fig: 6.23 in Appendix 6.4). Therefore, their relative intensity can be very sensitive to changes in molecular orientation. This effect is similar to what is observed for the C$-$H in-plane bending modes of DIP (Fig. 4.23). As noted above, segregated F6TCNNQ domains can be present even in the mixtures with excess DIP due to both thermodynamic and kinetic factors.

Peak 4 is assigned to the B_u mode red-shifted as a consequence of GS-CT interactions between DIP and F6TCNNQ within a supramolecular D:A complex. In our case, we assume we are able to sensibly detect only the strongest CT-affected B_u mode. The intensity of peak 4 *vs.* DIP:F6TCNNQ mixing ratio matches the trend of the intensity of the X-ray diffraction features for the D:A co-crystal (Fig. 4.22b-f), which supports the assignment.

Evaluation of the degree of GS-CT In Fig. 4.24b the peak positions as function of mixing ratio are shown. Overall, one can see that peak 1 and 2 exhibit a rather monotonic red-shift with increasing DIP content, with their position changing by ~ 5 cm^{-1} at most. The CT-affected peak 4 also exhibits a more or less monotonic red-shift as function of film composition by ~ 5 cm^{-1} as well. We attribute these shifts to the gradual change of the local molecular environment surrounding either F6TCNNQ domains (peak 1 and 2) or DIP:F6TCNNQ co-crystallites (peak 4). Since the crystals are much smaller than the wavelength, an effective medium approximation [144] can be applied for the mixtures of varying D:A ratio, which leads to a solvent-shift. Notice that peak 3 does not exhibit a clear trend with film composition. Note that mode-shifting due to the dielectric properties of the medium affects also the C$=$C stretching region (see Tab. 4.3), but we do not carry out any semi-quantitative analysis using the resonances of this region. We mention that it was noticed in the literature [332, 343] that the cyano-wings in F_4TCNQ are more exposed than the backbone to influences from the surrounding molecular environment.

Due to the observed mixing ratio-dependent position of peak 1,2 and 4, we use the intensity-weighted average position of 2217.3 $\pm$ 1.4 cm^{-1} for peak 1,2 in all films as reference for the zero-CT state (average from pristine F6TCNNQ and all DIP:F6TCNNQ mixtures). The average position of the CT peak is 2192.0 $\pm$ 1.4 cm^{-1}, therefore the experimental CT-induced red-shift is approximately 25 $\pm$ 3 cm^{-1}. Our DFT calculations for the isolated F6TCNNQ mono-anion give a red-shift of 32.5 cm^{-1} for the stronger B_u mode (see Fig. 6.23 in Appendix 6.4). Assuming a linear relationship [155], we calculate a partial CT of $\rho = 0.77 \pm 0.09$ e. This value is somehow higher than the 0.62 e estimated by means of FTIR for a dibenzotetrathiafulvalene (DBTTF):F6TCNNQ complex, in spite of the fact that F6TCNNQ is a stronger acceptor for DBTTF than for DIP [111]. However, also other factors like crystal structure and orbital symmetry [57, 344], beyond the mere HOMO(D)-LUMO(A) energy difference, determine the degree of GS-CT. For our system, averaging over the different mixtures allows to take into account the systematic peak shifts as a function of the mixing ratio and to obtain a number which is less dependent of it. Overall, it is possible to say that the supramolecular complex formed by DIP and F6TCNNQ belongs to the class of compounds exhibiting high degree of partial GS-CT.

4.4.5 PMIRRAS data for P3HT:F6TCNNQ mixtures and comparison with DIP:F6TCNNQ mixtures

For comparison, we consider now P3HT (Fig. 4.21) as donor for F6TCNNQ as recently introduced in Ref. [192]. We divide the discussion into two sections dedicated, respectively, to the analysis of the C$\equiv$N stretching region alone and to the parallel analysis of the C$\equiv$N and C$=$C stretching regions.

4.4.5.1 Comparison of C≡N stretching region

In order to add some information to the interesting D:A system represented by P3HT:F6TCNNQ [192], we show in Fig. 4.25 a comparison between the PMIRRAS spectra in the C≡N stretching region for pristine F6TCNNQ, DIP:F6TCNNQ 1:1 and P3HT:F6TCNNQ blends in different mixing ratios and preparation times, as specified in the figure caption.

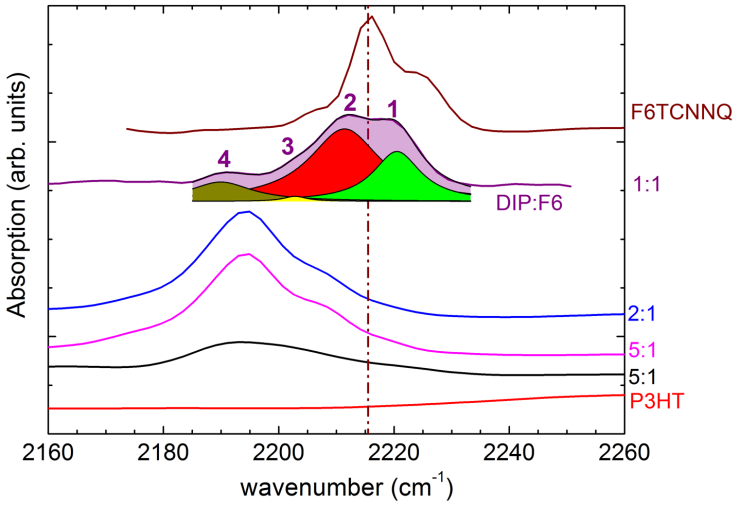

Figure 4.25: PMIRRAS spectra of DIP:F6TCNNQ 1:1 blend, P3HT:F6TCNNQ blends and pristine F6TCNNQ and P3HT in the C≡N stretching region. For the DIP:F6TCNNQ 1:1 blend, the same peak numbering as in Fig. 4.24 has been adopted, and the multi-peak Lorentzian fit is shown. The P3HT:F6TCNNQ blends in different molar ratios have been spin-coated from solutions with different mixing time: 5:1 (black curve), 30 min; 5:1 (magenta curve), 72 h; 2:1, 30 min. The vertical dash-dotted line marks 2215.5 cm^{-1}, which corresponds to the strongest Davydov component of the high energy B_u mode in pristine F6TCNNQ.

In P3HT:F6TCNNQ there is barely any trace of peak 1-3 of the pristine acceptor. The solution mixing seems therefore effective in dissolving the F6TCNNQ molecules between the polymer chains without leaving F6TCNNQ aggregates, as it is also confirmed by the increasing peak sharpness with longer mixing time for the 5:1 mixtures. The strongest C≡N stretching peak in all P3HT:F6TCNNQ blends is located at 2194 cm^{-1}. The same uncertainty in peak position obtained for DIP:F6TCNNQ mixtures can been assumed for the P3HT:F6TCNNQ mixtures. The high-energy shoulder of the peak at 2194 cm^{-1} in the mixtures might originate from different relative configurations of the complex formed locally by P3HT and F6TCNNQ [345]. Here, the most important finding is that the CT-affected C≡N stretching mode in P3HT:F6TCNNQ lies approximately at the same position as the CT peak in DIP:F6TCNNQ with no significant differences.

By the mere comparison of the C≡N stretching modes, the conclusion would be that GS-CT interactions in the two systems have very similar strength. However, the UV-vis-NIR absorption measurements presented in the literature [192] clearly show the presence of the anionic species of both donor and acceptor for P3HT:F6TCNNQ [53, 140], which is not the case for DIP:F6TCNNQ [162]. Therefore, two different scenarios are suggested. For DIP:F6TCNNQ, the data point towards the formation of a supramolecular complex with partial GS-CT, whereas for P3HT:F6TCNNQ integer GS-CT with formation of polaronic species of donor and acceptor is most likely. An integer CT picture in P3HT:F6TCNNQ is further supported by the established full ionization of donor and acceptor in F_4TCNQ-doped P3HT [140], considering that F6TCNNQ is an acceptor even stronger than F_4TCNQ. Overall, one has to conclude that the shift of the C≡N stretching modes alone does not give conclusive information about the nature of GS-CT interactions in P3HT:F6TCNNQ.

4.4.5.2 Comparison between C=C and C≡N stretching regions

In order to complement the information on P3HT:F6TCNNQ, wide-range PMIRRAS spectra are shown in Fig. 4.26 for the same samples as in Fig. 4.25.

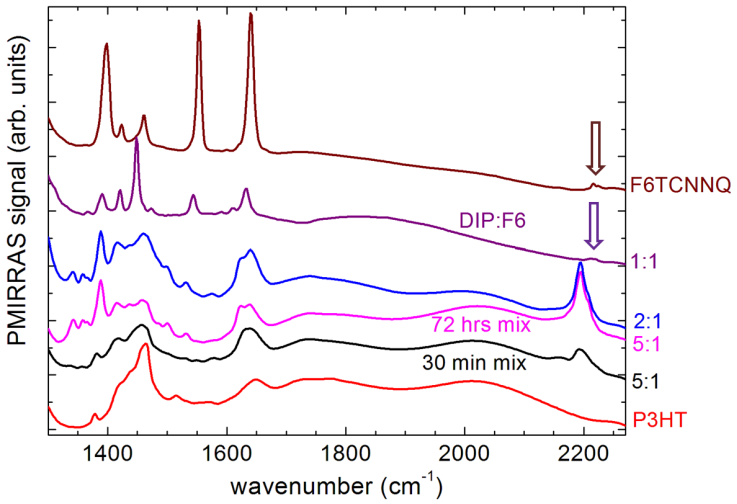

Figure 4.26: PMIRRAS spectra of DIP:F6TCNNQ 1:1 blend, P3HT:F6TCNNQ blends and pristine F6TCNNQ and P3HT. The arrows point to the C≡N stretching modes for DIP:F6TCNNQ 1:1 and pristine F6TCNNQ, which appear as tiny features relative to the much stronger C=C stretching modes in the fingerprint region.

For the P3HT:F6TCNNQ blends, assignment of the peaks in the C=C stretching region to either the donor polymer or the acceptor is not as straightforward as in DIP:F6TCNNQ. Here, we rather intend to stress the remarkable change in intensity of the C≡N stretching features relative to the C=C stretching features for the two systems DIP:F6TCNNQ and P3HT:F6TCNNQ, respectively. For the mixtures containing DIP as donor, the C≡N stretching modes exhibit a much lower cross-section relative to the C=C stretching modes, whereas in the polymeric system their relative intensity is similar. Such an effect is clearly not related to changes in molecular orientation of the F6TCNNQ units. Indeed, the mosaicity of locally ordered P3HT chains doped with F_4TCNQ [345] is similar to that of the DIP:F6TCNNQ co-crystals (Fig. 4.22) observed here.

Our DFT calculations performed on the isolated F6TCNNQ molecule (see Fig. 6.23 in Appendix 6.4) show that the intensity of the resonances in the C=C stretching region relative to the C≡N stretching region is much higher for the neutral F6TCNNQ than for its mono-anion. This corresponds to the experimental observation for P3HT:F6TCNNQ mixtures and further supports the conclusion that CT from P3HT to F6TCNNQ occurs in the GS *via* donation of a full electron and formation of polaronic species. DIP:F6TCNNQ is therefore a system for which a relatively strong GS-CT is observed, but the spectral features peculiar of the ionic species are not observed. Assuming for both D:A systems an energetically favored electron donation from the donor to the acceptor (Fig. 4.21), the different kinds of GS-CT, respectively, might be explained by the superior ability of P3HT to relax the positive counterpart of the generated polaron *via* charge delocalization along the polymeric backbone [346, 347].

The difficulty to obtain a reliable picture of the actual strength of GS-CT interactions in P3HT:F6TCNNQ from the C≡N stretching modes alone can be rationalized as follows. On the one hand, the impact of an integer CT on a given set of vibrational modes will depend on where the negative charge acquired by the acceptor is most likely localized. On the other hand, the two kinds of vibrations in F6TCNNQ, i.e. C=C and C≡N stretching, could be affected differently by GS-CT interactions depending on the solid state packing of the acceptor, which in one case is embedded in the co-crystal with DIP and in the other case in the polymer chains. For example, short (donor)C—H···N≡C(F6TCNNQ) contacts [199] more than the π-stacking might affect the C≡N stretching modes, whereas intermolecular D:A coupling, therefore also GS-CT coupling, occurs mainly *via* the π-stacking.

4.4.6 Summary of the results and possible applications

In conclusion, we show a comparative study of two representative D:A systems, DIP:F6TCNNQ and P3HT:F6TCNNQ. Characterization of the structure of DIP:F6TCNNQ films guides the interpretation of the FTIR-PMIRRAS spectra. This technique delivers an excellent signal-to-noise ratio and cancels out the signal from atmospheric gases, enabling the investigation in atmosphere of samples with very small amounts of material also in the fingerprint region. Inspection of the C=C stretching C—H bending region in DIP:F6TCNNQ blends reveals: a) the effect of molecular orientational changes on the relative intensity of the Davydov components of the strongest DIP mode, b) red shifts up to 10 cm^{-1} of the strongest modes of F6TCNNQ involving mostly endo-skeletal bonds. Such shifts are related to the formation of a DIP:F6TCNNQ supramolecular complex and to GS-CT interactions. Together with D:A co-crystallites, traces of phase-separated F6TCNNQ are detected in all the blends. In the C≡N stretching region, for DIP:F6TCNNQ we unambiguously identify one red shifted CT-affected mode, together with other three modes stemming from pristine F6TCNNQ, one of them being the strongest B_u mode affected by Davydov splitting. From the red shift of the C≡N stretching averaged over all mixtures we estimate a CT of $\rho = 0.77 \pm 0.09$ electrons.

For the D:A system P3HT:F6TCNNQ, we first consider shifts of the strongest C≡N stretching mode, which delivers a picture of GS-CT interactions very similar to DIP:F6TCNNQ. Conversely, a cross-comparison of oscillator strength for C=C relative to the C≡N stretching modes rather points towards stronger, integer CT-type interactions in the polymeric system, which agrees with the available UV-vis-NIR optical absorption data showing the presence of ionic species in P3HT:F6TCNNQ. These findings evidence that, apart from the exclusive analysis of the modes in the C≡N stretching region, a parallel inspection of the C=C stretching region is required to draw more solid conclusions about the nature of GS-CT in D:A systems. Such a cross-analysis is readily made possible by the use of PMIRRAS, which allows to collect reliable information also in the fingerprint region.

We envisage the use of PMIRRAS for the study of a wide variety of systems of potential interest for optoelectronic applications. We take as an example singlet fission, an efficient energy-conversion process which has been exploited in combination with Si-based solar cells to extend the harvested portion of sunlight towards longer wavelengths [328]. It has been shown, both theoretically [348] and experimentally [349], that the yield of singlet fission processes can be affected by the selective excitation of given vibrational modes in molecular semiconductors. The possibility to select the orientation of rod-like OSCs, as demonstrated in the Results section 4.3, in combination with the surface selection rules in PMIRRAS experiments allows to excite only a given set of molecular vibrations [350] , which might become a valuable tool to characterize systems capable of singlet fission.

The combination of molecular orientation and PMIRRAS is of special interest also for the characterization of charge transport due to the typically strong coupling between vibrations and carrier dynamics (see Fundamentals section 2.1). Indeed, for the prototypical OSC PEN it has been shown that vibrational modes along the long molecular axis contribute to charge transport more than modes along the short axis [351]. Such anisotropy of the contributions to charge transport is to be expected for a variety of rod-like OSCs and is therefore subject to be explored in greater detail thanks to the results obtained in the present and in the previous Results section 4.3.

4.5 Further donor:acceptor combinations [7]

We present a systematic study of the two donors DIP and DBTTF (Fig. 3.4a), each combined with the two acceptors TCNNQ (Fig. 3.7) and F6TCNNQ. For all these D:A combinations, the formation of CT complexes has been observed in the literature [111, 162, 274]. We divide our discussion based on the material used as donor, i.e. DIP or DBTTF.

In the first part, we compare DIP:TCNNQ to DIP:F6TCNNQ mixed films. The latter combination has been thoroughly studied throughout this thesis and some relevant data are presented again for comparison with DIP:TCNNQ. In particular, we study here the structural properties, including mixing behavior, i.e. co-crystal formation *vs* phase separation, and their impact on electrical conductivity. In the second part, we study the crystal structure of DBTTF and its co-crystals with TCNNQ and F6TCNNQ, respectively, by means of GIXD. The X-ray scattering data allow to fit the unit cell parameters of the DBTTF thin-film polymorph and of one polymorphic form of the DBTTF:TCNNQ co-crystal. For the DBTTF:F6TCNNQ co-crystal, the film texture does not allow to unambiguously fit the unit cell parameters. However, a qualitative comparison allows to draw some conclusions concerning the arrangement of the D:A supramolecular complexes in the respective unit cell.

4.5.1 Mixing behavior and electrical conductivity. DIP as donor, TCNNQ *vs.* F6TCNNQ as acceptors.

The energy diagram of DIP and and [F6]TCNNQ is shown in Fig. 4.27 for the frontier orbitals which we assume to have the strongest coupling in GS-CT.

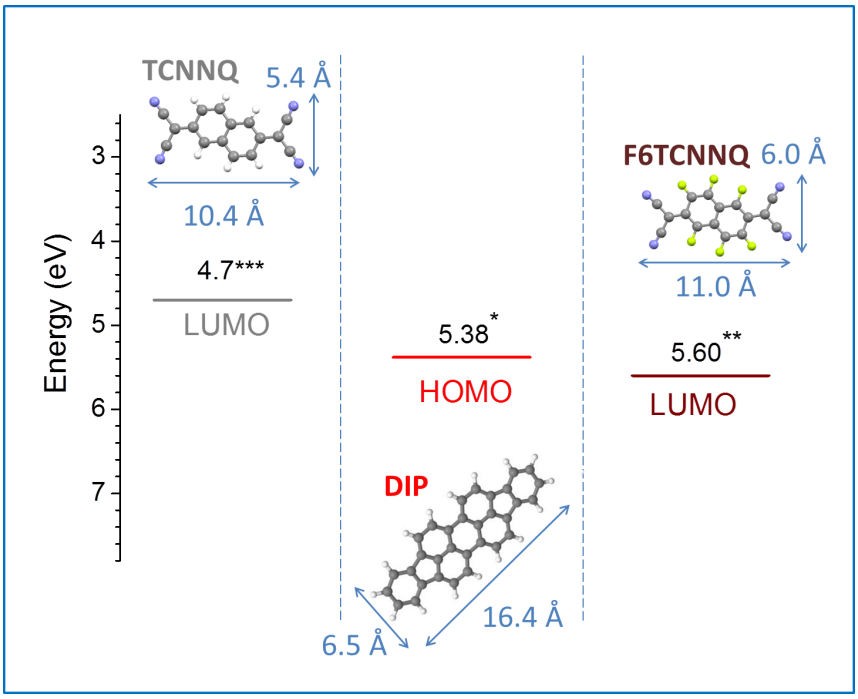

Figure 4.27: Energy levels and molecular structure of DIP, TCNNQ and F6TCNNQ. The HOMO and LUMO values were obtained by means of photoelectron spectroscopy for samples in solid films: * Ref. [262], from UPS measurements for standing-up molecules; ** Ref. [53], from IPES measurements; *** from Ref. [352], from IPES measurements. All values given as peak onsets.

As it can be seen, the HOMO level of DIP lies much closer to the LUMO of F6TCNNQ than of TCNNQ. From the frontier orbital energies one can therefore expect that GS-CT interactions between DIP and F6TCNNQ are stronger than between DIP and TCNNQ. The molecular structure

[7] Based on A. Opitz, in preparation

of the two acceptors is very similar apart from the nature of the substituent atoms. Replacing H with F on the conjugated core shifts the energy levels towards higher binding energies, with the effect, among others, of preventing oxidation [353, 354]. The electrostatic interactions with DIP might also be significantly affected, in particular showing interaction between static dipoles, for example of the kind C–H···F [199]. Overall, stronger DIP:F6TCNNQ than DIP:TCNNQ interactions are expected based on the energy-level alignment as well as on electrostatic arguments.

4.5.1.1 Thin Film structure

OMBD was used to prepare several D:A mixtures on native Si oxide, featuring DIP as donor and [F6]TCNNQ as acceptors in different mixing ratios, spanning a range from excess of the donor to excess of the acceptors. We show in Fig. 4.28a-d X-ray scattering data for the two series of mixtures. The XRR and GIXD data for DIP:F6TCNNQ are reproduced from Fig. 4.2.

We first analyze the X-ray scattering data for the DIP:TCNNQ mixtures. The diffraction features of DIP do not disappear by increasing the relative content of TCNNQ, as it can be seen in both the series of XRR and GIXD scans (Fig. 4.28a,c). This clearly indicates that DIP crystalline domains phase-separate from TCNNQ, at least in part. The XRR scans of all films containing DIP show Bragg peaks of phase-separated donor crystallites. For the 4:1 and 1:1 mixtures these peaks also show pronounced Laue side-fringes, indicating a vertical coherence length matching the entire film thickness as deduced from the Kiessig fringes. The latter are quite pronounced and, remarkably, demonstrate that also for DIP:TCNNQ the mechanisms of film smoothing in bulk heterojunctions is effective (see Results section 4.2). In the GIXD scan of the 1:2 mixture, the DIP Bragg peaks are sharper than in the mixtures with lower amount of the acceptor. For this mixing ratio, the excess of TCNNQ seems to promote a larger coherent size of the phase-separated DIP crystallites. The DIP Bragg peaks in the GIXD scans labeled "λ" stem from orientations of the DIP molecules different from the upright-standing (σ). The presence of a sizeable amount of DIP crystals in a nearly λ-orientation is peculiar of the DIP:TCNNQ mixed films and had not been observed for the DIP:F6TCNNQ films. The XRR of pristine TCNNQ does not denote any out-of-plane ordering, similar to pristine F6TCNNQ. However, in the GIXD of pristine TCNNQ several pronounced Bragg peaks are visible. These peaks can be found in part in the 1:1 and 1:2 mixtures, denoting here the presence of pristine TCNNQ crystalline domains. Some of the new peaks arising in the mixtures and not visible in the pristine films are attributed to a DIP:TCNNQ co-crystal (dashed green lines in Fig. 4.28a,c). In particular, the peaks in the range $Q_{||} = 1.85 - 1.95$ Å^{-1} are indicative of distances in real space that correspond to the stacking between the π-conjugated cores of donor and acceptor. A peak in this range of $Q_{||}$ is also visible for pristine TCNNQ and it might be therefore overlapped with the peaks from the co-crystal. The different crystal phases constituting the DIP:TCNNQ equimolar film are sketched in Fig. 4.28e. The red, gray and green domains represent DIP, TCNNQ and co-crystal grains, respectively. Phase-separated crystalline domains of different composition coexist. This scenario is similar to what observed for 6T:F6TCNNQ mixtures (Fig. 4.5e).

For the mixing behavior of the D:A pair DIP:F6TCNNQ (Fig. 4.5d), we recall the formation of homogeneous crystalline domains of the D:A co-crystal for equimolar mixtures, as sketched in Fig. 4.28f. This conclusion comes from inspection of the data in Fig. 4.28b,d. The diffraction features stemming from DIP gradually disappear going from the mixtures with DIP excess towards mixtures with F6TCNNQ excess. At the same time, new Bragg peaks arise which indicate the formation of a new crystal structure, namely, a D:A co-crystal where fairly strong GS-CT interactions take place (see Results section 4.4) within a D:A supramolecular complex. Therefore, for DIP:F6TCNNQ films the composition of the equimolar mixture is homogeneous and features only co-crystal domains.

The findings for DIP:[F6]TCNNQ can be ascribed to the D:A energy level alignment and, likely, electrostatic attraction between DIP and F6TCNNQ, both increasing the free energy gain for co-crystal formation (see Eq. 2.6), outweighing possible kinetical limitations due to, e.g., low diffusivity of F6TCNNQ [193]. Conversely, the coupling between DIP and TCNNQ is not sufficiently strong and kinetic factors partly outweigh the tendency to co-crystal formation, which nevertheless takes place as deduced from X-ray scattering.

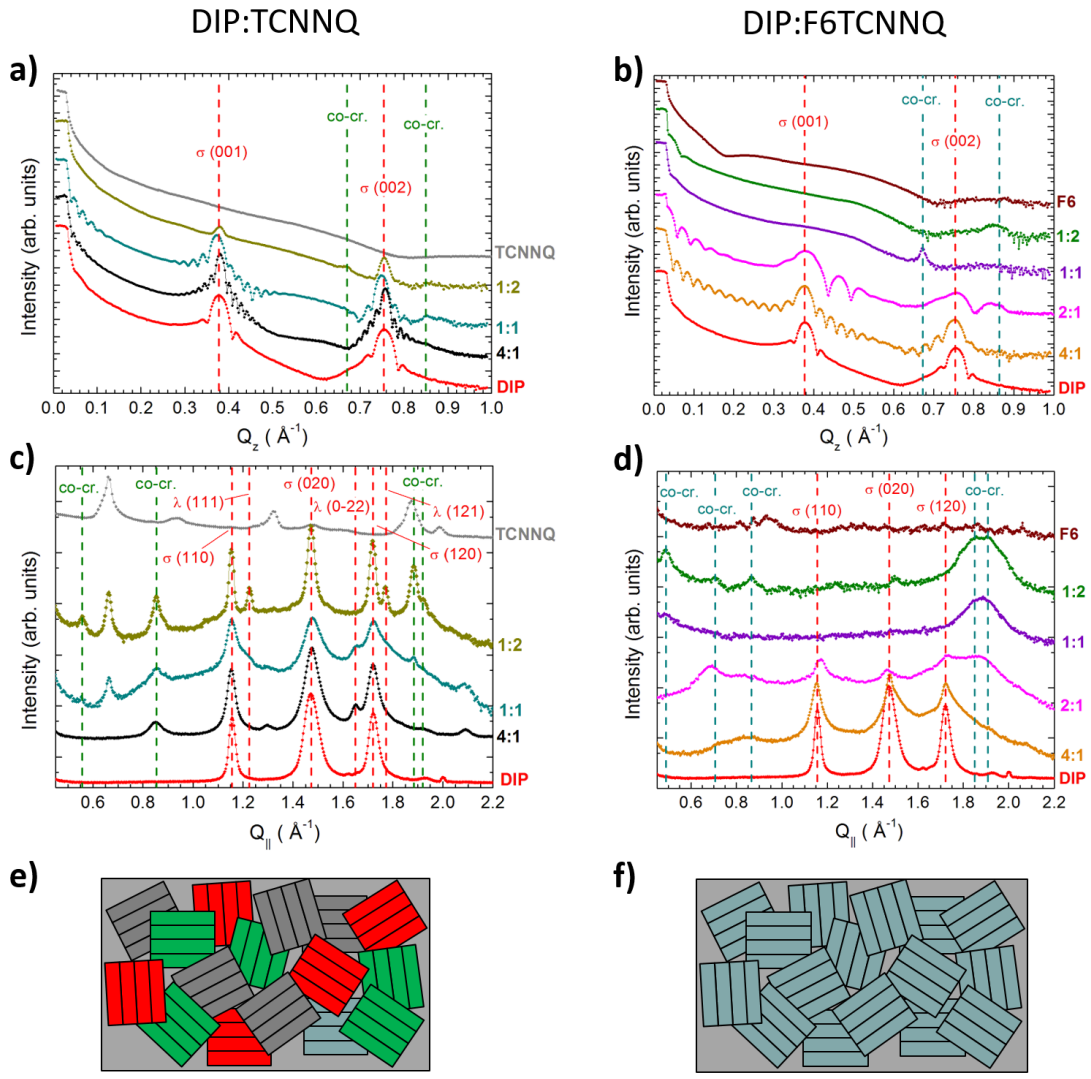

Figure 4.28: **a)** XRR and **c)** GIXD data for DIP:TCNNQ, **b)** XRR and **d)** GIXD data for DIP:F6TCNNQ mixtures in different mixing ratios as indicated. The data for DIP:F6TCNNQ are reproduced from Fig. 4.2, with the same meaning of the vertical dashed lines. For DIP:TCTNNQ mixtures, the vertical dashed lines indicate Bragg peaks attributed to DIP (red, where "σ" and "λ" refer to the molecular orientation) and to the DIP:TCNNQ co-crystal (green), respectively. Vertical lines corresponding to the Bragg peaks of the pristine acceptors have been omitted for clarity. **e)**,**f)** Sketches of mixing behavior for **e)** DIP:TCNNQ and **f)** DIP:F6TCNNQ films in a 1:1 mixing ratio. The squares represent crystallites with random in-plane orientation and their color corresponds to a given phase, as explained in the text.

4.5.1.2 Electrical conductivity

Electrical conductivity was measured by means of the setup illustrated in Fig. 3.29. The results are shown in Fig. 4.29a for both D:A pairs in several mixing ratios. To perform these measurements, thin films were deposited on both ITO contacts and supporting glass substrate, whereas the X-ray scattering data shown in the previous section were taken for samples on Si oxide. However, based on results from the literature [119, 168] we assume that the different substrate does not significantly affect the mixing behavior.

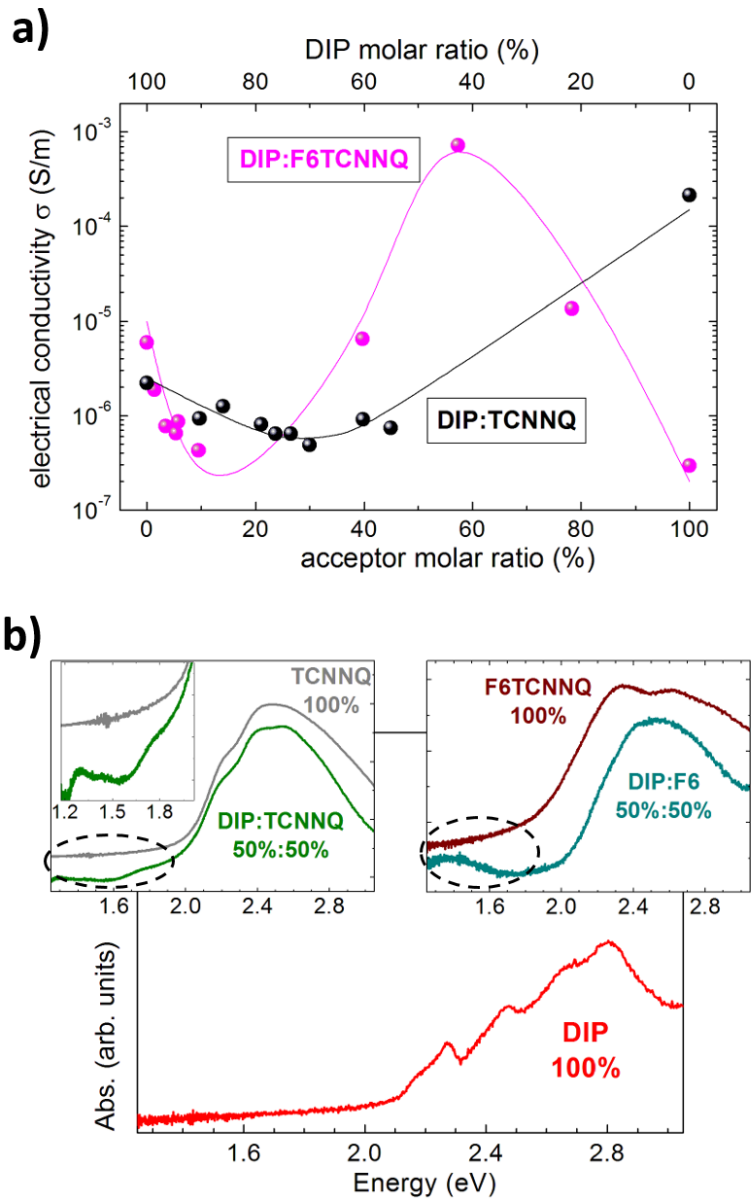

Figure 4.29: **a)** Electrical conductivity as function of D:A mixing ratio for DIP:[F6]TCNNQ mixtures. The dots represent experimental points and the continuous lines are guides to the eye. The error on the D:A mixing ratio is ±10%. These data were partly taken from Ref. [259] and partly are for courtesy of P. Beyer and A. Opitz (Humboldt Universität zu Berlin). **b)** UV-vis absorption measurements showing for both D:A couples the presence of new absorption features below the bandgap of the pristine compounds, denoting CT interactions within the respective D:A co-crystal.

The conductivity in pristine DIP is lower than in pristine TCNNQ, but higher than in pristine F6TCNNQ. In order to explain this, the morphology, structure and energy levels of the pristine films would need to be taken into account. The film morphology of pristine TCNNQ and F6TCNNQ is very similar, in both cases exhibiting pronounced de-wetting with separated islands [111]. The crystalline film texture of the two acceptors resembles a 2D-powder with some mosaicity for TCNNQ (Fig. 4.34a), and a 3D-powder, i.e. an isotropic crystalline network, for F6TCNNQ (Fig. 4.34b). Two further aspects concern: a) the nature of the charge carriers, b) the relative alignment of the transport levels of the OSCs with the Fermi level of ITO, which has a work function of $\sim$ 4.5 eV [355]. However, the detailed investigation of these aspects go beyond the

scope of this thesis. More relevant is the trend of the electrical conductivity, σ, *vs.* D:A mixing ratio, which we discuss below.

The conductivity for the mixed films exhibits a distinct behavior depending on the acceptor used. For DIP:F6TCNNQ, going from pristine DIP ($\sigma \sim 6 \times 10^{-6}$ S/m), after a steep decrease a minimum of $\sim 4 \times 10^{-7}$ S/m around 10% of acceptor content is reached. Afterward, the conductivity increases and reaches a maximum of $\sim 7 \times 10^{-4}$ S/m around 60% of acceptor content, dropping again for larger F6TCNNQ amounts until the lowest conductivity of $\sim 3 \times 10^{-7}$ S/m is reached for pristine F6TCNNQ. Notice that the common observation for molecularly doped OSCs is that the conductivity exhibits a maximum between few percent and ∼50% of molar ratio of the dopant [48, 49, 55, 111, 356]. This is the result of a balance between the decrease of charge mobility due to deterioration of the crystalline quality of the films with increasing amount of acceptor [356], on one side, and the increase of carrier density due to doping (see Eq. 2.9), on the other side. Both systems studied here deviate from this behavior.

For DIP:TCNNQ mixtures, the presence of a local minimum instead of a maximum is likely related to the partial phase-separation of donor and acceptor as deduced from X-ray scattering (Fig. 4.28e). Only a portion of the theoretically available D:A supramolecular complexes with consequent partial GS-CT is formed, leading to the presence of D:A co-crystallites dispersed between crystallites of the pristine materials. The new transitions observed in the UV-Vis-NIR spectra in Fig. 4.29b for a DIP:TCNNQ film in a 1:1 mixing ratio (or, analogously, 50%:50%) further demonstrate the presence of DIP:TCNNQ co-crystals. Due to the phase heterogeneity in DIP:TCNNQ mixtures, a diffusing charge carrier has a high probability to encounter an interface with a different crystalline phase, which represents an energetic barrier due to unfavorable alignment of the transport levels. Therefore, although formation of a DIP:TCNNQ supramolecular complex, which can dope the surrounding donor matrix [48], is observed, transport is more hindered in the mixtures compared to pristine DIP and TCNNQ due to the unfavorable energetic alignment of heterogeneous crystallites, which leads to scarcity of available charge percolation paths to the contacts.

As noted above, for DIP:F6TCNNQ a maximum around 1:1 D:A mixing ratio located between two minima is observed. To the best of our knowledge, this behavior is reported for the first time in OSCs. It seems quite straightforward to attribute this trend to the presence of homogeneously distributed D:A co-crystallites in 1:1 stoichiometry with no sizeable hint of phase-separation. For a DIP:F6TCNNQ mixing ratio of 1:1, the film is constituted of D:A co-crystals with a preferred uniaxial alignment, such that the π-stacking direction between donor and acceptor is roughly parallel to the substrate surface. The initial deterioration of the crystalline texture of pristine DIP by admixing of F6TCNNQ in few percent is largely compensated by the alignment of the co-crystals around 50% mixing ratio. New sub-bandgap optical transitions are observed as a result of CT interactions (Fig. 4.29b). Therefore, the strong CT interactions between DIP and F6TCNNQ seem to lead to a high doping efficiency, and the uniaxial alignment of the DIP:F6TCNNQ co-crystallites favors charge transport in the direction parallel to the substrate. Note that the conductivity behavior for DIP:F6TCNNQ mixtures seems to contradict the idea that the co-crystallites act as dopants for the OSC matrix [48]. However, such mechanism might not represent the only one at work, and the concomitant evolution of film crystalline structure and morphology might give rise to very complex scenarios.

4.5.2 Crystal structure and polymorphism. DBTTF as donor, TCNNQ *vs.* F6TCNNQ as acceptors

In this section, we consider the effect of the two different donors TCNNQ and F6TCNNQ on the structural properties of mixed films with the donor DBTTF. The energy diagram of DBTTF and and [F6]TCNNQ is shown in Fig. 4.30.

In Ref. [111], the formation of a DBTTF:TCNNQ complex is observed. From optical measurement it is deduced that the corresponding DBTTF:TCNNQ co-crystal exists in two polymorphs, respectively P1 and P2, although no X-ray scattering data are provided to identify the two crystal structures. Here, we provide some structural evidence which points towards the coexistence of P1 and P2 in the same film, although one polymorph dominates. Indeed, the difference in free energy between two polymorphic forms of the same co-crystal can be very small [76, 77] and the nucleation of a second polymorph might be provoked by local inhomogeneities in the surface potential, or might be a surface-effect. Also, subtle changes in the deposition rate of the molecular

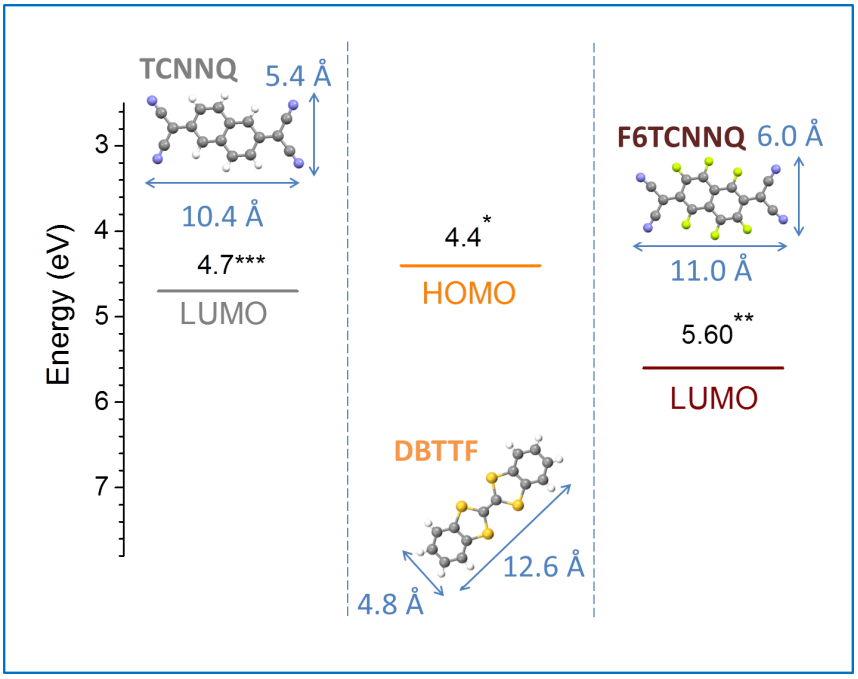

Figure 4.30: Energy levels and molecular structure of DBTTF, TCNNQ and F6TCNNQ. The HOMO and LUMO values were obtained by means of photoelectron spectroscopy for samples in solid films: * Ref. [357, 358], from UPS measurements; ** Ref. [53], from IPES measurements; *** from Ref. [352], from IPES measurements. All values given as peak onsets.

components have an effect on promoting the nucleation of either polymorph [111].

For the D:A pair DBTTF:F6TCNNQ, it has been observed that both integer and partial GS-CT occur in thin films thanks to the large energy gain for CT from the HOMO of DBTTF to the LUMO of F6TCNNQ (Fig. 4.30). It is known that not only energy level alignment, but also orbital symmetry is crucial to determine the degree of orbital overlap for the formation of a CT complex [57], which poses some requirement to the geometry of the molecular components. The two acceptors used here are planar and have the same symmetry, which allows to rule out arguments concerning molecular geometry from the discussion of the CT strength. Also in DBTTF:F6TCNNQ, partial GS-CT occurs *via* formation of a supramolecular complex [111]. A higher conductivity is measured in DBTTF:F6TCNNQ films compared to DBTTF:TCNNQ at 10% of acceptor content, which is attributed to the more efficient doping achieved *via* integer CT than *via* formation of a supramolecular complex. An integer-type GS-CT from the DBTTF units to F6TCNNQ is suggested to be favored by structural defects, which hinder the π-stacking configuration required for the formation of a CT complex and favor full ionization. The structural characterization presented in this section provides a further clue to clarify this point.

4.5.2.1 Unit cell parameters of the DBTTF thin-film phase

We first consider the crystal structure of pristine DBTTF. As mentioned in the Materials and Methods section, several polymorphs have been reported for this material. Ref. [129] contains a compendium of the polymorphs observed so far, and demonstrates that they can be discriminated by analysis of the lattice phonons by means of Raman spectroscopy. In particular, for thin films obtained by vacuum deposition and drop casting, the thin-film phase of DBTTF (or γ-polymorph) is identified. XRR and GIXD are then measured there for the γ-polymorph, but no details of the crystal structure are reported.

In Fig. 4.31 we show X-ray scattering data of a pristine DBTTF film. Next to the reciprocal space map, XRR scans are reported. The orange trace is the reflectivity scan measured on the same film as the Q-map, whereas the green trace has been reproduced from an out-of-plane scattering pattern from Ref. [129]. As it is evident, the positions of the out-of-plane Bragg peaks coincide.

In the Q-map, the Bragg peaks are sharp and denote a pronounced 2D-texture of the film with low mosaicity. The positions of several peaks around the sample horizont matches those extracted from an in-plane diffraction pattern measured in Ref. [129] (data not shown). Together, these data confirm that we have the same γ-polymorph observed in Ref. [129], which thus corresponds to the thin-film phase.

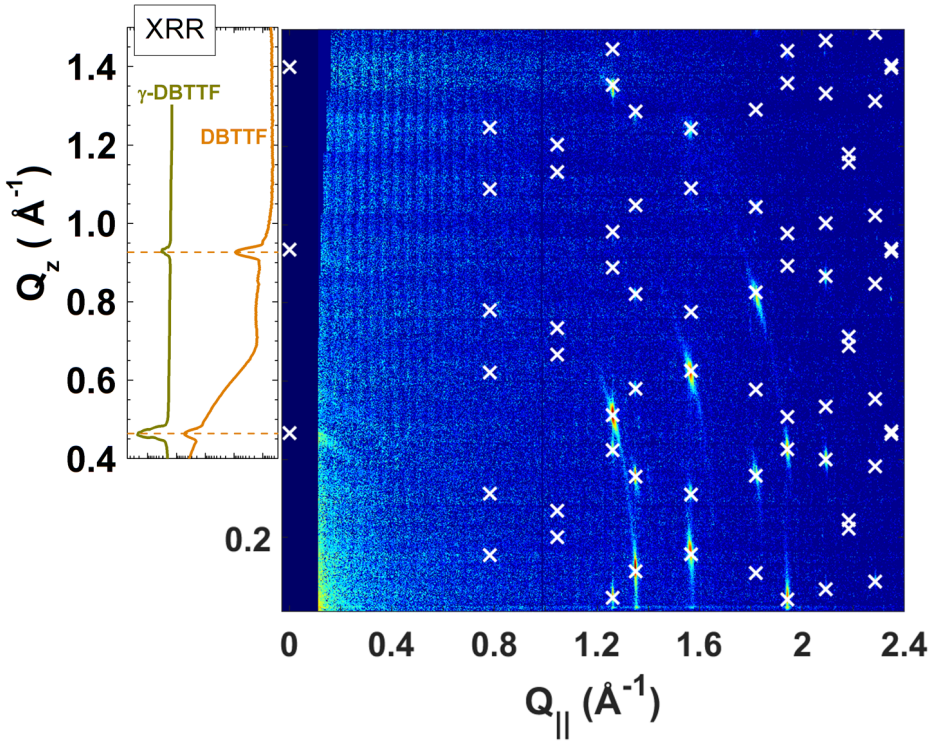

Figure 4.31: Reciprocal space map (right panel) and XRR scan (left panel) of pristine DBTTF films. The white crosses in the Q-map mark the fitted positions of the Bragg peaks. In the XRR scans, the green trace was reproduced from an out-of-plane scan of the γ-polymorph in Ref. [129].

The well-defined crystalline texture of this film allows to fit the position of the Bragg peaks in order to extract the unit cell parameters of the thin-film polymorph of DBTTF. As a starting guess, we used the unit cell of a tetrathiafulvalene derivative, (ethyl-enethio)(thiodimethylene)-tetrathiafulvalene (ETTDM-TTF), reported in Ref. [359]. The fitted unit cell parameters are reported in Tab. 4.4.

Table 4.4: Fitted unit cell parameters of thin film phase (or γ-polymorph) of DBTTF (Fig. 4.31).

parameter	**size [units]**
a	6.02 [Å]
b	8.05 [Å]
c	13.90 [Å]
α	100.29 [°]
β	99.90 [°]
γ	94.00 [°]
volume	649.09 [Å^3]

Comparing the unite cell volume reported in Tab. 4.4 with that of the α-polymorph reported in Refs. [188, 189], we deduce that also the the thin-film phase features two molecules in the unit cell. Interestingly, the latter is triclinic like the one of the known DBTTF δ-polymorph [190], whereas both the known α [188, 189] and β-polymorphs [129] have a monoclinic unit cell. However, by solely

fitting the Bragg peaks positions it is not possible to access the detailed molecular arrangement. This would require modeling of the structure factor, with inclusion of several corrections related to the data acquisition, in order to correctly reproduce peak intensity [135, 136], which is beyond the scope of this thesis.

4.5.2.2 Polymorphs of the DBTTF:[F6]TCNNQ co-crystals

In order to structurally resolve the presence of two polymorphs for the DBTTF:TCNNQ co-crystal, we show in Fig. 4.32 X-ray scattering data of a blended DBTTF:TCNNQ film in a 1:1 molar ratio.

Next to the reciprocal space map, an XRR scan of the same film is reported. Due to the overall higher mosaicity of the co-crystallites in this mixed film compared to pristine DBTTF (Fig. 4.31), part of the intensity of the XRR peaks is visible in the Q-map. Overall, the film exhibits a 2D-texture and the clear diffraction features allow to fit peak positions. As starting guess, we used the unit cell of the DBTTF:F4TCNQ co-crystal reported in Ref. [200]. The fitted unit cell parameters are reported in Tab. 4.5. The unite cell volume is similar to that of the NDT:F6TCNNQ co-crystal from Ref. [199] containing alternated DADA···DADA stacks and 2 NDT:F6TCNNQ dimers per unit cell. We therefore suggest for the DBTTF:TCNNQ a similar packing motif.

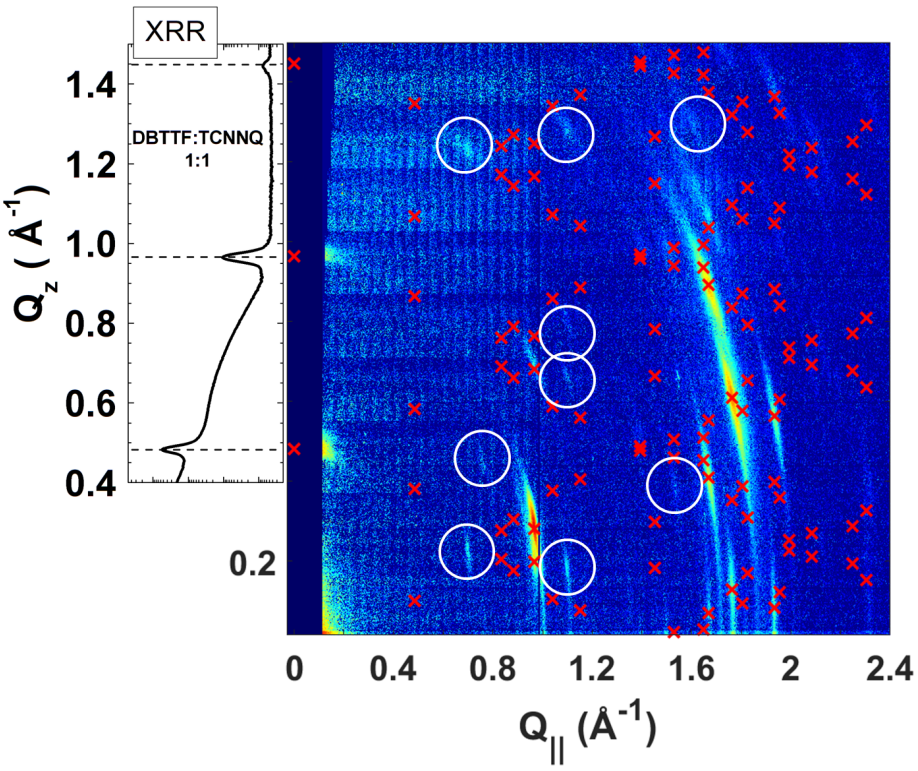

Figure 4.32: Reciprocal space map (right panel) and XRR scan (left panel) of a DBTTF:TCNNQ 1:1 film. The red crosses mark the fitted positions of the Bragg peaks for the first polymorphic form, P1, of the D:A co-crystal formed by DBTTF and TCNNQ. The white circles indicate diffraction features that do not belong to either of the pristine compounds or to the P1 co-crystal polymorph and therefore assigned to a second, less abundant polymorphic form, P2, of this D:A co-crystal.

As it can be seen from Fig. 4.32, the best fit of the triclinic unit cell can well reproduce the position of most of the measured Bragg peak, which we assign to the P1 co-crystal polymorph. However, the relatively weak features indicated by the white circles clearly do not belong to this crystal structure. Since these features also do not belong to the pristine compounds (Fig. 4.34), we conclude that they stem from the second polymorphic form, P2, of the DBTTF:TCNNQ co-crystal, which in this film is likely less abundant than P1.

In Fig. 4.33, we show the map of a DBTTF:F6TCNNQ mixture in molar ratio 1:1. Clear

Table 4.5: Fitted unit cell parameters of polymorph 1 (P1) of the DBTTF:TCNNQ co-crystal (Fig. 4.32).

parameter	**size [units]**
a	13.24 [Å]
b	7.66 [Å]
c	13.84 [Å]
α	105.86 [°]
β	75.95 [°]
γ	100.93 [°]
volume	1298.5 [Å^3]

diffraction features, which do not stem from the pristine donor or acceptor, are visible and therefore belong to the DBTTF:F6TCNNQ co-crystal observed in Ref. [111]. Unfortunately, we could not fit the corresponding unit cell parameters. None of the co-crystal structures available in the literature for chemically similar D:A compounds, like e.g. DBTTF:[F$_x$]TCNQ with $x = 0, 2, 4$ from Refs. [188, 200], or NDT:F6TCNNQ from Ref. [199], could provide a sufficiently close initial guess to fit peak position. For this reason, we also cannot resolve the presence of more than one DBTTF:F6TCNNQ crystal polymorph.

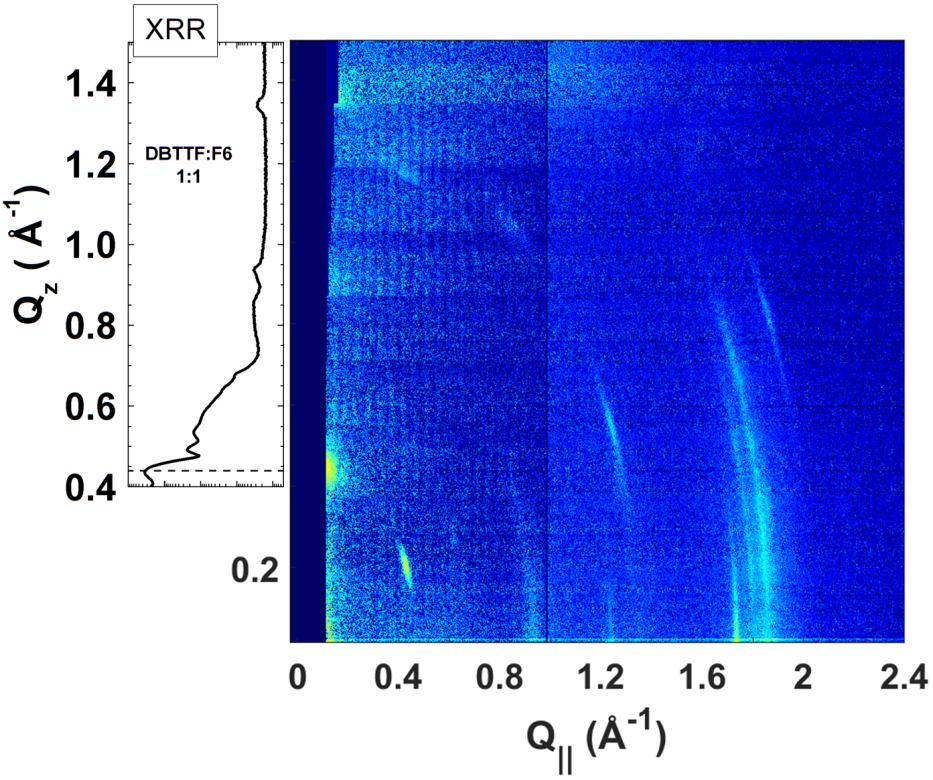

Figure 4.33: Reciprocal space map (right panel) and XRR scan (left panel) of a DBTTF:F6TCNNQ 1:1 film.

From a qualitative comparison of the Q-maps of the DBTTF:[F6]TCNNQ 1:1 films (Fig. 4.34), one can suggest that the molecular arrangement in the unit cell differs substantially for the two co-crystals. As in the case of the DIP:[F6]TCNNQ co-crystals, both the different energy level alignment and Van der Waals interactions due to the different substituents on the conjugated core of the acceptors contribute in determining the molecular packing. However, the usual π-stacking motif of D:A co-crystals seems confirmed also for these material combinations by the presence of relatively strong diffraction features having $Q_{tot} \approx 1.8$ Å^{-1}.

For DBTTF:[F6]TCNNQ, kinetic factors related to the film growth process do not significantly affect the formation of D:A co-crystallites. This seems to be related to: a) the stronger D:A coupling when DBTTF is used as donor compared to DIP, i.e. the fact that the HOMO of DBTTF lies above the LUMO of both acceptors in the solid state, b) the higher structural compatibility of DBTTF with the two acceptors compared to DIP, as seen by comparing the molecular sizes from Fig. 4.30 and Fig. 4.27, which also affects the free energy of formation of molecular layers on a substrate [92].

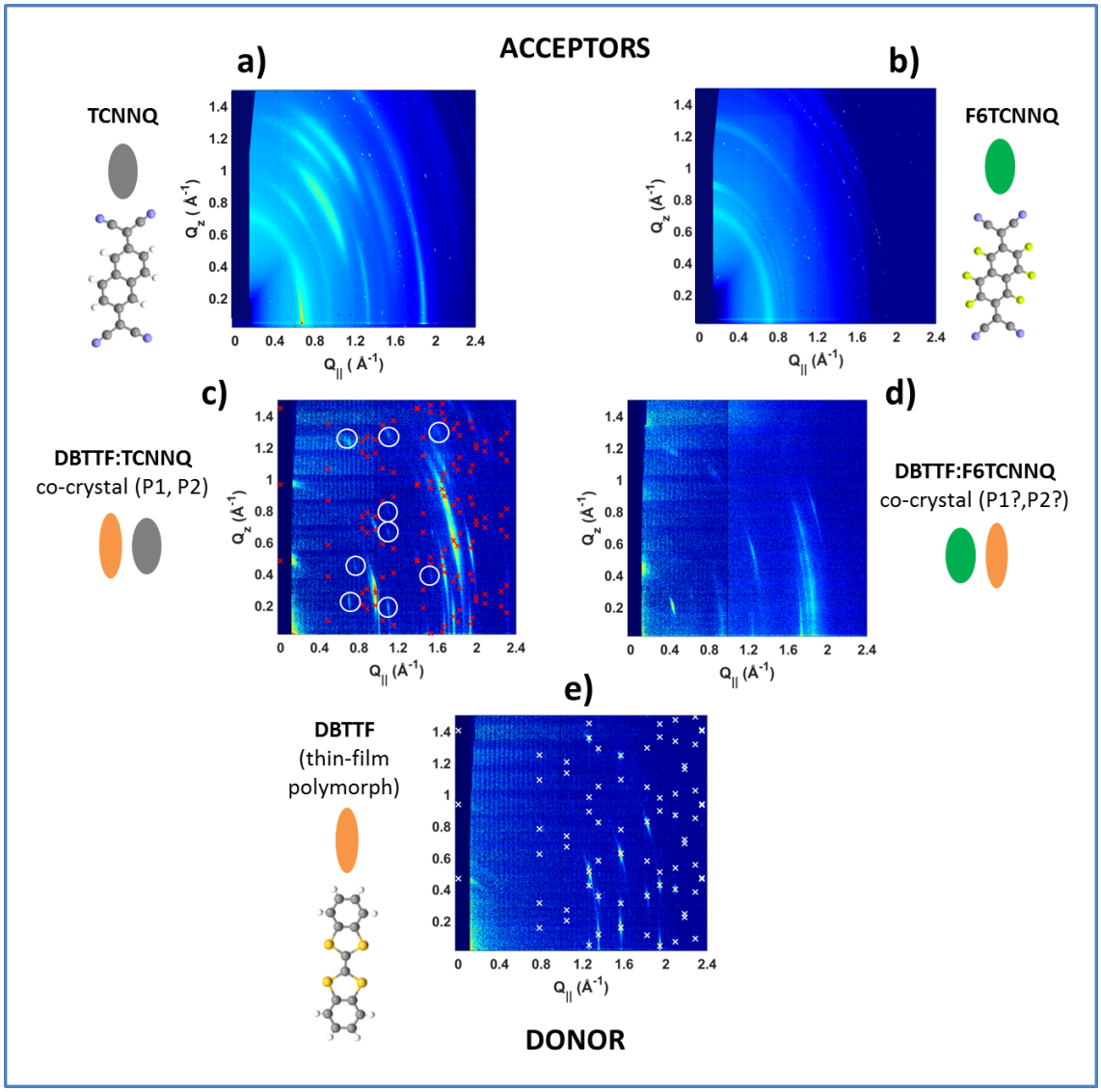

Figure 4.34: Overview of reciprocal space maps of: the acceptors **a)** TCNNQ and **b)** F6TCNNQ; the D:A co-crystals of DBTTF with **c)** TCNNQ and **d)** F6TCNNQ; **e)** the thin-film phase (or γ-polymorph) of the donor DBTTF. The uniform diffraction ring having $Q_{tot} = 0.71$ Å^{-1} in the map of pristine TCNNQ and F6TCNNQ comes from a Kapton window in the setup.

We recall that, in Ref. [111], it is observed that *both* formation of a DBTTF:F6TCNNQ supramolecular complex with partial GS-CT *and* full ionization of donor and acceptor occur in the co-evaporated films. There, a suggestion is made concerning the solid state environments which promotes one or the other type of GS-CT, as we discussed above in the introduction to this section. The overall 2D-texture of the DBTTF:F6TCNNQ 1:1 film suggests that the structural disorder in this blend is relatively small. However, traces of single acceptor molecules included as defects at grain boundaries would remain undetected by GIXD. Such structural defects have been suggested to be preferential centers where full ionization can occur, but the spectral signatures of the ac-

ceptor mono-anion were found to be very weak in co-evaporated films [111]. Our X-ray scattering data cannot resolve the presence of structural defects acting as doping centers *via* integer CT, but do clarify the formation of D:A co-crystallites exhibiting an overall 2D-powder texture with some mosaicity. The suggested scenarios are summarized in Fig. 4.34, where also reciprocal space maps measured for pristine films of the acceptor molecules are shown.

4.5.3 Summary of the results and possible applications

We have reported additional examples of D:A systems for which co-crystal formation is observed. The two materials, TCNNQ and its fluorinated version F6TCNNQ, have been used as acceptors in combination with the donors DIP and DBTTF, respectively. Overall, a significant influence of the energy level alignment on the mixing behavior emerges. Mixed DIP:TCNNQ films exhibit partial phase separation with domains of a D:A co-crystal coexisting with domains of the pristine materials. Conversely, DIP mixes well with F6TCNNQ, forming a homogeneous phase constituted of D:A co-crystallites with no hint of phase-separation. The trend of film electrical conductivity *vs.* D:A mixing ratio for the two materials combinations could be solidly related to such mixing behavior, where a maximum in conductivity is observed for the homogeneous DIP:F6TCNNQ co-crystal phase in the films with $\sim$ 1:1 mixing ratio.

Pristine films of DBTTF are constituted by the thin-film phase (or γ-polymorph), for which the unit cell parameters could be calculated by fitting of the Bragg peaks positions. Formation of homogeneous co-crystalline phases is deduced for DBTTF:[F6]TCNNQ mixed films and phase separation is not observed. DBTTF:TCNNQ films in 1:1 mixing ratio show the presence of two co-crystal polymorphs denominated P1 and P2. The unit cell parameters of the dominant P1 were fitted, whereas the diffraction features of the minoritary P2 polymorph are rather weak and in small number and do not provide sufficient data for fitting. It was not possible to fit the unit cell parameters of the DBTTF:F6TCNNQ co-crystal. For the latter D:A pair, we cannot exclude the presence of two different co-crystal polymorphs to explain the different GS-CT mechanisms observed in Ref. [111].

In general, by comparison of the molecular structure of TCNNQ and its perfluorinated version F6TCNNQ, it is difficult to quantify the contribution of the fluorine substituents in (de)stabilizing a co-crystal structure with a given donor. This contribution depends, among others, on the chemical structure of the donor molecule, which differs significantly between DIP and DBTTF. However, we suggest that, for the material combinations studied here, the relative contribution of orbital coupling dominates. This explanation, although probably oversimplified, has the benefit of providing guidelines for the choice of molecular materials in order to obtain a given mixing behavior. For example, in blends of OSCs it is possible to tune the length scales for phase separation by changing several parameters such as substrate temperature or growth rate [291, 292]. By finely controlling the length-scales of phase separation, it is then possible to maximize the efficiency of organic solar cells [27, 168]. The material system DIP:TCNNQ studied here exhibits partial phase-separation and thus represents an interesting case in which change of the substrate temperature might affect the phase abundance of pristine donor and acceptor relative to the co-crystal, affecting in turn the photovoltaic performance. Furthermore, the ability of the co-crystals to absorb light in the NIR range (Fig. 4.29b) adds one interesting feature to this system that could be exploited for optoelectronic applications.

CHAPTER 5

RELEVANCE OF THE RESULTS OBTAINED AND PERSPECTIVES

This chapter summarizes and connects the new results obtained in this thesis and stresses their relevance in a device-oriented perspective.

In this chapter we connect the results obtained throughout this thesis. Some of these connections have been already stressed in the course of the single chapters. Here we highlight the elements of innovation of our results compared to the state of the art, and we propose directions for future research on thin films of OSCs. Furthermore, we stress the relevance of our results and the possibilities to exploit them to achieve control of the functional properties of molecular layers for their targeted use in optoelectronic components.

5.1 Interplay between molecular structure and CT interactions to determine mixing behavior

The findings on the mixing behavior of DIP:F6TCNNQ, DIP:TCNNQ and 6T:F6TCNNQ reveal a complex scenario. First we notice that, by solely considering the energy level alignment, it is difficult to estimate how large is the driving force for CT. To illustrate this, we refer to the HOMO and LUMO values for DIP, 6T and F6TCNNQ in Fig. 4.1. They are all reported as peak *onsets* in the corresponding photoelectron spectra (UPS for DIP, IPES for F6TCNNQ). The position of peak maxima differs of several tenths of an eV, namely, $\sim$0.4 eV for DIP in σ-orientation [303], $\sim$0.5 eV for 6T in σ-orientation [263] and as much as $\sim$1 eV for F6TCNNQ [53] likely in random orientation. It is noticed in Ref. [53] that the *energetic* orbital overlap matters as driving force for CT, therefore peak onsets rather than maxima should be taken as reference values.

Taking these considerations into account, one still expects a larger driving force to CT for the system 6T:F6TCNNQ. However, the expected driving force to intermolecular coupling *via* CT is not reflected in the mixing behavior (see Results section 4.1). We suggest this to be related to the molecular structure of 6T (Fig. 4.1). The long axis of 6T is double the size of that of F6TCNNQ and the molecular backbone of 6T is more flexible than that of DIP. This seems to involve a smaller probability for 6T:F6TCNNQ to find an efficient conformation for orbital coupling within the time-scales of diffusion and self-assembly during thin film growth, leading ultimately to partial phase-separation in equimolar mixtures. However, thanks to the large driving force for CT and to the overall planar molecular geometry, a significant portion of the molecules can still assemble in D:A co-crystallites.

For DIP:F6TCNNQ, although the sizes of donor and acceptor also differ significantly (Fig. 4.1), no clear hints for phase-separation were found in the equimolar mixtures despite the seemingly smaller driving force for CT. Due to the stiffer molecular backbone of DIP compared to 6T, relative D:A conformations favorable to the formation of a D:A supramolecular complex are efficiently

found, provoking the nucleation and growth of co-crystallites.

The same phenomenon observed for 6T:F6TCNNQ mixtures is present for DIP:TCNNQ mixtures, i.e. D:A co-crystal formation with partial phase separation in equimolar mixtures (see first part of the Results section 4.5). For DIP:TCNNQ, due to the close similarity of the acceptor to F6TCNNQ, the above outlined factors related to the different molecular conformations can be singled out. We conclude that the partial phase separation of TCNNQ is observed due to the unfavorable energy level alignment (Fig. 4.27), involving an insufficient driving force for complex formation. However, as in the case of 6T:F6TCNNQ, sizable amounts of D:A co-crystallites are found.

The role of the driving force to complex formation for the mixing behavior of D:A systems can be rationalized in terms of the inter-particle interaction potential χ (Eq. 2.7). If the interaction potential for hetero-particles, V_{AB}, is strong enough, one obtains the case illustrated in Fig. 2.7b, i.e. a D:A complex is formed. In our case, we assume that the main contribution to V_{AB} is of electronic nature and represented by the driving force to CT and by the orbital coupling. In using this argument, we neglect multipolar and van der Waals contribution, which also determine the strength of intermolecular D:A interactions when comparing F6TCNNQ with TCNNQ. This simplified picture obviously does not take into account the non-equilibrium character of thin film growth. In our case, we observe a combination of the two scenarios illustrated in Fig. 2.7b,c for the equimolar mixtures of 6T:F6TCNNQ and DIP:TCNNQ, namely, domains of the corresponding D:A complex coexisting with domains of the pristine compounds. These two systems represent thus the first examples of kinetically limited formation of D:A complexes in thin films reported so far.

These findings suggest several perspectives, on one side for further research and, on the other side, for applications in optoelectronic devices. The optimal phase morphology in these devices must fulfill two requirements [27]: a) there has to be some degree of mixing between donor and an acceptor, so that the photogenerated excitons can be efficiently split in charge carriers at the D:A interfaces; b) the contacts should be covered with pristine domains well interconnected with the partially mixed domains in the same material in order to ensure efficient transport of the charge carriers to the external circuit. For these requirements, D:A mixtures that exhibit strong phase separation like DIP:C_{60} have been employed [95, 168]. The bulk heterojunction architectures employed in this thesis allow to maximize the number of donor domains interfacing acceptor domains and could therefore be "sandwiched" between domains constituted of pure donor and acceptor, respectively. In other words, the two concepts of bulk and planar heterojunction can be joined in one device (Fig. 1.2c,d).

In particular, we demonstrated two partially phase-separated systems mixed on the molecular level which show the additional presence of D:A co-crystals. Here, an important ingredient would be the ability to control the length scales of the phase separation [292] as well as the size of the crystallites in the direction perpendicular to the contacts. The co-crystals are intermixed in the phase-separated matrix (Fig. 1.2c) and can absorb in the NIR portion of the spectrum, which offers the possibility to harvest low-energy photons. However, the energetics at the interface between D:A co-crystals and pristine domains should be carefully studied in order to choose the best material combination to minimize charge recombination and avoid losses of the open circuit voltage.

5.2 OMBD combined with high sensitivity techniques

The use of OMBD and the possibility to systematically vary the D:A mixing ratio in thin films allows to extend the space of variables that affect a given film property and thereby to pinpoint specific effects. This approach has been applied to quantify two parameters for DIP:F6TCNNQ, the system most extensively characterized in this thesis: a) roughness evolution, b) degree of GS-CT.

5.2.1 Smoothing mechanisms in D:A mixtures investigated by *in situ* real-time X-ray reflectivity

In the Results section 4.2 we demonstrate the dependence of interface roughness on film thickness *and* D:A mixing ratio. This study is intended to complement and deepen the observations of film smoothing from the post-growth XRR data on DIP:F6TCNNQ mixtures with excess DIP

(Fig. 4.2a). A mechanism to explain the roughness evolution is proposed, which might be rather general for binary mixtures with co-crystal formation. In brief, the suggested mechanism invokes the different vertical growth rate of pristine donor crystallites and co-crystallites, respectively, the latter growing faster. Notice that a different vertical growth rate of DIP crystallites, respectively on grain boundaries and terraces, has been suggested to explain the rapid roughening in thin films of this OSC [105].

The systematic increase of acceptor content in DIP:F6TCNNQ mixtures provides a meaningful tool to track down effects related to the formation of the co-crystal, whose molar ratio relative to DIP increases with the F6TCNNQ content (Fig. 6.11). This experimental approach combined with the several theoretical models, as proposed in the Results section 4.2, is fundamental for gaining a reliable picture of a complicated system such as a binary mixture with phase heterogeneity. We stress the substantial novelty of our results by noticing that, to the best of our knowledge, the roughness evolution of a binary mixture has been published only in one work [62] where, however, only data for the equimolar mixture at two different substrate temperatures are shown. We therefore recommend the use of this approach for the study of further D:A systems in order to substantiate the suggested mechanism for heterogeneous phases.

5.2.2 Effects of ground-state charge-transfer interactions on molecular vibrations

For DIP:F6TCNNQ we have observe strong optical transitions in the NIR associated to the formation of a D:A co-crystal (see Results section 4.1). We then suggest that the lowest energy transition stems directly from the HOMO-LUMO transition within the D:A supramolecular complex formed as a consequence of GS-CT interactions. The next logical step is to quantify the GS-CT by means of FTIR. In order to do this, simple transmission measurements did not prove sensitive enough. We then turned to the PMIRRAS setup described in the Methods section 3.3 in order to gain sensitivity and be able to detect the relatively weak C$\equiv$N stretching from F6TCNNQ. Such vibration is the CT-sensitive vibration most used in the literature to quantify the degree of GS-CT and therefore represented the natural choice for this task. However, the use of PMIRRAS allows one to obtain very clear spectra also in the molecular fingerprint region since the signal from atmospheric gases cancels out. Information obtained from the C$\equiv$N stretching region and the C$=$C stretching region can be therefore joined with DFT calculations, and a more complete picture of GS-CT interactions for many D:A systems can be gained.

The approach of employing PMIRRAS to study CT-sensitive vibrations was already adopted in Ref. [57] for several D:A combinations. There, however, the mixing ratio was not varied. In our work, we produced a series of binary mixtures varying systematically the D:A mixing ratio. Among others, we could indicate the uncertainty on the calculated degree of GS-CT based on the systematic mode red-shift with D:A mixing ratio. Such shift is related to the average dielectric properties of the films in an effective medium approximation and, to the best of our knowledge, has been clearly reported by us for the first time for molecular materials. Based on DFT calculations and with the comparison of DIP:F6TCNNQ with P3HT:F6TCNNQ we also brought the attention on the fact that not only peak positions, but also peak intensities should be taken into account to correctly evaluate the nature of the CT interactions in these systems.

We recommend the use of PMIRRAS for investigating OSCs on those types of surfaces that find applications in devices, for instance ITO. The requirement of a highly conductive surface does not pose too severe restrictions to these studies as long as a suitable "buffer" layer can be deposited that mimicks the properties of the real surface. The organic material will then be deposited on top of this buffer layer, which should stay below $\sim$100 nm thickness [217] in order not affect too much the reflectivity of the conductive substrate underneath. This approach will be beneficial for future research.

5.3 A strategy for thin film preparation to select molecular orientation

Our findings concerning the possibility to select molecular orientation in polycrystalline films on any kind of substrate are probably the most relevant for device applications. As we recognized the potential interest of our thin film growth protocol, we decided to apply for patenting the growth procedure described in the Results section 4.3.

Our findings are likely to stimulate new ideas and alternative directions of fundamental research, which were in part illustrated in the Results section 4.3. For instance, the production of molecular films with selected orientation allows to discern changes in optical spectra uniquely due to orientational transitions from those due to other effects. We saw a concrete example of this in the interpretation of the PMIRRAS spectra in Fig. 4.23. Furthermore, it is an advantage to be able to experimentally "rotate" the unit cell of a given D:A co-crystal on a surface in order to constraint the problem of crystal structure solving. This aspect seems particularly important for those compounds whose thin film texture is not perfectly uniaxial, as seen for the DIP:F6TCNNQ co-crystal (Fig. 4.19). Another possibility for future research involves the realization of hetero-interfaces where the molecular components have a defined orientation in order to complement theoretical predictions for exciton generation and diffusion [360].

5.4 Compensating the low absorption of Si in the visible and NIR range

The much higher absorptivity of OSCs compared to Si in the spectral region below ∼3 eV is one of the features of these materials which renders them most attractive for applications in solar energy conversion, as it can be seen in Fig. 5.1 by comparison of the sun irradiance on Earth with the extinction coefficient k for the materials shown. As it can be seen, DIP films grown in an upright-standing (σ) do not show enhanced optical absorption compared to Si in the spectral range below ∼3 eV. Conversely, DIP films selectively grown in a lying-down (λ) molecular orientation can compensate the low k of Si significantly. Notice that the higher k of λ-DIP compared to σ-DIP can be already noticed by bare eye on glass (Fig. 5.1b).

In the energy range below ∼2 eV the absorption of Si drops drastically, therefore the low-energy photons of the solar radiation in this region are not efficiently harvested. This drop can be compensated by employing D:A co-crystallites (Fig. 5.1c) as absorbers. In Fig. 5.1a, an example is shown for the DIP:F6TCNNQ co-crystal. However, as seen in the Results section 4.1, also the 6T:F6TCNNQ co-crystal exhibits fairly strong absorption bands in this region of the spectrum.

Organic materials can be integrated as surface passivation layers in Si-based solar cells in order to improve light harvesting of NIR photons. This type of application should be thoroughly tested with several materials in order to tune the energy-level alignment at the organic/Si interface and optimize charge injection. Care must also be taken to minimize charge recombination in these layers, which leads to a drop in the open circuit voltage [361].

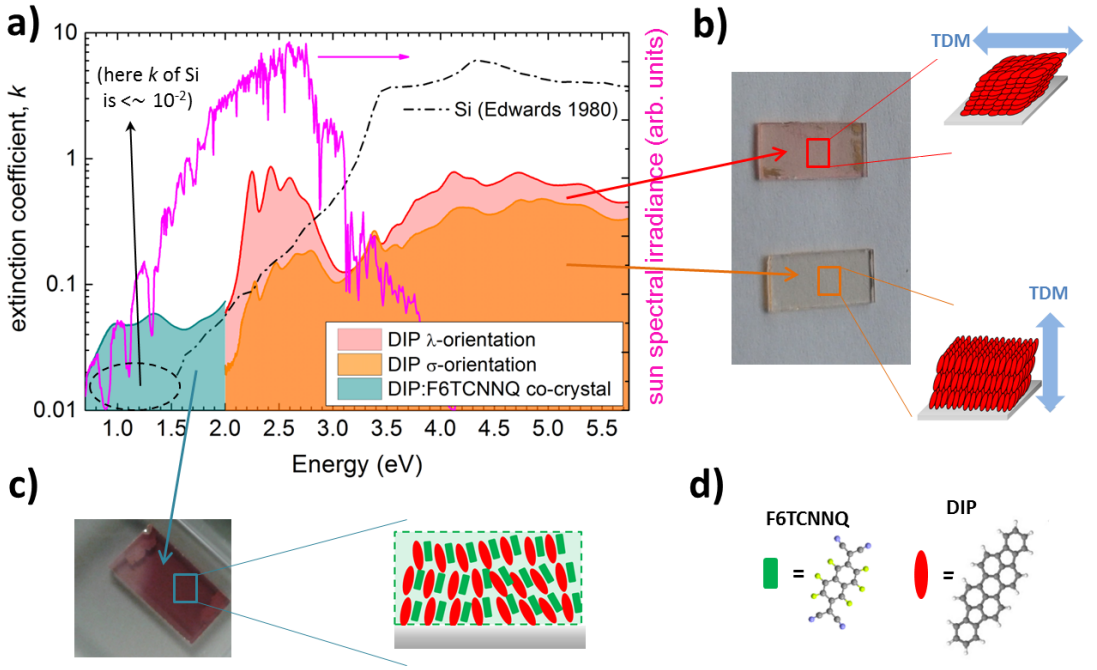

Figure 5.1: **a)** Comparison of the extinction coefficient k of Si [362] with that of DIP in σ- and λ-orientation (see also Fig. 6.16a) and of the DIP:F6TCNNQ co-crystal (see also Fig. 4.6). The solar spectral irradiance on Earth is shown for comparison [363]. **b)** Picture of the pristine DIP films (thickness: 20 nm) evaporated on glass slides, where one can notice the difference in absorption by eye. Sketches of the overall molecular orientation in the films and the corresponding orientation of the TDM are shown. **c)** Picture of the DIP:F6TCNNQ 1:1 film and sketch of the overall texture of the co-crystallites (see Fig. 4.5d). **d)** Molecular structure of DIP and F6TCNNQ (for which see also the Materials section 3.1).

5.5 Functional layers in organic solar cells

Non-transparent organic solar cells from Heliatek® have recently established the world record of 13.2% efficiency [179] and therefore represent a concrete technological application of OSCs for renewable energies. This kind of optoelectronic device can greatly benefit from our growth protocol to induce a stable λ molecular orientation in polycrystalline films, as illustrated in Fig. 5.2.

An organic solar cell consists typically of several functional layers, namely, a photoactive layer for photon harvesting inserted between two transport layers that ease exciton separation and charge transport to the contacts, as in the simplified schematics of Fig. 5.2a. Typically, doped organic films are used as functional layers [20]. Assuming for simplicity that only one OSC with is used as photoactive layer, if its HOMO-LUMO transition has a TDM oriented parallel to the long molecular axis (Fig. 5.2c) then it is obvious that a λ-orientation would maximize the light harvesting efficiency (see e.g. the example of DIP in Fig. 4.16).

Once excitons are generated, the optimal configuration of the transport layers would involve the constituting molecules to also exhibit a λ-orientation. Indeed, assuming the energy level alignment has been optimized by the choice of the materials, this would involve an optimal overlap of the π-orbitals and enhanced probability of exciton separation at the interface. The diffusion *via* hopping of the photogenerated charge carriers into the transport layers would then also occur under optimal conditions thanks to the overlap of the π-orbitals in the direction perpendicular to the contacts. All these processes are sketched in Fig. 5.2b.

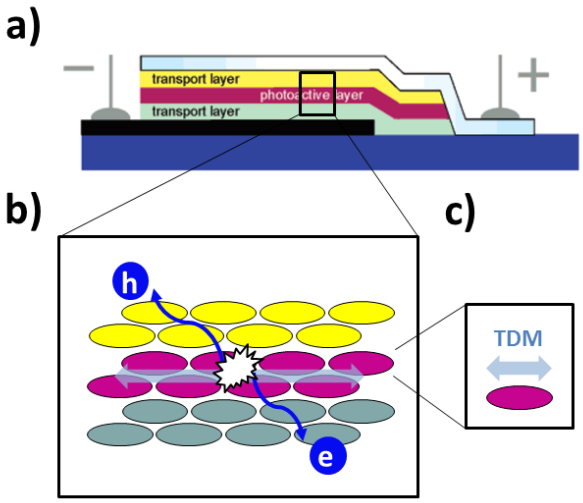

Figure 5.2: **a)** Simplified schematics of an organic solar cell with the molecular functional layers and the contacts displayed (see also 1.1).**b)** Magnification of the interfaces of the functional layers, where an overall λ-orientation of the molecules is shown. The process of exciton separation and charge-carrier migration ("e" electron, "h" hole) is represented. **c)** Orientation of the TDM for a single molecule constituting the photoactive layer. Adapted from Ref. [20].

In summary, the realization of molecular layers entirely in λ-orientation has a great potential to further increase the efficiency of organic solar cells. This perspective depends also on the ability to realize planar heterojunctions with defined interfaces, which for our growth procedure represents the challenge of controlling film morphology *via* fine tuning of the post-growth film annealing parameters.

CHAPTER 6

APPENDIXES

6.1 Additional data and comments on the comparative study of DIP/6T:F6TCNNQ mixed films [1]

Here we show complementary data to the Results section 4.1.

6.1.1 Tables with all Bragg peaks for DIP:F6TCNNQ and 6T:F6TCNNQ mixtures

Bragg peaks found in XRR and GIXD curves for both D:A systems are summarized in the following Tab. 6.1,6.2.

Table 6.1: Summary of Q_z peak positions in the XRR scans of DIP:F6TCNNQ and 6T:F6TCNNQ mixtures. Peak attribution is also indicated, where "LT" stands for low-temperature.

mixture	Q_z [Å^{-}1]	**attribution**
DIP: F6TCNNQ	0.38	DIP thin film σ(001)
	0.67	co-crystal
	0.76	DIP thin film σ(002)
	0.84	DIP LT
	0.86	co-crystal
6T: F6TCNNQ	0.26	6T β(200)
	0.52	6T β(400)
	0.56	6T LT(400)
	0.77	6T β(600)
	0.80	6T LT(110)
	0.84	6T LT(600)

In the XRR of the DIP:F6TCNNQ 1:1 mixture (Fig. 4.2a) we observe only one Bragg peak at $Q_z = 0.67$ Å^{-1}. Since we could not reasonably attribute it to any DIP polymorph, we suggest that it stems from a DIP:F6TCNNQ co-crystal. The peak disappears in the 1:2 mixture due probably to the increased out-of-plane disorder provoked by the molar excess of F6TCNNQ.

[1] Based on Ref. [162]

Table 6.2: Summary of $Q_{||}$ peak positions in the GIXD scans for DIP:F6TCNNQ and 6T:F6TCNNQ mixtures. Peak attribution is also indicated, where "LT" stands for low-temperature.

mixture	$Q_{\|\|}$ [Å^{-}1]	**attribution**
DIP:F6TCNNQ	0.49	co-crystal
	0.68	DIP other polymorph
	0.71	co-crystal
	0.84	DIP LT
	0.86	co-crystal
	0.87	F6TCNNQ
	0.93	F6TCNNQ
	1.15	DIP thin film σ(110)
	1.47	DIP thin film σ(020)
	1.72	DIP thin film σ(120)
	1.85	co-crystal
	1.91	co-crystal
6T:F6TCNNQ	0.56	6T LT(400)
	0.62	co-crystal
	0.67	co-crystal
	0.87	F6TCNNQ
	0.93	F6TCNNQ
	1.31	6T LT(011)
	1.34	6T LT(21-1)
	1.40	6T LT(41-1)
	1.38	6T β
	1.60	6T LT(011)
	1.81	co-crystal
	1.87	co-crystal
	1.95	6T LT(32-1)

6.1.2 Examples of D:A co-crystals

We show in Fig. 6.1a,b and 6.1a,b two examples of π-stacked D:A co-crystals taken from the literature [56, 266] in order to illustrate typical distances between the π-conjugated cores of donor and acceptor molecule. The green dashed lines and values in Å represent distances in real space, the white values are the corresponding transformations in reciprocal space. The crystal plane producing the peak with highest intensity in the $Q_{||}$ region $1.80 - 1.95$ Å^{-1} is also shown.

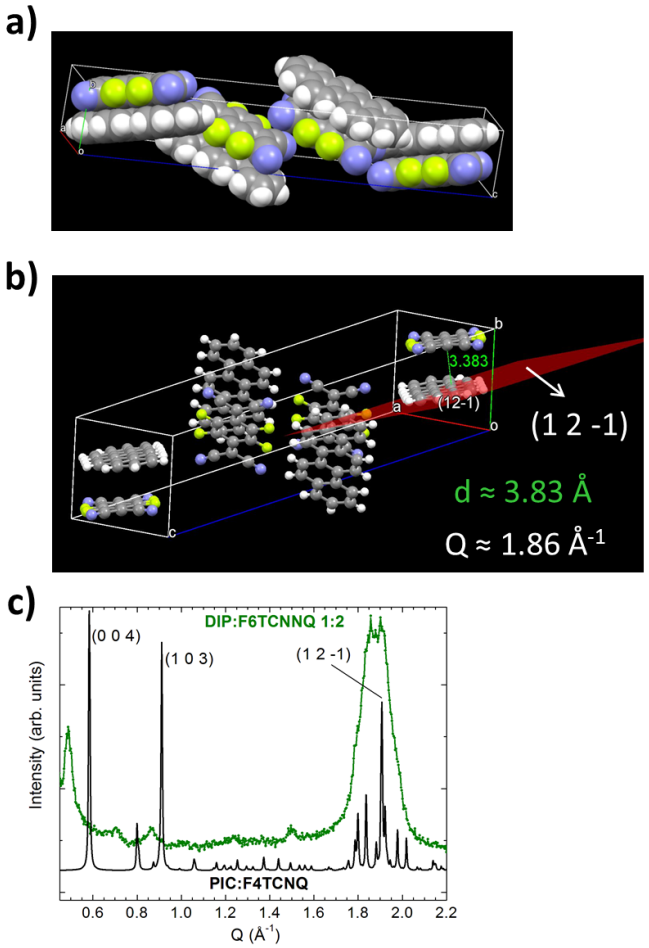

Figure 6.1: **a)** Molecular packing inside unit cell of the D:A co-crystal picene(PIC):F4TCNQ [56], where PIC is the donor and F4TCNQ the acceptor. **b)** Representative distance between the π-conjugated molecular cores of donor and acceptor in real space (in Å) converted in reciprocal space and crystal plane with highest structure factor in the Q region $1.80 - 1.95$ Å^{-1}. **c)** Comparison between calculated powder spectra of the PIC:F4TCNQ co-crystal from the literature (black traces) and the GIXD scans of the DIP:F6TCNNQ 1:2 mixture (colored trace, same scan as in Fig. 4.2b).

In Fig. 6.1c and 6.2c we compare the powder spectra of the two D:A co-crystals from the literature generated using the software Mercury [326] with the GIXD patterns of the 1:2 mixtures of both D:A combinations studied in this work. The position of the D:A co-crystal peaks in the range $Q_{||} = 1.80-1.95$ Å^{-1} in our GIXD profiles matches very well the strong diffraction features in the powder spectra that stem from crystallographic directions vicinal to or coincident with the π-π donor-acceptor stacking direction of the literature compounds despite the substantial mismatch of the rest of the spectral portions and different packing and symmetry within the respective unit cell.

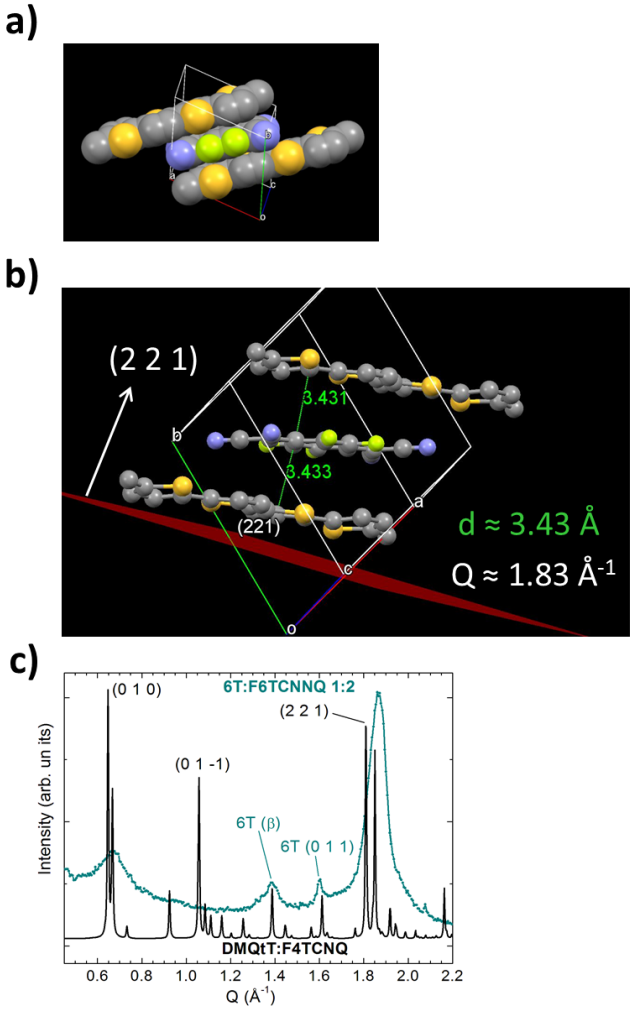

Figure 6.2: **a)** Molecular packing inside unit cell of the D:A co-crystal dimethyl-quarterthiophene(DMQtT):F4TCNQ [266], where DMQtT is the donor and F4TCNQ the acceptor. **b)** Representative distance between the π-conjugated molecular cores of donor and acceptor in real space (in Å) converted in reciprocal space and crystal plane with highest structure factor in the Q region $1.80-1.95$ Å^{-1}. **c)** Comparison between calculated powder spectra of the DMQtT:F4TCNQ co-crystal from the literature (black traces) and the GIXD scans of the 6T:F6TCNNQ 1:2 mixture (colored trace, same scan as in Fig. 4.3b).

6.1.3 UV-vis absorption data for DIP/6T:F6TCNNQ mixtures in several mixing ratios

In Fig. 6.3a,b we show normalized UV-Vis absorption data of the donors DIP and 6T, the acceptor F6TCNNQ, and several corresponding mixtures collected down to 1.25 eV. The spectra were scaled with the aim of showing the development of the overall spectral shape as function of the D:A mixing ratio. In the insets we show close-ups of the lower energy region of the spectra in order to highlight the development the new CT transitions in the mixtures located below the respective bandgaps of the materials in the pristine films. As shown in Fig. 4.6a,b, one or more additional absorption bands per D:A couple are located at lower energies and are therefore here not visible.

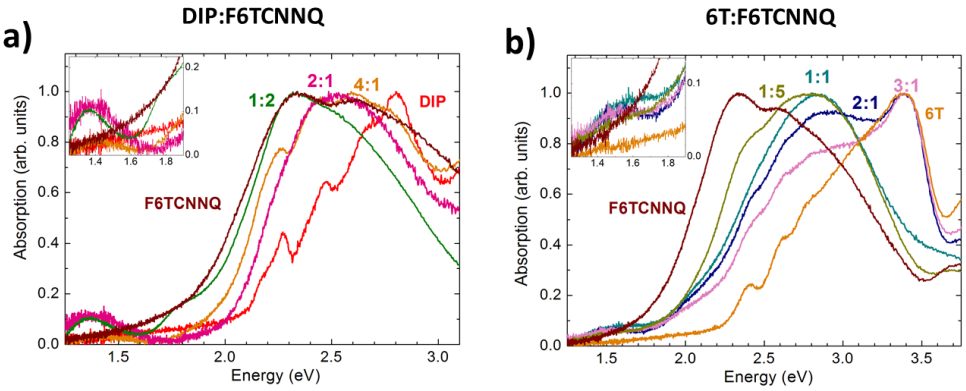

Figure 6.3: Normalized UV-Vis absorption spectra measured in transmission geometry down to 1.25 eV on **a)** DIP:F6TCNNQ and **b)** 6T:F6TCNNQ films with varying molar ratios of donor and acceptor. The spectral range of the main plots is chosen in order to include the most intense HOMO-LUMO transitions of the pristine compounds. The insets show magnifications of the lower-energy regions where the new CT-related optical absorptions are observed in the mixtures. Film thickness is: **a)** 25 nm (DIP), 101 nm (DIP:F6TCNNQ 1:1), 30 nm (DIP:F6TCNNQ 2:1), 103 nm (DIP:F6TCNNQ 1:2), 31 nm (F6TCNNQ); **b)** 24 nm (6T), 25 nm (6T:F6TCNNQ 3:1), 25 nm (DIP:F6TCNNQ 2:1), 23 nm (DIP:F6TCNNQ 1:1), 27 nm (DIP:F6TCNNQ 1:5), 16 nm (F6TCNNQ).

6.1.4 AFM scans of DIP:F6TCNNQ and 6T:F6TCNNQ 1:1 mixtures on different substrates

In order to choose a model for the ellipsometry raw data Ψ and Δ, we investigated the surface morphology of the DIP:F6TCNNQ 1:1 and 6T:F6TCNNQ 1:1 films by Atomic Force Microscopy (AFM).

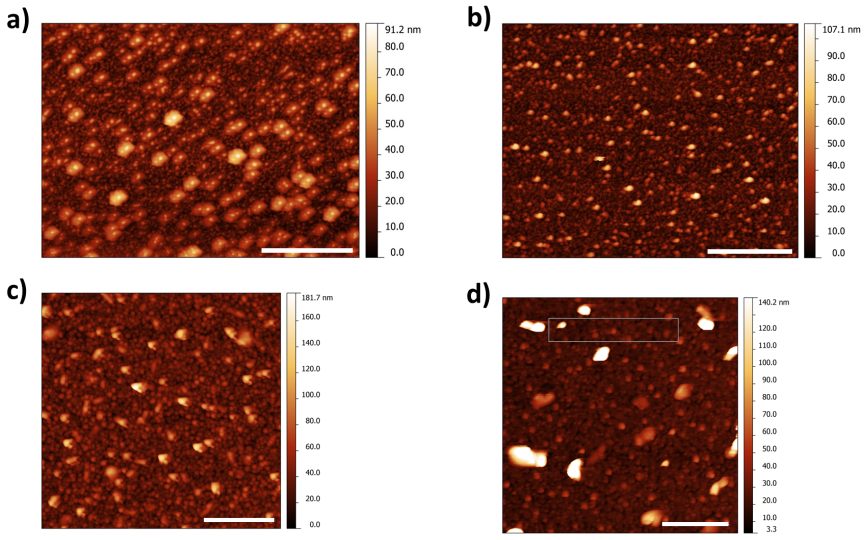

Figure 6.4: **a)**, **b)** AFM scans of the DIP:F6TCNNQ 1:1 film (103 nm) grown on **a)** native Si oxide and **b)** borosilicate glass. **c)**, **d)** AFM scans of the 6T:F6TCNNQ 1:1 film (23 nm) grown on **c)** native Si oxide and **d)** borosilicate glass. The inset bars corresponds to 2 μm. For more clarity, the limits for the color-scale in **d)** have been set to the area delimited on the image. The roughness values are: **a)** 10.7 nm, **b)** 10.3 nm, **c)** 17.3 nm, **d)** 25.3 nm.

We show in Fig. 6.4 AFM scans of the same samples investigated by ellipsometry, namely, the 1:1

mixtures on both native Si oxide and borosilicate glass. For both mixtures the morphology changes qualitatively between the film grown on Si oxide and on glass, respectively. For DIP:F6TCNNQ 1:1, despite the differences in the morphology, the roughness does not change significantly. For 6T:F6TCNNQ 1:1, the film on glass exhibits a $\sim 30\%$ increase in roughness.

6.2 Additional data and comments for roughness evolution of DIP:F6TCNNQ films for roughness evolution [2]

Here, the full real-time XRR datasets for the three DIP:F6TCNNQ mixtures are shown together with all the fits performed and parameters extracted. The data are further commented when necessary.

6.2.1 Fits with growth models for all DIP:F6TCNNQ mixtures

We show in Fig. 6.5 the time-evolution of the XRR curves measured for all DIP:F6TCNNQ mixed films. The reflectivity profiles as function of layer thickness extracted at specific Q_z points together with the corresponding fits are also shown.

From the fits in Fig. 6.5, the layer coverages θ_n and the model-specific growth parameters can be extracted, which is shown in Fig. 6.6 for all mixtures investigated here. Below we briefly comment on the boundary conditions imposed for the fits. In the Cohen fits in the low-thickness regime we do not impose any constraints on the relative magnitude of k_n for different n. In the Trofimov fits we initially impose a boundary condition on $\theta_{cr,n}$, namely $\theta_{cr,n} < \theta_{cr,n+1}$, to fit the time-dependent data at a given Q-point. Subsequently we relax this condition and perform a global fit of the entire dataset for a given D:A mixing ratio. Letting the relative magnitude of k_n to vary freely in the Cohen model leads overall to an increasing trend of k_n *vs* n, more clearly for the 2:1 and 6:1 mixtures (see insets in Fig. 6.6b,d,f).

[2] Based on G. Duva et al., in preparation

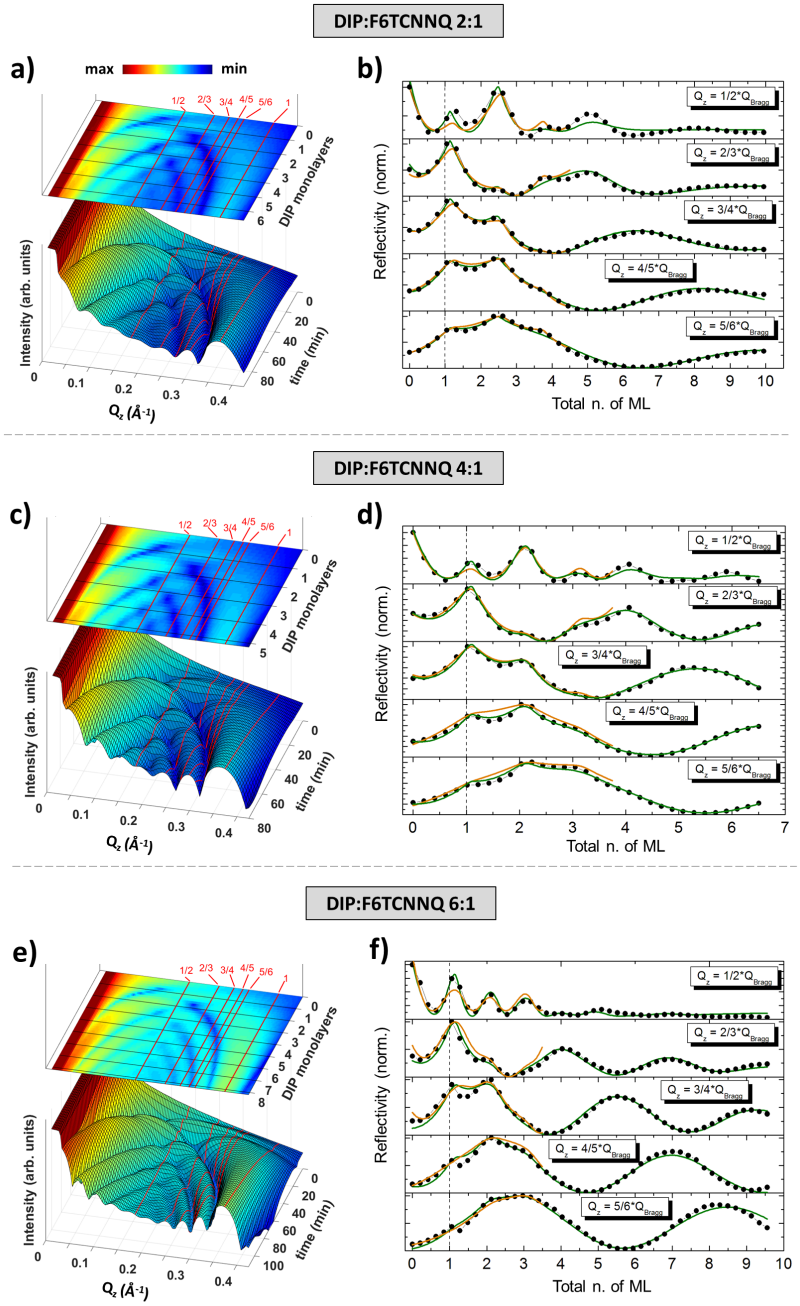

Figure 6.5: *In situ*, real-time XRR data of DIP:F6TCNNQ mixtures. **a)**, **c)**, **e)** Time evolution of the reflectivity profiles. The red lines indicate the fractional points along the curves in units of $Q_{z,Bragg}$. A value for $Q_{z,Bragg} = 0.375$ Å^{-1} is used. The curve at time "0" corresponds to the first curve measured after exposing the substrate molecular flux. In the lower 3D plot, each "pixel" along the time axis corresponds to one experimentally measured curve. **b)**,**d)**,**f)** Extracted profiles at the anti-Bragg point ($Q_z = (1/2) \cdot Q_{Bragg}$) and other fractions of $Q_{z,Bragg}$, as indicated in the plots. The fits are superimposed to the experimental data: the orange curves correspond to the Cohen fits in the low-thickness regime, the green curves correspond to the Trofimov fits in the entire thickness range. Fits of the monotonically increasing intensity of the Bragg peak ($Q_z = Q_{Bragg}$) are not shown. The vertical dashed line corresponds to the first total grown ML measured experimentally by means of the thickness monitor.

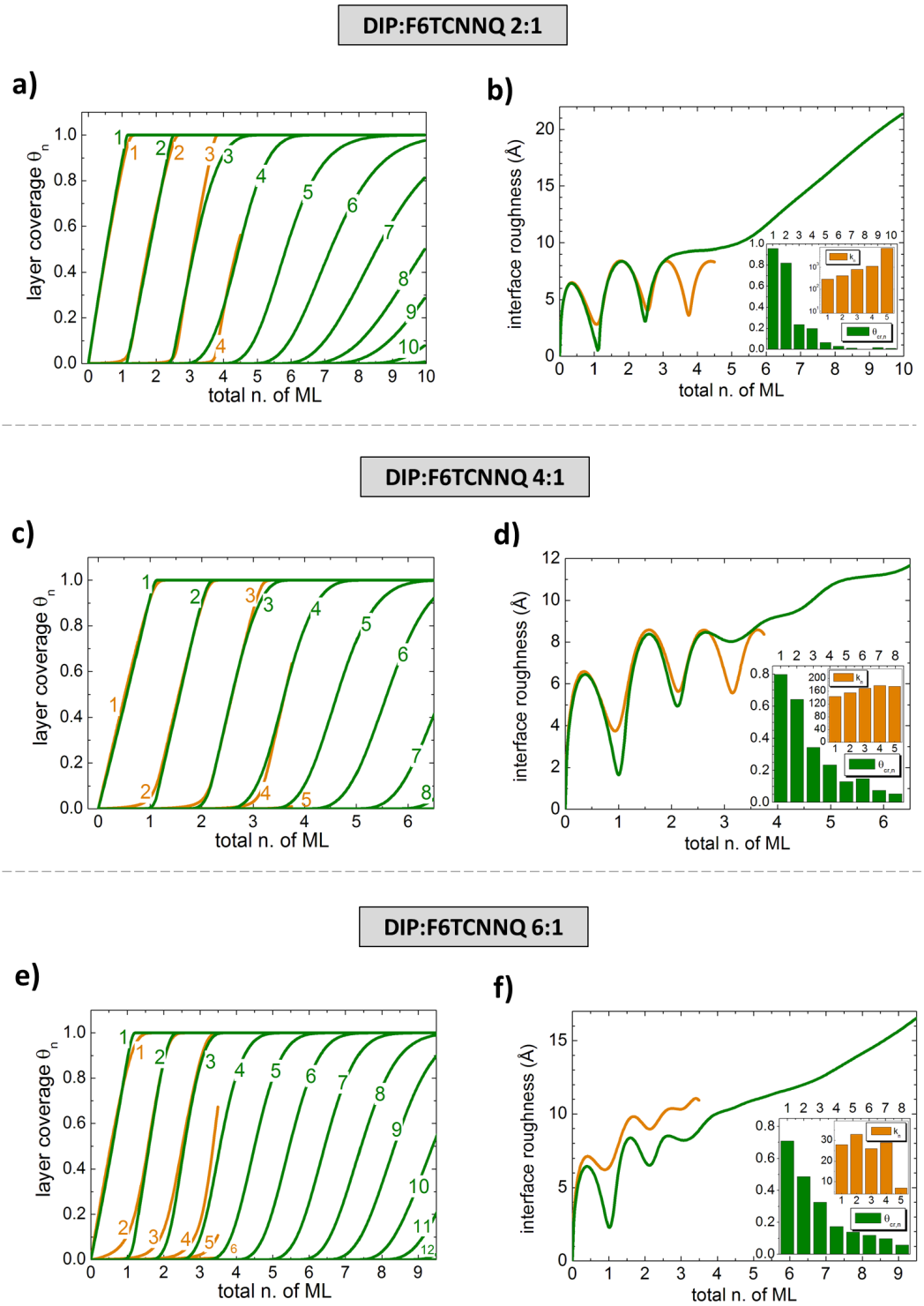

Figure 6.6: Parameters extracted from the fits of the DIP:F6TCNNQ mixtures using the Cohen model in the low-thickness regime (orange traces) and the Trofimov model in the entire thickness range (green traces). **a)**, **c)**,**e)** Layer coverages θ_n. **b)**, **d)**,**f)** Interface roughness calculated from Eq. 4.1. The insets show the jump rates k_n according to the Cohen model (see Eq. 3.12) and the critical layer coverages $\theta_{cr,n}$ according to the Trofimov model (see Eq. 3.11).

6.2.2 Parratt fits of real-time XRR data

In order to carry out the Parratt fits, we used the last real-time XRR curve measured for each DIP:F6TCNNQ mixing ratio to set up a suitable multilayer model, then we fitted the scans in decreasing film thickness. Fig. 6.7b shows an example of parameter set used to fit the last XRR scan of the time-series for the DIP:F6TCNNQ 4:1 mixture. In this "top-down" approach, uniquely the electron density, ρ_e, of the top layers were used as fit parameters. A lack of electron density compared to a full layer indicates partial filling (Fig. 6.7a). A multilayer model was created for each film, where void slabs are alternated with slabs "filled " with material in order to reproduce the contrast in electron density along the z-coordinate perpendicular to the substrate, which gives rise to Bragg peaks [225, 236]. Each layer has an associated roughness which determines how pronounced the inter-layer electron density contrast is, or, in other words, determines the amplitude of the electron density modulation.

a)

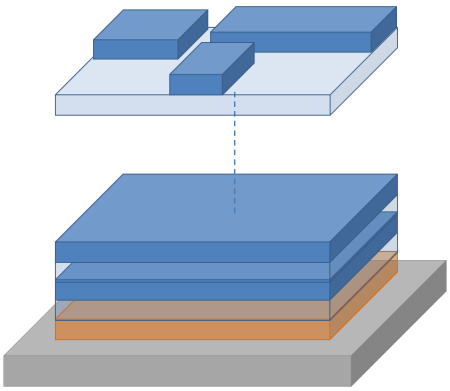

b)

DIP:F6TCNNQ 4:1

	d (Å)	ρ (10^{-6}Å^{-2})	σ (Å)
7 ML	12.07	5.60	3.71
space layer	4.76	0	3.72
6 ML	12.11	10.61	3.76
space layer	4.77	0	3.78
5 ML	12.13	11.53	3.80
space layer	4.78	0	3.84
4 ML	12.16	11.59	3.88
space layer	4.78	0	3.95
3 ML	12.16	11.59	4.03
space layer	4.77	0	4.10
2 ML	12.17	11.89	4.16
space layer	4.76	0	4.20
1 ML	12.17	12.11	4.20
space layer	4.77	0	4.20
initial adsorbants	1.50	7.01	1.08
SiO_x	25	18.9	7.10

Figure 6.7: **a)** Sketch of multilayer model for fitting XRR data with the Parratt formalism. **b)** Set of parameters used to fit the last XRR scan (i.e. thickest film) for the DIP:F6TCNNQ 4:1 mixing ratio where d indicates the layer thickness, ρ_e the electron density and σ the layer roughness. The color code of some layers matches their location in the sketch in **a)**.

To minimize the number of free parameters, we imposed boundary conditions for ρ_e , the inter-layer roughness and the monolayer thickness in the following way: a) an upper limit for ρ_e of a full layer was set, b) the values for the inter-layer roughness were set all equal, c) the monolayer thickness was set equal for all void+full pairs of slabs, with the additional constraint of an equal thickness for all void and full slabs, respectively. Note that, occasionally, we had to make these boundary conditions less stringent in order to achieve a better agreement of the fits to the data. However, minor deviations were necessary, amounting to less than 10% at most, as it is the case, e.g., for the layer roughness of the model for the 4:1 mixture in Fig. 6.7b. For choosing an upper limit for ρ_e, the nominal electron densities of the bulk high-T polymorph of DIP [124] and of the bulk crystalline form of F6TCNNQ [198] were averaged using the molar ratio of each compound as weight. This approach was enough to obtain reasonable fits for the 2:1 and 4:1 mixtures. For the 6:1 mixture, to obtain reasonable fits to the data it was necessary to set the maximal ρ_e higher than its nominal value. This might indicate that for the 6:1 mixture, due to the large excess of DIP, the growing crystallites incorporate fewer defects than in the 2:1 and 4:1 mixture, which leads to an overall higher film density.

We show in Fig. 6.8 the entire set of XRR curves fitted using the Parratt formalism for all DIP:F6TCNNQ mixtures. The vertical shift of the curves is identical for all the films. In Fig. 6.9, we show the electron density profiles and layer coverages extracted from the Parratt fits for the three DIP:F6TCNNQ mixtures.

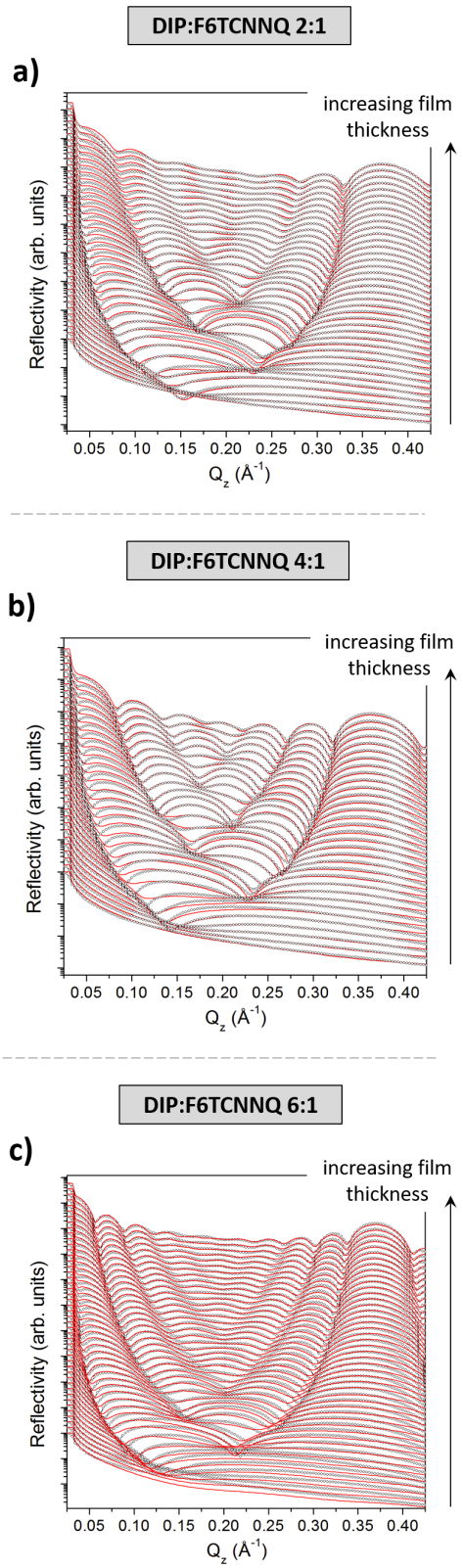

Figure 6.8: Experimental XRR scans (black dotted profiles) and fits using the Parratt formalism (red profiles). The curves are vertically shifted for clarity. The fits were performed using the software *Motofit* [279].

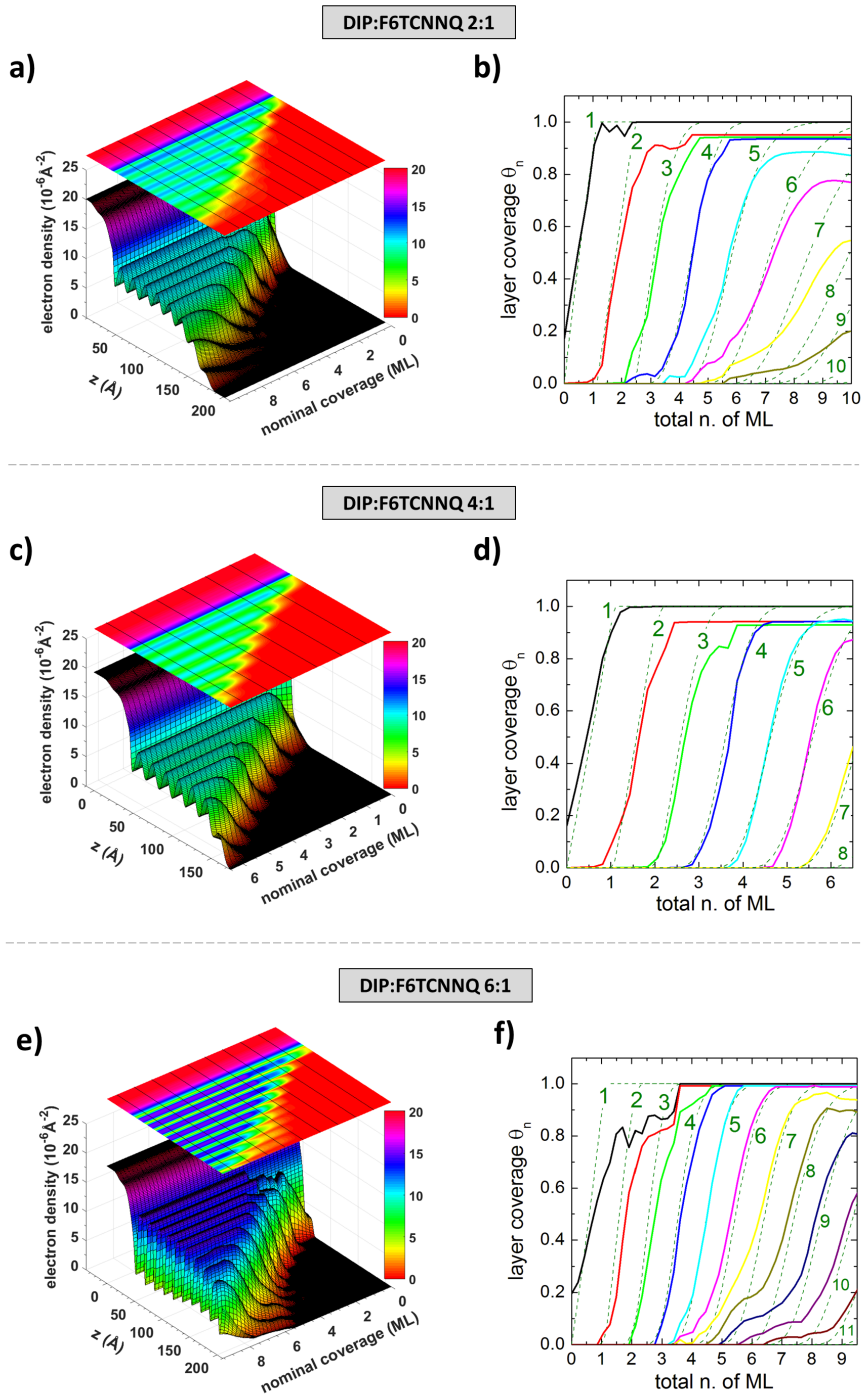

Figure 6.9: Parameters extracted from the Parratt fits of the real-time XRR data for all DIP:F6TCNNQ mixtures. **a),c),d)** Electron density (or scattering length density) as function of the z-coordinate perpendicular to the substrate and of the total number of deposited ML. The color scale for the electron density is indicated. The Si substrate is located at $z = 0$, i.e. the convention for the z-axis is inverted compared to Fig. 3.17. **b),d),f)** Layer coverages θ_n as function of the total number of deposited ML. The θ_n obtained from the Parratt fits (full colored lines) are compared to the θ_n obtained from the Trofimov fits (dashed green lines), to which the numbers also refer.

By simple inspection of the data starting from the very first growth stages of the film, it is evident that the 2:1 mixture exhibits the deepest intensity modulation with a minimum around $Q_z = 0.15$ Å^{-1}. Therefore, already by visual inspection, the mixture with the highest F6TCNNQ content exhibits the most pronounced layer-by-layer growth fashion in this monolayer-thickness regime, i.e. the lowest interface roughness, as confirmed by the RMS extracted from the fits. An overview of the obtained parameters from all models employed for all DIP:F6TCNNQ mixtures is shown if Fig. 6.10. In particular, the interface roughness extracted from the growth models and the Parratt formalism, respectively, show qualitatively similar trends, with the 2:1 mixture exhibiting the most pronounced layer-by-layer growth fashion in the early growth stages but roughening faster than the other two mixtures in the later growth stages.

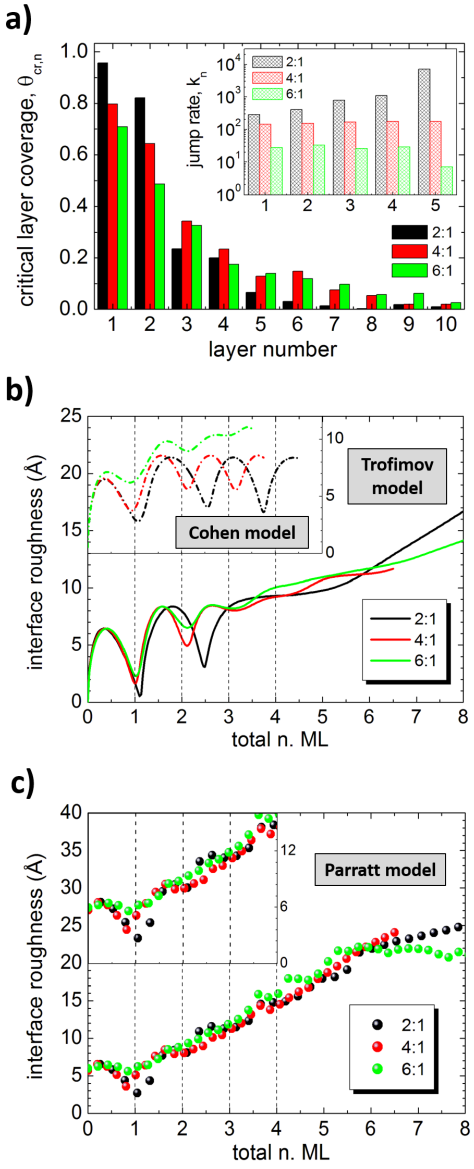

Figure 6.10: **a)** Critical layer coverages $\theta_{cr,n}$ according to the Trofimov model, and inter-layer jump rates k_n according to the Cohen model (inset) obtained from the fits of the data for the three DIP:F6TCNNQ mixtures in different D:A molar ratios. **b)** Interface roughness extracted using the Trofimov model for the full thickness range and the Cohen model for the low-thickness regime (inset). **c)** Interface roughness extracted using the Parratt formalism. In **b)** and **c)**, the vertical lines correspond to the deposition of the first 4 nominal ML.

6.2.3 Post-growth GIXD scans

In Fig. 6.11a we show GIXD scans measured for the as-grown DIP:F6TCNNQ films studied by real-time XRR in all mixing ratios. The DIP Bragg peaks were fitted with Gaussian curves in order to extract the FWHM, from which the lateral (or in-plane) coherent grain size D was calculated using the Scherrer formula:

$$D = \frac{2\pi K}{FWHM} \tag{6.1}$$

where $K = 0.94$ is a geometrical factor. For each film, the values of D obtained from the different Bragg peaks were averaged in order to obtain a mean value. The results are plotted in Fig. 6.11b.

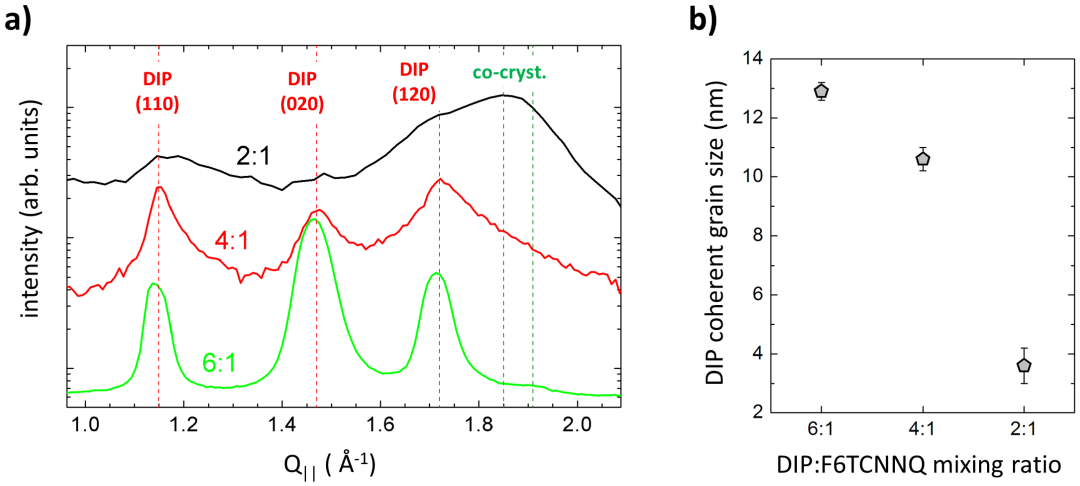

Figure 6.11: GIXD scans of as-grown DIP:F6TCNNQ mixtures with the indicated mixing ratios. The Bragg peaks stemming from DIP and from the DIP:F6TCNNQ co-crystal, respectively, are indicated.

Clearly, the in-plane coherent size of the DIP crystallites becomes smaller as the F6TCNNQ content increases. At the same time, the feature stemming from the DIP:F6TCNNQ co-crystal become stronger relative to those of DIP, which qualitatively confirms the increasing amount of co-crystal relative to pristine DIP in the mixtures.

6.3 Additional data for orientation control of DIP, PEN and 6T films [3]

Here we show complementary data to the Results section 4.3.

6.3.1 Post-growth, *in situ* GIXD can of DIP film in lying-down orientation

In Fig. 6.12 we show diffraction patterns of a DIP film measured in GIXD geometry *in situ* at $T_{sub} = 123$ K right after film deposition.

In Fig. 6.12a,b, a broad peak is visible. The slits gap is assumed to not significantly affect the estimation of peak width. The broad but clear (001) Bragg peak stemming from the λ orientation of DIP denotes the presence of DIP domains with some degree of coherence. The lateral coherent grain size can estimated using the Debye-Scherrer formula (Eq. 6.1). Taking a FWHM of 0.135 Å^{-1} as given by the fit in Fig. 6.12b we obtain D = 4.4 nm, which corresponds to less than three times

[3] Based on Ref. [284]

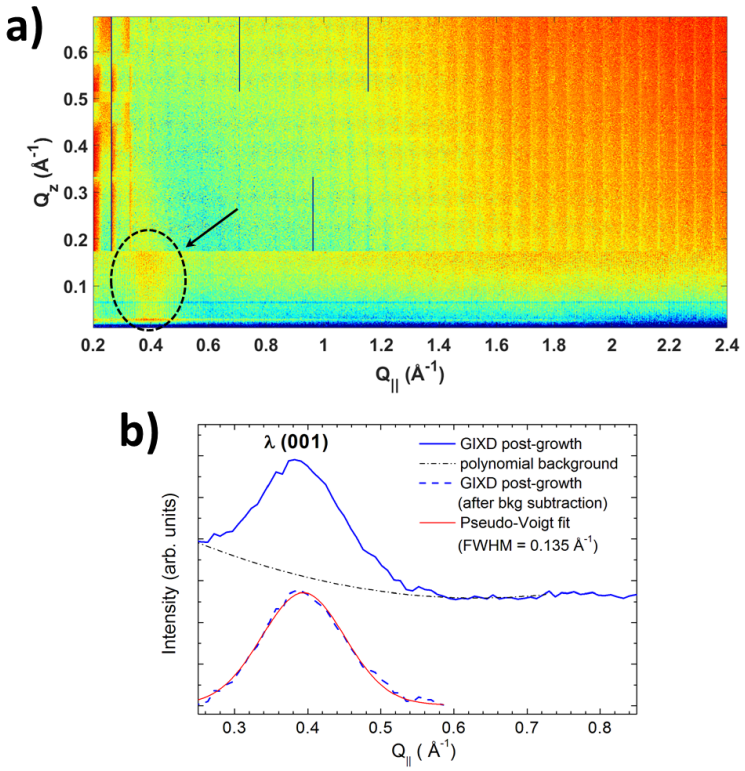

Figure 6.12: *In situ* **a)** reciprocal space map and **b)** GIXD scan measured right after the growth of a DIP film at T_{sub} = 123 K. In **a)**, the high intensity coming from the range near $Q_{||}$=0 Å^{-1} in the top part of the map stems from spurious scattering. Such intensity is then efficiently cut out by the more closed slits in the bottom part of the map, where the arrow points at the only visible diffraction feature from the organic film. In **b)**, the feature is attributed to the (001) Bragg reflection of the λ-orientation of DIP. [TOP trace, full line]: GIXD scan with corresponding fit of the background likely arising from air scattering of the direct beam. [BOTTOM trace, dashed line]: Bragg peak after background subtraction. The peak was fitted using a single pseudo-Voigt curve consisting of a linear combination of a Lorentzian and a Gaussian curve.

the long molecular axis assuming a λ-orientation. The DIP grains formed at this T_{sub} exhibit therefore only short-range order, but still more pronounced than, e.g., the OSC rubrene, as in Ref. [364].

6.3.2 Post-Annealing GIXD Scan of DIP Film with λ-Orientation

Fig. 6.13 shows the GIXD scan of the same DIP film with λ-orientation presented in Fig. 4.16c,d of the Results section 4.3. The GIXD scan was extracted directly from the reciprocal space map and therefore the peak width is not affected by slits broadening.

From Eq. 6.1 we obtain from the λ-(001) Bragg peak D≈49 nm, which represents a ten-fold increase in the coherent grain size compared to the as-grown film.

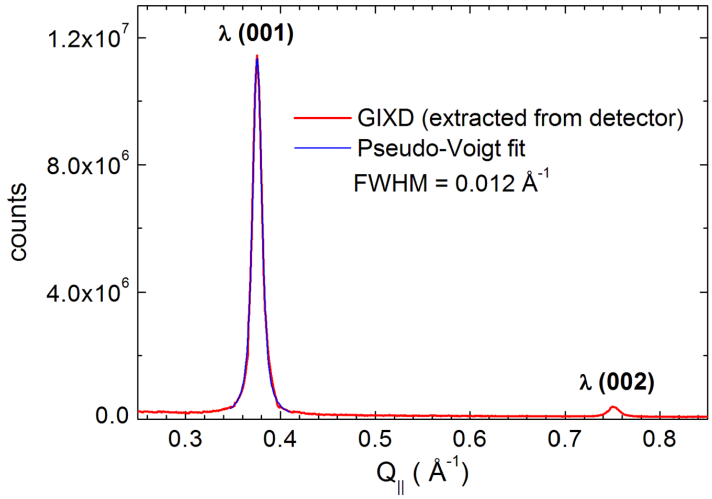

Figure 6.13: *Ex situ* GIXD scan extracted from Q-map after annealing of a DIP film up to T_{sub} = 413 K and subsequent cooling to room T. The peak was fitted using a single pseudo-Voigt curve.

6.3.3 Mosaicity of DIP Film with λ-Orientation

The reciprocal space map of a DIP film in λ-orientation measured *ex situ* is shown in Fig. 4.16c.

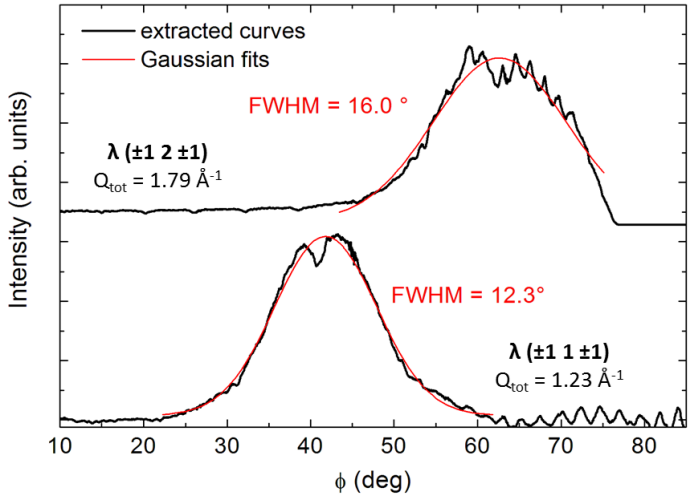

Figure 6.14: Angular distribution of the diffracted intensity of Bragg peaks belonging to the (± 1 k ± 1) truncation rod of DIP with λ-orientation extracted from the Q-map of another DIP film, which is completely similar to the map shown in Fig. 4.16c. The Gaussian fits used to extract the mosaicity are shown. The angle ϕ is measured by placing 0° at Q_z = 0 Å^{-1}. The intensity profile with Q_{tot} = 1.23 Å^{-1} has been corrected for the background. The intensity profile with Q_{tot} = 1.79 Å^{-1} attains the limits of the measured Q-range for $\phi \to 90°$, therefore the portion above $\phi \approx 75°$ is flat and affects the quality of the Gaussian fit. Some sawtooth-like shaped artifacts visible in the extracted profiles are due to the stitching of several images from the 2D detector.

The intensity of the Bragg peaks belonging to different truncation rods has some spread along the same value of the total Q, which denotes mosaicity of the DIP crystallites. The intensity profiles are plotted as function of the radial angle ϕ. From the Gaussian fits of intensity *vs* ϕ we extracted the FWHM values and used them as an estimation of the mosaicity of the DIP film with λ-orientation. We take an average value of 14° from Fig. 6.14, which therefore corresponds to a

mosaicity of ± 7°.

6.3.4 Surface morphology of α-sexithiophene films

The different growth conditions of the thin films prepared in σ- and λ-orientation, respectively, has relevant consequences on film morphology. In Fig. 6.15 we show AFM scans of 6T films in σ-orientation grown on native Si oxide (Fig. 6.15a) and on fused silica (Fig. 6.15c) during the same growth experiment. The surface consists of separated grains of $\sim$ 500 nm in size. Except the slightly higher island density for the sample grown on Si oxide, no major differences are to be noticed.

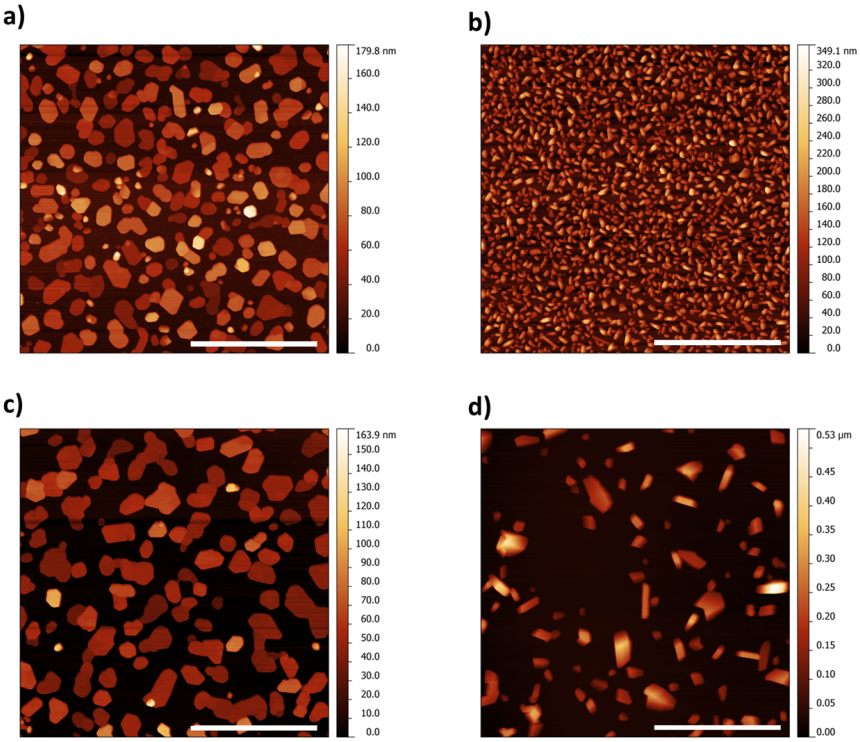

Figure 6.15: AFM images (10x10 μm^2) taken for 6T films in **a),c)** σ- and **b),d)**λ-orientation deposited on **a),b)** native Si oxide and **c),d)** fused silica glass. The inset bar corresponds to 4 μm. The differences between the morphology of our 6T films in σ-orientation and of the films reported in Ref. [271] is due to the fact that our films are annealed to 393 K, which enhances molecular diffusion is enhanced and provokes significant changes in film morphology for this system.

The AFM scans of of 6T films in λ-orientation grown simultaneously on native Si oxide (Fig. 6.15b) and on fused silica (Fig. 6.15d) show, instead, dramatic differences. The morphology is still dominated by islands, but they are much smaller and their density is much higher on native Si oxide than on glass. This huge difference must be related to the diffusion mechanisms taking place on the surface of the single substrates, which in general exhibit slightly different energy landscapes and might therefore affect differently molecular diffusion and self-assembly during the annealing step.

For completeness, we mention that DIP and PEN barely exhibit differences in surface morphology on native Si oxide and glass, respectively.

6.3.5 UV-vis absorption data on films with standing-up and lying-down molecular orientation

In order to obtain an independent estimation of the optical properties in the in-plane direction for our films beyond the VASE fits shown in Fig. 4.16b,d and Fig. 4.17e-h of the main text, we

measured UV-vis absorption spectroscopy in transmission geometry on all films grown on fused silica glass slides in both σ- and λ-orientation, and calculated the extinction coefficient k assuming the contributions from the reflection and the diffused scattering from the glass to be negligible. The results are reported in Fig. 6.16 for the energy range 1.4-6 eV.

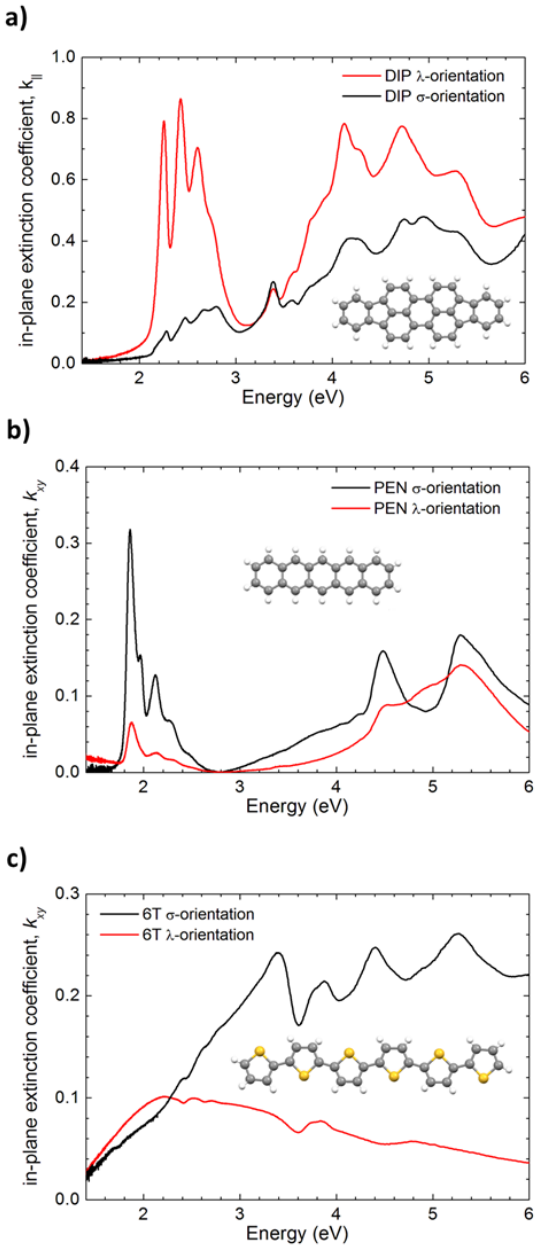

Figure 6.16: In-plane component of the extinction coefficient, $k_{||}$, estimated by UV-vis absorption spectroscopy in transmission geometry for a) DIP, b) PEN and c) 6T films in σ- and λ-orientation grown on fused silica slides. The following total film thicknesses from the fits of the VASE data were taken to calculate $k_{||}$: 18 nm (σ- and λ-DIP); 17 nm (σ-PEN), 40 nm (λ-PEN); 27 nm (σ-6T), 65 nm (λ-6T).

For the calculation of k, the thickness values obtained from the fits of the VASE data were used. These values show for PEN and 6T clearly higher thicknesses for the films in λ-orientation than for the films in σ-orientation, which is consistent with the analysis of additional X-ray scattering and AFM data (not shown here). This difference is easily ascribed to the much lower T_{sub} during

deposition for the films in λ-orientation compared to the films in σ-orientation. The different T_{sub} causes the molecular sticking coefficient to be higher at 123 K than at room T, therefore the effective film thickness is in general lower for the samples in σ-orientation than for the samples in λ-orientation, respectively. However, for DIP the different deposition T does not seem to have a significant effect on the molecular sticking coefficient. The differences in sticking coefficient, which we qualitatively evaluated from the final film thicknesses, correlate very well with the sublimation T necessary to deposit the starting material from the evaporation cells. As a general trend, the higher the sublimation T, the less pronounced is the dependence of the molecular sticking coefficient on T_{sub}.

As it can be seen in Fig. 6.16a,b, for DIP and PEN the results for $k_{||}$ in the spectral range between 1.4 and 3.5 eV substantially match those obtained from ellipsometry in Fig. 4.16b,d and Fig. 4.17e,f of the main text. This is not the case for 6T, as it can be seen by comparison Fig. 6.16c with Fig. 4.17g,h of the main text. For the latter, the film morphology shown in Fig. 6.15 renders the estimation of $k_{||}$ from simple transmission measurements highly inaccurate. Additionally, for both 6T samples measured in transmission, light-scattering effects provoked by the island-like morphology provoke an apparent light absorption at energies well below the material gap, which his especially pronounced for the 6T film in λ-orientation.

For DIP, the in-plane component of the optical absorption is much stronger for the λ-orientation. Interestingly, the cross section of the transition located at $\sim$3.4 eV is nearly unaffected by the different molecular orientation, whereas from $\sim$3.4 eV to higher energy the absorption for DIP in λ-orientation is roughly two times stronger than for the σ-orientation. Therefore, a horizontal alignment of the DIP molecules also leads to enhance absorption of UV radiation, which might have interesting technological applications.

For PEN in λ-orientation, the absorption measurements shows only the low-energy Davydov component at $\sim$1.88 eV, in complete agreement with the ellipsometry data.

6.4 Additional data for the PMIRRAS study on DIP:F6TCNNQ mixtures [4]

In this section we present additional data collected for the DIP:F6TCNNQ mixtures grown on PECVD-SiO_x/Au substrates for PMIRRAS studies in the Results section 4.4.

6.4.1 AFM scans of DIP:F6TCNNQ mixtures

We show in Fig. 6.17 AFM topographic scans and corresponding height distributions of the same films presented in Fig. 4.22.

The morphology of the pristine DIP film exhibits small grains with some taller islands. This morphology is clearly inherited from the finely granulated SiO_x surface covering the Au substrate (Fig. 3.10b) and is very different from that of DIP grown on native Si oxide [105]. The 4:1 blend also exhibits small grains, but their size is slightly larger than for pristine DIP and their height is more uniformly distributed.

The morphology of the blends from 2:1 to 1:4 consists of a relatively smooth background on which taller islands are present. The height distributions reported for each scan give qualitative information about the average island height. The island density increases from the 2:1 to the 1:2 blend. For the latter, islands of intermediate height are also present. For the 1:4 blend the number of taller islands decreases again. Combining the morphological information with the X-ray scattering data of Fig. 4.22, we conclude that the taller islands in the mixtures from the 2:1 up to the 1:2 constitute crystalline domains where mainly D:A co-crystals have nucleated. This conclusion is supported by the elongated shape of the taller islands in these mixtures. The islands in the 1:4 mixture, in turn, are rather isotropic and most probably constituted of segregated F6TCNNQ due to its molar excess in this film. However, since the X-ray diffraction pattern in Fig. 4.22f shows strong features from the D:A co-crystal for this mixture, such D:A crystalline domains must be numerous and might decorate the F6TCNNQ islands in the 1:4 mixture.

[4] Based on Ref. [156]

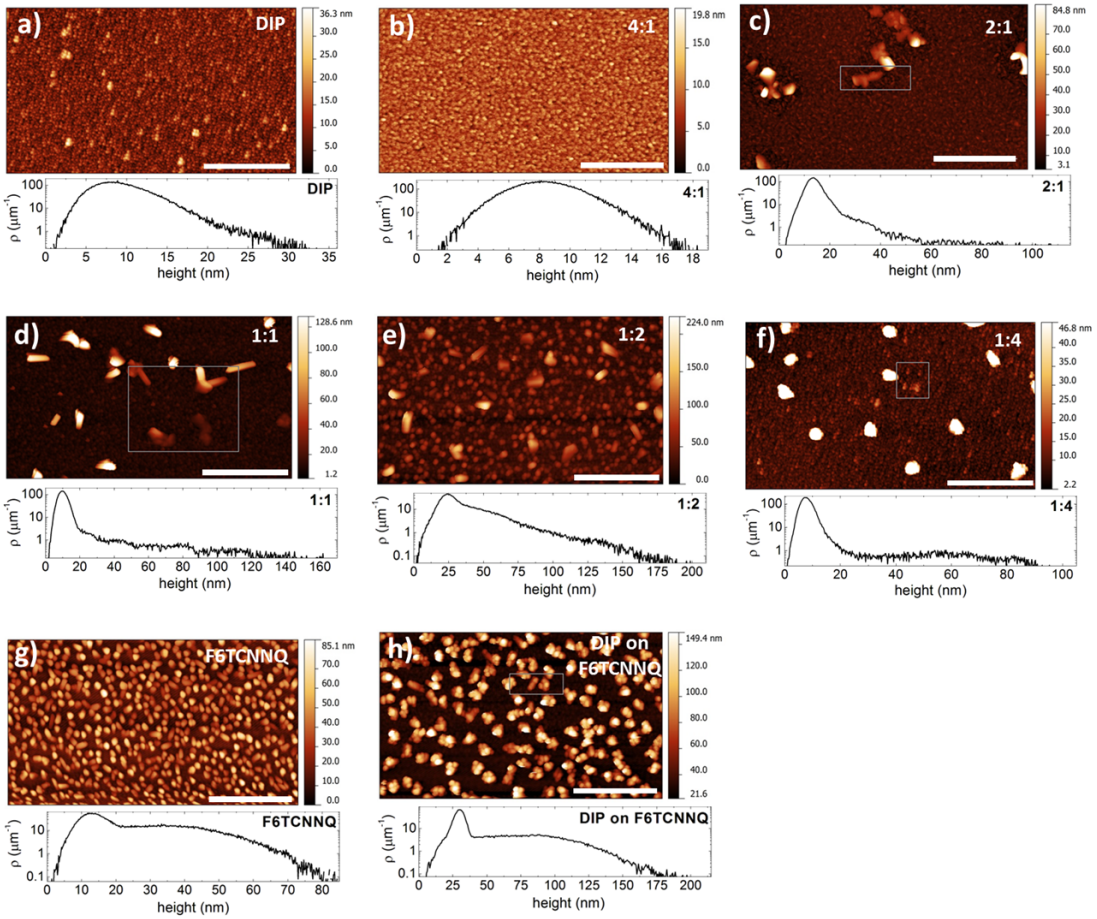

Figure 6.17: 4x7 μm^2 AFM scans of DIP:F6TCNNQ blends in varying mixing ratios grown on SiO_x/Au substrates. For the scans of the samples 2:1, 1:1, 1:4 and "DIP on F6TCNNQ", the extremes of the color scale were set on the area delimited by the rectangles. The inset bar corresponds to 2 μm. Height distributions are reported below the corresponding image. The root-mean square roughness of the images are: 3.4 nm (DIP), 2.0 nm (4:1), 8.8 nm (2:1), 18.2 nm (1:1), 23.4 nm (1:2), 10.6 nm (1:4), 15 nm (F6TCNNQ), 33.1 nm (DIP on F6TCNNQ).

The pristine F6TCNNQ film (Fig. 6.17g) exhibits a completely de-wetted morphology of in-plane isotropic islands, similarly to the sample with DIP on F6TCNNQ (Fig. 6.17h). For the latter, by comparison with the X-ray scattering data it seems likely that rather randomly oriented DIP crystals decorate the F6TCNNQ islands. The surface roughness between the islands for the sample with DIP on F6TCNNQ matches that of the bare SiO_x substrate (Fig. 3.10b), therefore we assume that DIP crystallites preferentially nucleate on the body of the F6TCNNQ islands leaving the inter-island space free. This morphology demonstrates that isolated, extended domains of F6TCNNQ have been coated by a DIP matrix, at the same time assuring a minimized number of D:A interfaces between the two materials.

The root-mean square roughness values indicated in caption of Fig. 6.17 are in agreement with the qualitative analysis of the morphology. The roughness is minimal for the 4:1 mixture, which can be explained by a smoothing effect of F6TCNNQ on the excess DIP. The roughness then increases steadily for the blends with increasing relative amount of F6TCNNQ until the 1:4 molar ratio is reached, for which the roughness decreases. One can explain this by a smoothing effect of DIP on the excess F6TCNNQ, analogous to the reverse effect in the 4:1 mixture. This trend of roughness as function of mixing ratio matches our observations for this system on native Si oxide [162].

For the AFM scans of the different DIP:F6TCNNQ blends presented in Fig. 6.17b-f and 6.17h,

the channel measuring the phase shift (see the Methods section 3.3) is shown in Fig. 6.18.

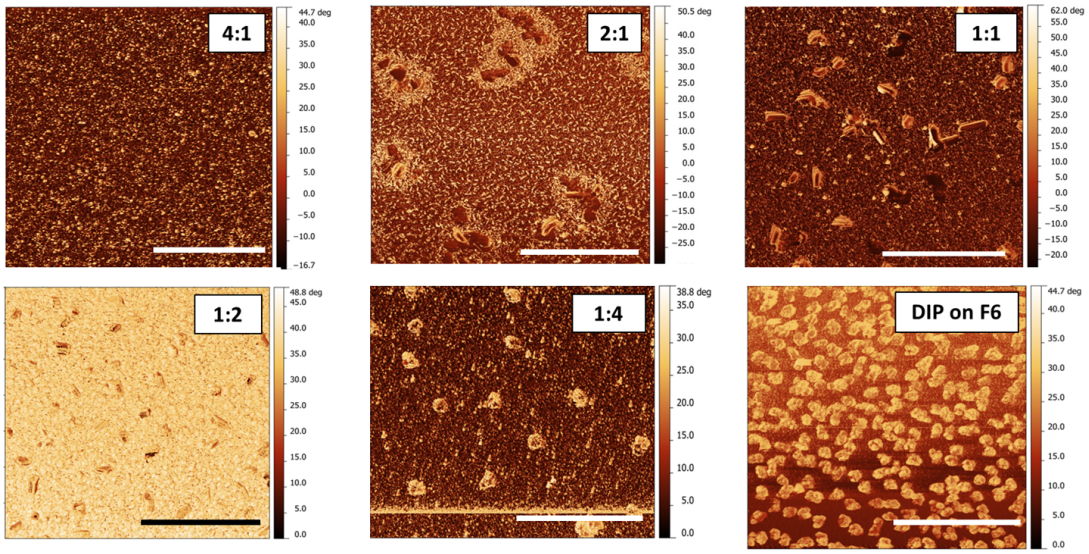

Figure 6.18: Lock-in phase channel recorded for the AFM scans of the different DIP:F6TCNNQ mixed films. The inset bar corresponds to 3 μm.

Phase-shift imaging is very sensitive to the frictional properties and can therefore be used to resolve single domains based, for instance, on their degree of crystallinity or on their composition. From Fig. 6.18 we see that the domains exhibiting phase-contrast have a nearly 1:1 correspondence with the islands visible in the topographic images of Fig. 6.17. For the mixtures from 2:1 to 1:4 there is an additional peculiar intra-island contrast originating from the different surface properties of the exposed crystal facets, supporting the conclusion that the elongated islands are constituted of DIP:F6TCNNQ co-crystals. For the 1:4 mixture the islands exhibit an isotropic shape, but the dark-bright intra-island contrast is still visible, supporting the hypothesis made above that these islands might have an F6TCNNQ core but they are decorated by co-crystallites.

Notice for the 2:1 mixture the remarkable contrast between the segregated islands of D:A co-crystallites (dark) and the surrounding DIP-rich domains with small needle-like grains (bright), which are themselves surrounded by a homogeneous matrix where the phase-separation between DIP and F6TCNNQ on a length scale of few tens of nm is evident. This phase-contrast scan illustrates the possibly very complicated scenarios of co-crystal formation *vs* phase separation for the material system DIP:F6TCNNQ [121].

6.4.2 PMIRRAS data analysis

As outlined in the Methods section 3.3 relative to PMIRRAS, the raw spectra are convoluted with the Bessel functions originating from the polarization modulation of the incident beam [252]. Using the software OPUS (Bruker) and following the procedure illustrated in the Bruker manual [248] it is possible to remove the background arising from the polarization modulation by "pinning" specific points along the spectrum and fitting them to a polynomial of arbitrary degree. If a spectrum of the bare SiO_x/Au substrate is measured with the same modulation parameters, it provides a precise guideline for the fitting and subtraction procedure.

In Fig. 6.19a we show the peculiar shape of a PMIRRAS spectrum right after the operation of Fourier transformation. The very intense peak at $\sim$ 1235 cm^{-1} dominating the spectrum (marked with "*") stems from the transverse asymmetric Si-O-Si stretching of the SiO_x layer and is commonly observed in Si oxide-coated metal surfaces (see e.g. Ref. [217, 253]). The two inset magnifications show the region of the C$=$C and C$\equiv$N stretching, respectively. In the C$\equiv$N stretching region, the broad feature marked with "**" represents an overtone of the Si-O-Si stretching peak at 1235 cm^{-1}. The overtone has been fitted using two different functions and then

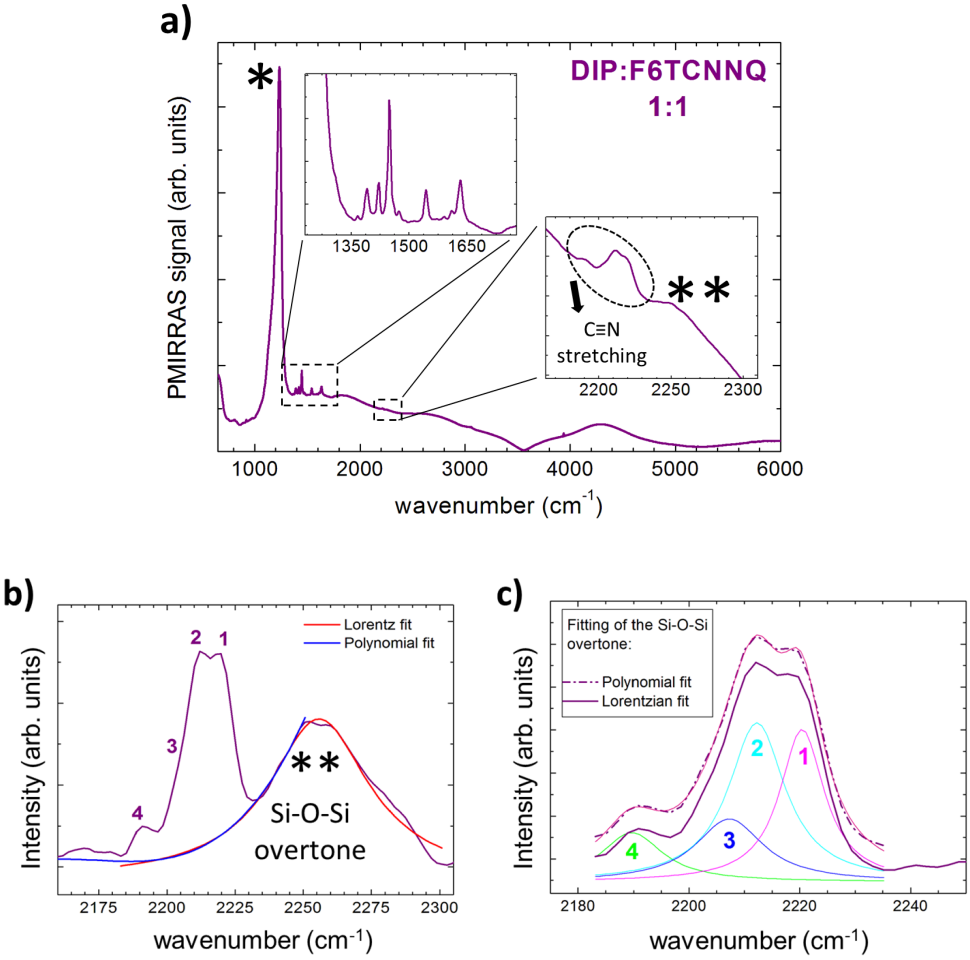

Figure 6.19: **a)** Full-range raw PMIRRAS spectrum of the DIP:F6TCNNQ 1:1 blend before subtraction of the Bessel background arising from the polarization modulation. The "*" on the strongest peak of the spectrum marks the asymmetric Si-O-Si stretching mode at $\sim$ 1235 cm^{-1}. The first inset from the left shows a magnification of the C=C stretching region; the second inset shows a magnification of the C≡N stretching region, where "**" marks the overtone of the main Si-O-Si stretching peak. **b)** Magnification of the C≡N stretching region after subtraction of the Bessel background, where the overtone of the Si-O-Si stretching has been marked. A simple Lorentzian function as well as a 5th-degree polynomial, respectively, were used to remove this broad peak. Note that with the Lorentzian function it is possible to fits the whole peak, while the polynomial only allows fitting of the low-energy edge which is overlapped with the molecular C≡N stretching modes. **c)** Comparison of the two spectral profiles in the C≡N stretching region obtained after subtraction of the overtone band using the Lorentz and the polynomial fit, respectively. The two profiles show no difference for what concerns the relevant F6TCNNQ peaks. Here the fit to the C≡N stretching vibrations and the corresponding numbering of the four Lorentzian peaks are also shown. The global fit is colored in pink and overlaps almost perfectly with the dash-dotted profile.

subtracted, as shown in Fig. 6.19b. Finally, in Fig. 6.19c the remaining C≡N stretching peaks have been fitted with a sum of Lorentzian curves in order to extract peak position. For these fits, a total number of 3 or 4 Bragg peaks has been assumed depending on the sample. Notice that with these fits no quantitative information can be extracted on peak intensity: however, peak position and qualitative information on relative peak strength are still accessible [365].

In Tab. 6.3 we report the fitted peak positions for all DIP:F6TCNNQ blends and for the planar heterostructure DIP on F6TCNNQ. The corresponding statistical error bars associated with the fits can be inspected in Fig. 4.24 of the Results section 4.4.

Table 6.3: Summary of the fitted C≡N stretching peak positions. The letter "w" indicates that the corresponding peak has qualitatively rather low intensity.

sample	DIP	4:1	2:1	1:1	1:2	1:4	F6TCNNQ	DIP on F6TCNNQ
peak 1 (cm^{-1})	-	2220.0	2220.5	2220.4	2221.6	2222.4	2224.1	2223.8
peak 2 (cm^{-1})	-	2210.4	2212.7	2212.2	2214.5	2214.9	2215.5	2215.4
peak 3 (cm^{-1})	-	2201.6 w	2205.2 w	2207.3	2204.5	2204.7	2207.0	2204.0
peak 4 (cm^{-1})	-	-	2190.9	2189.7	2192.7	2195.0	-	-

6.4.3 Details of the spectra in the C=C stretching region

In Fig. 4.23 of the Results section 4.4, PMIRRAS spectra of DIP:F6TCNNQ blends and pristine compounds in the C=C stretching region are shown . There, we discussed the red-shift of the strongest modes of F6TCNNQ, suggesting its origin to be in the ground-state CT interactions between the donor DIP and the acceptor F6TCNNQ. We also discussed the presence of phase-separated F6TCNNQ domains in each bulk heterojunction, even those with molar excess of DIP. To further support this last point, we show in Fig. 6.20a,b the presence of a high-energy shoulder of given red-shifted F6TCNNQ modes in the bulk heterojunctions.

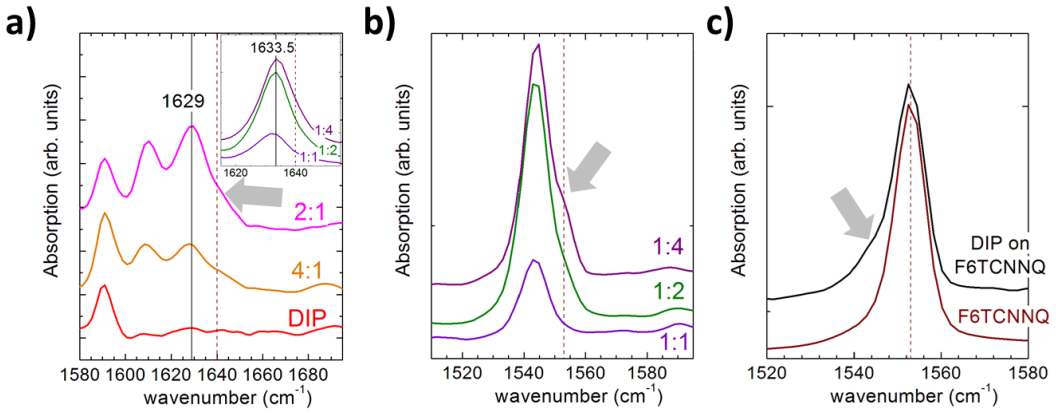

Figure 6.20: Magnifications of selected F6TCNNQ resonance modes. The spectral portions are adapted from the spectra of Fig. 4.23. The arrows indicate shoulders of the strongest peaks. The vertical dashed lines are in correspondence of the most intense peaks in the pristine F6TCNNQ film, namely at 1640 cm^{-1} in **a)** and 1553 cm^{-1} in **b)** and **c)**. In **a)**, the vertical continuous line in the main panel is located at 1629 cm^{-1}, whereas in the inset it is located at 1633.5 cm^{-1}, and it evidences the further red-shift of the CT-affected peak when going from blends with excess F6TCNNQ to blends with excess DIP.

Additionally, from inspection of the X-ray scattering data of the planar heterojunction (Fig. 4.22h of the Results section 4.4) we concluded the presence of a relatively small amount of D:A co-crystal at the interface between the F6TCNNQ islands and the DIP atop. This is confirmed by the presence of a low-energy shoulder of the strongest F6TCNNQ modes in this film, an example of which is shown in Fig. 6.20c.

Comparing the inset of Fig. 6.20a with its main panel it is possible to identify a red shift by roughly 4.5 cm^{-1} of the CT-affected F6TCNNQ peak. We recall that such peak is already shifted towards lower energies in the bulk heterojunctions compared to pristine F6TCNNQ as a result of CT interactions. The additional red shift when going from blends with excess F6TCNNQ to blends with excess DIP closely matches the observations in the C≡N stretching region (see Fig. 4.24) and confirms that the local molecular environment affects peak position similarly to a solvent-shift.

In Fig. 4.23, the two peaks marked with red squares have been assigned to pristine DIP, whose orientation with respect to the substrate surface changes in the mixtures with F6TCNNQ. This orientation-transition manifests in both nucleation of DIP crystallites in a more lying-down

orientation (λ-orientation) and inclusion of DIP molecules in the DIP:F6TCNNQ co-crystal. In Fig. 6.21 we prove this by comparing the PMIRRAS spectrum of a DIP film in σ-orientation with a film in which DIP has been "artificially" produced having a λ-orientation according a procedure detailed elsewhere [284].

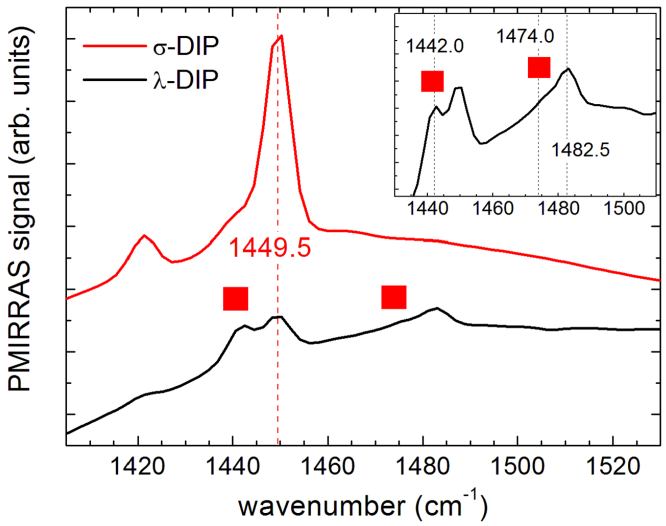

Figure 6.21: Raw PMIRRAS spectra of two films of pristine DIP in standing-up (σ) and lying-down (λ) orientation, respectively, on SiO_x layers on Au substrates. The DIP film in λ-orientation has been produced using a procedure detailed elsewhere [284]. The films were grown by Alexander Mann (Universität Tübingen).

The red squares in Fig. 6.21 mark the same features as in Fig. 4.23. In σ-DIP, the peak at 1442.0 cm^{-1} is just a shoulder of the strongest peak at 1449.5 cm^{-1}, whereas in λ-DIP the relative intensity of the two peaks is comparable. Our DFT calculations reproduce very well the experimental IR spectrum of pristine DIP (Fig. 6.22), in particular they correctly predict the strongest mode. However, no low-energy shoulder is expected by the calculations. We therefore assign the shoulder at 1442.0 cm^{-1} to a Davydov splitting of the peak at 1449.5 cm^{-1}. The relative intensity of the two Davydov components changes pronouncedly when going from the pristine DIP film to the mixtures due to re-orientation DIP in both pristine crystallites and co-crystallites, as discussed in the Results section 4.4. The presence of Davydov splitting also in the co-crystallites denotes pronounced inter-molecular interactions.

DFT also predicts the presence of the two peaks at 1474.0 and 1482.5 cm^{-1} for isolated DIP (Fig. 6.22, inset). In the λ-oriented DIP sample of Fig. 6.21 their relative intensity is inverted compared to what observed for the DIP:F6TCNNQ mixtures in Fig. 4.23. The relative intensity of these two peaks might be affected by the finer details of the molecular orientation and by the presence of DIP:F6TCNNQ co-crystals with consequent CT interactions in the mixture. However, clearly the increase of the strength of these two features relative to the others is related to the orientational transition of the DIP molecules, i.e. they are *not* new features emerging as a consequence of D:A interactions.

6.4.4 DFT calculations of infrared spectra for isolated molecules [5]

We show in Fig. 6.23 DFT calculations of the vibrational modes of the neutral F6TCNNQ molecule and of the F6TCNNQ anion, respectively. Additionally, in Fig. 6.22 we show the same calculations for the neutral form of isolated DIP. The B3LYP functional was used with the 631Gd basis set. The wavenumber axis of the vibrational spectra was scaled by the factor 0.97 [366]. In the previous paragraph we considered how the DIP modes are affected by changes in molecular orientation and by comparison with DFT calculations we identified the Davydov splitting of the strongest DIP mode. Here we focus on F6TCNNQ.

[5] Calculations performed by Reinhard Scholz (T.U. Dresden).

Considering the C=C stretching range, all five modes are red shifted for the anionic form, but the amount of red-shift depends on the peak considered. The largest shift in this range is exhibited by the second highest-frequency mode located around 1550 cm^{-1} in the calculations, which qualitatively corresponds to the experiment. Such mode is composed by the stretching of endo- and hexoskeletal bonds. For neutral F6TCNNQ, the kind of vibrations that dominate the strongest modes observed in the experiment are described in the calculated spectra of Fig. 6.23.

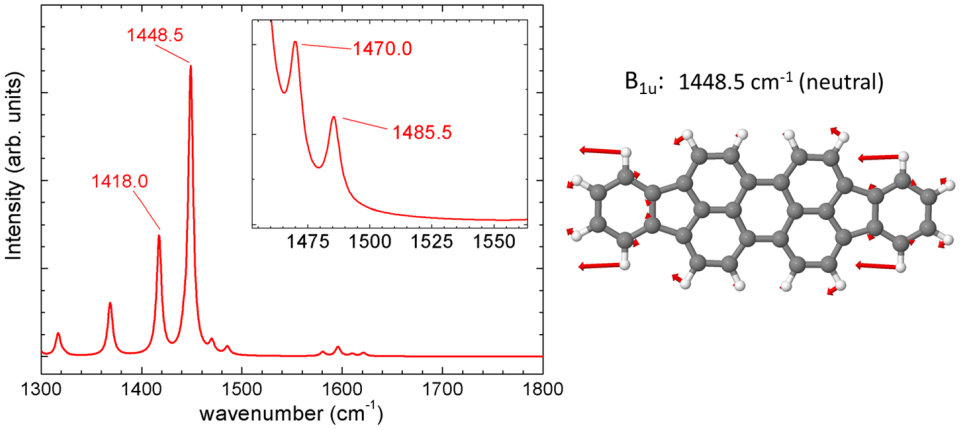

Figure 6.22: DFT simulation of IR-active molecular vibrations for isolated DIP in the neutral state. [LEFT] Simulated IR spectra in the range 1300-2260 cm^{-1}. The inset shows a magnification of the two peaks on the high-energy side of the most intense one. Rescaling of the abscissa due to anharmonicity of the molecular potential has been performed using the factor 0.97. [RIGHT] Illustration and energy position of the strongest IR-active mode for the neutral molecule.

For the C≡N stretching range, the high energy peak shifts by 33.0 cm^{-1}, whereas the low energy peak shifts by 43.5 cm^{-1}. It is quite likely that only the stronger B_u mode of the anionic F6TCNNQ calculated by DFT (right side of Fig. 6.22) can be detected experimentally in a meaningful way, which therefore represents our assignment of the observed peak 4 in Fig. 4.24. The average red shift exhibited by the experimental CT peak with its systematic uncertainty is 25.0±3 cm^{-1} (see Results section 4.4). We calculate the degree of CT, ρ, using the empirical linear relationship suggested in Ref. [155] and taking the red-shift obtained from the DFT calculation for the F6TCNNQ mono-anion as reference for case of integer CT. The stronger B_u mode exhibits a red-shift of 32.5 cm^{-1} from the neutral to the fully charged situation, which gives the degree of CT for F6TCNNQ $\rho = 0.77 \pm 0.09$ cm^{-1}.

DFT calculations on single molecule can accurately reproduce the relative intensity of IR-active modes [367]. Apart from the well-known red-shift of the resonance peaks due to the quinoid-to-benzenoid transition which accompanies the ionization process, another important difference between the calculated spectra of the neutral molecule and the mono-anion is the intensity of the C≡N stretching peaks relative to the peaks in the C=C stretching region, namely the relative strength of the C≡N stretching peaks is much higher for the mono-anion. The reason for this behavior is the pronounced increase in the net charge on the C≡N wings for the anion compared with the neutral molecule, which renders the transition dipole moment for the IR-allowed C≡N stretching modes much stronger and therefore increases their oscillator strength. The increase in net charge delocalized on the molecular backbone is not as strong due to the electron-withdrawing effect of the fluorine atoms. As a result, the oscillator strength of the C=C stretching modes does not increase as much as for the C≡N bonds. Therefore, inspection of the relative intensity of the resonances in the C≡N and C=C stretching range of experimental IR spectra can give qualitative information to discriminate between the two border-cases of full and no ionization, respectively.

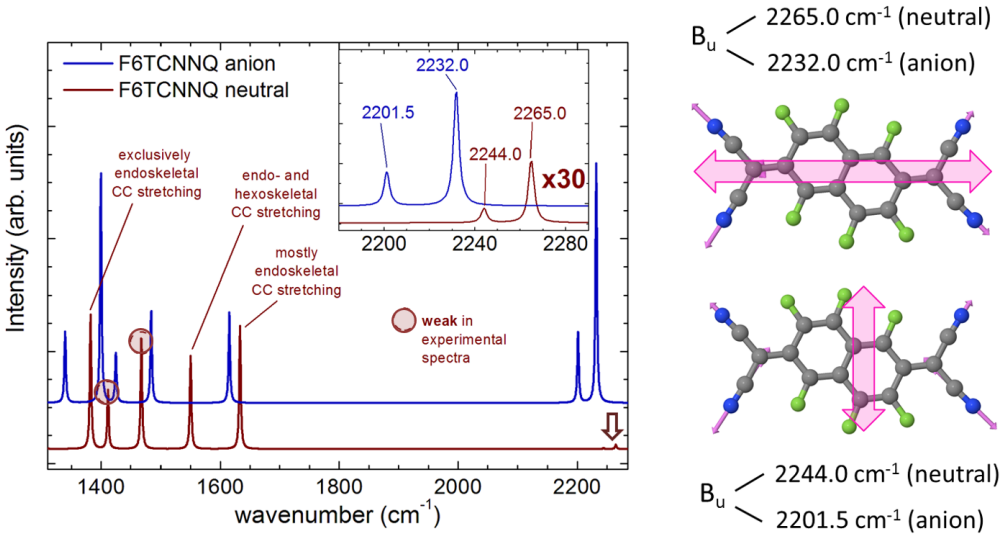

Figure 6.23: DFT simulation of IR-active molecular vibrations for isolated F6CNNQ in both the neutral state and the mono-anion. [LEFT] Simulated IR spectra in the range 1300-2275 cm^{-1}. The inset shows a magnification of the C≡N stretching region, where the peaks of the neutral molecule multiplied by 30 in order to render them comparable with those of the mono-anion, which are red-shifted due to the quinoid-to-benzenoid transition upon ionization. The arrows point to the tiny C≡N stretching modes for pristine F6TCNNQ. Rescaling of the abscissa due to anharmonicity of the molecular potential has been performed using the factor 0.97. [RIGHT] Illustration and energy position of the two IR-active asymmetric C≡N stretching modes for the neutral molecule and the mono-anion, where the magenta arrows represent the orientation of the corresponding TDM.

6.5 Experimental setups at synchrotron facilities

Below, the experimental setups realized for surface diffraction experiments with a portable vacuum chamber at two synchrotron facilities are shown. The beam path, the portable vacuum chambers for OMBD growth and the detectors are highlighted for clarity.

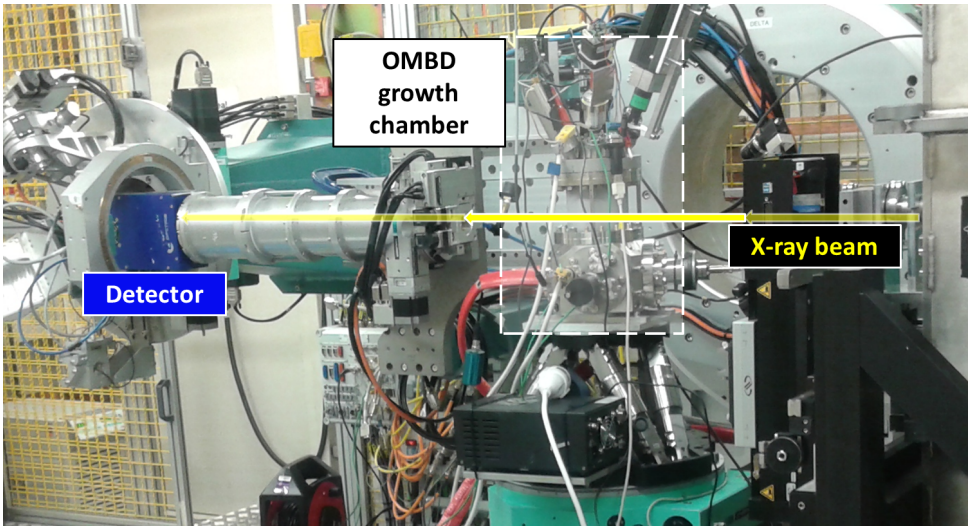

Figure 6.24: Picture of setup during experiments at I07 beamline at Diamond Light Source (DLS) in Oxford, January 2016.

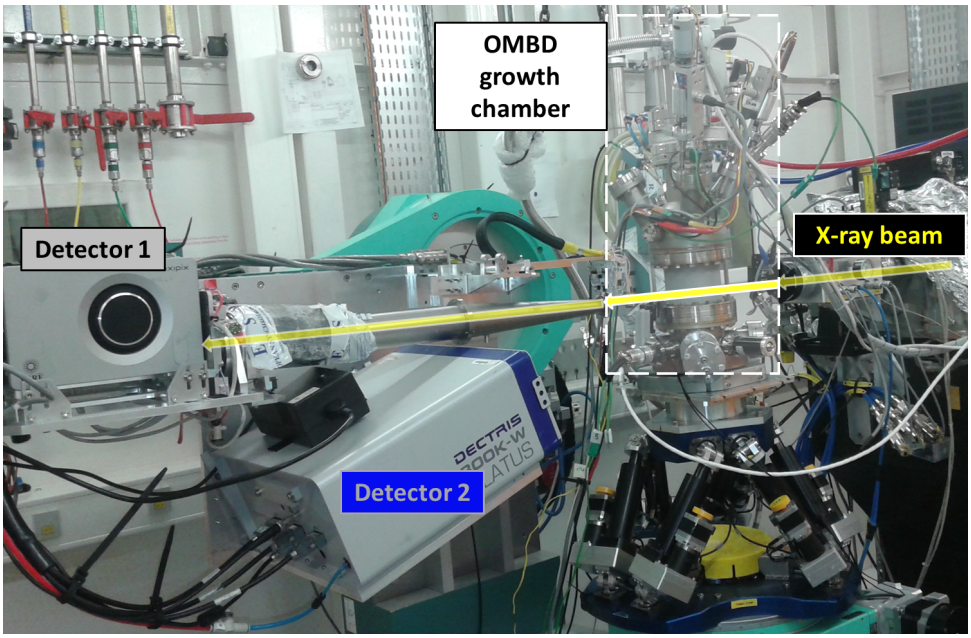

Figure 6.25: Picture of setup during experiments at ID03 beamline at European Synchrotron Research Facility (ESRF) in Grenoble, July 2017.

BIBLIOGRAPHY

[1] C. K. Chiang, C. R. Fincher, Y. W. Park, A. J. Heeger, H. Shirakawa, E. J. Louis, S. C. Gau and A. G. MacDiarmid, Electrical Conductivity in Doped Polyacetylene, *Phys. Rev. Lett.*, 1977, **39**, 1098–1101.

[2] A. Facchetti, Semiconductors for organic transistors, *Mater. Today*, 2007, **10**, 28–37.

[3] H. Sirringhaus, N. Tessler and R. H. Friend, Integrated optoelectronic devices based on conjugated polymers, *Science*, 1998, **280**, 1741–1744.

[4] H. Sirringhaus, P. J. Brown, R. H. Friend, M. M. Nielsen, K. Bechgaard, B. M. W. Langeveld-Voss, A. J. H. Spiering, R. A. J. Janssen, E. W. Meijer, P. Herwig and D. M. de Leeuw, Two-dimensional charge transport in self-organized, high-mobility conjugated polymers, *Nature*, 1999, **401**, 685–688.

[5] Y. Abe, T. Hasegawa, Y. Takahashi, T. Yamada and Y. Tokura, Control of threshold voltage in pentacene thin-film transistors using carrier doping at the charge-transfer interface with organic acceptors, *Appl. Phys. Lett.*, 2005, **87**, 153506.

[6] C. K. Chan, W. Zhao, S. Barlow, S. Marder and A. Kahn, Decamethylcobaltocene as an efficient n-dopant in organic electronic materials and devices, *Org. Electron.*, 2008, **9**, 575–581.

[7] F. G. del Pozo, S. Fabiano, R. Pfattner, S. Georgakopoulos, S. Galindo, X. Liu, S. Braun, M. Fahlman, J. Veciana, C. Rovira, X. Crispin, M. Berggren and M. Mas-Torrent, Single Crystal-Like Performance in Solution-Coated Thin-Film Organic Field-Effect Transistors, *Adv. Funct. Mater.*, 2016, **26**, 2379–2386.

[8] I. G. Lezama, M. Nakano, N. A. Minder, Z. Chen, F. V. Di Girolamo, A. Facchetti and A. F. Morpurgo, Single-crystal organic charge-transfer interfaces probed using Schottky-gated heterostructures, *Nature Mater*, 2012, **11**, 788–794.

[9] M. Mas-Torrent, P. Hadley, S. T. Bromley, N. Crivillers, J. Veciana and C. Rovira, Single-crystal organic field-effect transistors based on dibenzo-tetrathiafulvalene, *Appl. Phys. Lett.*, 2005, **86**, 012110.

[10] Y. Inoue, Y. Sakamoto, T. Suzuki, M. Kobayashi, Y. Gao and S. Tokito, Organic Thin-Film Transistors with High Electron Mobility Based on Perfluoropentacene, *Jpn. J. Appl. Phys.*, 2005, **44**, 3663.

[11] M. Bronner, A. Opitz and W. Brütting, Ambipolar charge carrier transport in organic semiconductor blends of phthalocyanine and fullerene, *Phys. Stat. Sol. (a)*, 2008, **205**, 549–563.

[12] M. Kraus, S. Richler, A. Opitz, W. Brütting, S. Haas, T. Hasegawa, A. Hinderhofer and F. Schreiber, High-mobility copper-phthalocyanine field-effect transistors with tetratetracontane passivation layer and organic metal contacts, *J. Appl. Phys.*, 2010, **107**, 094503–6.

[13] A. Opitz, M. Horlet, M. Kiwull, J. Wagner, M. Kraus and W. Brütting, Bipolar charge transport in organic field-effect transistors: Enabling high mobilities and transport of photogenerated charge carriers by a molecular passivation layer, *Org. Electron.*, 2012, **13**, 1614–1622.

[14] B. Lüssem, M. L. Tietze, H. Kleemann, C. Hoßbach, J. W. Bartha, A. Zakhidov and K. Leo, Doped organic transistors operating in the inversion and depletion regime, *Nat. Comms*, 2013, **4**, 2775.

[15] T. Someya, Y. Kato, T. Sekitani, S. Iba, Y. Noguchi, Y. Murase, H. Kawaguchi and T. Sakurai, Conformable, flexible, large-area networks of pressure and thermal sensors with organic transistor active matrixes, *Proc. Natl. Acad. Sci. U. S. A.*, 2005, **102**, 12321–12325.

[16] T. Someya, A. Dodabalapur, J. Huang, K. C. See and H. E. Katz, Chemical and Physical Sensing by Organic Field-Effect Transistors and Related Devices, *Adv. Mater.*, 2010, **22**, 3799–3811.

[17] H. Shen, Y. Zou, Y. Zang, D. Huang, W. Jin, C.-a. Di and D. Zhu, Molecular antenna tailored organic thin-film transistors for sensing application, *Mater. Horiz.*, 2018, **5**, 240–247.

[18] J.-N. Tisserant, S. Beck, M.-M. Barf, W. Kowalsky and R. Lovrincic, Nanoporous Organic Field-Effect Transistors Employing a Calixarene Dielectric for Sub-ppb Gas Sensing, *Adv. Electron. Mater.*, 2018, 1800362.

[19] X. Wu, S. Mao, J. Chen and J. Huang, Strategies for Improving the Performance of Sensors Based on Organic Field-Effect Transistors, *Adv. Mater.*, 2018, **30**, 1705642.

[20] K. Walzer, B. Maennig, M. Pfeiffer and K. Leo, Highly Efficient Organic Devices Based on Electrically Doped Transport Layers, *Chem. Rev.*, 2007, **107**, 1233–1271.

[21] S. Reineke, M. Thomschke, B. Lüssem and K. Leo, White organic light-emitting diodes: Status and perspective, *Rev. Mod. Phys.*, 2013, **85**, 1245–1293.

[22] H.-H. Fang, J. Yang, J. Feng, T. Yamao, S. Hotta and H.-B. Sun, Functional organic single crystals for solid-state laser applications, *Laser Photon. Rev.*, 2014, **8**, 687–715.

[23] W. Brütting, Organic LEDs and solar cells united, *Nat. Mater.*, 2019, **18**, 432–433.

[24] S. Ullbrich, J. Benduhn, X. Jia, V. C. Nikolis, K. Tvingstedt, F. Piersimoni, S. Roland, Y. Liu, J. Wu, A. Fischer, D. Neher, S. Reineke, D. Spoltore and K. Vandewal, Emissive and charge-generating donor–acceptor interfaces for organic optoelectronics with low voltage losses, *Nat. Mater.*, 2019, **18**, 459–464.

[25] B. Maennig, J. Drechsel, D. Gebeyehu, P. Simon, F. Kozlowski, A. Werner, F. Li, S. Grundmann, S. Sonntag, M. Koch, K. Leo, M. Pfeiffer, H. Hoppe, D. Meissner, N. Sariciftci, I. Riedel, V. Dyakonov and J. Parisi, Organic p-i-n solar cells, *Appl. Phys. A*, 2004, **79**, 1–14.

[26] S. Günes, H. Neugebauer and N. S. Sariciftci, Conjugated Polymer-Based Organic Solar Cells, *Chem. Rev.*, 2007, **107**, 1324–1338.

[27] A. Opitz, J. Wagner, W. Brütting, I. Salzmann, N. Koch, J. Manara, J. Pflaum, A. Hinderhofer and F. Schreiber, Charge separation at molecular donor-acceptor interfaces: correlation between morphology and solar cell performance, *IEEE J. Sel. Top. Quant.*, 2010, **16**, 1707.

[28] B. H. Soffer and B. B. McFarland, Continuously tunable, narrow-band organic dye lasers, *Appl. Phys. Lett.*, 1967, **10**, 266–267.

[29] N. Karl, Laser emission from an organic molecular crystal, *Phys. Stat. Sol. (a)*, 1972, **13**, 651–655.

[30] N. Tessler, G. J. Denton and R. H. Friend, Lasing from conjugated-polymer microcavities, *Nature*, 1996, **382**, 695–697.

[31] V. G. Kozlov, V. Bulovi'c, P. E. Burrows and S. R. Forrest, Laser action in organic semiconductor waveguide and double-heterostructure devices, *Nature*, 1997, **389**, 362–364.

[32] N. Tessler, Lasers Based on Semiconducting Organic Materials, *Adv. Mater.*, 1999, **11**, 363–370.

[33] A. J. C. Kuehne and M. C. Gather, Organic Lasers: Recent Developments on Materials, Device Geometries, and Fabrication Techniques, *Chem. Rev.*, 2016, **116**, 12823–12864.

[34] S. R. Forrest, The path to ubiquitous and low-cost organic electronic appliances on plastic, *Nature*, 2004, **428**, 911–918.

[35] P. M. Beaujuge and J. M. J. Fréchet, Molecular Design and Ordering Effects in π-Functional Materials for Transistor and Solar Cell Applications, *J. Am. Chem. Soc.*, 2011, **133**, 20009–20029.

[36] Z. B. Henson, K. Müllen and G. C. Bazan, Design strategies for organic semiconductors beyond the molecular formula, *Nature Chem.*, 2012, **4**, 699–704.

[37] A. Hinderhofer and F. Schreiber, Organic-organic heterostructures: Concepts and applications, *Chem. Phys. Chem.*, 2012, **13**, 628–643.

[38] A. Hinderhofer, *Ph.D. thesis*, Eberhard Karls Universität Tübingen, Tübingen, 2011.

[39] A. J. Heeger, Semiconducting and Metallic Polymers: The Fourth Generation of Polymeric Materials (Nobel Lecture), *Angew. Chem. Int. Ed.*, 2001, **40**, 2591–2611.

[40] M. Lögdlund, R. Lazzaroni, S. Stafstrom, W. Salaneck and J. Brédas, Direct Observation of Charge-Induced π-Electronic Structural Changes in a Conjugated Polymer, *Phys. Rev. Lett.*, 1989, **63**, 1841–1844.

[41] G. Parthasarathy, C. Shen, A. Kahn and S. R. Forrest, Lithium doping of semiconducting organic charge transport materials, *J. Appl. Phys.*, 2001, **89**, 4986–4992.

[42] T. Glaser, S. Beck, B. Lunkenheimer, D. Donhauser, A. Köhn, M. Kröger and A. Pucci, Infrared study of the MoO_3 doping efficiency in 4,4′-bis(N-carbazolyl)-1,1′-biphenyl (CBP), *Org. Electron.*, 2013, **14**, 575–583.

[43] M. Pfeiffer, T. Fritz, J. Blochwitz, A. Nollau, B. Plönnigs, A. Beyer and K. Leo, Advances in Solid State Physics 39, Berlin, Heidelberg, 1999, pp. 77–90.

[44] W. Gao and A. Kahn, Controlled *p*-doping of zinc phthalocyanine by coevaporation with tetrafluorotetracyanoquinodimethane: A direct and inverse photoemission study, *Appl. Phys. Lett.*, 2001, **79**, 4040–4042.

[45] W. Gao and A. Kahn, Controlled *p*-doping of the hole-transport molecular material *N*,*N*′-diphenyl-*N*,*N*′-bis(1-naphthyl)-1,1′-biphenyl-4,4′-diamine with tetrafluorotetracyanoquinodimethane, *J. Appl. Phys.*, 2003, **94**, 359–366.

[46] K. Harada, M. Riede, K. Leo, O. R. Hild and C. M. Elliott, Pentacene homojunctions: Electron and hole transport properties and related photovoltaic responses, *Phys. Rev. B*, 2008, **77**, 195212.

[47] I. Salzmann and G. Heimel, Toward a comprehensive understanding of molecular doping organic semiconductors (review), *J. Electron Spectrosc. Relat. Phenom.*, 2015, **204**, 208–222.

[48] H. Méndez, G. Heimel, S. Winkler, J. Frisch, A. Opitz, K. Sauer, B. Wegner, M. Oehzelt, C. Röthel, S. Duhm, D. Többens, N. Koch and I. Salzmann, Charge-transfer crystallites as molecular electrical dopants, *Nat. Comms*, 2015, **6**, 8560.

[49] I. Salzmann, G. Heimel, M. Oehzelt, S. Winkler and N. Koch, Molecular Electrical Doping of Organic Semiconductors: Fundamental Mechanisms and Emerging Dopant Design Rules, *Acc. Chem. Res.*, 2016, **49**, 370–378.

[50] M. L. Tietze, J. Benduhn, P. Pahner, B. Nell, M. Schwarze, H. Kleemann, M. Krammer, K. Zojer, K. Vandewal and K. Leo, Elementary steps in electrical doping of organic semiconductors, *Nat Commun*, 2018, **9**, 1182.

[51] P. Pingel, L. Zhu, K. S. Park, J.-O. Vogel, S. Janietz, E.-G. Kim, J. P. Rabe, J.-L. Brédas and N. Koch, Charge-Transfer Localization in Molecularly Doped Thiophene-Based Donor Polymers, *J. Phys. Chem. Lett.*, 2010, **1**, 2037–2041.

[52] J. Li, C. W. Rochester, I. E. Jacobs, S. Friedrich, P. Stroeve, M. Riede and A. J. Moulé, Measurement of Small Molecular Dopant F4TCNQ and $C_{60}F_{36}$ Diffusion in Organic Bilayer Architectures, *ACS Appl. Mater. Interfaces*, 2015, **7**, 28420–28428.

[53] F. Zhang and A. Kahn, Investigation of the High Electron Affinity Molecular Dopant F6-TCNNQ for Hole-Transport Materials, *Adv. Funct. Mater.*, 2018, **28**, 1703780.

[54] I. Salzmann, G. Heimel, S. Duhm, M. Oehzelt, P. Pingel, B. George, A. Schnegg, K. Lips, R.-P. Blum, A. Vollmer and N. Koch, Intermolecular Hybridization Governs Molecular Electrical Doping, *Phys. Rev. Lett.*, 2012, **108**, 035502.

[55] H. Méndez, G. Heimel, A. Opitz, K. Sauer, P. Barkowski, M. Oehzelt, J. Soeda, T. Okamoto, J. Takeya, J.-B. Arlin, J.-Y. Balandier, Y. Geerts, N. Koch and I. Salzmann, Doping of Organic Semiconductors: Impact of Dopant Strength and Electronic Coupling, *Angew. Chem. Int. Ed.*, 2013, **52**, 7751–7755.

[56] B. Mahns, O. Kataeva, D. Islamov, S. Hampel, F. Steckel, C. Hess, M. Knupfer, B. Büchner, C. Himcinschi, T. Hahn, R. Renger and J. Kortus, Crystal Growth, Structure, and Transport Properties of the Charge-Transfer Salt Picene/2,3,5,6-Tetrafluoro-7,7,8,8-tetracyanoquinodimethane, *Cryst. Growth Des.*, 2014, **14**, 1338–1346.

[57] Q. Zhang, X. Liu, F. Jiao, S. Braun, M. J. Jafari, X. Crispin, T. Ederth and M. Fahlman, Ground-state charge transfer for NIR absorption with donor/acceptor molecules: interactions mediated via energetics and orbital symmetries, *J. Mater. Chem. C*, 2017, **5**, 275–281.

[58] S. M. Sze and K. K. Ng, *Physics of semiconductor devices*, Wiley-Interscience, Hoboken, NJ, 3rd edn., 2007, p. 815 pages.

[59] H. Bässler, Charge Transport in Disordered Organic Photoconductors a Monte Carlo Simulation Study, *Phys. Stat. Sol. (b)*, 1993, **175**, 15–56.

[60] V. Coropceanu, J. Cornil, D. A. da Silva Filho, Y. Olivier, R. Silbey and J.-L. Brédas, Charge Transport in Organic Semiconductors, *Chem. Rev.*, 2007, **107**, 926–952.

[61] I. Salzmann, S. Duhm, G. Heimel, J. P. Rabe, N. Koch, M. Oehzelt, Y. Sakamoto and T. Suzuki, Structural Order in Perfluoropentacene Thin Films and Heterostructures with Pentacene, *Langmuir*, 2008, **24**, 7294–7298.

[62] A. Hinderhofer, C. Frank, T. Hosokai, A. Resta, A. Gerlach and F. Schreiber, Structure and morphology of coevaporated pentacene-perfluoropentacene thin films, *J. Chem. Phys.*, 2011, **134**, 104702.

[63] J. P. Reinhardt, A. Hinderhofer, K. Broch, U. Heinemeyer, S. Kowarik, A. Vorobiev, A. Gerlach and F. Schreiber, Structural and Optical Properties of Mixed Diindenoperylene-Perfluoropentacene Thin Films, *J. Phys. Chem. C*, 2012, **116**, 10917–10923.

[64] J. Dieterle, K. Broch, A. Hinderhofer, H. Frank, J. Novák, A. Gerlach, T. Breuer, R. Banerjee, G. Witte and F. Schreiber, Structural Properties of Picene–Perfluoropentacene and Picene–Pentacene Blends: Superlattice Formation versus Limited Intermixing, *J. Phys. Chem. C*, 2015, **119**, 26339–26347.

[65] P. Peumans, S. Uchida and S. R. Forrest, Efficient bulk heterojunction photovoltaic cells using small-molecular-weight organic thin films, *Nature*, 2003, **425**, 158–162.

[66] F. Schreiber, Organic molecular beam deposition: Growth studies beyond the first monolayer, *Phys. Stat. Sol. (a)*, 2004, **201**, 1037–1054.

[67] B. H. Bransden and C. J. Joachain, *Physics of atoms and molecules*, Prentice Hall, Harlow ; Munich [u.a.], 2nd edn., 2003, pp. XIV, 1114 Pages.

[68] L. Salem, *The molecular orbital theory of conjugated systems*, Benjamin, New York [u.a.], 1966, pp. XVI, 576 Pages.

[69] U. of Liverpool, *ChemTube3D: Structure and Bonding*, `http://www.chemtube3d.com`.

[70] N. H. Morgon, Estudo teórico das transições eletrônicas usando métodos simples e sofisticados, *Quim. Nova*, 2013, **36**, 593–599.

[71] W. B. Jensen, in *The Free-Electron Model*, ACS Publications, 2013, ch. 4, pp. 117–137.

[72] J. Autschbach, Why the Particle-in-a-Box Model Works Well for Cyanine Dyes but Not for Conjugated Polyenes, *Journal of Chemical Education*, 2007, **84**, 1840.

[73] J. R. Platt and co workers, *Systematics of the electronic spectra of conjugated molecules*, 1949-1964, `https://searchworks.stanford.edu/view/1851485`.

[74] C. Cocchi, D. Prezzi, A. Ruini, M. J. Caldas and E. Molinari, Anisotropy and Size Effects on the Optical Spectra of Polycyclic Aromatic Hydrocarbons, *J. Phys. Chem. A*, 2014, **118**, 6507–6513.

[75] M. Schwörer and H. C. Wolf, *Organic Molecular Solids*, Wiley-VCH Verlag GmbH & Co., Weinheim, 2007, pp. XI, 427 Pages.

[76] G. M. Day, T. G. Cooper, A. J. Cruz-Cabeza, K. E. Hejczyk, H. L. Ammon, S. X. M. Boerrigter, J. S. Tan, R. G. Della Valle, E. Venuti, J. Jose, S. R. Gadre, G. R. Desiraju, T. S. Thakur, B. P. van Eijck, J. C. Facelli, V. E. Bazterra, M. B. Ferraro, D. W. M. Hofmann, M. A. Neumann, F. J. J. Leusen, J. Kendrick, S. L. Price, A. J. Misquitta, P. G. Karamertzanis, G. W. A. Welch, H. A. Scheraga, Y. A. Arnautova, M. U. Schmidt, J. van de Streek, A. K. Wolf and B. Schweizer, Significant progress in predicting the crystal structures of small organic molecules - a report on the fourth blind test, *Acta Cryst. B*, 2009, **65**, 107–125.

[77] J. Yang, S. De, J. E. Campbell, S. Li, M. Ceriotti and G. M. Day, Large-Scale Computational Screening of Molecular Organic Semiconductors Using Crystal Structure Prediction, *Chem. Mater.*, 2018, **30**, 4361–4371.

[78] S. Schiefer, M. Huth, A. Dobrinevski and B. Nickel, Determination of the Crystal Structure of Substrate-Induced Pentacene Polymorphs in Fiber Structured Thin Films, *J. Am. Chem. Soc.*, 2007, **129**, 10316–10317.

[79] J. Vrbancich and G. L. D. Ritchie, Quadrupole Moments of Benzene, Hexafluorobenzene and Other Non-dipolar Aromatic Molecules, *J. Chem. Soc., Faraday Trans. 2*, 1980, **76**, 648–659.

[80] J. H. Williams, The molecular electric quadrupole moment and solid-state architecture, *Acc. Chem. Res.*, 1993, **26**, 593–598.

[81] M. Nishio, M. Hirota and Y. Umezawa, *The CH-π interaction: evidence, nature, and consequences*, Wiley-VCH, New York, 1998, pp. XIII, 217 Pages.

[82] E. A. Meyer, R. K. Castellano and F. Diederich, Interactions with Aromatic Rings in Chemical and Biological Recognition, *Angew. Chem. Int. Ed.*, 2003, **42**, 1210–1250.

[83] T. Breuer and G. Witte, Thermally activated intermixture in pentacene-perfluoropentacene heterostructures, *J. Chem. Phys.*, 2013, **138**, 114901.

[84] J. B. Torrance, J. E. Vazquez, J. J. Mayerle and V. Y. Lee, Discovery of a Neutral-to-Ionic Phase Transition in Organic Materials, *Phys. Rev. Lett.*, 1981, **46**, 253–257.

[85] Z. G. Soos, S. Mazumdar and T. T. P. Cheung, Valence Bond Theory of Organic Charge-Transfer Salts, *Mol. Cryst. Liq. Cryst.*, 1979, **52**, 397–406.

[86] M. Meneghetti, R. Bozio, C. Bellitto and C. Pecile, Electronic and structural characterization of a charge transfer crystal with strong electronic correlations through infrared and Raman spectroscopy: TMPD-TCNQF4, *J. Chem. Phys.*, 1988, **89**, 2704.

[87] M. Pope and C. E. Swenberg, *Electronic processes in organic crystals and polymers*, Oxford University Press, New York [u.a.], 2nd edn., 1999, pp. XXIX, 1328 Pages.

[88] P. Hu, H. Li, Y. Li, H. Jiang and C. Kloc, Single-crystal growth, structures, charge transfer and transport properties of anthracene-F_4TCNQ and tetracene-F_4TCNQ charge-transfer compounds, *Cryst. Eng. Comm.*, 2017, **19**, 618–624.

[89] R. H. Blessing and P. Coppens, Crystallography of the TTF-TCNQ salt at reduced temperatures, *Solid State Commun.*, 1974, **15**, 215–221.

[90] A. I. Kitajgorodskij, *Molecular crystals and molecules*, Acad. Press, New York [u.a.], 1973, pp. XII, 553 Pages.

[91] A. I. Kitajgorodskij, *Mixed crystals*, Springer, Berlin; Heidelberg [u.a.], 1984, pp. XIV, 388 Pages.

[92] A. Aufderheide, K. Broch, J. Novák, A. Hinderhofer, R. Nervo, A. Gerlach, R. Banerjee and F. Schreiber, Mixing-Induced Anisotropic Correlations in Molecular Crystalline Systems, *Phys. Rev. Lett.*, 2012, **109**, 156102.

[93] K. Broch, *Ph.D. thesis*, Eberhard Karls Universität Tübingen, Tübingen, 2013.

[94] K. Broch, A. Aufderheide, L. Raimondo, A. Sassella, A. Gerlach and F. Schreiber, Optical Properties of Blends: Influence of Mixing-Induced Disorder in Pentacene:Diindenoperylene versus Perfluoropentacene:Diindenoperylene, *J. Phys. Chem. C*, 2013, **117**, 13952–13960.

[95] R. Banerjee, J. Novák, C. Frank, C. Lorch, A. Hinderhofer, A. Gerlach and F. Schreiber, Evidence for Kinetically Limited Thickness Dependent Phase Separation in Organic Thin Film Blends, *Phys. Rev. Lett.*, 2013, **110**, 185506.

[96] C. Lorch, R. Banerjee, C. Frank, J. Dieterle, A. Hinderhofer, A. Gerlach and F. Schreiber, Growth of competing crystal phases of α-sexithiophene studied by real-time X-ray scattering, *J. Phys. Chem. C*, 2015, **119**, 819–825.

[97] F. Schreiber, Structure and Growth of Self-Assembling Monolayers, *Prog. Surf. Sci.*, 2000, **65**, 151–257.

[98] S. R. Forrest, Ultrathin organic films grown by organic molecular beam deposition and related techniques, *Chem. Rev.*, 1997, **97**, 1793–1896.

[99] I. V. Markov, *Crystal growth for beginners: fundamentals of nucleation, crystal growth and epitaxy*, World Scientific, 5 Toh Tuck Link, Singapore, 2014, pp. IV, 546 pages.

[100] S. Kowarik, K. Broch and F. Schreiber, Beim Wachstum zusehen, *Physik J.*, 2014, **13**, 33–39.

[101] S. R. Forrest, F. F. So and D. Y. Zang, *U.S. Patent. Polarization-Selective Integrated Optoelectronic Devices Incorporating Crystalline Organic Thin Films*, 1992.

[102] P. Clancy, Application of Molecular Simulation Techniques to the Study of Factors Affecting the Thin-Film Morphology of Small-Molecule Organic Semiconductors, *Chem. Mater.*, 2011, **23**, 522–543.

[103] G. Hlawacek and C. Teichert, Nucleation and growth of thin films of rod-like conjugated molecules, *J. Phys.: Condens. Matter*, 2013, **25**, 143202.

[104] J. Krug, Origins of scale invariance in growth processes, *Adv. Phys.*, 1997, **46**, 139–282.

[105] A. C. Dürr, F. Schreiber, K. A. Ritley, V. Kruppa, J. Krug, H. Dosch and B. Struth, Rapid Roughening in Thin Film Growth of an Organic Semiconductor (Diindenoperylene), *Phys. Rev. Lett.*, 2003, **90**, 016104.

[106] J. Krug, Power laws in surface physics: The deep the shallow and the useful, *Physica A*, 2004, **340**, 647–655.

[107] T. Michely and J. Krug, *Islands, Mounds, and Atoms. Patterns and Processes in Crystal Growth Far from Equilibrium*, Springer, Berlin, 2004.

[108] F. Brochard-Wyart, J. M. Di Meglio, D. Quere and P. G. De Gennes, Spreading of nonvolatile liquids in a continuum picture, *Langmuir*, 1991, **7**, 335–338.

[109] S. Kowarik, A. Gerlach, S. Sellner, F. Schreiber, L. Cavalcanti and O. Konovalov, Real-time observation of structural and orientational transitions during growth of organic thin films, *Phys. Rev. Lett.*, 2006, **96**, 125504.

[110] S. Kowarik, A. Gerlach, M. W. A. Skoda, S. Sellner and F. Schreiber, Real-time studies of thin film growth: Measurement and analysis of X-ray growth oscillations beyond the anti-Bragg point, *Eur. Phys. J. Special Topics*, 2009, **167**, 11–18.

[111] P. Beyer, D. Pham, C. Peter, N. Koch, E. Meister, W. Brütting, L. Grubert, S. Hecht, D. Nabok, C. Cocchi, C. Draxl and A. Opitz, State-of-Matter-Dependent Charge-Transfer Interactions between Planar Molecules for Doping Applications, *Chem. Mater.*, 2019, **31**, 1237–1249.

[112] S. Bommel, N. Kleppmann, C. Weber, H. Spranger, P. Schäfer, J. Novák, S. Roth, F. Schreiber, S. Klapp and S. Kowarik, Unravelling the multilayer growth of the fullerene C_{60} in real time, *Nat. Comm.*, 2014, **5**, 5388.

[113] L. Pithan, *Ph.D. thesis*, Humboldt Universität, Berlin, 2017.

[114] Y. Zeng, B. Tao and Z. Yin, Molecular Orientation Transformation of Pentacene on Amorphous SiO_2: A Computational Study on the Initial Growth Stage of Physical Vapor Deposition, *J. Cryst. Growth*, 2014, **405**, 73–80.

[115] L. Muccioli, G. D'Avino and C. Zannoni, Simulation of Vapor-Phase Deposition and Growth of a Pentacene Thin Film on C_{60}(001), *Adv. Mater.*, 2011, **23**, 4532–4536.

[116] M. A. Loi, E. D. Como, F. Dinelli, M. Murgia, R. Zamboni, F. Biscarini and M. Muccini, Supramolecular Organization in Ultra-Thin Films of α-Sexithiophene on Silicon Dioxide, *Nat. Mater.*, 2005, **4**, 81–85.

[117] A. Dürr, B. Nickel, V. Sharma, U. Täffner and H. Dosch, Observation of Competing Modes in the Growth of Diindenoperylene on SiO_2, *Thin Solid Films*, 2006, **503**, 127.

[118] S. Kowarik, A. Gerlach, S. Sellner, L. Cavalcanti, O. Konovalov and F. Schreiber, Real-time X-ray diffraction measurements of structural dynamics and polymorphism in diindenoperylene growth, *Appl. Phys. A*, 2009, **95**, 233–239.

[119] A. Hinderhofer, T. Hosokai, K. Yonezawa, A. Gerlach, K. Kato, K. Broch, C. Frank, J. Novák, S. Kera, N. Ueno and F. Schreiber, Post-growth surface smoothing of thin films of diindenoperylene, *Appl. Phys. Lett.*, 2012, **101**, 033307.

[120] A. Y. Lee, D. Erdemir and A. S. Myerson, Crystal Polymorphism in Chemical Process Development, *Ann. Rev. Chem. Biomol. Eng.*, 2011, **2**, 259–280.

[121] J. H. ter Horst and P. W. Cains, Co-Crystal Polymorphs from a Solvent-Mediated Transformation, *Cryst. Growth Des.*, 2008, **8**, 2537–2542.

[122] R. A. Chiarella, R. J. Davey and M. L. Peterson, Making Co-Crystals: The Utility of Ternary Phase Diagrams, *Cryst. Growth Des.*, 2007, **7**, 1223–1226.

[123] J. Bernstein, Polymorphism: A Perspective, *Cryst. Growth Des.*, 2011, **11**, 632–650.

[124] M. A. Heinrich, J. Pflaum, A. K. Tripathi, W. Frey, M. L. Steigerwald and T. Siegrist, Enantiotropic Polymorphism in Di-indenoperylene, *J. Phys. Chem. C*, 2007, **111**, 18878–18881.

[125] C. C. Mattheus, A. B. Dros, J. Baas, G. T. Oostergetel, A. Meetsma, J. L. de Boer and T. T. Palstra, Identification of polymorphs of pentacene, *Synth. Met.*, 2003, **138**, 475–481.

[126] C. C. Mattheus, G. A. de Wijs, R. A. de Groot and T. T. M. Palstra, Modeling the polymorphism of pentacene, *J. Am. Chem. Soc.*, 2003, **125**, 6323.

[127] G. Horowitz, B. Bachet, A. Yassar, P. Lang, F. Demanze, J.-L. Fave and F. Garnier, Growth and characterization of sexithiophene single crystals, *Chem. Mater.*, 1995, **7**, 1337–1341.

[128] T. Siegrist, R. Fleming, R. Haddon, R. Laudise, A. Lovinger, H. Katz, P. Bridenbaugh and D. Davis, The crystal structure of the high-temperature polymorph of α-hexathienyl (α-6T/HT), *J. Mater. Res.*, 1995, **10**, 2170–2173.

[129] A. Brillante, I. Bilotti, R. G. Della Valle, E. Venuti, S. Milita, C. Dionigi, F. Borgatti, A. N. Lazar, F. Biscarini, M. Mas-Torrent, N. S. Oxtoby, N. Crivillers, J. Veciana, C. Rovira, M. Leufgen, G. Schmidt and L. W. Molenkamp, The four polymorphic modifications of the semiconductor dibenzo-tetrathiafulvalene, *Cryst. Eng. Comm.*, 2008, **10**, 1899.

[130] T. Mori and H. Inokuchi, Crystal Structure of the Mixed-Stacked Salt of Bis(ethylenedithio)tetrathiafulvalene (BEDT-TTF) and Tetracyanoquinodimethane (TCNQ), *Bull. Chem. Soc. Jpn.*, 1987, **60**, 402–404.

[131] K. P. Goetz, J. Tsutsumi, S. Pookpanratana, J. Chen, N. S. Corbin, R. K. Behera, V. Coropceanu, C. A. Richter, C. A. Hacker, T. Hasegawa and O. D. Jurchescu, Polymorphism in the 1:1 Charge-Transfer Complex DBTTF-TCNQ and Its Effects on Optical and Electronic Properties, *Adv. Electron. Mater.*, 2016, **2**, 1600203.

[132] A. O. F. Jones, B. Chattopadhyay, Y. H. Geerts and R. Resel, Substrate-Induced and Thin-Film Phases: Polymorphism of Organic Materials on Surfaces, *Adv. Funct. Mater.*, 2016, **26**, 2233–2255.

[133] L. Pithan, C. Cocchi, H. Zschiesche, C. Weber, A. Zykov, S. Bommel, S. J. Leake, P. Schäfer, C. Draxl and S. Kowarik, Light Controls Polymorphism in Thin Films of Sexithiophene, *Cryst. Growth Des.*, 2015, **15**, 1319–1324.

[134] A. Dodobalapur, L. Torsi and H. E. Katz, Organic Transistors- 2-Dimensional Transport and Improved Electrical Characteristics, *Science*, 1995, **268**, 270–271.

[135] D. Nabok, P. Puschnig, C. Ambrosch-Draxl, O. Werzer, R. Resel and D.-M. Smilgies, Crystal and electronic structures of pentacene thin films from grazing-incidence X-ray diffraction and first-principles calculations, *Phys. Rev. B*, 2007, **76**, 235322.

[136] L. Pithan, D. Nabok, C. Cocchi, P. Beyer, G. Duva, J. Simbrunner, J. Rawle, C. Nicklin, P. Schäfer, C. Draxl, F. Schreiber and S. Kowarik, Molecular structure of the substrate-induced thin-film phase of tetracene, *J. Chem. Phys.*, 2018, **149**, 144701.

[137] F. Wooten, *Optical properties of solids*, Acad. Pr., New York [u.a.], 1972, pp. XII, 260 Pages.

[138] J. A. Woollam, *Guide to Using WVASE. Spectroscopic Ellipsometry Data Acquisition and Analysis Software*, J. A. Woollam Co., Inc.

[139] M. Kasha, H. R. Rawls and M. A. El-Bayoumi, The exciton model in molecular spectroscopy, *Pure App. Chem.*, 1965, **11**, 371.

[140] P. Pingel and D. Neher, Comprehensive picture of p-type doping of P3HT with the molecular acceptor F4TCNQ, *Phys. Rev. B*, 2013, **87**, 115209.

[141] E. W. Weisstein, *Cauchy Principal Value*, `http://mathworld.wolfram.com/CauchyPrincipalValue.html`.

[142] J. Dieterle, *Ph.D. thesis*, Eberhard Karls Universität Tübingen, Tübingen, 2016.

[143] J. B. Theeten and D. E. Aspnes, The determination of interface layers by spectroscopic ellipsometry, *Thin Solid Films*, 1979, **60**, 183–192.

[144] H. Tompkins and E. A. Irene, *Handbook of ellipsometry*, William Andrew, Norwich, NY, 2005, pp. XII, 891 pages.

[145] D. E. Aspnes, Optical properties of thin films, *Thin Solid Films*, 1982, **89**, 249–262.

[146] U. Heinemeyer, *Ph.D. thesis*, Eberhard Karls Universität Tübingen, Tübingen, 2009.

[147] M. J. Hollas, *Modern Spectroscopy*, John Wiley & Sons, Chichester, England, 4th edn., 2004, pp. XIII, 704 pages.

[148] U. Heinemeyer, R. Scholz, L. Gisslén, M. I. Alonso, J. O. Ossó, M. Garriga, A. Hinderhofer, M. Kytka, S. Kowarik, A. Gerlach and F. Schreiber, Exciton-phonon coupling in diindenoperylene thin films, *Phys. Rev. B*, 2008, **78**, 085210.

[149] N. S. Bayliss and E. G. McRae, Solvent effects in organic spectra: dipole forces and the Franck-Condon principle, *J. Phys. Chem.*, 1954, **58**, 1002.

[150] J. B. Birks, *Photophysics of aromatic molecules*, Wiley-Interscience, London, England, 4th edn., 1970, pp. XI, 691 pages.

[151] G. M. Grosso and G. Pastori Parravicini, *Solid state physics*, Academic Press, San Diego, California, 2nd edn., 2003, p. 727 pages.

[152] A. S. Davydov, The theory of molecular excitons, *Sov. Phys. Usp.*, 1964, **7**, 145–178.

[153] D. Beljonne, H. Yamagata, J. L. Brédas, F. C. Spano and Y. Olivier, Charge-Transfer Excitations Steer the Davydov Splitting and Mediate Singlet Exciton Fission in Pentacene, *Phys. Rev. Lett.*, 2013, **110**, 226402.

[154] R. Scholz, M. Friedrich, G. Salvan, T. U. Kampen, D. R. T. Zahn and T. Frauenheim, Infrared spectroscopic study of the morphology of 3,4,9,10-perylene tetracarboxylic dianhydride films grown on H-passivated Si(111), *J. Phys.: Condens. Matter*, 2003, **15**, S2647.

[155] J. S. Chappell, A. N. Bloch, W. A. Bryden, M. Maxfield, T. O. Poehler and D. O. Cowan, Degree of charge transfer in organic conductors by infrared absorption spectroscopy, *J. Am. Chem. Soc.*, 1981, **103**, 2442–2443.

[156] G. Duva, P. Beyer, R. Scholz, V. Belova, A. Opitz, A. Hinderhofer, A. Gerlach and F. Schreiber, Ground-state charge-transfer interactions in donor:acceptor pairs of organic semiconductors – a spectroscopic study of two representative systems, *Phys. Chem. Chem. Phys.*, 2019, **21**, 17190–17199.

[157] V. Belova, P. Beyer, E. Meister, T. Linderl, M.-U. Halbich, M. Gerhard, S. Schmidt, T. Zechel, T. Meisel, A. V. Generalov, A. S. Anselmo, R. Scholz, O. Konovalov, A. Gerlach, M. Koch, A. Hinderhofer, A. Opitz, W. Brütting and F. Schreiber, Evidence for Anisotropic Electronic Coupling of Charge Transfer States in Weakly Interacting Organic Semiconductor Mixtures, *J. Am. Chem. Soc.*, 2017, **139**, 8474–8486.

[158] J.-L. Bredas, Mind the gap!, *Mater. Horiz.*, 2014, **1**, 17–19.

[159] T. Ameri, G. Dennler, C. Lungenschmied and C. J. Brabec, Organic tandem solar cells: A review, *Energy Environ. Sci.*, 2009, **2**, 347.

[160] K. Broch, U. Heinemeyer, A. Hinderhofer, F. Anger, R. Scholz, A. Gerlach and F. Schreiber, Optical evidence for intermolecular coupling in mixed films of pentacene and perfluoropentacene, *Phys. Rev. B*, 2011, **83**, 245307.

[161] F. Anger, J. O. Ossó, U. Heinemeyer, K. Broch, R. Scholz, A. Gerlach and F. Schreiber, Photoluminescence spectroscopy of pure pentacene, perfluoropentacene, and mixed thin films, *J. Chem. Phys.*, 2012, **136**, 054701.

[162] G. Duva, L. Pithan, C. Zeiser, B. Reisz, J. Dieterle, B. Hofferberth, P. Beyer, L. Bogula, A. Opitz, S. Kowarik, A. Hinderhofer, A. Gerlach and F. Schreiber, Thin-Film Texture and Optical Properties of Donor/Acceptor Complexes. Diindenoperylene/F6TCNNQ vs Alpha-Sexithiophene/F6TCNNQ, *J. Phys. Chem. C*, 2018, **122**, 18705–18714.

[163] J. Als-Nielsen and D. McMorrow, *Elements of Modern X-ray Physics*, John Wiley & Sons, Ltd, Chichester, 2nd edn., 2011.

[164] T. U. Graz, *Atomic form factors*, `http://lampx.tugraz.at/~hadley/ss1/crystaldiffraction/atomicformfactors/formfactors.php`.

[165] P. Willmott, *An Introduction to Synchrotron Radiation.Techniques and Applications*, Wiley-Blackwell, Chichester, England, 2nd edn., 2019, pp. VIII, 544 pages.

[166] *International Tables for Crystallography*, `http://xrpp.iucr.org/Ab/ch9o1v0001/`.

[167] A. K. Tripathi and J. Pflaum, Correlation between ambipolar transport and structural phase transition in diindenoperylene single crystals, *Appl. Phys. Lett.*, 2006, **89**, 082103.

[168] J. Wagner, M. Gruber, A. Hinderhofer, A. Wilke, B. Bröker, J. Frisch, P. Amsalem, A. Vollmer, A. Opitz, N. Koch, F. Schreiber and W. Brütting, High fill factor and open circuit voltage in organic photovoltaic cells with diindenoperylene as donor material, *Adv. Funct. Mater.*, 2010, **20**, 4295–4303.

[169] A. C. Dürr, F. Schreiber, M. Münch, N. Karl, B. Krause, V. Kruppa and H. Dosch, High structural order in thin films of the organic semiconductor diindenoperylene, *Appl. Phys. Lett.*, 2002, **81**, 2276–2278.

[170] A. C. Dürr, N. Koch, M. Kelsch, A. Rühm, J. Ghijsen, R. L. Johnson, J.-J. Pireaux, J. Schwartz, F. Schreiber, H. Dosch and A. Kahn, Interplay between morohology and structure and and electronic properties at diindenoperylene-gold interfaces, *Phys. Rev. B*, 2003, **68**, 115428.

[171] C. Frank, J. Novák, R. Banerjee, A. Gerlach, F. Schreiber, A. Vorobiev and S. Kowarik, Island size evolution and molecular diffusion during growth of organic thin films followed by time-resolved specular and off-specular scattering, *Phys. Rev. B*, 2014, **90**, 045410 (1–6).

[172] B. Servet, S. Ries, M. Trotel, P. Alnot, G. Horowitz and F. Garnier, X-ray determination of the crystal structure and orientation of vacuum evaporated sexithiophene films, *Adv. Mater.*, 1993, **5**, 461–464.

[173] B. Servet, G. Horowitz, S. Ries, O. Lagorsse, P. Alnot, A. Yassar, F. Deloffre, P. Srivastava and R. Hajlaoui, Polymorphism and Charge Transport in Vacuum-Evaporated Sexithiophene Films, *Chem. Mater.*, 1994, **6**, 1809–1815.

[174] F. Garnier, G. Horowitz, X. Peng and D. Fichou, An all-organic "soft" thin film transistor with very high carrier mobility, *Adv. Mater.*, 1990, **2**, 592–594.

[175] G. Horowitz, D. Fichou, X. Peng, Z. Xu and F. Garnier, Field-effect transistor based on conjugated alpha-sexithienyl, *Solid State Commun.*, 1989, **72**, 381–384.

[176] F. Song-Qui, X. Guang-Zhong, T. Hui-Ling, X. Li and P. Sun, The 2010 International Conference on Apperceiving Computing and Intelligence Analysis Proceeding, 2010, pp. 105–108.

[177] U. Hörmann, C. Lorch, A. Hinderhofer, A. Gerlach, M. Gruber, J. Kraus, B. Sykora, S. Grob, T. Linderl, A. Wilke, A. Opitz, R. Hansson, A. S. Anselmo, Y. Ozawa, Y. Nakayama, H. Ishii, N. Koch, E. Moons, F. Schreiber and W. Brütting, V_{OC} from a Morphology Point of View: the Influence of Molecular Orientation on the Open Circuit Voltage of Organic Planar Heterojunction Solar Cells, *J. Phys. Chem. C*, 2014, **118**, 26462–26470.

[178] C. Lorch, R. Banerjee, J. Dieterle, A. Hinderhofer, A. Gerlach, J. Drnec and F. Schreiber, Templating Effects of α-Sexithiophene in Donor-Acceptor Organic Thin Films, *J. Phys. Chem. C*, 2015, **119**, 23211.

[179] Heliatek, *Technology: in-house development of organic materials*, `https://www.heliatek.com/en/solar-films/technology`.

[180] A. Moser, I. Salzmann, M. Oehzelt, A. Neuhold, H.-G. Flesch, J. Ivanco, S. Pop, T. Toader, D. R. Zahn, D.-M. Smilgies and R. Resel, A disordered layered phase in thin films of sexithiophene, *Chem. Phys. Lett.*, 2013, **574**, 51–55.

[181] C. C. Mattheus, A. B. Dros, J. Baas, A. Meetsma, J. L. d. Boer and T. T. M. Palstra, Polymorphism in pentacene, *Acta Crystallogr. C: Cryst. Struct. Commun.*, 2001, **57**, 939–941.

[182] I. Bouchoms, W. Schoonveld, J. Vrijmoeth and T. Klapwijk, Morphology identification of the thin film phases of vacuum evaporated pentacene on SiO_2 substrates, *Synth. Met.*, 1999, **104**, 175–178.

[183] A. Hinderhofer, U. Heinemeyer, A. Gerlach, S. Kowarik, R. M. J. Jacobs, Y. Sakamoto, T. Suzuki and F. Schreiber, Optical properties of pentacene and perfluoropentacene thin films, *J. Chem. Phys.*, 2007, **127**, 194705.

[184] R. B. Campbell, J. M. Robertson and J. Trotter, The crystal structure of hexacene, and a revision of the crystallographic data for tetracene, *Acta Cryst*, 1962, **15**, 289–290.

[185] M. Halik, H. Klauk, U. Zschieschang, G. Schmid, C. Dehm, M. Schütz, S. Maisch, F. Effenberger, M. Brunnbauer and F. Stellacci, Low-voltage organic transistors with an amorphous molecular gate dielectric, *Nature*, 2004, **431**, 963–966.

[186] J. B. Torrance, The difference between metallic and insulating salts of tetracyanoquinodimethone (TCNQ): how to design an organic metal, *Acc. Chem. Res.*, 2002, **12**, 79–86.

[187] L. Coleman, M. Cohen, D. Sandman, F. Yamagishi, A. Garito and A. Heeger, Superconducting fluctuations and the peierls instability in an organic solid, *Solid State Commun.*, 1973, **12**, 1125–1132.

[188] T. J. Emge, F. M. Wiygul, J. S. Chappell, A. N. Bloch, J. P. Ferraris, D. O. Cowan and T. J. Kistenmacher, Crystal Structure for the Electron Donor Dibenzotetrathiafulvalene, DBTTF, and Its Mixed-stack Charge-transfer Salts with the Electron Acceptors 7,7,8,8-tetracyano-p-quinodimethane, TCNQ, and 2,5-difluoro-7,7,8,8-tetracyano-p-quinodimethane, 2,5-TCNQF2, *Mol. Cryst. Liq. Cryst.*, 1982, **87**, 137–161.

[189] R. P. Shibaeva, R. M. Lobkovskaya and V. N. Klyuev, Crystal and molecular structure of delta-2,2′-bi-d-benzo-1,3-dithiol, C14H8S4, *Cryst. Struct. Commun.*, 1982, **11**, 835–839.

[190] M. Mamada and Y. Yamashita, Triclinic polymorph of dibenzotetrathiafulvalene, *Acta Crystallogr. E Struct. Rep. Online*, 2009, **65**, 2083–2083.

[191] M. T. Dang, L. Hirsch and G. Wantz, P3HT:PCBM, Best Seller in Polymer Photovoltaic Research, *Adv. Mater.*, 2011, **23**, 3597–3602.

[192] Y. Karpov, T. Erdmann, M. Stamm, U. Lappan, O. Guskova, M. Malanin, I. Raguzin, T. Beryozkina, V. Bakulev, F. Günther, S. Gemming, G. Seifert, M. Hambsch, S. Mannsfeld, B. Voit and A. Kiriy, Molecular Doping of a High Mobility Diketopyrrolopyrrole-Dithienylthieno[3,2-b]thiophene Donor-Acceptor Copolymer with F6TCNNQ, *Macromolecules*, 2017, **50**, 914–926.

[193] P. K. Koech, A. B. Padmaperuma, L. Wang, J. S. Swensen, E. Polikarpov, J. T. Darsell, J. E. Rainbolt and D. J. Gaspar, Synthesis and Application of 1,3,4,5,7,8-Hexafluorotetracyanonaphthoquinodimethane (F6-TNAP): A Conductivity Dopant for Organic Light-Emitting Devices, *Chem. Mater.*, 2010, **22**, 3926–3932.

[194] M. Hofmann, J. Birnstock, N. J. Blochwitz, A. Werner, M. Pfeiffer and K. Harada, *Eur. Patent Application EP19122681713136 A1 20061018*, 2006.

[195] O. Zeika, J. Birnstock, M. Limmert and M. Vehse, *Eur. Patent Application EP1912268 A1 20080416*, 2008.

[196] I. E. Jacobs and A. J. Moulé, Controlling Molecular Doping in Organic Semiconductors, *Adv. Mater.*, 2017, **29**, 1703063.

[197] S. Duhm, I. Salzmann, B. Bröker, H. Glowatzki, R. L. Johnson and N. Koch, Interdiffusion of molecular acceptors through organic layers to metal substrates mimics doping-related energy level shifts, *Appl. Phys. Lett.*, 2009, **95**, 093305.

[198] J. Li, I. Duchemin, O. M. Roscioni, P. Friederich, M. Anderson, E. Da Como, G. Kociok-Köhn, W. Wenzel, C. Zannoni, D. Beljonne, X. Blase and G. D'Avino, Host dependence of the electron affinity of molecular dopants, *Mater. Horiz.*, 2018, **6**, 107–114.

[199] P. Hu, S. Wang, A. Chaturvedi, F. Wei, X. Zhu, X. Zhang, R. Li, Y. Li, H. Jiang, Y. Long and C. Kloc, Impact of C–H···X (X = F, N) and π-πInteractions on Tuning the Degree of Charge Transfer in F_6TNAP-Based Organic Binary Compound Single Crystals, *Cryst. Growth Des.*, 2018, **18**, 1776–1785.

[200] T. J. Emge, W. A. Bryden, F. M. Wiygul, D. O. Cowan, T. J. Kistenmacher and A. N. Bloch, Structure of an organic charge-transfer salt derived from dibenzotetrathiafulvalene and tetrafluorotetracyanoquinodimethane (DBTTF-TCNQF4). Observation of a high-temperature phase transition, *J. Chem. Phys.*, 1982, **77**, 3188–3197.

[201] F. Sanz and J. J. Daly, Crystal and molecular structure of the 1:2 complex of methyltriphenylphosphonium with $\alpha\alpha\alpha'\alpha'$-tetracyano-3,7-naphthoquinodimethane, $(Ph_3PMe)^3$ $[(tnap)_2]^-$, *J. Chem. Soc., Perkin Trans. 2*, 1975, **0**, 1141–1145.

[202] G. R. Johnson, M. G. Miles and J. D. Wilson, Electrically Conducting Salts of 11, 11, 11 12, 12-Tetracyano-2,6-Naphthoquinodimethane (TNAP), *Mol. Cryst. Liq. Cryst.*, 2007, **33**, 67–75.

[203] K. Kanai, T. Ikame, Y. Ouchi and K. Seki, Molecular orientation and electronic structure of 11,11,12,12-tetracyanonaphtho-2,6-quinodimethane vacuum-deposited on metal substrates: Charge transfer, complexation, and potassium doping, *J. Appl. Phys.*, 2009, **105**, 023703.

[204] P. A. Berger, D. J. Dahm, G. R. Johnson, M. G. Miles and J. D. Wilson, Structure, conductivity, and electron spin resonance of tetrathiafulvalene 11,11,12,12-tetracyanonaphtho-2, 6-quinodimethane (TTF)(TNAP), *Phys. Rev. B*, 1975, **12**, 4085–4089.

[205] W. Shi, Y. Zheng, J. Yu, A. D. Taylor and H. E. Katz, Mobility enhancement of organic field-effect transistor based on guanine trap-neutralizing layer, *Appl. Phys. Lett.*, 2016, **109**, 143301.

[206] B. E. Lassiter, R. R. Lunt, C. K. Renshaw and S. R. Forrest, Structural templating of multiple polycrystalline layers in organic photovoltaic cells, *Opt. Express*, 2010, **18**, A444.

[207] C. Schünemann, D. Wynands, K.-J. Eichhorn, M. Stamm, K. Leo and M. Riede, Evaluation and Control of the Orientation of Small Molecules for Strongly Absorbing Organic Thin Films, *J. Phys. Chem. C*, 2013, **117**, 11600–11609.

[208] U. Heinemeyer, A. Hinderhofer, M. I. Alonso, J. O. Ossó, M. Garriga, M. Kytka, A. Gerlach and F. Schreiber, Uniaxial anisotropy of organic thin films determined by ellipsometry, *Phys. Stat. Sol. (a)*, 2008, **205**, 927.

[209] D. Wynands, M. Erber, R. Rentenberger, M. Levichkova, K. Walzer, K.-J. Eichhorn and M. Stamm, Spectroscopic ellipsometry characterization of vacuum-deposited organic films for the application in organic solar cells, *Org. Electron.*, 2012, **13**, 885–893.

[210] A. H. Al-Bayati, K. G. Orrman-Rossiter, J. van den Berg and D. Armour, Composition and structure of the native Si oxide by high depth resolution medium energy ion scatering, *Surf. Sci.*, 1991, **241**, 91–102.

[211] N. V. Rumak, V. V. Khatko and V. N. Plotnikov, Structure and properties of silicon dioxide thermal films I. SiO2 films of up to 50 nm thickness, *Phys. Stat. Sol. (a)*, 1984, **86**, 93–100.

[212] N. V. Rumak and V. V. Khatko, Structure and properties of silicon dioxide thermal films II. 110 nm thick SiO2 films, *Phys. Stat. Sol. (a)*, 1984, **86**, 477–484.

[213] P. Laube, *Oxidation: Fabrication of oxide layers.. 1. Thermal oxidation*, `https://www.halbleiter.org/en/oxidation/oxidation/#Thermal_oxidation`.

[214] S. AG, *BOROFLOAT® (NEXTERION® Glass B)*, `https://www.schott.com/nexterion/english/products/uncoated-substrates/borofloat33.html`.

[215] U. Optics, *FUSED QUARTZ COVER SLIPS*, `https://www.uqgoptics.com/catalogue/Windows/FUSED_QUARTZ_COVER_SLIPS.aspx`.

[216] S. L. Warring, D. A. Beattie and A. J. McQuillan, Surficial Siloxane-to-Silanol Interconversion during Room-Temperature Hydration/Dehydration of Amorphous Silica Films Observed by ATR-IR and TIR-Raman Spectroscopy, *Langmuir*, 2016, **32**, 1568–1576.

[217] I. Zawisza, G. Wittstock, R. Boukherroub and S. Szunerits, PMIRRAS Investigation of Thin Silica Films Deposited on Gold. Part 1. Theory and Proof of Concept, *Langmuir*, 2007, **23**, 9303–9309.

[218] D. Nečas and P. Klapetek, Gwyddion: an open-source software for SPM data analysis, *Cent. Eur. J. Phys.*, 2012, **10**, 181–188.

[219] G. F. Weston, *Ultrahigh vacuum practice*, Butterworths, London, 1985, pp. VIII, 288 pages.

[220] J. F. O'Hanlon, *A User's Guide to Vacuum Science and Technology*, John Wiley & Sons, Hoboken, New Jersey, 2003, pp. XXIV, 516 pages.

[221] H. Okamoto, N. Kawasaki, Y. Kaji, Y. Kubozono, A. Fujiwara and M. Yamaji, Air-assisted High-performance Field-effect Transistor with Thin Films of Picene, *J. Am. Chem. Soc.*, 2008, **130**, 10470–10471.

[222] T. Hosokai, A. Hinderhofer, A. Vorobiev, C. Lorch, T. Watanabe, T. Koganezawa, A. Gerlach, N. Yoshimoto, Y. Kubozono and F. Schreiber, In situ structural characterization of picene thin films by X-ray scattering: Vacuum versus O_2 atmosphere, *Chem. Phys. Lett.*, 2012, **544**, 34.

[223] K. Ritley, B. Krause, F. Schreiber and H. Dosch, A Portable UHV Organic Molecular Beam Deposition System For In Situ X-Ray Diffraction Measurements, *Rev. Sci. Instrum.*, 2001, **72**, 1453–1457.

[224] S. Kowarik, *Ph.D. thesis*, Wadham College, Oxford, 2006.

[225] V. Belova, B. Wagner, B. Reisz, C. Zeiser, G. Duva, J. Rozbořil, J. Novák, A. Gerlach, A. Hinderhofer and F. Schreiber, Real-Time Structural and Optical Study of Growth and Packing Behavior of Perylene Diimide Derivative Thin Films: Influence of Side-Chain Modification, *J. Phys. Chem. C*, 2018, **122**, 8589–8601.

[226] M. Tolan, *X-ray scattering from soft-matter thin films : materials science and basic research*, Springer, Berlin, 1999.

[227] M. Fukuto, O. Gang, K. J. Alvine and P. S. Pershan, Capillary wave fluctuations and intrinsic widths of coupled fluid-fluid interfaces: An x-ray scattering study of a wetting film on bulk liquid, *Phys. Rev. E*, 2006, **74**, 031607.

[228] M. K. Sanyal, The use of grazing incidence X-ray scattering techniques to probe chemical reactions at the liquid–liquid interface: the formation and ordering of gold nanoparticles, *J. Mater. Chem.*, 2009, **19**, 4300.

[229] W. Bu and M. L. Schlossman, in *Synchrotron X-Ray Scattering from Liquid Surfaces and Interfaces*, ed. E. Jaeschke, S. Khan, J. R. Schneider and J. B. Hastings, Springer International Publishing, Cham, 2014, pp. 1–33.

[230] L. G. Parratt, Surface studies of solids by total reflection of X-rays, *Phys. Rev.*, 1954, **95**, 359–369.

[231] L. Névot and P. Croce, Characterisation of surfaces by grazing x-ray reflection - Application to study of polishing of some silicate glasses, *Revue de Physique Appliquée*, 1980, **15**, 761.

[232] D. K. G. de Boer, X-ray reflection and transmission by rough surfaces, *Phys. Rev. B*, 1995, **51**, 5297–5305.

[233] P. Cohen, G. Petrich, P. Pukite, G. Whaley and A. Arrott, Birth-death models of epitaxy: I. Diffraction oscillations from low index surfaces, *Surf. Sci.*, 1989, **216**, 222–248.

[234] V. I. Trofimov and V. G. Mokerov, Rate equations model for layer epitaxial growth kinetics, *Thin Solid Films*, 2003, **428**, 66–71.

[235] A. R. Woll, T. V. Desai and J. R. Engstrom, Quantitative modeling of in situ X-ray reflectivity during organic molecule thin film growth, *Phys. Rev. B*, 2011, **84**, 075479.

[236] M. Sparenberg, A. Zykov, P. Beyer, L. Pithan, C. Weber, Y. Garmshausen, F. Carlá, S. Hecht, S. Blumstengel, F. Henneberger and S. Kowarik, Controlling the growth mode of para-sexiphenyl (6P) on ZnO by partial fluorination, *Phys. Chem. Chem. Phys.*, 2014, **16**, 26084–26093.

[237] L. Pithan *et al.*, *in preparation*.

[238] H. Dosch, *Critical Phenomena at Surfaces and Interfaces*, Springer, Berlin, 1992, pp. V, 145 pages.

[239] S. Kowarik, L. Bogula, S. Boitano, F. Carlá, H. Pithan, P. Schäfer, H. Wilming, A. Zykov and L. Pithan, A novel 3D printed radial collimator for x-ray diffraction, *Rev. Sci. Instrum.*, 2019, **90**, 035102.

[240] N. W. Ashcroft and N. D. Mermin, *Solid State Physics*, Brooks/Cole Cengage Learning, 2003, pp. XXI, 826 pages.

[241] L. J. Barbour, EwaldSphere: an interactive approach to teaching the Ewald sphere construction, *J Appl Crystallogr*, 2018, **51**, 1734–1738.

[242] C. M. Schlepütz, R. Herger, P. R. Willmott, B. D. Patterson, O. Bunk, C. Brönnimann, B. Henrich, G. Hülsen and E. F. Eikenberry, Improved data acquisition in grazing-incidence X-ray scattering experiments using a pixel detector, *Acta Cryst. A*, 2005, **61**, 418–425.

[243] B. Rupp, *Biomolecular Crystallography: Principles, Practice, and Application to Structural Biology*, Garland Science, Taylor & Francis, 270 Madison Avenue, NY, USA, 2010, pp. 1–809.

[244] P. R. Evans, Rotations and rotation matrices, *Acta Cryst. Sec. D*, 2001, **57**, 1355–1359.

[245] C. Zeiser, *Bachelor thesis*, Eberhard Karls Universität Tübingen, Tübingen, 2016.

[246] Understanding FT-IR data processing, 1985.

[247] M. W. A. Skoda, *Ph.D. thesis*, Wadham College, Oxford, 2007.

[248] Bruker, *PMA 50 user's manual*, Rudolf-Plank-Str. 27, 76275 Ettlingen, 2013.

[249] Bruker, *OPUS user's manual*, Rudolf-Plank-Str. 27, 76275 Ettlingen, 2004.

[250] H. Instruments, *PEM-90 Photoelastic Modulator Systems. User Manual*, 3175 NW Aloclek Drive, Hillsboro, OR, 1998.

[251] S. R. Systems, *Model SR830. DSP Lock-In Amplifier*, 1290-D Reamwood Avenue, Sunnyvale, California 94089, 1993.

[252] K. W. Hipps and G. A. Crosby, Applications of the photoelastic modulator to polarization spectroscopy, *J. Phys. Chem.*, 1979, **83**, 555–562.

[253] I. E. Dunlop, S. Zorn, G. Richter, V. Srotc, M. Kelsch, P. A. van Aken, M. Skoda, A. Gerlach, J. P. Spatz and F. Schreiber, Titanium-silicon oxide film structures for polarization-modulated infrared reflection absorption spectroscopy, *Thin Solid Films*, 2009, **517**, 2048–2054.

[254] J. M. Florence, C. C. Allshouse, F. W. Glaze and C. H. Hahner, Absorption of Near-Infrared Energy by Certain Glasses, *J. Res. Natl. Bur. Stand.*, 1950, **45**, 121.

[255] J. I. AG, *NanoWizard® AFM Handbook*, Bouchestrasse 12, 12435 Berlin, Germany, 2012.

[256] G. Binnig, C. F. Quate and C. Gerber, Atomic force microscope, *Phys. Rev. Lett.*, 1986, **56**, 930–933.

[257] G. Binnig and H. Rohrer, The scanning tunneling microscope, *Sci. Am.*, 1985, **253**, 50–56.

[258] T. Kajiyama, K. Tanaka, I. Ohki, S.-R. Ge, J.-S. Yoon and A. Takahara, Imaging of Dynamic Viscoelastic Properties of a Phase-Separated Polymer Surface by Forced Oscillation Atomic Force Microscopy, *Macromolecules*, 1994, **27**, 7932–7934.

[259] T. Meisel, *M.Sc. thesis*, Humboldt-Universität zu Berlin, 2015.

[260] G. Witte and C. Wöll, Molecular Beam Deposition and Characterization of Thin Organic Films on Metals for Applications in Organic Electronics, *Phys.Stat. Sol. (a)*, 2008, **205**, 497–510.

[261] A. Opitz, A. Wilke, P. Amsalem, M. Oehzelt, R.-P. Blum, J. P. Rabe, T. Mizokuro, U. Hörmann, R. Hansson, E. Moons and N. Koch, Organic heterojunctions: Contact-induced molecular reorientation, interface states, and charge re-distribution, *Sci. Rep.*, 2016, **6**, 21291.

[262] W. Han, K. Yonezawa, R. Makino, K. Kato, A. Hinderhofer, R. Murdey, R. Shiraishi, H. Yoshida, N. Sato, N. Ueno and K. S., Quantitatively identical orientation-dependent ionization energy and electron affinity of diindenoperylene, *Appl. Phys. Lett.*, 2013, **103**, 253301.

[263] S. Duhm, G. Heimel, I. Salzmann, H. Glowatzki, R. L. Johnson, A. Vollmer, J. P. Rabe and N. Koch, Orientation-dependent ionization energies and interface dipoles in ordered molecular assemblies, *Nat. Mater.*, 2008, **7**, 326–332.

[264] C. Nicklin, T. Arnold, J. Rawle and A. Warne, Diamond beamline I07: a beamline for surface and interface diffraction, *J. Synchrotron Rad.*, 2016, **23**, 1245–1253.

[265] C. Lorch, J. Novák, R. Banerjee, S. Weimer, J. Dieterle, C. Frank, A. Hinderhofer, A. Gerlach, F. Carla and F. Schreiber, Influence of C60 co-deposition on the growth kinetics of diindenoperylene- From rapid roughening to layer-by-layer growth in blended organic films, *J. Chem. Phys.*, 2017, **146**, 052807.

[266] S. Hotta and H. Kobayashi, Crystal and molecular structure of a charge-transfer complex between α,α'-dimethylquaterthiophene and 2,3,5,6-tetrafluoro-7,7,8,8-tetracyanoquinodimethane, *Synth. Met.*, 1994, **66**, 117–122.

[267] G. Hlawacek, P. Puschnig, P. Frank, A. Winkler, C. Ambrosch-Draxl and C. Teichert, Characterization of step-edge barriers in organic thin-film growth, *Science*, 2008, **321**, 108–111.

[268] W. Porzio, S. Destri, M. Mascherpa and S. Bruckner, Structural aspects of oligothienyl series from X-ray powder diffraction data, *Acta Polymer.*, 1993, **44**, 266–272.

[269] D. Greiner, V. Hinrichs, S. Wiesner, W. Ludwig, K. Fostiropoulos, D. Keiper, P. Baumann, N. Meyer, M. Heuken, M. Rusu and M. Lux-Steiner, Optical constants of diindenoperylene in the dependence of preparation temperature and pressure, *Thin Solid Films*, 2013, **534**, 255–259.

[270] A. Opitz, R. Banerjee, S. Grob, M. Gruber, A. Hinderhofer, U. Hörmann, J. Kraus, T. Linderl, C. Lorch, A. Steindamm, A. K. Topczak, A. Wilke, N. Koch, J. Pflaum, F. Schreiber and W. Brütting, in *Charge Separation at Nanostructured Molecular Donor–Acceptor Interfaces*, ed. K. Leo, Springer International Publishing, Cham, 2017, pp. 77–108.

[271] B. Reisz, S. Weimer, R. Banerjee, C. Zeiser, C. Lorch, G. Duva, J. Dieterle, K. Yonezawa, J.-P. Yang, N. Ueno, S. Kera, A. Hinderhofer, A. Gerlach and F. Schreiber, Structural, optical, and electronic characterization of perfluorinated sexithiophene films and mixed films with sexithiophene, *J. Mater. Res.*, 2017, **32**, 1908–1920.

[272] A. Girlando, Comment on Polymorphism in the 1:1 Charge-Transfer Complex DBTT-TCNQ and Its Effects on Optical and Electronic Properties, *Adv. Electron. Mater.*, 2017, **3**, 1600437.

[273] K. P. Goetz, J. Tsutsumi, S. Pookpanratana, J. Chen, N. S. Corbin, R. K. Behera, V. Coropceanu, C. A. Richter, C. A. Hacker, T. Hasegawa and O. D. Jurchescu, Reply to Comment on Polymorphism in the 1:1 Charge-Transfer Complex DBTTF-TCNQ and Its Effects on Optical and Electronic Properties, *Adv. Electron. Mater.*, 2017, **3**, 1600521.

[274] A. Opitz *et al.*, *in preparation.*

[275] K.-F. Braun and S. W. Hla, Charge transfer in the TCNQ-sexithiophene complex, *J. Chem. Phys.*, 2008, **129**, 064707.

[276] P. Lane, X. Wei, Z. Vardeny, J. Poplawski, E. Ehrenfreund, M. Ibrahim and A. Frank, Absorption spectroscopy of charged excitations in α-sexithiophene: evidence for charge conjugation symmetry breaking, *Chem. Phys.*, 1996, **210**, 229–234.

[277] J. Yang, S. Yim and T. S. Jones, Molecular-Orientation-Induced Rapid Roughening and Morphology Transition in Organic Semiconductor Thin-Film Growth, *Sci. Rep.*, 2015, **5**, 9441.

[278] P. Beyer, T. Breuer, S. Ndiaye, A. Zykov, A. Viertel, M. Gensler, J. P. Rabe, S. Hecht, G. Witte and S. Kowarik, Lattice Matching as the Determining Factor for Molecular Tilt and Multilayer Growth Mode of the Nanographene Hexa-*peri*-hexabenzocoronene, *ACS Appl. Mater. Interfaces*, 2014, **6**, 21484–21493.

[279] A. Nelson, Co-refinement of multiple-contrast neutron/X-ray reflectivity data using *MOTOFIT*, *J. Appl. Crystallogr.*, 2006, **39**, 273–276.

[280] S. Kowarik, A. Gerlach, S. Sellner, L. Cavalcanti and F. Schreiber, Dewetting in an organic semiconductor thin film observed in real-time, *Adv. Eng. Mater.*, 2009, **11**, 291–294.

[281] A. Hinderhofer, A. Gerlach, S. Kowarik, F. Zontone, J. Krug and F. Schreiber, Smoothing and coherent structure formation in organic-organic heterostructure growth, *Europhys. Lett.*, 2010, **91**, 56002 (1–5).

[282] C. Lorch, K. Broch, V. Belova, G. Duva, A. Hinderhofer, A. Gerlach, M. Jankowski and F. Schreiber, Growth and annealing kinetics of α-sexithiophene and fullerene C60 mixed films, *J. Appl. Crystallogr.*, 2016, **49**, 1266–1275.

[283] G. Koller, S. Surnev, M. G. Ramsey and F. P. Netzer, Sexiphenyl on a Ni(110)(2x1)-O surface: A single-molecule STM study, *Surf. Sci.*, 2004, **559**, L187–L193.

[284] G. Duva, A. Mann, L. Pithan, P. Beyer, J. Hagenlocher, A. Gerlach, A. Hinderhofer and F. Schreiber, Template-Free Orientation Selection of Rod-Like Molecular Semiconductors in Polycrystalline Films, *J. Phys. Chem. Lett.*, 2019, **10**, 1031–1036.

[285] R. Noriega, J. Rivnay, K. Vandewal, F. P. V. Koch, N. Stingelin, P. Smith, M. F. Toney and A. Salleo, A general relationship between disorder, aggregation and charge transport in conjugated polymers, *Nature Mater.*, 2013, **12**, 1038–1044.

[286] G. Witte and C. Wöll, Growth of Aromatic Molecules on Solid Substrates for Applications in Organic Electronics, *J. Mater. Res.*, 2004, **19**, 1889–1916.

[287] L. Pithan, P. Beyer, L. Bogula, A. Zykov, P. Schäfer, J. Rawle, C. Nicklin, A. Opitz and S. Kowarik, Direct Photoalignment and Optical Patterning of Molecular Thin Films, *Adv. Mater.*, 2017, **29**, 1604382.

[288] T. V. Desai, A. R. Woll, F. Schreiber and J. R. Engstrom, Nucleation and Growth of Perfluoropentacene on Self-Assembled Monolayers: Significant Changes in Island Density and Shape with Surface Termination, *J. Phys. Chem. C*, 2010, **114**, 20120.

[289] T. V. Desai, E. R. Kish, A. R. Woll and J. R. Engstrom, Hyperthermal Growth of *N,N'*-Ditridecylperylene-3,4,9,10-tetracarboxylic Diimide on Self-Assembled Monolayers: Adsorption Dynamics and Sub- and Multilayer Thin Film Growth, *J. Phys. Chem. C*, 2011, **115**, 18221–18234.

[290] C. Frank, J. Novák, A. Gerlach, G. Ligorio, K. Broch, A. Hinderhofer, A. Aufderheide, R. Banerjee, R. Nervo and F. Schreiber, Real-time X-ray scattering studies on temperature dependence of perfluoropentacene thin film growth, *J. Appl. Phys.*, 2013, **114**, 043515.

[291] R. Banerjee, A. Hinderhofer, M. Weinmann, B. Reisz, C. Lorch, A. Gerlach, M. Oettel and F. Schreiber, Interrupted Growth to Manipulate Phase Separation in DIP:C60 Organic Semiconductor Blends, *J. Phys. Chem. C*, 2018, **122**, 1839–1845.

[292] C. Lorch, H. Frank, R. Banerjee, A. Hinderhofer, A. Gerlach, G. Li Destri and F. Schreiber, Controlling length-scales of the phase separation to optimize organic semiconductor blends, *Appl. Phys. Lett.*, 2015, **107**, 201903.

[293] D. de Oteyza, E. Barrena, S. Sellner, J. Ossó and H. Dosch, Structural Rearrangements During the Initial Growth Stages of Organic Thin Films of F_{16}CuPc on SiO_2, *J. Phys. Chem. B*, 2006, **110**, 16618–16623.

[294] D. Guo, K. Sakamoto, K. Miki, S. Ikeda and K. Saiki, Orientation Control of Pentacene Molecules and Transport Anisotropy of the Thin Film Transistors by Photoaligned Polyimide Film, *Appl. Phys. Lett.*, 2007, **90**, 102117.

[295] J. Ivanco, T. Haber, J. Krenn, F. Netzer, R. Resel and M. Ramsey, Sexithiophene films on ordered and disordered TiO_2(110) surfaces: Electronic, structural and morphological properties, *Surf. Sci.*, 2007, **601**, 178–187.

[296] M. B. Casu, I. Biswas, B. E. Schuster, M. Nagel, P. Nagel, S. Schuppler and T. Chassé, Molecular orientation in diindenoperylene thin films deposited on polycrystalline gold, *Appl. Phys. Lett.*, 2008, **93**, 024103.

[297] D. de Oteyza, E. Barrena, M. Ruiz-Osés, I. Silanes, B. Doyle, J. Ortega, A. Arnau, H. Dosch and Y. Wakayama, Crystallographic and Electronic Structure of Self-Assembled DIP Monolayers on Au(111) Substrates, *J. Phys. Chem. C*, 2008, **112**, 7168–7172.

[298] M. Koini, T. Haber, O. Werzer, S. Berkebile, G. Koller, M. Oehzelt, M. Ramsey and R. Resel, Epitaxial order of pentacene on Cu(110)-(2 x 1)O: One dimensional alignment induced by surface corrugation, *Thin Solid Films*, 2008, **517**, 483–487.

[299] T. Haber, J. Ivanco, M. Ramsey and R. Resel, Epitaxial growth of sexithiophene on TiO_2 (110), *J. Cryst. Growth*, 2008, **310**, 101–109.

[300] Y. L. Huang, W. Chen, H. Huang, D. C. Qi, S. Chen, X. Y. Gao, J. Pflaum and A. T. S. Wee, Ultrathin Films of Diindenoperylene on Graphite and SiO_2, *J. Phys. Chem. C*, 2009, **113**, 9251–9255.

[301] C. Simbrunner, G. Hernandez-Sosa, M. Oehzelt, T. Djuric, I. Salzmann, M. Brinkmann, G. Schwabegger, I. Watzinger, H. Sitter and R. Resel, Epitaxial growth of sexithiophene on mica surfaces, *Phys. Rev. B*, 2011, **83**, 115443.

[302] G. Schwabegger, T. Djuric, H. Sitter, R. Resel and C. Simbrunner, Morphological and Structural Investigation of Sexithiophene Growth on KCl (100), *Cryst. Growth Des.*, 2013, **13**, 536–542.

[303] W. N. Han, K. Yonezawa, R. Makino, K. Kato, A. Hinderhofer, R. Murdey, R. Shiraishi, H. Yoshida, N. Sato, N. Ueno and S. Kera, Quantitatively identical orientation-dependent ionization energy and electron affinity of diindenoperylene, *Appl. Phys. Lett.*, 2013, **103**, 253301.

[304] O. Guskova, C. Schünemann, K.-J. Eichhorn, K. Walzer, M. Levichkova, S. Grundmann and J.-U. Sommer, Light Absorption in Organic Thin Films: The Importance of Oriented Molecules, *J. Phys. Chem. C*, 2013, **117**, 17285–17293.

[305] S. Yu, A. Opitz, S. Grob, R. Resel, M. Oehzelt, W. Brütting, I. Salzmann and N. Koch, Performance Enhancement of Diindenoperylene-Based Organic Photovoltaic Cells by Nanocolumn-Arrays, *Org. Electron.*, 2014, **15**, 2210–2217.

[306] L. Zhang, S. S. Roy, N. S. Safron, M. J. Shearer, R. M. Jacobberger, V. Saraswat, R. J. Hamers, M. S. Arnold and T. L. Andrew, Orientation Control of Selected Organic Semiconductor Crystals Achieved by Monolayer Graphene Templates, *Adv. Mater. Interfaces*, 2016, **3**, 1600621.

[307] M. Hodas, P. Siffalovic, P. Nádaždy, N. Mrkyvková, M. Bodík, Y. Halahovets, G. Duva, B. Reisz, O. Konovalov, W. Ohm, M. Jergel, E. Majková, A. Gerlach, A. Hinderhofer and F. Schreiber, Real-Time Monitoring of Growth and Orientational Alignment of Pentacene on Epitaxial Graphene for Organic Electronics, *ACS Appl. Nano Mater.*, 2018, **1**, 2819–2826.

[308] N. Shioya, R. Murdey, K. Nakao, H. Yoshida, T. Koganezawa, K. Eda, T. Shimoaka and T. Hasegawa, Alternative Face-on Thin Film Structure of Pentacene, *Sci. Rep.*, 2019, **9**, .

[309] A. Gujral, L. Yu and M. Ediger, Anisotropic organic glasses, *Curr. Opin. Solid State Mater. Sci.*, 2018, **22**, 49–57.

[310] S. S. Dalal, D. M. Walters, I. Lyubimov, J. J. de Pablo and M. D. Ediger, Tunable molecular orientation and elevated thermal stability of vapor-deposited organic semiconductors, *Proc. Natl. Acad. Sci. USA*, 2015, **112**, 4227–4232.

[311] A. Gujral, J. Gómez, J. Jiang, C. Huang, K. A. O'Hara, M. F. Toney, M. L. Chabinyc, L. Yu and M. D. Ediger, Highly Organized Smectic-like Packing in Vapor-Deposited Glasses of a Liquid Crystal, *Chem. Mater.*, 2017, **29**, 849–858.

[312] H. Ullah Khan, R. Li, Y. Ren, L. Chen, M. M. Payne, U. S. Bhansali, D.-M. Smilgies, J. E. Anthony and A. Amassian, Solvent Vapor Annealing in the Molecular Regime Drastically Improves Carrier Transport in Small-Molecule Thin-Film Transistors, *ACS Appl. Mater. Interfaces*, 2013, **5**, 2325–2330.

[313] S. Grob, A. N. Bartynski, A. Opitz, M. Gruber, F. Grassl, E. Meister, T. Linderl, U. Hörmann, C. Lorch, E. Moons, F. Schreiber, M. E. Thompson and W. Brütting, Solvent vapor annealing on perylene-based organic solar cells, *J. Mater. Chem. A*, 2015, **3**, 15700–15709.

[314] F. Iwatsu, Crystal behavior of zinc phthalocyanine films in alcohols, *J. Cryst. Growth*, 1985, **71**, 629–638.

[315] M. Brinkmann, J. Wittmann, C. Chaumont and J. André, Effects of solvent on the morphology and crystalline structure of lithium phthalocyanine thin films and powders, *Thin Solid Films*, 1997, **292**, 192–203.

[316] I. Salzmann, S. Duhm, R. Opitz, R. L. Johnson, J. P. Rabe and N. Koch, Structural and Electronic Properties of Pentacene-Fullerene Heterojunctions, *J. Appl. Phys.*, 2008, **104**, 114518.

[317] D. Guo, S. Ikeda, K. Saiki, H. Miyazoe and K. Terashima, Effect of annealing on the mobility and morphology of thermally activated pentacene thin film transistors, *J. Appl. Phys.*, 2006, **99**, 094502.

[318] T. Ahn, H. Jung, H. J. Suk and M. H. Yi, Effect of postfabrication thermal annealing on the electrical performance of pentacene organic thin-film transistors, *Synth. Met.*, 2009, **159**, 1277–1280.

[319] M. Nothaft and J. Pflaum, Thermally and seed-layer induced crystallization in rubrene thin films, *Phys. Stat. Sol. (b)*, 2008, **245**, 788–792.

[320] N. R. Armstrong, P. A. Veneman, E. Ratcliff, D. Placencia and M. Brumbach, Oxide Contacts in Organic Photovoltaics: Characterization and Control of Near-Surface Composition in Indium-Tin Oxide (ITO) Electrodes, *Acc. Chem. Res.*, 2009, **42**, 1748–1757.

[321] T. D. Schmidt, T. Lampe, D. Sylvinson M. R., P. I. Djurovich, M. E. Thompson and W. Brütting, Emitter Orientation as a Key Parameter in Organic Light-Emitting Diodes, *Phys. Rev. Applied*, 2017, **8**, 037001.

[322] U. Heinemeyer, K. Broch, A. Hinderhofer, M. Kytka, R. Scholz, A. Gerlach and F. Schreiber, Real-Time Changes in the Optical Spectrum of Organic Semiconducting Films and Their Thickness Regimes during Growth, *Phys. Rev. Lett.*, 2010, **104**, 257401.

[323] S. B. Jo, H. H. Kim, H. Lee, B. Kang, S. Lee, M. Sim, M. Kim, W. H. Lee and K. Cho, Boosting Photon Harvesting in Organic Solar Cells with Highly Oriented Molecular Crystals Graphene-Organic Heterointerface, *ACS Nano*, 2015, **9**, 8206–8219.

[324] R. Hesse, W. Hofberger and H. Bässler, Absorption Spectra of Disordered Solid Tetracene and Pentacene, *Chem. Phys.*, 1980, **49**, 201.

[325] D. Faltermeier, B. Gompf, M. Dressel, A. K. Tripathi and J. Pflaum, Optical Properties of Pentacene Thin-Films and Single Crystals, *Phys. Rev. B*, 2006, **74**, 125416.

[326] C. F. Macrae, I. J. Bruno, J. A. Chisholm, P. R. Edgington, P. McCabe, E. Pidcock, L. Rodriguez-Monge, R. Taylor, J. van de Streek and P. A. Wood, Mercury CSD 2.0 - features for the visualization and investigation of crystal structures, *J. Appl. Crystallogr.*, 2008, **41**, 466–470.

[327] Y. Zeng, B. Tao, J. Chen and Z. Yin, Temperature-Dependent Orientation Study of the Initial Growth of Pentacene on Amorphous SiO_2 by Molecular Dynamics Simulations, *J. Cryst. Growth*, 2015, **429**, 35–42.

[328] R. W. MacQueen, M. Liebhaber, J. Niederhausen, M. Mews, C. Gersmann, S. Jäckle, K. Jäger, M. J. Y. Tayebjee, T. W. Schmidt, B. Rech and K. Lips, Crystalline silicon solar cells with tetracene interlayers: the path to silicon-singlet fission heterojunction devices, *Mater. Horiz.*, 2018, **5**, 1065–1075.

[329] Y. Xu, O. T. Hofmann, R. Schlesinger, S. Winkler, J. Frisch, J. Niederhausen, A. Vollmer, S. Blumstengel, F. Henneberger, N. Koch, P. Rinke and M. Scheffler, Space-Charge Transfer in Hybrid Inorganic-Organic Systems, *Phys. Rev. Lett.*, 2013, **111**, 226802.

[330] R. Schlesinger, Y. Xu, O. T. Hofmann, S. Winkler, J. Frisch, J. Niederhausen, A. Vollmer, S. Blumstengel, F. Henneberger, P. Rinke, M. Scheffler and N. Koch, Controlling the work function of ZnO and the energy-level alignment at the interface to organic semiconductors with a molecular electron acceptor, *Phys. Rev. B*, 2013, **87**, 155311.

[331] I.-W. Hwang, D. Moses and A. J. Heeger, Photoinduced Carrier Generation in P3HT/PCBM Bulk Heterojunction Materials, *J. Phys. Chem. C*, 2008, **112**, 4350–4354.

[332] M. Meneghetti and C. Pecile, Charge-transfer organic crystals: Molecular vibrations and spectroscopic effects of electron-molecular vibration coupling of the strong electron acceptor TCNQF4, *J. Chem. Phys.*, 1986, **84**, 4149–4162.

[333] M. Rudloff, K. Ackermann, M. Huth, H. O. Jeschke, M. Tomic, R. Valentá, B. Wolfram, M. Bröring, M. Bolte, D. Chercka, M. Baumgarten and K. Müllen, Charge transfer tuning by chemical substitution and uniaxial pressure in the organic complex tetramethoxypyrene-tetracyanoquinodimethane, *Phys. Chem. Chem. Phys.*, 2015, **17**, 4118–4126.

[334] T. Salzillo, M. Masino, G. Kociok-Köhn, D. Di Nuzzo, E. Venuti, R. G. Della Valle, D. Vanossi, C. Fontanesi, A. Girlando, A. Brillante and E. Da Como, Structure, Stoichiometry, and Charge Transfer in Cocrystals of Perylene with TCNQ-F, *Cryst. Growth Des.*, 2016, **16**, 3028–3036.

[335] P. Hu, K. Du, F. Wei, H. Jiang and C. Kloc, Crystal Growth, HOMO-LUMO Engineering, and Charge Transfer Degree in Perylene-F$_x$TCNQ (x = 1, 2, 4) Organic Charge Transfer Binary Compounds, *Cryst. Growth Des.*, 2016, **16**, 3019–3027.

[336] F. Ghani, A. Opitz, P. Pingel, G. Heimel, I. Salzmann, J. Frisch, D. Neher, A. Tsami, U. Scherf and N. Koch, Charge transfer in and conductivity of molecularly doped thiophene-based copolymers, *J. Polym. Sci. Part B: Polym. Phys.*, 2015, **53**, 58–63.

[337] L. Müller, D. Nanova, T. Glaser, S. Beck, A. Pucci, A. K. Kast, R. R. Schröder, E. Mankel, P. Pingel, D. Neher, W. Kowalsky and R. Lovrincic, Charge-Transfer-Solvent Interaction Predefines Doping Efficiency in p-Doped P3HT Films, *Chem. Mater.*, 2016, **28**, 4432–4439.

[338] D. Nanova, S. Beck, A. Fuchs, T. Glaser, C. Lennartz, W. Kowalsky, A. Pucci and M. Kroeger, Charge transfer in thin films of donor-acceptor complexes studied by infrared spectroscopy, *Organic Electronics*, 2012, **13**, 1237–1244.

[339] D. Nanova, S. Beck, M. Alt, T. Glaser, A. Pucci, K. Schultheiß, L. Dieterle, R. R. Schröder, J. Pflaum, W. Kowalsky and M. Kroeger, Phase separation in ternary charge-transfer-complexes, *Appl. Phys. A*, 2012, **112**, 1019–1025.

[340] S. Szunerits and R. Boukherroub, Preparation and Characterization of Thin Films of SiO_x on Gold Substrates for Surface Plasmon Resonance Studies, *Langmuir*, 2006, **22**, 1660–1663.

[341] L. Romaner, G. Heimel, J. L. Brédas, A. Gerlach, F. Schreiber, R. L. Johnson, J. Zegenhagen, S. Duhm, N. Koch and E. Zojer, Impact of bidirectional charge transfer and molecular distortions on the electronic structure of a metal-organic interface, *Phys. Rev. Lett.*, 2007, **99**, 256801.

[342] H. Peisert, I. Biswas, L. Zhang, M. Knupfer, M. Hanack, D. Dini, D. Batchelor and T. Chassé, Molecular orientation of substituted phthalocyanines: Influence of the substrate roughness, *Surf. Sci.*, 2006, **600**, 4024–4029.

[343] A. Morherr, S. Witt, A. Chernenkaya, J.-P. äcker, G. Schönhense, M. Bolte and C. Krellner, Crystal growth of new charge-transfer salts based on π-conjugated donor molecules, *Physica B Condens. Matter*, 2016, **496**, 98 – 105.

[344] E. Kampar and O. Neilands, Degree of Charge Transfer in Donor-Acceptor Systems of the π-π Type, *Russian Chemical Reviews*, 1986, **55**, 334–342.

[345] D. T. Duong, C. Wang, E. Antono, M. F. Toney and A. Salleo, The chemical and structural origin of efficient p-type doping in P3HT, *Org. Electron.*, 2013, **14**, 1330–1336.

[346] M. Zamadar, S. Asaoka, D. C. Grills and J. R. Miller, Giant infrared absorption bands of electrons and holes in conjugated molecules, *Nat. Commun.*, 2013, **4**, 2818.

[347] A. M. Valencia and C. Cocchi, Electronic and Optical Properties of Oligothiophene-F4TCNQ Charge-Transfer Complexes: The Role of Donor Conjugation Length, *J. Phys. Chem. C*, 2019, **123**, 9617–9623.

[348] N. Renaud and F. C. Grozema, Intermolecular Vibrational Modes Speed Up Singlet Fission in Perylenediimide Crystals, *J. Phys. Chem. Lett.*, 2015, **6**, 360–365.

[349] C. Grieco, E. R. Kennehan, A. Rimshaw, M. M. Payne, J. E. Anthony and J. B. Asbury, Harnessing Molecular Vibrations to Probe Triplet Dynamics During Singlet Fission, *J. Phys. Chem. Lett.*, 2017, **8**, 5700–5706.

[350] G. Duva *et al.*, *unpublished*.

[351] A. A. Bakulin, R. Lovrincic, X. Yu, O. Selig, H. J. Bakker, Y. L. A. Rezus, P. K. Nayak, A. Fonari, V. Coropceanu, J.-L. Brédas and D. Cahen, Mode-selective vibrational modulation of charge transport in organic electronic devices, *Nat. Comms*, 2015, **6**, 7880.

[352] K. Kanai, K. Akaike, K. Koyasu, K. Sakai, T. Nishi, Y. Kamizuru, T. Nishi, Y. Ouchi and K. Seki, Determination of electron affinity of electron accepting molecules, *Appl. Phys. A*, 2008, **95**, 309–313.

[353] H. Peisert, M. Knupfer, T. Schwieger, G. G. Fuentes, D. Olligs, J. Fink and T. Schmidt, Fluorination of copper phthalocyanines: Electronic structure and interface properties, *J. Appl. Phys.*, 2003, **93**, 9683–9692.

[354] F. Anger, T. Breuer, A. Ruff, M. Klues, A. Gerlach, R. Scholz, S. Ludwigs, G. Witte and F. Schreiber, Enhanced Stability of Rubrene against Oxidation by Partial and Complete Fluorination, *J. Phys. Chem. C*, 2016, **120**, 5515–5522.

[355] Y. Park, V. Choong, Y. Gao, B. R. Hsieh and C. W. Tang, Work function of indium tin oxide transparent conductor measured by photoelectron spectroscopy, *Appl. Phys. Lett.*, 1996, **68**, 2699–2701.

[356] H. Kleemann, C. Schuenemann, A. A. Zakhidov, M. Riede, B. Lüssem and K. Leo, Structural phase transition in pentacene caused by molecular doping and its effect on charge carrier mobility, *Org. Electron.*, 2012, **13**, 58–65.

[357] P. Nielsen, Substrate dependent ionization and polarization energies of molecules: Dibenztetrathiafulvalene, *Solid State Commun.*, 1978, **26**, 835–838.

[358] N. Sato, H. Inokuchi and I. Shirotani, Polarization energies of tetrathiafulvalene derivatives, *Chem. Phys.*, 1981, **60**, 327–333.

[359] M. Mas-Torrent, P. Hadley, S. T. Bromley, X. Ribas, J. Tarriés, M. Mas, E. Molins, J. Veciana and C. Rovira, Correlation between Crystal Structure and Mobility in Organic Field-Effect Transistors Based on Single Crystals of Tetrathiafulvalene Derivatives, *J. Am. Chem. Soc.*, 2004, **126**, 8546–8553.

[360] C. Brückner, M. Stolte, F. Würthner, J. Pflaum and B. Engels, QM/MM calculations combined with the dimer approach on the static disorder at organic-organic interfaces of thin-film organic solar cells composed of small molecules, *J. Phys. Org. Chem.*, 2017, **30**, 1–13.

[361] PVEducation, *Open-Circuit Voltage*, `https://www.pveducation.org/pvcdrom/solar-cell-operation/open-circuit-voltage`.

[362] D. F. Edwards and E. Ochoa, Infrared refractive index of silicon, *Appl. Opt.*, 1980, **19**, 4130–4131.

[363] PVLighthouse, *Solar Spectrum Calculator*, `https://www2.pvlighthouse.com.au/calculators/solar%20spectrum%20calculator/solar%20spectrum%20calculator.aspx`.

[364] S. Kowarik, A. Gerlach, S. Sellner, F. Schreiber, J. Pflaum, L. Cavalcanti and O. Konovalov, Anomalous roughness evolution of rubrene thin films observed in real time during growth, *Phys. Chem. Chem. Phys.*, 2006, **8**, 1834.

[365] R. J. Meier, On art and science in curve-fitting vibrational spectra, *Vib. Spectrosc.*, 2005, **39**, 266–269.

[366] NIST, *Vibrational scaling factors*, `https://cccbdb.nist.gov/vibscalejust.asp`.

[367] F. Anger, R. Scholz, A. Gerlach and F. Schreiber, Vibrational modes and changing molecular conformation of perfluororubrene in thin films and solution, *J. Chem. Phys.*, 2015, **142**, 224703.

LIST OF FIGURES

LIST OF ABBREVIATIONS

Miscellaneous

OSCs Organic semiconductors

OPV Organic photovoltaics

OLED Organic light-emitting diode

OFET Organic field-effect transistor

D:A Donor:acceptor

HOMO Highest occupied molecular orbital

LUMO Lowest unoccupied molecular orbital

GS Ground-state

CT Charge-transfer

ES Ehrlich-Schwöbel (barrier)

ρ_e Electron density

Q_z Momentum transfer along z-direction (perpendicular to substrate)

$Q_{||}$ Momentum transfer along xy-direction (parallel to substrate)

Materials

DIP Diindenoperylene

6T α-Sexithiophene

PEN Pentacene

DBTTF Dibenzo-tetrathiafulvalene

P3HT Poly(3-hexylthiophene)

F6TCNNQ 1,3,4,5,7,8-Hexafluoro-tetracyanonaphthoquinodimethane

TCNNQ Tetracyanonaphthoquinodimethane

Experimental methods

OMBD Organic molecular beam deposition

XRR X-ray reflectivity

GIXD Grazing incidence X-ray diffraction

VASE Variable angle spectroscopic ellipsometry

PMIRRAS Polarization-modulation infrared reflection-absorption spectroscopy

UV-vis-NIR Ultraviolet - visible - near-infrared

AFM Atomic force microscopy

LIST OF PUBLICATIONS

- G. Duva, L. Pithan, C. Zeiser, B. Reisz, J. Dieterle, B. Hofferberth, P. Beyer, L. Bogula, A. Opitz, S. Kowarik, A. Hinderhofer, A. Gerlach, and F. Schreiber, Thin Film Texture and Optical Properties of Donor/Acceptor Complexes. Diindenoperylene/F6TCNNQ vs. Alpha-Sexithiophene/F6TCNNQ, *J. Phys. Chem. C*, **122**, 2018, 18705-18714.

- G. Duva, A. Mann, L. Pithan, P. Beyer, J. Hagenlocher, A. Gerlach, A. Hinderhofer, and F. Schreiber, Template-Free Orientation Selection of Rod-Like Molecular Semiconductors in Polycrystalline Films, *J. Phys. Chem. Lett.*, **10**, 2019, 1031-1036.

- G. Duva, P. Beyer, R. Scholz, V. Belova, A. Opitz, A. Hinderhofer, A. Gerlach, and F. Schreiber, Ground-state charge-transfer interactions in donor:acceptor pairs of organic semiconductors - a spectroscopic study of two representative systems, *Phys. Chem. Chem. Phys.*, **21**, 2019, 17190-17199.

- C. Lorch, K. Broch, V. Belova, G. Duva, A. Hinderhofer, A. Gerlach, M. Jankowski, and F. Schreiber, Growth and annealing kinetics of α-sexithiophene and fullerene C60 mixed films, *J. Appl. Crystallogr.*, **49**, 2016, 1266.

- J. Dieterle, K. Broch, H. Frank, G. Duva, T. Storzer, A. Hinderhofer, A. Gerlach, F. Schreiber, Delayed Phase Separation in Growth of Organic Semiconductor Blends with Limited Intermixing, *Phys. Stat. Sol. (RRL)*, **11**, 2017, 1600428.

- B. Reisz, S. Weimer, R. Banerjee, C. Zeiser, C. Lorch, J. Dieterle, G. Duva, K. Yonezawa, J.-P. Yang, S. Kera, N. Ueno, A. Hinderhofer, A. Gerlach, and F. Schreiber, Structural, Optical and Electronic Characterization of Perfluorinated Sexithiophene Films and Mixed Films with Sexithiophene, *J. Mat. Res.*, **32**, 2017, 1908.

- T. Storzer, A. Hinderhofer, C. Zeiser, J. Novák, V. Belova, B. Reisz, S. Maiti, G. Duva, R. K. Hallani, A. Gerlach, J. E. Anthony, and F. Schreiber. Growth, Structure and Anisotropic Optical Properties of Difluoro-Anthradithiophene Thin Films, *J. Phys. Chem. C*, **121,** 2017, 21011.

- V. Belova, B. Wagner, B. Reisz, C. Zeiser, G. Duva, J. Rozbořil, J. Novák, A. Gerlach, A. Hinderhofer, and F. Schreiber, Real-time structural and optical study of growth and packing behavior of perylene diimide derivative thin films: The influence of side-chain modification, *J. Phys. Chem. C*, **122,** 2018, 8589.

- M. Hodas, P. Siffalovic, P. Nádaždy, N. Mrkyvková, M. Bodík, Y. Halahovets, G. Duva, B. Reisz, O. Konovalov, W. Ohm, M. Jergel, E. Majková, A. Gerlach, A. Hinderhofer, and F. Schreiber, Real-time monitoring of growth and orientational alignment of pentacene on epitaxial graphene for organic electronics, *ACS Appl. Nano. Mater.*, **1**, 2018, 2819.

- L. Pithan, D. Nabok, C. Cocchi, P. Beyer, G. Duva, J. Simbrunner, J. Rawle, C. Nicklin, P. Schäfer, C. Draxl, F. Schreiber, and S. Kowarik, Molecular structure of the substrate-induced thin-film phase of tetracene, *J. Chem. Phys.*, **149**, 2018, 144701.

ACKNOWLEDGEMENTS

I wish to thank all those who have supported me during the course of my doctoral studies. Especially I would like to thank Prof. Dr. Frank Schreiber for the possibility to carry out my doctoral project, for the outstanding tutoring during the entire doctoral studies and for his trust in me.

J. Prof. Katharina Broch for being the second reviewer of my thesis.

The German Research Foundation for the funding within the project SCHR700/20-1 "Charge transfer at organic semiconductor hetero-interfaces", and warmly the Carl-Zeiss-Stiftung for a fellowship in the period June 2015 - May 2018.

Dr. Alexander Hinderhofer for the excellent opportunity to collaborate with him and for the tutoring.

Dr. Alexander Gerlach for the collaboration and the many (non) scientific discussions.

Dr. Linus Pithan (ESRF ID03, earlier Humboldt Universität zu Berlin), without the collaboration with him a big part of this thesis would not have been possible. Thanks also for the critical proofreading of parts of my thesis.

Prof. Dr. Wolfgang Brütting (Universität Augsburg), Dr. Andreas Opitz (Humboldt Universität zu Berlin) and Dr. Paul Beyer (ESRF, earlier Humboldt Universität zu Berlin) for the very nice collaboration and the discussions within the CT-Project. Thanks to Dr. Andreas Opitz also for the critical proofreading of parts of my thesis.

Dr. Valentina Belova for the four years-long common work within the CT-Projekt.

Dr. Ronny Löffler (Universität Tübingen) and Dr. Tanja Martin (Universität Tübingen) for the help with the preparation and characterization of the PECVD-SiO_x layers on the Au substrates.

Dr. Christopher Lorch for giving me an introduction to the vacuum equipment in the laboratories of the group.

Alexander Mann for the collaboration within his master thesis.

To all the colleagues of the Schreiber group for the absolutely pleasant working atmosphere. With special urgency I would like to thank Dr. Martin Hodas, Dr. Antoni Franco Cañellas, Dr. Olga Matsarskaia, Berthold Reisz, Herrn Bernd Hofferberth, Frau Hanna Maurer und Frau Aleksandre Rötschke. Especially Jan Hagenlocher and Clemens Zeiser for the critical proofreading of parts of my thesis.

Unfortunately it is not possible to mention all the names at this stage, therefore I would like to thank at least Andreas Früh (Universität Tübingen) and Dr. Jiří Novák (Masaryk University).

In addition would like to thank Dr. Oleg Konovalov (ESRF, ID10), Dr. Chris Nicklin (DLS, I07) and Dr. Jonathan Rawle (DLS, I07) for supervising the experiments carried out at the respective synchrotron facilities.

My friends in Rome, with whom I have spent many beautiful moments during my holidays.

I also wish to thank my family for the support.

Last but not least is my biggest thanksgiving to Noémia, who since three years has enriched my life like nobody else and whose big support and encouragement have significantly contributed to the realization of this work. Thanks Noéminha!

DANKSAGUNG

Ich möchte mich bei allen bedanken, die mich im Laufe meiner Promotion unterstützt haben. Insbesondere danke ich Herrn Prof. Dr. Frank Schreiber für die Möglichkeit, in seiner Arbeitsgruppe mein Doktorprojekt durchzuführen, die hervorragende Betreuung während der gesamten Promotion und für das Vertrauen.

Frau JProf. Katharina Broch für die zweite Begutachtung meiner Dissertation.

Der Deutschen Forschungsgesellschaft für die Förderung im Rahmen des Projektes SCHR700/20-1 “Charge transfer at organic semiconductor hetero-interfaces”, und herzlich der Carl-Zeiss-Stiftung für ein Stipendium in den Zeitraum Juni 2015 - Mai 2018.

Herrn Dr. Alexander Hinderhofer für die ausgezeichnete Gelegenheit auf Zusammenarbeit und Betreuung während der gesamten Promotion.

Herrn Dr. Alexander Gerlach für die Zusammenarbeit und die viele (nicht) wissenschaftlichen Diskussionen.

Herrn Dr. Linus Pithan (ESRF, früher Humboldt Universität zu Berlin), ohne dessen Kooperation wäre ein großer Teil dieser Arbeit nicht möglich gewesen. Danke auch für das kritische Korrekturlesen von Teilen meiner Dissertation.

Herrn Prof. Dr. Wolfgang Brütting (Universität Augsburg), Herrn Dr. Andreas Opitz (Humboldt Universität zu Berlin) und Herrn Dr. Paul Beyer (ESRF, früher Humboldt Universität zu Berlin)für die sehr gute Kooperation und die Diskussionen im Rahmen des CT-Projektes. Danke an Dr. Andreas Opitz auch für das kritische Korrekturlesen von Teilen meiner Dissertation.

Frau Dr. Valentina Belova für die vier Jahre lange Zusammenarbeit im Rahmen des CT-Projektes.

Herrn Dr. Ronny Löffler (Universität Tübingen) und Frau Dr. Tanja Martin (Universität Tübingen) für die Hilfe mit der Herstellung und Charakterisierung der PECVD-SiO_x Schichen auf den Au Substraten.

Herrn Dr. Christopher Lorch für die Einführung auf die Vakuumsysteme in den Laboren der AG Schreiber.

Alexander Mann für die Zusammenarbeit im Rahmen seiner Masterthesis.

Allen Mitarbeitern der AG Schreiber für das ausgesprochen angenehme Arbeitsklima. Besonders hervorheben möchte ich Dr. Martin Hodas, Dr. Antoni Franco Cañellas, Dr. Olga Matsarskaia, Berthold Reisz, Herrn Bernd Hofferberth, Frau Hanna Maurer und Frau Aleksandre Rötschke. Insbesondere Jan Hagenlocher und Clemens Zeiser für das kritische Korrekturlesen von Teilen meiner Dissertation.

Es ist leider nicht möglich alle Namen an dieser Stelle aufzuschreiben, daher möchte ich mich zumindest bei Andreas Früh (Universität Tübingen) und Jiří Dr. Novák (Masaryk University) bedanken.

Zusätzlich möchte ich mich bei Dr. Oleg Konovalov (ESRF, ID10), Dr. Chris Nicklin (DLS, I07) und Dr. Jonathan Rawle (DLS, I07) für die Betreuung der Experimente an den jeweiligen Synchrotron-Einrichtungen bedanken.

Meinen Freunden in Rom, mit denen ich während meiner Urlaubstagen viele schöne gemeinsame Stunden verbracht habe.

Einen Dank möchte ich meiner Familie für die Unterstützung.

Zu guter Letzt gilt mein größter Dank Noémia, die mein Leben seit drei Jahren wie kein anderer Mensch bereichert und deren große Unterstützung und Anstoß maßgeblich zum Gelingen dieser Arbeit beigetragen haben. Danke Noéminha!